

**ON THE SHAPE AND DIMENSIONS
OF “SURFACE NANOBUBBLES”
IN ATOMIC FORCE MICROSCOPY**

DISSERTATION

zur Erlangung des Grades eines Doktors

der Naturwissenschaften

vorgelegt von

M.Sc. Wiktoria Wałczyk

eingereicht bei der Naturwissenschaftlich-Technischen Fakultät

der Universität Siegen

Siegen 2014

Vorsitzender: Prof. Dr. Holger Schönherr

Besitzer: PD Dr. habil. Brunero Cappella

Prof. Dr. Ulrich Jonas

Prof. Dr. Reinhard Trettin

Eingereicht am: 23-07-2014

Tag der mündlichen Prüfung: 25-09-2014

*The problems we face cannot be solved
by thinking the way we thought when we created them.*

Albert Einstein

Contents

Chapter 1	Bubbles on different length scales	1
1.1	Big and small bubbles	3
1.2	Study of surface nanobubbles – thesis structure	6
1.3	References	8
Chapter 2	Interfacial phenomena in water and aqueous solutions on the nanoscale – nanobubbles and micropancakes	11
2.1	The water/air interface – droplets and bubbles	13
2.1.1	Water in contact with surfaces	13
2.1.2	Bubbles in contact with surfaces	15
2.1.3	Water and wetting at the nanoscale	17
2.2	Early evidence for surface nanobubbles	19
2.3	Experimental techniques to study surface nanobubbles	22
2.3.1	Atomic Force Microscopy	22
2.3.2	Other techniques	28
2.4	Occurrence and morphology of surface nanobubbles	30
2.4.1	Morphology	30
2.4.2	Substrates	33
2.4.3	Gases	35
2.4.4	Liquids	37
2.5	Formation of surface nanobubbles	37
2.5.1	Nucleation methods	37
2.5.2	Origin and formation of surface nanobubbles	41

2.6 Stability of surface nanobubbles	46
2.6.1 Surface charges	46
2.6.2 Dynamic equilibrium model	47
2.6.3 Contamination	50
2.6.4 Contact line pinning and slow gas diffusion	51
2.6.5 Dense gas aggregate	53
2.7 Applications of surface nanobubbles	54
2.8 References	56
Chapter 3 Motivation and research objectives	69
3.1 Motivation	71
3.2 Research objective	75
3.3 References	76
Chapter 4 Surface nanobubbles on defined substrates	79
Binary Self-Assembled Monolayers of Alkanethiols on Gold: Deposition from Solution versus Microcontact Printing and the Study of Surface Nanobubbles	83
Published as:	
Haider Bayat, Davide Tranchida, Bo Song, Wiktoria Walczyk, Elena Sperotto and Holger Schönherr*	
<i>Langmuir</i> 2011 , <i>27</i> , 1353–1358.	
Introduction	83
Experimental Section	84
Results and Discussion	85
Conclusions	88
Supporting Information	89
Contact Angles of Surface Nanobubbles on Mixed Self-Assembled Monolayers with Systematically Varied Macroscopic Wettability by Atomic Force Microscopy	93
Published as:	
Bo Song, Wiktoria Walczyk, and Holger Schönherr*	
<i>Langmuir</i> 2011 , <i>27</i> , 8223–8232.	
Introduction	93
Experimental Section	94

Results and Discussion	95
Conclusions	101
Supporting Information	103
Chapter 5 The apparent shape of surface nanobubbles in tapping mode AFM	111
Closer Look at the Effect of AFM Imaging Conditions on the Apparent Dimensions of Surface Nanobubbles	115
Published as:	
Wiktoria Walczyk and Holger Schönherr*	
<i>Langmuir</i> 2013 , <i>29</i> , 620–632.	
Introduction	115
Experimental Section	116
Results and Discussion	116
Relevance of Setpoint Ratio and Amplitude in Studying Surface Nanobubbles	117
Constant Setpoint Ratio and Different Amplitudes	119
Constant Amplitudes and Different Setpoint Ratios	120
Size Dependence	124
Conclusions	125
Supporting Information	129
Chapter 6 The apparent shape of surface nanobubbles in Peak Force Tapping AFM	135
The effect of PeakForce tapping mode AFM imaging on the apparent shape of surface nanobubbles	139
Published as:	
Wiktoria Walczyk, Peter Schön, and Holger Schönherr*	
<i>J. Phys.: Condens. Matter</i> 2013 , <i>25</i> , 184005.	
Introduction	139
Experimental details	140
Results and Discussion	141
PeakForce TM AFM on surface nanobubbles	141
Dependence of the apparent nanobubble size on the scanning force in PFT AFM	142
Dependence of the apparent nanobubble size on the force in PeakForce TM as a function of the bubble size	145

Comparison of PeakForce tapping mode and tapping mode AFM	146
Conclusions	148
Supporting Information	151
Chapter 7 The interaction between AFM tips and surface nanobubbles	157
Characterization of the Interaction between AFM Tips and Surface Nanobubbles	161
Published as:	
Wiktorja Walczyk and Holger Schönherr*	
<i>Langmuir</i> 2014 , <i>30</i> , 7112–7126.	
Introduction	161
Experimental section	162
Results and Discussion	163
Force Volume AFM Measurements	163
Modelling of the Tip-Nanobubble Interaction	165
Nanobubble Stiffness	169
Bubble Deformation in AFM Experiments: Hydrophilic versus Hydrophobic Tip	171
Conclusions	173
Supporting Information	177
Chapter 8 Hydrodynamic effect of the tip movement on surface nanobubbles	191
Hydrodynamic effects of the tip movement on surface nanobubbles: A combined tapping mode, lift mode and force volume mode AFM study	195
Published as:	
Wiktorja Walczyk and Holger Schönherr*	
<i>Soft Matter</i> 2014 , DOI: 10.1039/C4SM01024H.	
Introduction	195
Experimental	196
Results	197
Discussion	200
Conclusions	203

Chapter 9	On the shape and deformation of surface nanobubbles in AFM	205
	On the Dimensions and the Profile of Surface Nanobubbles: Tip-Nanobubble Interactions and Nanobubble Deformation in Atomic Force Microscopy	209
	Wiktorja Walczyk and Holger Schönherr*	
	Manuscript submitted for publication	
	Introduction	211
	Experimental	214
	Results	216
	Discussion	228
	Conclusions	239
	Supporting Information	247
	Conclusions and outlook	257
	Summary	269
	Zusammenfassung	273
	Acknowledgements	277
	About the author	281

1

Bubbles on different length scales

Bubbles are ubiquitous in nature and our daily life, but their ephemeral character and “transparent” appearance often causes that they go unnoticed. Fragile and short-lived, bubbles of different sizes are essential for proper functioning of numerous systems and processes in contemporary technology and science. With bubbles being so common, it is surprising that their behavior and role in various phenomena is not yet fully understood and still needs to be investigated. In this introductory chapter that provides the background to the material presented in the thesis it is shown that bubbles are a fascinating topic. In addition, at the end of the chapter, the content of the following chapters is briefly described.

1.1 Big and small bubbles

When one puts water on a surface, the surface becomes wet. Depending on the characteristic of the surface, the water spreads easily forming a film or a puddle or breaks into droplets. When one looks very closely at the region, where water contacts the solid, one may be surprised to find out that not all solid surface is covered with water. Small features may appear between the liquid and the solid that are so tiny that they are not visible to the naked eye and their dimensions cannot be measured using a conventional optical microscope. Their tiny size was the main reason why they remained unnoticed for a very long time. Their observation was not possible until the 90's of the last century, when the techniques were developed that allowed one to study solid/liquid interface with nanoscale resolution. Shortly after the first discovery, the term 'surface nanobubbles' has been coined to name these small domains. The name is used until this day even though the word 'cavity' would be a more accurate description than the word 'bubble' (this issue is further described in Chapter 2).

Surface nanobubbles became the youngest member of a large family of bubbles. We all have experience with bubbles (and cavities) and we encounter them on a daily basis (see Figure 1.1), while dealing with liquids; for example: boiling water or blowing soap bubbles. Without bubbles, a shampoo would not foam and there would not be any carbonated beverage. It is the bubbles that make a whipped egg white fluffy and a yeast dough rise. Bubbles are also responsible for holes in cheese, bread and bath sponges.



Figure 1.1. Bubbles can be found in many places.

Knowing more about bubbles may help to understand why beer bubbles sink¹ or learn the best way to serve champagne.² However, the realm of bubbles extends far beyond every-day experience. In fact, bubbles can be found in many liquids and on every length scale from very large bubbles in liquid lava to microscopic size air bubbles in the bloodstream.

In nature, there are many systems where bubbles are not only welcomed but they are necessary. For example, bubbles have important role in many physical, chemical and biological processes occurring at the sea water/air interface. Bubbles formed in breaking waves^{3,4} are the main factor responsible for the transfer of oxygen between the air and the sea,⁵ transport of organic material and bacteria to the sea surface,⁶ and production of aerosols.⁷ They are also a source of underwater ambient noise⁸ and scatterers of underwater sound.^{9,10} Bubbles are also responsible for the underwater sound of rain. Most remarkably, the sound is not generated by an impact of a raindrop falling on a water surface. Instead, the impact of a drop creates a small bubble that oscillates and emits sound waves with a frequency in the audible range.¹¹

Bubbles of vaporized seawater form in lava during submarine eruptions and play a role in the creation of material that constitutes the oceanic crust.¹² Bubbles trapped in ice may provide information about the atmosphere on the earth hundreds of thousands of years ago.¹³

Many insects rely on bubbles, while diving using the air trapped inside a bubble as a supply of oxygen to breathe underwater.^{14,15} Other animals exhale bubbles underwater and use them for smelling.¹⁶ Examples are shown in Figure 1.2. Very small bubbles may be also a powerful weapon – it has been shown that certain shrimps use them to kill their prey.¹⁷

Presence of bubbles in vivo may pose threat equally for humans and for animals. The formation of bubbles from the gasses dissolved inside the body after leaving a high-pressure environment causes decompression sickness.¹⁸ Nanoscopic bubbles may be playing a role as nuclei for the growth of larger bubbles responsible for this condition.¹⁹ It has been discussed if exposition to acoustic waves produced by a sonar might enhance the formation of gas bubbles in blood vessels and organs causing death of whales and dolphins.^{20,21} It is also possible that bats flying near wind turbines die because of bubbles in lungs and hearts caused by low pressure created by the fast turning blades.²²

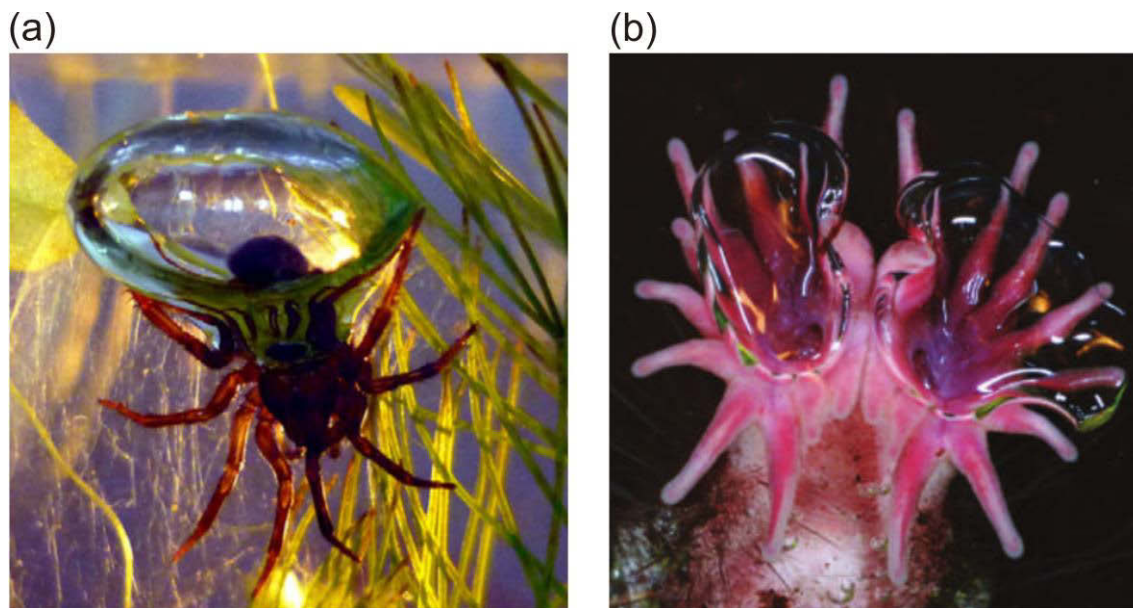


Figure 1.2. (a) Diving water spider (*Argyroneta aquatica*) carrying a small air bubble captured at the water surface. The spider uses oxygen from the bubble to breathe underwater (Reproduced with permission from ref. [15]). (b) Nose of the star-nose mole (*Condylura cristata*) breathing air bubbles in order to sniff while underwater (Reprinted by permission from Macmillan Publishers Ltd from reference [16], copyright 2006).

Another infamous phenomenon that involves bubbles is cavitation, first studied by Lord Rayleigh in the beginning of 20th century.²³ Microscopic size bubbles that are generated in low-pressure water zones near fast turning propellers of boats or submarines may damage the propellers when they collapse next to them. Shock waves created during collapse of thousands or millions individual bubbles are strong enough to cause such a large damage that cavitation became a limiting factor for the speed of boats and ships.

While the elimination of cavitation is a major concern in systems that involve machines moving fast through water, such as propellers, turbines or pumps, the damage caused by collapsing bubbles is a desirable phenomenon in ultrasonic cleaning. In industry, cavitation is often used for water purification and cleaning of contaminated surfaces and instruments. It plays also an important role in many medical and dental techniques, for example the destruction of kidney or bladder stones with focused ultrasonic pulses. Furthermore, the cavitation is used for homogenization, mixing or emulsification of various products such as milk, paint, mayonnaise or salad dressings.

Another important application of cavitating bubbles is sonochemistry²⁴ and sonoluminescence.²⁵ Bubble collapse induced by cavitation produces intense local heating and high pressures that may trigger or enhance the rates of chemical reactions. Under the conditions of controlled and stable cavitation, the bubble does not become destroyed but periodically shrinks and expands emitting short pulses of light in each oscillation cycle. During the shrinking phase, the pressure, temperature and chemical activity inside the bubble are significantly increased.²⁶

Besides being a source of energy, bubbles have several other applications. In fact, many branches of contemporary technology and science would not advance without the presence of bubbles. Bubbles are important in various industrial processes that require boiling or steam production, in cleaning and flotation processes e.g. in water treatment and mineral industry, in aeration systems, in ink-jet printing, in chemical industry, food industry, and in many other applications and areas. Oil industry uses bubbles to separate oil-water emulsions and benefits from gas-lift technology – bubbles injected in heavy oil to facilitate its production and transport. Microscopic size coated bubbles are used in medicine as ultrasound contrast agents and carriers for drug delivery. Furthermore, bubbles play a main role in production of foams such as porous polymers used for insulation, packing and sponges. Recently, novel methods, which were developed to produce materials filled with ordered and nearly uniform bubbles, provide a new sort of foams that may be formed into sheets and threads that can be used as membranes, acoustic filters or even may be woven into fabrics.^{27,28} Finally, bubbles have a range of applications in microfluidic systems and micro-chip laboratories – from mixing²⁹ to on-chip bubble logic.³⁰

1.2 Study of surface nanobubbles – thesis structure

Compared to other bubbles, surface nanobubbles are still relatively little known and belong to the anomalous behavior of water on the nanoscale. In particular, they exhibit a number of peculiar properties compared to macro- and microscopic bubbles, including unusually long-term stability and large contact angle values.^{31,32,33}

Why is it important to study nanobubbles? Water wets surfaces and this behavior is well understood from a theoretical and an experimental point of view on a macro- or microscopic length scale. However, our understanding of liquids on real surfaces on nanoscale is still incomplete. The phenomena involving water on (hydrophobic) surfaces have been studied for many years, but the nature of solid/water and air/water

interfaces on the nanoscale remains controversial. Studying surface nanobubbles contribute to the knowledge of the behavior and properties of three-phase contact line on the nanoscale. Nanoscopic insight into wetting phenomena offered by nanobubbles is crucial to characterize the full behavior of a solid/water system, also at the macroscopic scale. In addition, detailed investigations of the properties of surface nanobubbles would help to clarify the issue that has emerged recently that nanobubbles are not gaseous bubbles but may be nanodroplets of liquid contamination.³⁴

The aim of this thesis is to investigate the effect of Atomic Force Microscopy (AFM) on the measured apparent dimensions and shape of surface nanobubbles. The knowledge of the bubble shape is crucial and should precede any discussion about long-term stability of nanobubbles and related phenomena. This issue is explained in detail in Chapter 2 that collects basic information on wetting and surface nanobubbles and reviews the experimental and theoretical work done on nanobubbles so far. For clarity, the material is divided in several sections covering a range of topics, such as formation, occurrence, morphology and stability of surface nanobubbles as well as experimental techniques applied and current and possible applications of nanobubbles.

Chapter 3 provides the reader with the motivation behind the research done and points out the aims of individual AFM experiments on surface nanobubbles described in the following chapters.

Chapter 4 deals with the apparent high contact angles of surface nanobubbles. The issue has been addressed by investigating bubbles on defined substrates with precisely controlled wettability. The first part of the chapter provides a detailed description of the method used to produce substrates utilized in the experiments described in the second part of the chapter.

The next two chapters describe empirical data on apparent nanobubble shape in AFM images for varying scanning conditions in different AFM modes. Chapter 5 focuses on tapping mode (TM) AFM, in particular, on the effect of the amplitude of the cantilever oscillation and the amplitude setpoint ratio on the apparent bubble shape and dimensions. Chapter 6 describes the results of a complementary Peak Force AFM study that investigated the changes in the nanobubble appearance for varying peak scanning force.

Next, in Chapter 7, the interaction between an AFM tip and a nanobubble during the AFM scanning is investigated by performing and analyzing force-distance data acquired on nanobubbles in Force Volume mode AFM. In addition, the results of the experiment performed in lift mode AFM, described in Chapter 8, bring more insight into this issue. Finally, the shape and shape deformation of nanobubbles during the AFM scanning are the central questions in Chapter 9 that expands on the force measurement performed on nanobubbles.

The material in chapters 4 to 8 is presented in the form of articles, as it has been published in scientific journals. Chapter 9 is a manuscript submitted for publication.

1.3 References

- 1 Benilov, E. S.; Cummins, C. P.; Lee, W. T. Why do bubbles in Guinness sink? *Am. J. Phys.* **2013**, *81*, 88–91.
- 2 Liger-Belair, G.; Bourget, M.; Villaume, S.; Jeandet, P.; Pron, H.; Polidori, G. On the Losses of Dissolved CO₂ during Champagne Serving. *J. Agric. Food Chem.* **2010**, *58*, 8768–8775.
- 3 Lamarre, E.; Melville, W. K. Air entrainment and dissipation in breaking waves. *Nature* **1991**, *351*, 469–472.
- 4 Deane, G. B.; Stokes, M. D. Scale dependence of bubble creation mechanisms in breaking waves. *Nature* **2002**, *418*, 839–844.
- 5 Farmer, D. M.; McNeil, C. L.; Johnson, B. D. Evidence for the importance of bubbles in increasing air–sea gas flux. *Nature* **1993**, *361*, 620–623.
- 6 Blanchard, D. C.; Syzdek, L. D. Mechanism for the water-to-air transfer and concentration of bacteria. *Science* **1970**, *170*, 626–628.
- 7 Wu, J. Evidence of sea spray produced by bursting bubbles. *Science* **1981**, *212*, 324–326.
- 8 Prosperetti, A. Bubble-related ambient noise in the ocean. *J. Acoust. Soc. Am.* **1988**, *84*, 1042–1054.
- 9 Medwin, H. In situ acoustic measurements of bubble populations in coastal ocean waters. *J. Geophys. Res.* **1970**, *75*, 599–611.
- 10 Ye, Z.; Feuillade, C. Sound scattering by an air bubble near a plane sea surface. *J. Acoust. Soc. Am.* **1997**, *102*, 798–805.
- 11 Prosperetti, A.; Oguz, H. N. The impact of drops on liquid surfaces and the underwater noise of rain. *Annu. Rev. Fluid Mech.* **1993**, *25*, 577–602.
- 12 Perfitt, M. R.; Cann, J. R.; Fornarl, D. J.; Engels, J.; Smith, D. K.; Ridley, W. I.; Edwards, M. H. Interaction of sea water and lava during submarine eruptions at mid-ocean ridges. *Nature* **2003**, *426*, 62–65.

- 13 Bender, M.; Sowers, T.; Brook, E. Gases in ice cores. *Proc. Natl. Acad. Sci. USA* **1997**, *94*, 8343–8349.
- 14 Matthews, P. G. D.; Seymour, R. S. Diving insects boost their buoyancy bubbles. *Nature* **2006**, *441*, 171–171.
- 15 Seymour, R. S.; Hetz, S. K. The diving bell and the spider: the physical gill of *Argyroneta aquatica*. *J. Exp. Biol.* **2011**, *214*, 2175–2181.
- 16 Catania, K. C. Underwater ‘sniffing’ by semi-aquatic mammals. *Nature* **2006**, *444*, 1024–1025.
- 17 Versluis, M.; v. d. Heydt, A.; Schmitz, B.; Lohse, D. How snapping shrimp snap: through cavitating bubbles. *Science* **2000**, *289*, 2114–2117.
- 18 Francis, T. J. R.; Mitchell, S. J. 10.6: Manifestations of Decompression Disorders. *Bennett and Elliott's physiology and medicine of diving (5th Revised eds. Brubakk, A. O.; Neuman, T. S.)* United States: Saunders, **2003**, 578–599.
- 19 Craig, V. S. J. Formation of Micronuclei Responsible for Decompression Sickness. *J. Colloid Interface Sci.* **1996**, *183*, 260–268.
- 20 Piantadosi, C. A.; Thalmann, E. D. Pathology: Whales, sonar and decompression sickness. *Nature* **2004**, *428*, 1–1.
- 21 Fernández, A.; Arbelo, M.; Deaville, R.; Patterson, I. A. P.; Castro, P.; Baker, J. R.; Degollada, E.; Ross, H. M.; Herráez, P.; Pocknell, A. M.; Rodríguez, E.; Howie, F. E.; Espinosa, A.; Reid, R. J.; Jaber, J. R.; Martin, V.; Cunningham, A. A.; Jepson, P. D. Pathology: Whales, sonar and decompression sickness (reply). *Nature* **2004**, *428*, 1–2.
- 22 Curry, A. Deadly Flights. *Science* **2009**, *325*, 386–387.
- 23 Strutt, J. W. (Lord Rayleigh) On the Pressure Developed in a Liquid During the Collapse of a Spherical Cavity. *Philos. Mag.* **1917**, *34*, 94–98.
- 24 Suslick, K. S. Sonochemistry. *Science*, **1990**, *247*, 1439–1445.
- 25 Gaitan, D. F.; Crum, L. A.; Church, C. C.; Roy, R. A. Sonoluminescence and bubble dynamics for a single, stable, cavitation bubble. *J. Acoust. Soc. Am.* **1992**, *91*, 3166–3183.
- 26 Didenko, Y. T.; Suslick, K. S. The energy efficiency of formation of photons, radicals and ions during single-bubble cavitation. *Nature* **2002**, *418*, 394–397.
- 27 v. d. Net, A.; Gryson, A.; Ranft, M.; Elias, F.; Stubenrauch, C.; Drenckhan, W. Highly structured porous solids from liquid foam templates. *Colloids and Surfaces A* **2009**, *346*, 5–10.
- 28 Leroy, V.; Bretagne, A.; Fink, M.; Willaime, H.; Tabeling, P.; Tourin, A. Design and characterization of bubble phononic crystals. *Appl. Phys. Lett.* **2009**, *95*, 171904.
- 29 Garstecki, P.; Fuerstman, M. J.; Fischbach, M. A.; Sia, S. K.; Whitesides, G. M. Mixing with bubbles: a practical technology for use with portable microfluidic devices. *Lab Chip* **2006**, *6*, 207–212.
- 30 Prakash, M.; Gershenfeld, N. Microfluidic Bubble Logic. *Science* **2007**, *315*, 832–835.
- 31 Hampton, M. A.; Nguyen, A. V. Nanobubbles and the nanobubble bridging capillary force. *Adv. Coll. Interf. Sci.* **2010**, *154*, 30–55.

- 32 Craig, V. S. J. Very small bubbles at surfaces – the nanobubble puzzle. *Soft Matter* **2011**, *7*, 40–48.
- 33 Seddon, J. R. T.; Lohse, D. Nanobubbles and micropancakes: gaseous domains on immersed substrates. *J. Phys.: Condens. Matter* **2011**, *23*, 133001.
- 34 Berkelaar, R. P.; Dietrich, E.; Kip, G.; Kooij, S.; Zandvliet, H.; Lohse, D. Exposing nanobubble-like objects to a degassed environment. *Soft Matter* **2014**, *10*, 4947–4955.

2

Interfacial phenomena in water and aqueous solutions on nanoscale – nanobubbles and micropancakes

Without doubt, water is the most ubiquitous and one of the most studied liquids. It is also possible that water possesses the most complex and intriguing properties among all known fluids. This statement is especially true if one looks at the properties of water near interfaces. The phenomena that occur at the point where water contacts an other state of matter appear to be more complicated, the more closely one looks. The existence of surface nanobubbles that seemingly violates the widely accepted theoretical predictions, may serve as an example of the manifestation of this effect. This chapter presents a summary of the current knowledge on surface nanobubbles and related phenomena, which includes both theoretical considerations and experimental evidence.

2.1 The water/air interface – droplets and bubbles

When liquid water is in contact with a different phase, an interface is formed. Unlike bulk molecules that have neighbors in all directions, at the interface, the two phases of matter meet such that the molecules have neighbors of the same type only on one side. Thus, surface molecules are different from those in the bulk. Moreover, the presence of different phase of matter affects not only the first layer of molecules forming the border, but may reflect on the properties of the molecules that are in direct vicinity of the two-phase contact region.

The behavior and properties of liquid water in the proximity of a gas phase are especially interesting in the context of this thesis. Therefore, before one focuses on a detailed description of surface nanobubbles, basic information about water and the air/water interface on the macro- and nanoscale are presented and parameters are defined that will be used throughout the following chapters.

2.1.1 Water in contact with surfaces

From an everyday experience, we know that a small amount of water deposited on a smooth horizontal solid surface forms a droplet. The droplet tends to minimize the surface area of all its interfaces, which manifests itself in curving of its air/water interface to a spherical cap-shape (this holds under the assumption that the droplet is small). At the points of the three-phase contact line, the droplet makes contact with the solid at an angle θ called Young's angle, which is given by

$$\cos \theta = \frac{\sigma_{sv} - \sigma_{sl}}{\sigma_{lv}} \quad (2.1)$$

where σ_{ij} denotes the interfacial energy between phases s (solid), l (liquid) and v (vapor).

The contact angle provides a measure of the wettability of a surface. The principle of this phenomenon is shown in Figure 2.1. As the material is more hydrophilic, the tendency of a droplet to spread across the surface increases and its contact angle decreases. In the opposite situation, when the material is more hydrophobic, the droplet tends to minimize the contact surface area with the solid and its contact angle increases.

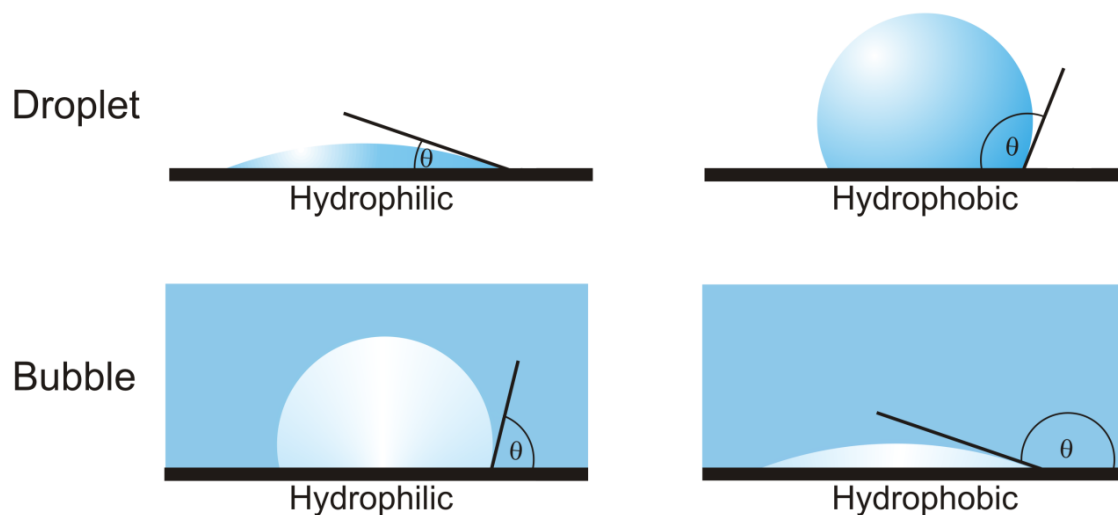


Figure 2.1. Illustration of contact angles formed by liquid drops and gas bubbles on smooth homogeneous solid surfaces with different wettability.

One can consider the situation when the liquid and the vapor phase are inversed and one deals with a vapor bubble resting on the solid surface (termed 'surface bubble'). The curvature of the bubble has the opposite sign, as compared to the droplet, and its contact angle is defined on the liquid side i.e. outside the bubble. Unlike a droplet, on a hydrophilic material, the bubble tends to *decrease* its contact surface area with the solid that leads to a decrease in its contact angle. On a hydrophobic material, the bubble tends to *increase* its contact surface area and spreads so that its contact angle increases. Therefore, bubbles on hydrophobic substrates will tend to flatten whereas droplets will protrude more than on hydrophilic substrates. Because the issue of the contact angle of bubbles will be extensively discussed in the next chapters, it is important to keep this difference between bubbles and droplets in mind.

For water droplets, a contact angle less than 90° (low contact angle) indicates a hydrophilic material for which wetting of the surface is very favorable. Contact angles greater than 90° (high contact angle) describe a hydrophobic material, for which the wetting is unfavorable. Superhydrophobic surfaces have contact angles greater than 150° , showing almost no contact between the drop and the surface, and almost complete spreading of the bubble.

2.1.2 Bubbles in contact with surfaces

Before proceeding, the distinction has to be made between a common and an actual meaning of the word ‘bubble’. As a widespread mistake, any entity of gas or vapor separated from a surrounding material, will it be gas, or liquid or solid, is called a ‘bubble’. However, as shown in Figure 2.2a, a real bubble has two liquid interfaces that separate the gas inside the bubble from the gas outside the bubble. A classic example of an actual bubble is a soap bubble that has two air/water interfaces – one that contacts the gas trapped inside the bubble, and the other one that contacts the gas outside the bubble. On the contrary, a void filled with gas surrounded by different medium is called a ‘cavity’. Unlike a bubble, a cavity has only one interface. Depending on the surrounding medium, a cavity may have either a gas/liquid interface or a gas/solid interface. For example, gas in sparkling water or holes in aerated chocolate bars are examples of voids, even though they are commonly called ‘bubbles’. Also nanobubbles discussed in this thesis are, according to the definition, not actual bubbles but voids. However, because the name ‘nanobubble’ is used in practically all material published on the topic, similar nomenclature is followed in this thesis.

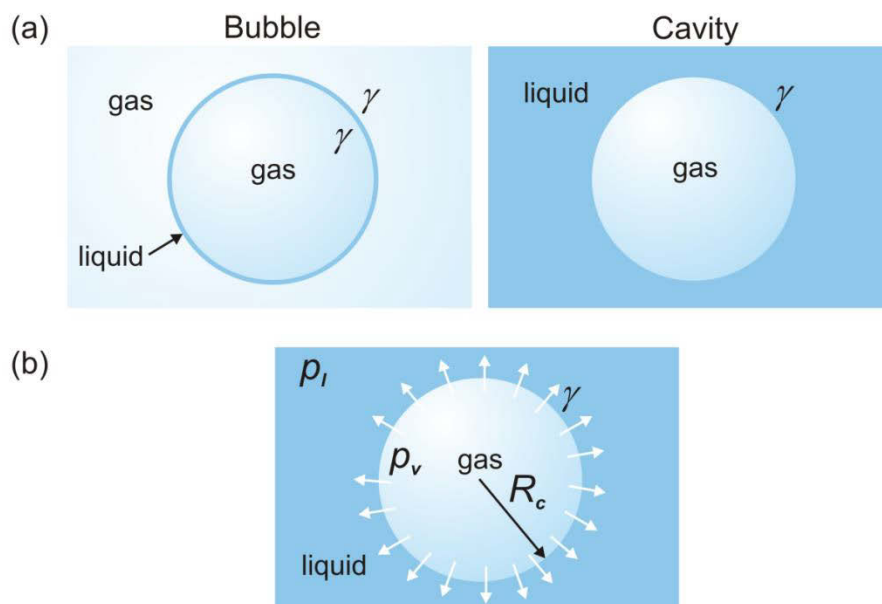


Figure 2.2. (a) An example of a gas bubble with two gas/liquid interfaces and a gas cavity with one gas/liquid interface. (b) Pressure difference across the gas/liquid interface drives the outward gas diffusion.

Obviously, a gas cavity or a bubble surrounded by liquid constitutes an entirely different system than a drop of liquid surrounded by gas. Unlike the droplet, which is in thermal equilibrium and is stable, the bubble is out of equilibrium and tends to dissolve. As long as the surrounding liquid is not supersaturated, the gas inside the bubble will be released into the liquid through the bubble wall, as shown schematically in Figure 2.2b. At the atmospheric pressure (or at any pressure), all free bubbles dissolve because the gas pressure near the bubble wall is greater than the one in the bulk liquid far away from the bubble. This causes a positive Laplace pressure Δp_L inside the bubble

$$\Delta p_L = p_v - p_l = \frac{2\gamma}{R_c} \quad (2.2)$$

with γ the surface tension and R_c the radius of curvature of the bubble surface. The Laplace pressure increases for smaller bubbles.

According to Henry's law, the increased pressure near the bubble wall causes an increased gas concentration, which drives the diffusion of gas away from the bubble. As the bubble dissolves, it shrinks and the increasing pressure inside the bubble causes a further increase in the diffusive outflux of gas that accelerates the dissolution.

The dissolution times of bubbles τ can be estimated from the following dependence based on the diffusion equation that describes the transport of gas out of the bubble

$$\tau \sim \frac{R_{c0}^2}{D} \quad (2.3)$$

with R_{c0} the initial radius of the bubble and D the diffusion constant. For an air bubble with initial $R_{c0} = 100$ nm that has an excess pressure between one and two atmospheres, the lifetime estimated from this formula is of the order of 100 μ s.^{1,2}

The analysis was derived for free gas bubbles in the liquid. However, if the bubble interface is not pinned to the solid substrate, it may be applied to a spherical cap-shaped surface bubble as well.

2.1.3 Water and wetting at the nanoscale

In many systems, physical, chemical, and biological processes that occur at the atomic-length scale often have an impact at processes visible on the macroscopic level. Because many of these processes take place at water/solid or water/air interfaces, it is important to understand the properties and behavior of water near such interfaces at nanoscale. The ubiquity of water and the fact that it can be found in systems on all length scales from living cells to distant planets, makes this topic particularly interesting.

Compared to other liquids, water displays several unusual and intriguing properties. This statement is especially true at the nanoscale. It is known that bulk water, water near surfaces and confined water have unique properties when investigated at the nanoscopic level. In particular, the behavior of gas at liquid/solid interface on the nanoscale is usually different than in the bulk state.^{3,4}

According to the phase diagram, the phase state of water is defined by its temperature and pressure. At the nanoscale, the situation may be different. Near a solid wall, the molecules are compelled to organize more efficiently than in the bulk and they create orderly layers.⁵ Nanoscale volumes of water may also be in different state than predicted by the macroscale phase diagram.^{6,7,8,9} The density of water near the water/air interface at room temperature may be increased and comparable to the density of bulk water at a lower temperature.¹⁰ It has been reported that water inside the capillary bridges at room temperature is in a liquid-ice condensate state that is neither liquid, nor solid.^{11,12} In addition, dense, ice-like structured water adsorbed at surfaces has been found.^{13,14,15,16} On the other hand, the persistence of water in the liquid state at temperatures far below 0 °C, when close to a solid surface, was termed 'supercooling'.¹⁷ Finally, greater ice nucleation at the surface was observed in undercooled water.¹⁸ Another reported unusual properties of water at the nanoscale include a melting point depression¹⁹ and the metastability of small volumes of water.^{20,21,22}

The proximity to solid surfaces, also known as 'nanoconfinement', results in a significant transition in the properties of water at the atomic-length scale. For example, reduced mobility²³ and increased viscosity^{24,25,26} of nanoconfined water have been observed. In addition, nanoconfinement affects the thermal expansion of water^{27,28} and the thermal transport of surfaces.²⁹

The phenomenon of wetting of surfaces at the nanoscale is an important scientific issue with implications in many areas of technology. The topic was extensively studied on the macroscale, while on the micro- or nanoscale many issues still need to be addressed. It is likely that at small length scales, a proximity of a hydrophobic surface affects the water structure and its properties differently than the proximity of a hydrophilic surface.³⁰

The size of nanoscopic droplets and bubbles may be comparable with the range of molecular interactions. Importantly, the influence of gravity is negligible compared to the influence of surface tension so the droplet or the bubble can be approximated as part of a sphere.³¹ In addition, the wetting behavior on the nanoscale may be significantly influenced by line tension and liquid evaporation or bubble dissolution (both are usually negligible on the macroscale). As the size of the droplet/bubble decreases, the effect of line tension becomes more significant compared to the effect of surface tension^{32,33} and may affect the contact angle.³⁴ Consequently, the macroscopic definition of surface tension has to be adjusted to nanoscopic droplets and bubbles. This is usually done by modifying the Young's equation to account for the effect of line tension.^{33,35} However, from experimental evidence, it is not clear what a proper description of the contact angle on the nanoscale should be. Contradicting results on the role of line tension and the character of the contact angle dependence on the droplet size were reported for various liquids including water.^{36,37,38,39,40,41,42,43} Interestingly, Cheng *et al.*⁴⁴ showed that lotus leaves lost their superhydrophobic character ('lotus effect') when water microdroplets were deposited on the leaf.

It is possible that at the nanoscale, small surface heterogeneities are responsible for the observed variation in contact angle when the droplet size is decreased. Physical roughness, chemical inhomogeneities, microscopic defects or contamination may affect the wetting behavior of small drops and bubbles in ways that are not yet well understood. For example, pinning of the three-phase contact line influences the shape of nanoscopic drops changing the local nanoscopic contact angle^{45,46} and possibly affecting the macroscopic contact angle. In particular, the pinned contact line will cause the change in the contact angle of the droplet/bubble during evaporation/dissolution^{47,48} In addition, in the case of pinning of the contact line, the determined contact angle does not entirely characterize the hydrophobic properties of the surface.



Figure 2.3. On the nanoscale, the shape of bubbles may deviate from a spherical cap and the contact angle may be over- or underestimated.

As shown in Figure 2.3, in general, it is not clear if the macroscopic definition of the contact angle may be applied to nanoscopic droplets and bubbles because the shape of the three-phase contact line near the air/liquid/solid contact point may deviate from a spherical profile.⁴⁶ If this is the case, the contact angle estimated by fitting an arc to the entire profile may differ from the actual contact angle.

So far, the wetting theories on the nanoscale were tested mainly on ultrasmall droplets on solid surfaces. Nanoscopic size bubbles on surfaces, described in the next sections of this chapter, present an alternative system to investigate the contact angle phenomenon, wetting behavior and properties of water near surfaces on the nanoscale.

2.2 Early evidence for surface nanobubbles

The hypothesis for the existence of surface nanobubbles was put forward in 1994, when Parker and his co-workers reported on possible causes of the increased long-range attraction between hydrophobic surfaces immersed in water.⁴⁹ In order to explain a shape of an AFM approach force-distance curve (Figure 2.4) showing a stepwise increase in attraction with decreasing separation between the surfaces, the authors suggested the existence of tiny bubbles between the surfaces. As the surfaces were brought together and were approximately hundred nanometers apart, the bubbles from the one surface would jump toward the other surface bridging the gap and creating attraction increasing in steps (jumps) visible in the force curve. The hydrophobic attraction was observed earlier⁵⁰ but could not be explained by the theory existing at this time.

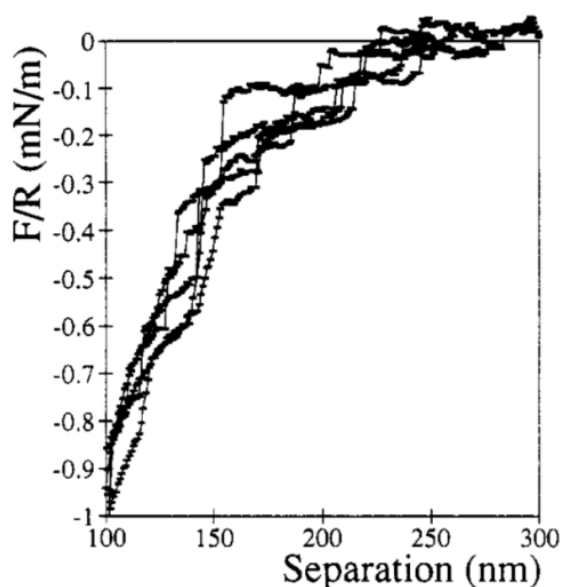


Figure 2.4. Force-separation curve with discrete jumps measured while approaching two (tridecafluoro-1,1,2,2-tetrahydrooctyl)dimethylchlorosilane surfaces in water (Reprinted with permission from ref: [49]; Copyright (1994) American Chemical Society).

The hypothesis of the presence of stable nanobubbles contradicting theoretical predictions was controversial and has been questioned several times over the years.^{51,52,53,54} Several authors might deal with nanobubbles before Parker *et al.* published their findings but considered them a sort of contamination.^{55,56}

One of the first experimental evidences confirming the existence of (gaseous) nanobubbles on surfaces was provided by Miller *et al.*⁵⁷ in 1999. The spectra of butane-saturated water on hydrophobised silicon surface obtained in the experiment done with Fourier transform infrared spectroscopy suggested the presence of butane gas, with only small amount of butane adsorbed on the surface. The amount of gas butane increased for more hydrophobic surface, as compared to a more hydrophilic surface, and diminished with time suggesting that the bubbles were dissolving.

A short time later, first direct evidence of the existence of surface nanobubbles in the form of AFM (Atomic Force Microscopy) images of nanobubbles (shown in Figure 2.5) was reported independently by two research groups.^{58,59} The nanobubbles detected on a hydrophobised substrate had an estimated diameter of approximately 650 nm and a height of 40 nm or less, hence they displayed different shapes than macroscopic bubbles, having a much higher contact angle. It has been established that they are soft, presumably gaseous domains that may deform during the AFM imaging.

Lou *et al.*⁶⁰ showed the dependence of nanobubble appearance on the treatment and history of the sample and introduced a protocol to nucleate surface nanobubbles, known as ethanol-water exchange, which has been employed in many experiments afterwards.

The introduction of, what seemed, a reliable method of producing nanobubbles initiated a rapid growth of number of studies done on the topic. Worth mention is the contribution of Tyrrell *et al.*^{61,62} who analyzed force-distance curves acquired on the nanobubbles and correlated the separation distance of a jump-in point with the apparent nanobubble height measured from the topographic AFM image. The authors also showed that nanobubbles could be moved over the substrate and that they could coalesce with neighboring bubbles when sufficiently large forces were applied on the AFM tip.

In the following, the existence of surface nanobubbles has been tested and confirmed in numerous experiments. The bubbles were reported on many substrates, mostly hydrophobic, and subjected to various experimental conditions in order to test their formation, appearance, spatial and temporal stability and other properties. Nowadays, 20 years after Parker *et al.* introduced their hypothesis of bridging nanobubbles, many questions have been answered. The knowledge and experimental evidence acquired over the years brought current research on surface nanobubbles to an advanced level. The next sections of this chapter summarize and review the work published so far and present the remaining challenges and issues that still need to be addressed.

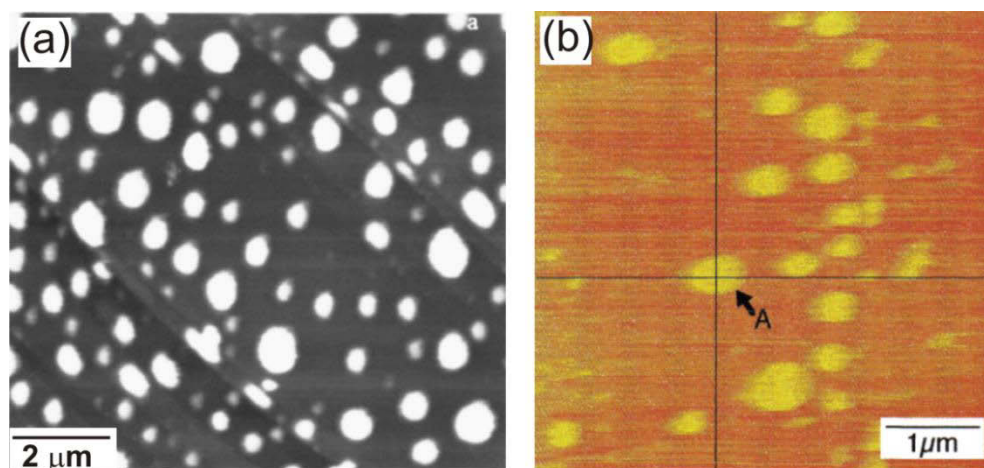


Figure 2.5. Two of the first AFM topographic images of surfaces nanobubbles (a) on HOPG (highly oriented pyrolytic graphite) (Reprinted with permission from ref. [58]. Copyright (2000), American Vacuum Society), (b) on OTS (octadecyltrichlorosilane) coated Si. (Reprinted with permission from ref. [59]. Copyright (2000) American Chemical Society).

2.3 Experimental techniques to study surface nanobubbles

Due to small size of nanobubbles and their liquid environment, a limited number of techniques have been utilized to investigate them. The most prominent among them is Atomic Force Microscopy (AFM).⁶³ Compared to other techniques, AFM has become the standard technique for analyzing surface nanobubbles mainly because of its ability to investigate the shape and the size of nanobubbles simultaneously with nanometer scale resolution. The following section provides basic information on AFM and briefly describes AFM scanning modes utilized to investigate surface nanobubbles.

2.3.1 Atomic Force Microscopy

In AFM, the surface is imaged based on sensing interaction forces between atoms of a sharp tip mounted on a flexible cantilever and atoms of the sample. During the measurement, depending on the microscope model, the cantilever and the tip is lowered toward the sample or the sample is lifted toward the tip until the “contact” is made. The displacement of the cantilever is detected via a laser beam reflected from the top side of the cantilever onto a photodetector. Any change in the deflection of the cantilever in response to varying interaction forces acting on the tip end causes a displacement of the laser beam, and is detected as a change in photodetector output voltage. The cantilever is moved in a certain way over the sample (usually lines) and the information over the surface is gathered. The spatial resolution depends on the tip shape and the microscope model but is in nanometer range. With a proper calibration, changes in the voltage are transformed into changes of the sample topography or other parameters.

So far, a number of imaging modes were employed to study surface nanobubbles. They are based on different principles, operate in different force regimes and are able to provide a range of different information about the sample.

Contact mode AFM

Contact mode or CM is the simplest AFM mode. During imaging, the tip remains “in contact” with the sample at all times. The force exerted on the tip is equal to the deflection of the cantilever multiplied with the spring constant of the cantilever. The deflection, and hence the force is kept constant at all points

of the sample. The ‘height’ is obtained from the changes in the vertical position of the tip controlled via a feedback loop.

As shown schematically in Figure 2.6, contact mode is considered not suitable for sensing surface nanobubbles because of relatively large lateral forces, which may lead to a severe deformation of soft samples.^{64,65,66} So far, only few authors reported successful imaging of surface nanobubbles in the CM AFM.^{58,61,67,68}

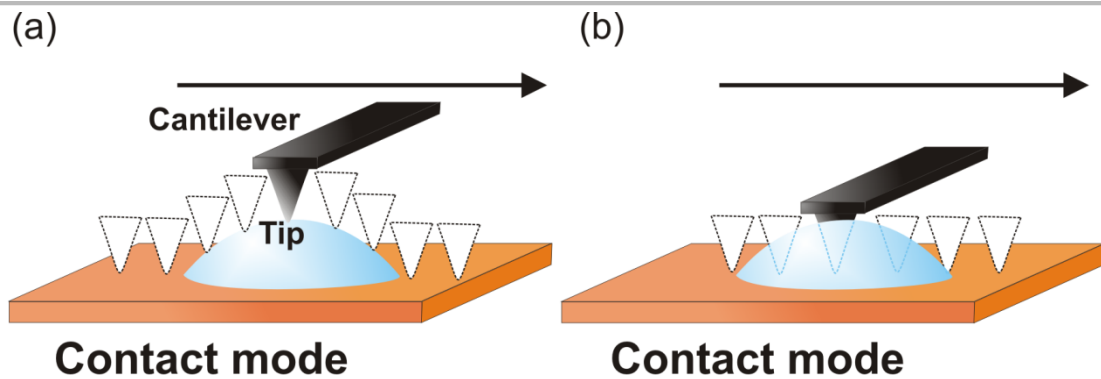


Figure 2.6. In the contact mode AFM, the cantilever with the tip moves horizontally and the tip apex follows the sample surface. (a) Idealized behaviour of the tip on a nanobubble. (b) In practice, large lateral imaging forces and low nanobubble resistance to the tip movement are the main reasons that bubbles do not appear in the CM topographic images.

Tapping Mode AFM

An alternative to contact mode is the so-called intermittent, or tapping mode (TM) AFM (Figure 2.7). Contrary, to contact mode, in TM imaging, the cantilever is oscillated at (or close to) its resonance frequency f_0 with an amplitude A . When the tip is far from the sample surface, A is equal to the free (maximum) amplitude A_0 . When the tip is lowered toward the sample during a topographic scan, A_0 is damped by the interaction forces between the tip apex and the surface. In the vicinity of the surface, the amplitude is decreased to minimum (zero).

In a particular tapping mode experiment, the extent of damping of the oscillation upon establishing ‘‘contact’’ with the surface is defined by a setpoint amplitude A_{sp} or the setpoint ratio $(A_{sp}/A_0) \times 100\%$. In general, a large setpoint value means smaller damping and, because the amplitude and the force dependences are related,⁶⁹ it also means smaller force exerted on the sample and experienced by the tip.

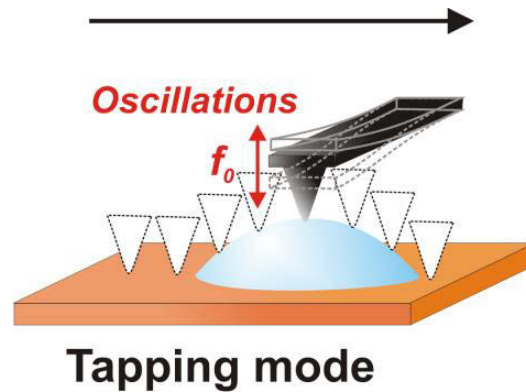


Figure 2.7. In tapping mode AFM, the cantilever is oscillated near its resonant frequency, while the tip is moved horizontally over the sample surface. The interaction forces cause damping of the oscillation amplitude.

Upon contact with the sample, not only the amplitude of the cantilever oscillation will be damped but also the frequency of oscillation will change causing a shift in a phase signal between the drive frequency and the actual frequency. The magnitude of this phase shift depends on mechanical and adhesive properties of the sample (energy dissipation). The phase signal may be acquired in TM along with a topographic image. Phase images provide information on changes in the material properties of the surface. However, they provide only qualitative data.^{70,71}

Although not mentioned in many descriptions, in TM AFM, in addition to oscillatory movement of the cantilever and damping, the cantilever may also be deflected when in contact with the sample. Whereas most of the interaction energy is used to damp the oscillation, a part of energy may be transferred into a change in shape (bending) of the cantilever. The resulting deflection is usually very small (few nanometres for standard conditions – small amplitudes and large setpoint ratios) hence, much smaller than in CM AFM.

In sum, due to repeated very rapid engaging and disengaging with the sample surface, the tapping mode AFM allows less harsh scanning conditions than the contact mode making it suitable for investigating soft samples like surface nanobubbles.^{58,59,61,72,73,74,75} Lateral forces are greatly reduced. Forces exerted on the sample by the tip are on average lower than in contact mode, but the interaction is complex. Experiments done on nanobubbles in TM AFM are described in Chapter 4 and in Chapter 5.

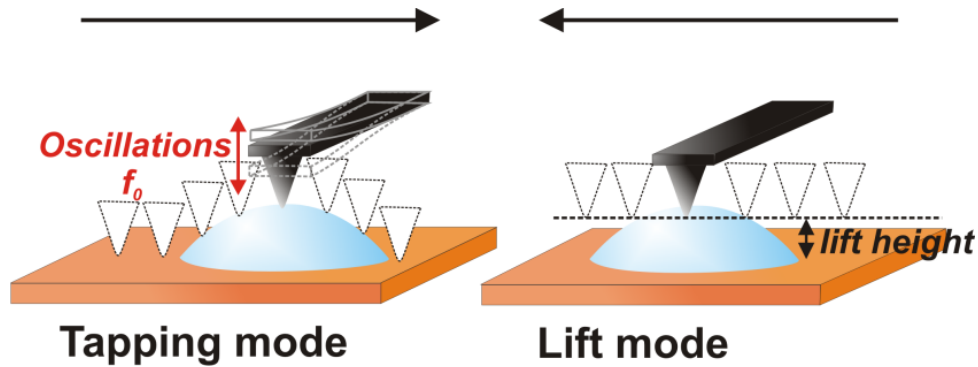


Figure 2.8. The movement of the AFM tip for a single scan line during the measurement done in lift mode AFM: on the way forward, the scan is done in tapping mode AFM; on the way back, the line is rescanned with the tip moved horizontally at the fixed separation distance (lift height) to the sample.

Lift mode AFM

In experiments done on surface nanobubbles, lift mode AFM is correlated with TM. The cantilever is moved over the sample line by line similarly as it is done in other AFM modes. As shown in Figure 2.8, during the imaging, each line is scanned in TM in one direction (trace), then the tip is lifted above the sample for a certain height and the line is rescanned in reversed direction (retrace) in the lift mode at constant height. The height offset is called the lift height. As the tip is being moved over the sample during scanning in lift mode, the deflection of the cantilever is measured and the data is collected in a deflection image.

Only one experiment on surface nanobubbles done in the lift mode AFM has been reported so far.⁷² Another experiment is described in Chapter 8 of this thesis.

Non-contact mode AFM

During the imaging done in this mode, the cantilever is oscillated at very small amplitudes of a few nanometers and the tip does not contact the sample surface. Changes in the oscillation amplitude or phase due to long-range forces (van der Waals, electrostatic) are used to determine the position of the surface and to adjust the cantilever position so that the tip stays out of contact with the sample at all times. Moreover, non-contact mode AFM does not suffer from tip or sample degradation effects that are sometimes observed after taking numerous scans in CM or TM AFM.

This makes the non-contact AFM suitable for measuring soft samples like surface nanobubbles.⁷⁶

Frequency Modulation mode AFM

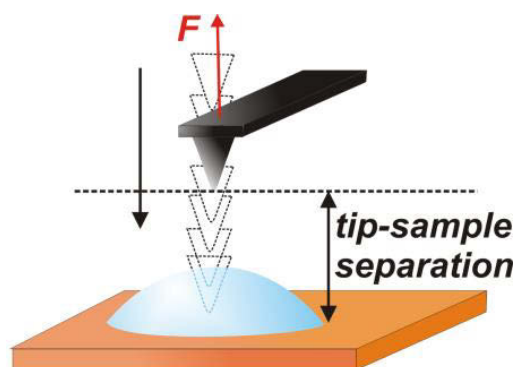
In the frequency modulation (FM) AFM, the cantilever is oscillated at its resonant frequency. During the measurement, the amplitude of cantilever oscillation is kept constant while the change of its resonant frequency due to interaction forces between the tip and the sample is detected. Topographic images show the profile of the surface with constant frequency shift i.e. constant difference between the resonant frequency of free cantilever and the resonant frequency of interacting cantilever. FM AFM is usually used in ultra-high vacuum but can also be used in liquid.

Two experiments done on surface nanobubbles in FM AFM were reported recently.^{77,78}

Force-Volume AFM

Besides imaging, AFM cantilever can be used as a force sensor to measure interaction forces between a tip and a sample. The technique is called Force-Volume (FV) AFM or force mapping AFM (Figure 2.9). The cantilever is usually not oscillated, and its deflection is monitored as a function of the tip separation to the surface. In a single cycle, a force-displacement curve is generated as the tip is moved vertically perpendicular to the sample surface and is brought into and out of contact with a surface. Alternatively, the cantilever is oscillated and a decrease in the oscillation amplitude due to interaction forces is measured as a function of the tip-sample separation. The force-displacement or amplitude-displacement curves may be acquired sequentially on different positions on the sample in order to create a force image or amplitude image, respectively. In the image, each pixel represents a distinct horizontal position of the tip over the sample and contains a set of data acquired at this point.

The Force- (and Amplitude-) Volume mode is commonly used to study mechanical properties of the sample or forces between surfaces on the nanoscale in air and in liquid environment. So far, a FV AFM experiment conducted on surface nanobubbles was reported by Peng *et al.*⁷⁹



Force Volume mode

Figure 2.9. In the Force-Volume AFM mode, the tip is moved vertically toward the sample and subsequently away from the sample. During the movement, the force exerted on the tip is measured.

Peak Force Tapping mode AFM

The Peak Force Tapping (PFT) mode is an AFM imaging mode based on force spectroscopy. Apart from topographic images of the sample, it provides high resolution maps of several parameters calculated from the force-displacement curve: stiffness, deformation, adhesion (pull-off force) and energy dissipation.

In the PFT, unlike in the TM, the tip is oscillated out of resonance at a frequency of 1-10 kHz, which is lower than in standard TM in liquid. The amplitude of the cantilever oscillation may be varied from fractions of a nanometer to a few micrometers. At each point of the scanned area of the sample, the cantilever is first lowered toward the surface and then it is withdrawn. In each oscillation cycle, a force-displacement curve is measured. The parameter maintained constant during the measurement is the peak load force, so that at each point of the sample, the nominal force exerted on the surface is the same.

Recent reports of Zhao *et al.*⁸⁰, Yang *et al.*⁷⁷ and Song *et al.*⁸¹ describe experiments performed on surface nanobubbles in Peak Force AFM. The results of another experiment are presented in Chapter 6.

2.3.2 Other techniques

In addition to direct evidence of surface nanobubbles provided in abundance by the AFM, a number of experiments have been conducted by several different techniques. The investigations performed using these techniques aimed rather at confirming or denying the existence of surface nanobubbles than to provide the information on their appearance or dimensions.

Among the earliest experiments on nanobubbles are the ones done with neutron reflectometry. They first confirmed⁸² but later denied^{56,83} the presence of surface nanobubbles on substrates. The latter was supported by the results of X-ray reflectivity experiments^{84,85,86} that proved low density of water near a hydrophobic surface, but no evidence of surface nanobubbles. However, as remarked later by Craig,⁸⁷ these results are not surprising since in none of these experiments the conditions were suitable to produce nanobubbles. In addition, ellipsometric studies did not find evidence for vapor or gas layers at the interface between water and hydrophobic surfaces.^{88,89} Most likely, the nanobubbles, even if present on the surface, had too low surface coverage so that the produced signals were too weak to be detected. Other techniques such as attenuated total internal reflection infrared spectroscopy,^{57,90,91} and recently scanning transmission soft X-ray microscopy⁹² confirmed the presence of nanobubbles (or gas).

The issue with the presented methods is that they do not provide topological images of surface nanobubbles and the substrate but only the indication that the bubbles may be present in the system. Similar limitation concerns the experiments done on nanobubbles with quartz crystal microbalance (QCM).^{93,94,95,96} The experiments showed that exchanging degassed water with air-rich water caused an increase in the resonant frequency that indicated a loss of mass on the resonator, which was attributed to the formation of surface nanobubbles.

An interesting experiment is the one done by Switkes and Ruberti⁹⁷ using rapid cryofixation/freeze fracture – a technique well established for imaging biological samples. The silicon substrates bare (SiO_2) and hydrophobised (coated Si) were covered with water and frozen at a very rapid rate so that any structures present on the solid/water interface were reproduced in ice without modification. After removing the substrate and making platinum replicas of the interface, the samples were imaged by scanning electron microscopy. The water layer on the hydrophilic surface was smooth and featureless whereas several circular voids were found

on the hydrophobic surface. The voids were similar in size with nanobubbles in images obtained by AFM.

An important step forward has been made very recently, when first non-invasive methods to visualize surface nanobubbles were utilized. Using optical interference microscopy,⁹⁸ transmission electron microscopy,⁹⁹ and total internal reflection fluorescence (TIRF) microscopy,¹⁰⁰ two different groups obtained the first optical images of surface nanobubbles that confirmed their presence on a solid/water interface. An example is shown in Figure 2.10.

Importantly, almost all presented measuring techniques have one important advantage over the AFM, namely a high temporal resolution. With these techniques, it is possible to obtain information about the sample surface within microseconds, as opposed to several minutes that are required to capture a single AFM image of surface nanobubbles. In addition, one is able to access the information directly or very shortly after the water contacts the sample substrate. In comparison, a skilled (and lucky) AFM user can obtain an AFM image of nanobubbles several minutes after depositing water on the sample (and this time does not include another several minutes necessary for the system to equilibrate). In fact, it is likely that most of the AFM images of nanobubbles presented in the reports were acquired minutes or even hours after the moment the bubbles appeared on the sample. Other drawbacks of AFM in the context of investigating surface nanobubbles are described in Chapter 3.

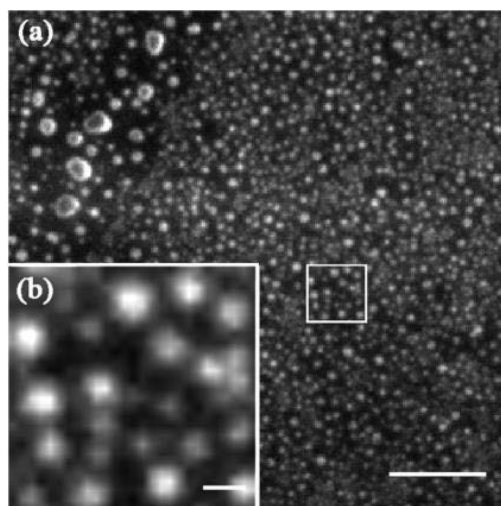


Figure 2.10. Nanobubbles observed using TIRF microscopy. The square area in (a) is zoomed into (b). Scale bar is 5 μm in (a) and 500 nm in (b). (Reproduced with permission from ref. [100]. Copyright (2012) by the American Physical Society).

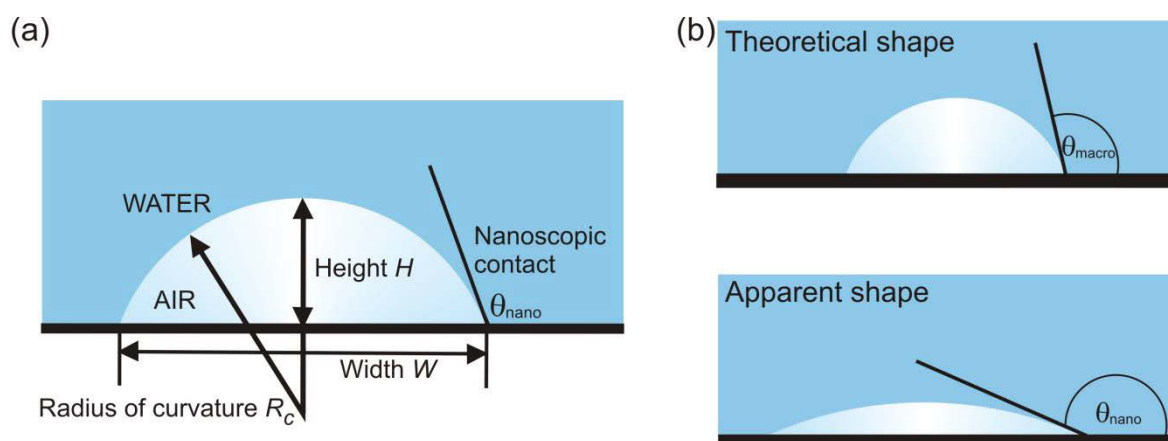


Figure 2.11. (a) Schematic cross-section of a surface nanobubble. (b) Comparison of curvatures of theoretically predicted and experimentally measured nanobubbles of equal volume. The height of the lower nanobubble is much smaller than its width.

2.4 Occurrence and morphology of surface nanobubbles

To date, the issue of shape and size of surface nanobubbles has been among the most debated and, seemingly, one of the most difficult issues to resolve. It is probably also the one most important because, in addition to simply describing nanobubbles, the size and shape of a nanobubble together with its stiffness and internal pressure are the factors that determine nanobubble stability. Here, the experimental evidence on the nanobubble appearance in AFM images is summarized and the overview of solid, liquid and gas materials tested experimentally is presented.

2.4.1 Morphology

A common assumption states that surface nanobubbles are spherical cap-like domains residing on a flat solid surface immersed in water. A schematic cross-sectional profile of an ideal nanobubble is shown in Figure 2.11a. The bubble has a shape of a spherical cap with a radius of curvature R_c and a circular base with the diameter (width) W . The contact line is elevated by the height H above the surface and forms a nanoscopic contact angle θ_{nano} with the solid surface.

The spherical cap-shape of surface nanobubbles has its source in the assumption that macroscopic laws can be directly applied to the nanoscale and that nanoscopic and macroscopic bubbles have similar shapes. However, if surface nanobubbles are

indeed gaseous domains and not liquid contaminants⁵³, substantial AFM evidence gathered over the years allows one to question the validity of this assumption. The controversial results on the nanobubble sizes measured from the first AFM images of surface nanobubbles by Lou *et al.*⁵⁸ and Ishida *et al.*⁵⁹ were confirmed in numerous experiments afterwards. The apparent nanobubble heights vary between 10 and 100 nm and their apparent widths vary between 50 nm and 1 μm . Typically the bubble height measured in an AFM image is much smaller than its apparent width and is comparable with the size of AFM tip apex. The reported values of apparent nanoscopic contact angles on the water side are surprisingly high and range from 120° up to 175°, which makes them significantly larger than macroscopic contact angles.^{72,73,75,80,101,102,103,104} Interestingly, this observation seems almost independent from the substrate or other experimental conditions used. However, as described in Chapter 4, this is not always the case, and the contact angle of nanobubbles on hydrophilic substrates is lower than on hydrophobic ones.¹⁰⁵ It needs to be stressed that an AFM tip cannot be used to accurately resolve shapes of bubbles with contact angles $\leq 90^\circ$.

So far, as long as we assume that surface nanobubbles are gaseous domains, the origin of their high apparent contact angles remains unclear. The possible influence of line tension is discussable because the experimental results and theoretical predictions are contradicting.^{106,107,108,109,110} It has been suggested that the values of nanobubble contact angle differ from the macroscopic values because nanobubbles form on top of a layer of adsorbed gas molecules^{79,110,111,112} or because the three-phase contact line is pinned to the substrate.^{106,113,114,115} Other reports emphasize the role of electric double layer.^{116,117} In addition, it has been discussed if the nanobubble contact angle depends on the nanobubble size (radius of curvature) but no consensus has been reached so far.^{75,103,110,118} Interestingly, similar questions were debated also for nanoscopic droplets.^{36,37,38,39,43}

According to the experimental evidence, surface nanobubbles are very flat as compared to macroscopic bubbles. As an example, the difference in curvature of two nanobubbles of similar volume predicted theoretically and measured experimentally is shown schematically in Figure 2.11b. The low apparent curvature of surface nanobubbles has serious implications on bubble Laplace pressure and stability.^{1,2,119} Various reports agree that the pressure inside a nanobubble exceeds the atmospheric pressure, however, the values reported by different authors are contradicting and likely dependent on the bubble size (for details see Chapter 5 and Chapter 6).^{90,91,120,121,122,123} The predicted lifetimes of nanobubbles are well below a second,^{87,112,119} which is in contradiction with long-term stability of nanobubbles

observed experimentally.^{58,59,90} The issue of unusual nanobubble stability will be discussed further in Section 2.6.

Other interesting and still debated issues concern the possible existence of preferential sizes or preferential separations of surface nanobubbles^{68,106,108,111,124,125,126} So far, the explanation favoring this scenario is based on the assumption that there is gas exchange between the bubble interior and the surrounding liquid¹⁰⁶ that requires a nanobubble-free zone on the substrate around each bubble, from which they attract gas.

It is important to notice that the assumed spherical cap-shape of surface nanobubbles is an idealization of the apparent bubble shape measured from the AFM height image similar to the one shown in Figure 2.12a. A simple procedure to determine the size and shape of a particular nanobubble assumes fitting an arc to the entire 2-dimensional bubble profile (Figure 2.12b) measured from the AFM height image along a scan line approximately crossing the bubble center (or the most elevated point of the bubble). The sample surface is assumed flat and horizontal. The arc height, width and the contact angle it makes with the sample surface can be used to describe the nanobubble. This method is frequently used to measure dimensions of nanobubbles, even though the estimation of bubble size obtained this way may be poor. In order to measure the bubble dimensions more accurately, a complete 3-dimensional structure of the bubble (Figure 2.12c) visible in the AFM image must be analyzed.⁷⁵ However, disregarding the method used, one must be critical about the results it provides, especially when the bubble surface in the AFM image seems rough or when the bubble shape is far from an ideal spherical cap e.g. due to tip imaging or thermal drift.

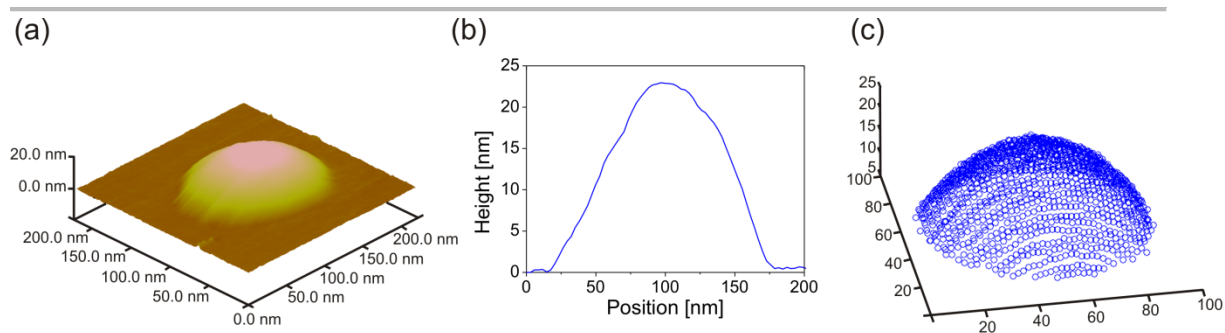


Figure 2.12. (a) Three-dimensional topographic TM AFM image of a surface nanobubble on HOPG; (b) two-dimensional cross-sectional nanobubble profile; (c) three-dimensional representation of the nanobubble (created with MATLAB 7.10.0.499 (R2010a) software); the data points (circles) represent pixels in the AFM topographic image.

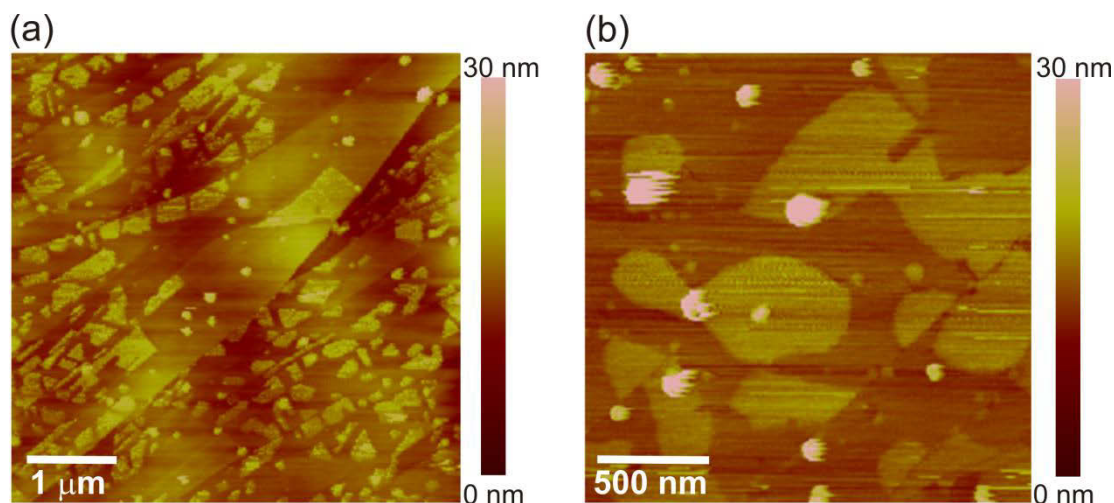


Figure 2.13. TM AFM topographic images of (a) micropancakes, (b) nanobubble-micropancake composites on HOPG.

Finally, it is interesting to note that beside spherical cap-shaped surface nanobubbles, several other (possibly gaseous) structures have been reported on substrates immersed in water. Micropancakes^{104,127,128,129,130,131,132,133} (Figure 2.13a) are irregularly shaped flat structures 1-5 nm high and several microns in diameter. Nanobubble-micropancake composites^{127,132} (Figure 2.13b) and multi-layer micropancakes¹²⁹ have also been reported. However, there is thus far no evidence that these structures are composed of gas.

2.4.2 Substrates

To date, surface nanobubbles were detected on a variety of substrates, both hydrophobic and hydrophilic, spanning a wide range of macroscopic contact angles. Most experiments were performed on mica,^{58,60,103,134,135} gold,^{67,95,96,108,136} highly oriented pyrolytic graphite (HOPG),^{58,60,72,75,77,79,80,81,101,103,104,127,128,129,132,137,138,139,140,141,142} glass,¹⁰⁰ polystyrene,^{68,74,124,133,143,144,145} hydrophobised Si or Au,^{59,72,73,90,91,96,98,107,110,113,125,130,146} Teflon,¹⁴⁷ and platinum.^{148,149}

Unsuccessful attempts to create nanobubble on certain surfaces do not prove that it is impossible. In many cases, the absence of nanobubbles may be caused by either not good liquid/gas or temperature conditions for nucleation (for details see the next section). Alternatively, especially for hydrophilic surfaces, nanobubbles scanned with the AFM may attach to the tip and be dragged away from the scanning area or coalesce and detach from the surface.^{61,74,145,105}

An important issue that is often overlooked is surface roughness. It has been reported that increased roughness may enhance nanobubble nucleation, cause pinning of the three-phase contact line and affect the bubble contact angle.^{75,113,114,145} In this context, HOPG deserves special attention, being the preferred substrate of several working groups. Properly cleaved HOPG sample offers atomically flat microns wide terraces that are separated by atomic steps. It has been observed that nanobubbles on HOPG has preferential positions next to defects of the sample and along the edges of terraces (Figure 2.14), though from the discussion it is still not clear whether the bubbles sit more preferably on the top of the atomic steps (possibly more hydrophobic) than on the base of the steps (more hydrophilic).^{73,75,138}

Another substrate parameter that may be important in the context of surface nanobubbles is softness of the sample. It has been reported that several structures appeared on polystyrene samples exposed to nanobubbles such as rims, nanoindentations, and surface lifting.^{143,145} Interestingly, similar effect was observed on HOPG where nanobubbles caused exfoliation and wrapping of the top graphene layers in graphene shells,¹⁵⁰ resembling capillary origami.¹⁵¹

Finally, several attempts have been made to create nanobubbles on patterned substrates with controlled geometry and/or wettability.^{68,147,152,153} This kind of samples bear a promise that one is able to control the bubble appearance and dimensions, which would be a milestone step toward the applications of surface nanobubbles.

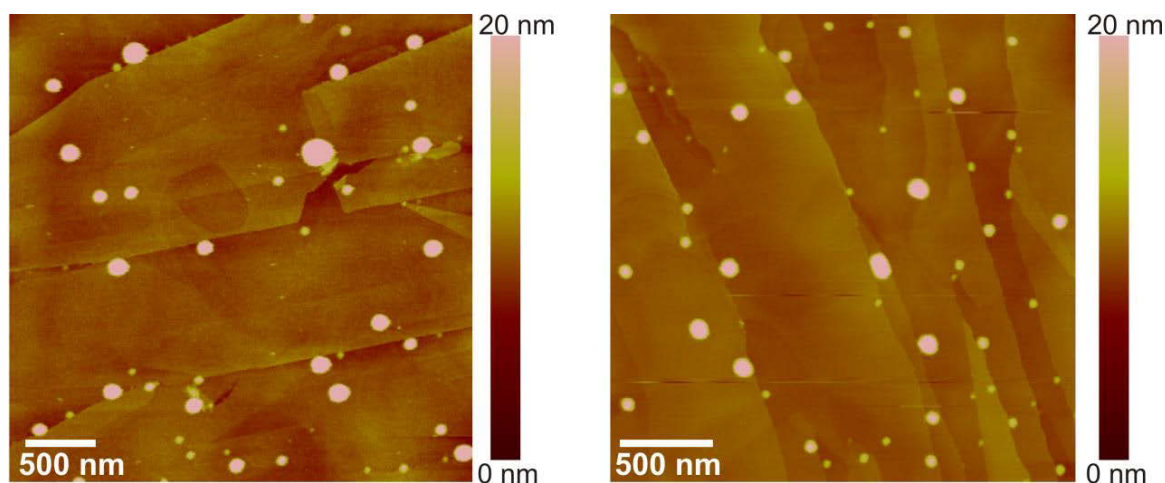


Figure 2.14. TM AFM topographic images of surface nanobubbles on HOPG. Bubbles formed preferentially along the atomic steps and near sample defects (Reprinted from ref. [154]).

2.4.3 Gases

Are surface nanobubbles gaseous, as implied by their name, or are they contamination? This question has been discussed since the hypothesis of surface nanobubbles was put forward, but the issue has not yet been resolved.

There are several arguments often put forward in support of the hypothesis that nanobubbles are indeed gaseous. First, it has been shown that nanobubbles are sensitive to the amount of gas dissolved in water. Several authors claimed to be unable to detect nanobubbles on samples treated with degassed water or observed that nanobubbles disappeared from the sample when the air-saturated water was replaced with degassed water.^{92,97,101,113,127,134,137} As an example, Figure 2.15 shows two AFM images of the substrate with nanobubbles in water (before degassing) and without nanobubbles (after degassing). In addition, the FTIR experiment performed by Miller *et al.*⁵⁷ confirmed that gaseous butane was present on the hydrophobic surface immersed in butane-saturated water. Similar results were obtained by Zhang *et al.*^{90,91} – nanobubbles formed in CO₂-saturated water. In another experiment done by scanning transmission soft X-ray microscopy (STXM), Zhang *et al.*⁹² demonstrated images of stable gaseous nanobubbles filled with SF₆ and Ne. An additional piece of evidence comes from the experiments, in which electrolysis was used as a nanobubble nucleation technique.^{103,137,140,155}

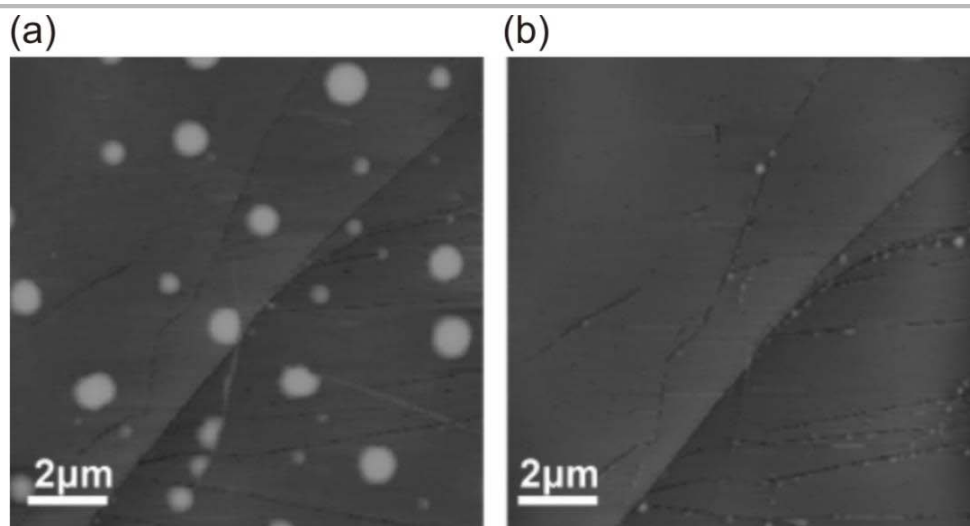


Figure 2.15. Nanobubbles in water on HOPG disappear from TM AFM topographic images after degassing: (a) before degassing, (b) the same area of the sample after degassing for 2 h. (Reprinted with permission from ref. [101]. Copyright (2006) American Chemical Society).

It is important to note that the hypothesis of gaseous surface nanobubbles has been questioned recently. Berkelaar et al.⁵³ claimed that nanobubble-like objects visible in AFM images are in fact nanodroplets of liquid contamination (polydimethylsiloxane) originating from plastic syringes and disposable needles used to handle water in the experiment. The authors showed that small, round, soft features in the AFM images in many ways resembled nanobubbles. However, when exposed to a flow of degassed water for a prolonged period of time, nanobubble-like objects remained stable, which clearly contradicts earlier experimental results.¹⁰¹ Interestingly, in the earlier report, Janda et al.¹⁵⁰ remarked that the solution pre-degassing did not prevent nanobubble appearance on the HOPG sample.

Most of the experimental evidence published so far was acquired (presumably) on surface nanobubbles filled with air. This approach is preferred because it does not require pre-saturating water with a specific gas, which simplifies the experimental protocol. However, it offers less control on the content of nanobubbles, which may affect the experimental results.

In addition to the research done on air nanobubbles, several experiments have been performed on bubbles filled with nitrogen,^{98,109,156,157} carbon dioxide,^{73,90,91,96,107,158} oxygen,^{137,140,159} hydrogen,^{103,140,148,149,155,160,161,162} and argon^{110,156,157}. The CO₂ bubbles were smaller and had larger number density,⁹⁶ and air bubbles had lower contact angle than hydrogen bubbles.¹⁰³ In addition, a specially designed experiment was conducted to examine the nucleation of surface nanobubbles as a function of the gas dissolved in water.¹¹⁰ Nanobubbles filled with hydrogen, methane, nitrogen, oxygen, argon, helium, and carbon dioxide were compared. The sample was hydrophobised silicon and was similar in all experiments. The authors found that nanobubble nucleation was a combined function of temperature and gas type.

Recently, the properties and mobility of gas constituting surface nanobubbles have received increased attention because they may provide information on nanobubble formation and account for their unusual stability. In particular, gas diffusion and circulation have been widely discussed as possible mechanisms determining bubble dimensions and distribution on the sample. The details on the discussion are presented in the following sections.

2.4.4 Liquids

Surface nanobubbles seem to be a phenomenon exclusively assigned to pure water and water solutions. Replacing water with pure alcohol results in nanobubble disappearance from the sample^{128,163} most likely because the alcohol removes the excess gas from the sample surface and from the system.

Several authors studied nanobubbles in dilute alcohol^{73,128} and dilute acid environments^{129,137,148} or investigated the effect of salts^{49,72,116,129,145,150} and pH of the liquid^{62,72,145} on nanobubble formation and properties.

Nanobubbles were found to be sensitive to the presence of surface active materials in the solution. Several authors investigated the effect of added surfactants on the nanobubble properties experimentally^{72,73,79,81,104} and theoretically,^{118,120,121} and found that the presence of surfactant reduced the number and the apparent sizes of the bubbles, and changed the stiffness of the bubble interface and the strength of the AFM tip-nanobubble interaction.

2.5 Formation of surface nanobubbles

On the one hand, nanobubbles were reported for a variety of experimental conditions. On the other hand, a re-creation of nanobubbles in seemingly similar experimental conditions is frequently unsuccessful. Their nucleation seems to be very sensitive to substrate and liquid preparation and possibly to other experimental conditions. This section presents an overview of several methods of creating nanobubbles and describes the current hypotheses on their origin and formation process.

2.5.1 Nucleation methods

Solvent-water exchange

The alcohol-water exchange is a technique of nanobubble creation that was established by Lou *et al.*⁵⁸ in one of the first AFM experiments done on surface nanobubbles. So far, it is the most conventional method used to nucleate nanobubbles because it is relatively simple and provides a high surface coverage of nanobubbles on the sample. The procedure is quite straightforward – the AFM liquid cell is filled with alcohol that is subsequently replaced by pure water. The idea is based on the fact

that air is more soluble in alcohol than in water. The mixing of alcohol and water increases the temperature of the liquid and decreases the saturation level of gases dissolved in liquid,¹⁶⁴ resulting in the local supersaturation. Because the gas diffusion is relatively slow, after replacing alcohol with water, the excess gas remains in the liquid and gathers on the substrate in the form of nanobubbles. It has been shown that the alcohol-water exchange procedure may even lead to a micron size bubbles, which are visible with optical microscopy.⁷²

Importantly, the use of the ethanol-water exchange technique was not limited to AFM but was utilized in the experiments done on nanobubbles by means of other techniques such as QCM,⁹⁴ spectroscopy,^{90,91} and others.^{98,100,165}

Different alcohols have been used to nucleate nanobubbles, with ethanol being at the top of the list. Using propanol in the exchange procedure led to larger nanobubbles, and using methanol led to smaller nanobubbles than created using the ethanol-water exchange.^{73,102}

Although widely used, the ethanol-water exchange procedure has certain drawbacks. The water may still contain traces of alcohol after the exchange is performed.¹¹⁸ Moreover, alcohol is frequently used to purify the elements of the system (liquid cell, tubes, samples etc.) prior an experiment. The purity of commercially available ethanol used in different experiments on nanobubbles varied from 99.9% to ~94% or less, which raises the question of possible contamination introduced to the nanobubble system. A recent report⁷⁹ indicated the influence of the ethanol-water exchange procedure on the forces measured on the HOPG sample with nanobubbles, which was assigned to the formation of interfacial gas enrichment (IGE) covering the area between nanobubbles. The IGE could not be removed with a cantilever tip by contact mode scanning in pure water.

Recently, a saline solution-water exchange was introduced as a method for nanobubble generation.¹⁶⁶ It is similar to the alcohol-water exchange procedure and the same mechanism is employed, namely, the liquid of lower gas solubility replaces the liquid of higher gas solubility leading to oversaturation and bubble formation.

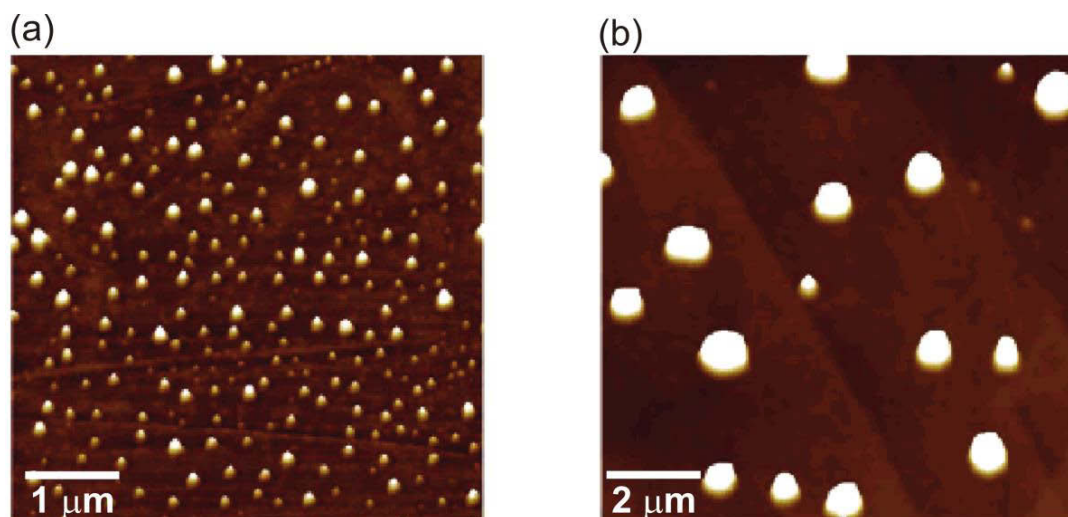


Figure 2.16. TM AFM topographic images of electrochemically created surface nanobubbles on HOPG for applied voltage of (a) -2.0 V for 5 s, (b) -1.4 V for 20 s. (Reprinted with permission from ref. [137]. Copyright (2006) American Chemical Society).

Electrolysis

Electrochemically generated nanobubbles form from the gas produced at substrate in a chemical reaction initialized by applying a potential difference across the liquid layer.

The nucleation of nanobubbles on HOPG through electrolysis was studied by several authors. According to Zhang *et al.*,^{103,137} the nucleation time depended on the potential applied, and nanobubbles appeared preferentially at the edge of atomic steps (Figure 2.16) suggesting that impurities of the sample enhanced nanobubble nucleation. In addition, continually applying the potential led to growth of nanobubbles into microbubbles and their subsequent detachment from the substrate due to buoyancy. This observation was confirmed later by Hui *et al.*¹⁵⁵ On the contrary, Yang *et al.*¹⁴⁰ observed that the coverage and volume of nanobubbles increased with increased voltage during electrolysis, but the size of the bubbles saturated and they did not further grow, even though the potential difference was applied. However, the authors noticed that big bubbles detached from the surface, which is similar to the observation made by Zhang *et al.*

In the recent experiments,^{148,149,162} the authors investigated the nucleation, growth and dissolution of electrochemically formed surface nanobubbles and addressed several

issues such as growth mechanism and timescale, conditions of the gas diffusion and nanobubble stability. In addition, nanobubbles created electrochemically were used to clean the surfaces fouled with proteins¹⁶⁷ and to synthesize hollow nanoparticles.¹⁶⁰

Temperature change

In theory, an increase in the temperature of water should result in the formation of surface nanobubbles. Heating the liquid leads to an increase in gas saturation, which is similar to the effect of performing the solvent exchange.

Two methods of temperature change have been utilized to nucleate nanobubbles: preheating the substrate to create the temperature gradient prior the deposition of water on the sample^{127,140} and changing the temperature of the liquid after the water deposition.^{127,129,132} The latter is usually done by replacing the low temperature water (4 °C) with high temperature water (25-40 °C). So far, the authors were successful in creating nanobubbles at the HOPG-water interface.

Direct water deposition

The simplest one-step method of producing surface nanobubbles was proposed by Borkent *et al.*⁷⁵ According to the authors, in order to successfully create nanobubbles, a drop of pure water may be put directly on a sample surface. In addition to its simplicity, the biggest advantage of this method is the fact that the only solvent that is in contact with the sample is pure water. Since the ethanol is eliminated, the possibility of contaminating the system is significantly reduced.

The main drawback of the direct water deposition method is that the sizes and number density of nanobubbles created this way are usually smaller as compared to nanobubbles produced by other methods (especially by alcohol-water exchange).¹⁰² It is not unusual that with this method, it is extremely difficult to obtain nanobubbles or that their surface coverage is very low. The possible solution is the application of water pre-saturated with gas.

2.5.2 Origin and formation of surface nanobubbles

Long after the existence of surface nanobubbles has been accepted, their origin is still debated. Even though already several methods of creating surface nanobubbles are known, their nucleation mechanism remains unclear.

To date, a substantial part of evidence on nanobubbles has been provided by AFM. Unfortunately, compared to other techniques, a major limitation of most commercial AFMs is their low temporal resolution for experiments in liquids. Usually, in an experiment, due to the long equilibration time of the nanobubble system and the additional time needed to set the scanning parameters and to engage the tip, the first AFM image of the surface is acquired several minutes after depositing water on the surface. Therefore, with AFM one cannot access the first moments of nanobubble nucleation.

In the early days of nanobubble research, some authors claimed that nanobubbles visible in AFM images were not present on the sample prior to the measurement but were nucleated by an AFM tip when it was in close proximity to the substrate during the imaging.^{83,88} The main argument was that a bubble may be produced during separating two hydrophobic surfaces in water.¹⁶⁸ This idea was later abandoned since no evidence was found to support the hypothesis.¹⁶⁹ The majority of the tips used in imaging nanobubbles was hydrophilic and the dimensions and distribution of nanobubbles on a sample did not change with time and did not depend on how many times the same area was scanned. In addition, the existence of nanobubbles on surfaces was confirmed by methods other than AFM.^{98,99,100}

Controlling the formation of surface nanobubbles

Poor reproducibility of nanobubble nucleation in the experiments performed in seemingly similar conditions raised a question about the ideal conditions for nanobubbles to form. The factors that were considered were the temperature and the concentration of gas in the liquid.

It has been reported that temperature was important in the nucleation process and that it influenced the number density of nanobubbles created on the sample.^{73,134,162} Several authors investigated the effect of an increase of the temperature *in situ* i.e. after nanobubbles had formed on the sample at a given temperature, on the bubble size and formation. Yang *et al.*⁷³ showed that heating the (HOPG) substrate led to spontaneous formation of nanobubbles, which allowed a comparison

of the surface topology without and with the nanobubbles. In addition, an increase in a water temperature resulted in smaller nanobubbles but increased nanobubble number density. Zhang *et al.*¹³⁵ studied nanobubbles on mica and found that the apparent nanobubble height did not change with an increase of temperature, whereas the apparent lateral bubble size and the number density first increased, reaching a maximum at about 37 °C, and then decreased at the temperatures above 42°C. This finding was partly confirmed by Berkelaar *et al.*¹⁷⁰ who tracked geometrical changes of nanobubbles as the temperature was decreased from 51 °C to 25 °C. Interestingly, nanobubbles of the same size reacted differently to the temperature change – some of them grew whilst others shrank. The total nanobubble volume per unit area had a maximum around 33 °C, which is comparable with the results of Zhang *et al.*¹³⁵ In addition, in the recent experiments,^{171,172} the authors found that nanobubbles were stable and could withstand a temperature increase up to temperatures close to the boiling point of bulk water without nucleating microbubbles.

Recently, Limbeek *et al.*¹¹⁰ studied nanobubbles filled with different gases and found that nanobubble nucleation was a strong function of gas type and was maximized at an optimal system temperature of ~35–40°C weakly dependent on gas type. In order to investigate this issue in detail, Seddon *et al.*¹³⁰ performed a systematic study of the influence of gas concentration, temperature of the liquid, and temperature of the substrate on nanobubble nucleation. The parameters were independently controlled in a series of carefully designed experiments. The authors discovered that gas concentration/liquid temperature phase space could be divided in distinct areas corresponding to no nucleation, nanobubble nucleation, and micropancake nucleation (Figure 2.17). Interestingly, the region corresponding to nanobubble nucleation was very small. Consequently, a 1–2 K temperature difference, or a 1–2% variation in gas concentration might lead to unsuccessful nanobubble nucleation. These results likely explain the difficulties in reproducing nanobubbles reported to date. Surprisingly, the authors found that local supersaturation of gas next to the substrate surface is *not* a necessary condition for nanobubble nucleation. In addition, although it is believed that the ethanol-water exchange procedure that has been successfully employed to create nanobubbles in numerous experiments led to the supersaturation of gas in water, it is possible that most of these experiments have been performed with unsaturated water.¹¹²

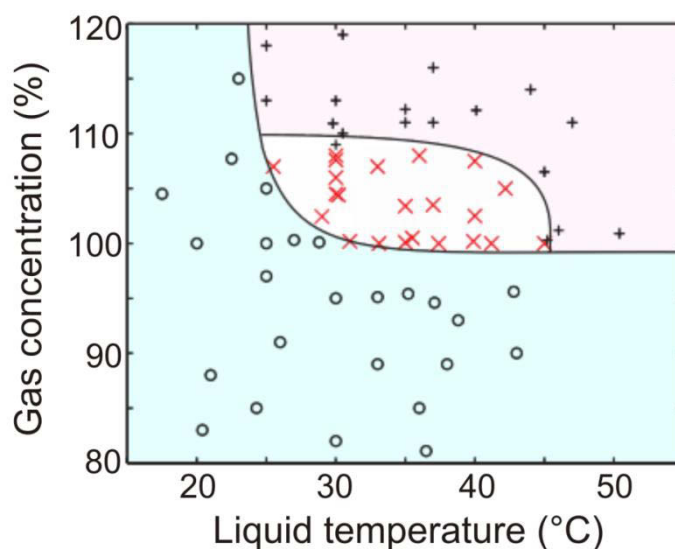


Figure 2.17. Depending on the choice of gas concentration and liquid temperature prior to deposition on the substrate (with temperature 21°C) one may shift between the regions in the parameter space assigned to no nucleation (circles), nanobubbles nucleation (crosses) and micropancakes nucleation (pluses). (Reprinted with permission from ref. [130]. Copyright (2011) by the American Physical Society).

Gas enrichment and nanobubble nucleation and growth

Despite the fact that one is able to create the optimal gas/substrate/liquid experimental conditions to nucleate surface nanobubbles, the mechanisms behind the nucleation and growth of nanobubbles remain unclear. In order to gain insight into the dynamics of nanobubble formation, the experimental evidence and the results of molecular dynamics simulations on this topic are summarized below.

As explained in the previous section, a common assumption states that surface nanobubbles are gaseous. However, considering typical apparent sizes, dimensions and unusually long lifetimes of nanobubbles observed experimentally, the properties of the gas inside a nanobubble are intriguing.

So far, there is not much experimental evidence available on the timescales of nanobubble nucleation and growth. In the QCM experiment performed by Zhang *et al.*,⁹⁴ nanobubbles formed in less than 1 minute after solvent exchange was performed. Karpitshka *et al.*⁹⁸ demonstrated in his combined AFM and optical interference-enhanced reflection microscopy experiment that surface nanobubbles formed in less than a few seconds after ethanol-water exchange. Recently, another group reported that nanobubbles can be formed in $\sim 10 \mu\text{s}$.¹⁶²

The reason of nanobubble nucleation that is brought up most frequently, is a depletion of water density in the boundary layer near a hydrophobic substrate. Lum *et al.*³⁰ predicted that if sufficiently large surfaces are close each other, the capillary evaporation may create bubbles between them. Indeed, the gas enrichment and liquid depletion in the interfacial region was observed for hydrophobic substrates and was absent for hydrophilic substrates.^{82,84,85,173} According to different authors, the thickness of the depletion layer varied between a fraction of nanometer up to few nanometers. The experimental evidence is supported by the results of molecular dynamics simulations^{78,111,174,175,176,177} suggesting that the liquid structure in the boundary layer is considerably modified (for two examples see Figure 2.18). This leads to an enhanced wall slip (increased slip length and higher velocity of a fluid moving near the wall) and makes surface more hydrophobic.^{146,177,178,179,180,181}

The simulations predicted that dissolved gas particles could enrich and adsorb at hydrophobic solid/liquid interfaces in the form of patches or a (dense) gas layer covering the entire area of hydrophobic solid/water interface.^{111,176} In an AFM experiment performed on HOPG, Lu *et al.*⁷⁸ observed nucleation and growth of an epitaxial monolayer on the HOPG surface, probably caused by adsorption of nitrogen molecules dissolved in water. The subsequent adsorption process resulted in flat structures that resembled micropancakes observed experimentally on HOPG samples.^{104,127,128,129,130,132,131}

So far, it is unclear if nanobubbles tend to sit or “float” on the patches, as suggested by several authors,^{111,112,182} or are only surrounded by a thin gas layer. Wang *et al.*¹⁸³ predicted that the gas molecules can accumulate at the HOPG interface and form one of two states according to the ratio of gas molecules number to the square of sample surface: gas films (micropancakes) are formed for a larger ratio and nanobubbles for a smaller ratio. In addition, the authors claimed that both nanobubbles and micropancakes are high-density gas state at the interface between water and graphite.

In addition to a spherical cap and a micropancake, the molecular simulation performed by Peng *et al.*¹⁷⁶ predicted a variety of shapes of gaseous domains including aggregates and cylindrical caps. Interestingly, spherical cap gas domains that formed during the simulation were unstable and always reverted to another type of gas domain. The authors also reported that the contact angle of the cylindrical cap was 141°, which was greater than 85° observed for water on HOPG and much closer

to the 150° contact angle observed for nanobubbles in experiments. An unusually large contact angle of nanoscopic gas domains was observed also by Wang *et al.*¹⁴¹ Weijs *et al.*¹⁸² proposed that the flattening of nanobubbles was caused by the fact, that an increased density of gas near the wall weakened the attraction between solid and liquid. According to the authors, the gas layer present between a nanobubble and a substrate made the wall more hydrophobic causing lowering of the contact angle. This mechanism may serve as an explanation of one universal (gas dependent) contact angle of surface nanobubbles observed experimentally.

Undoubtedly, gas enrichment near the substrate for hydrophobic surfaces favors spontaneous bubble formation.^{175,182,184} Lu *et al.*⁷⁸ proposed that gas molecules dissolved in water may aggregate into clusters in bulk water that, as they grow above a critical size, may undergo a transition into a gas bubble. Weijs *et al.*¹⁸² pointed out that nanobubbles may also form from a gas trapped on the substrate during the water deposition. This scenario was already proposed by Borkent *et al.*⁷⁵ as a possible mechanism responsible for nanobubble nucleation by direct water deposition. Finally, in the recent report, Lhuissier *et al.*¹²⁶ suggested that nanobubbles grow by diffusion of the gas from the bulk rather than by diffusion of the gas adsorbed on the surface. Clearly, the exact mechanism of nanobubble formation is yet to be discovered.

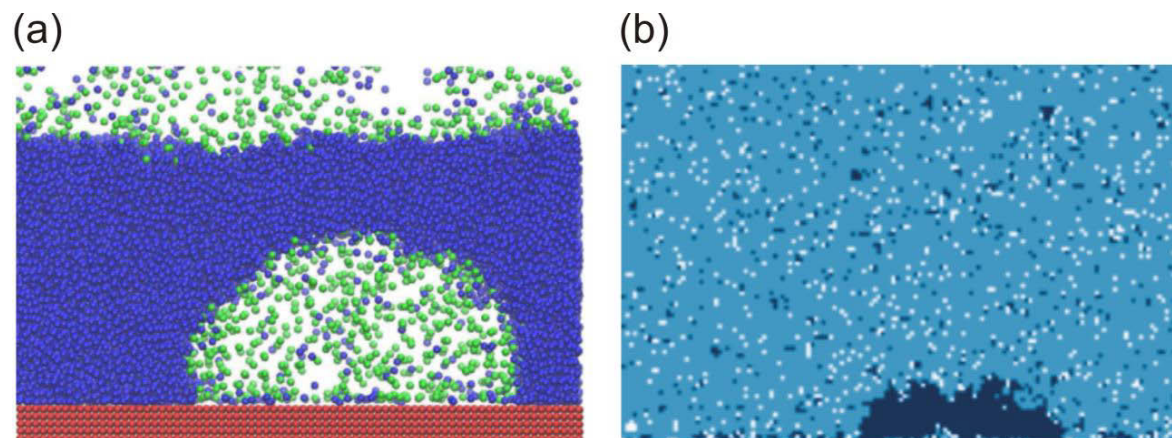


Figure 2.18. Snapshots of numerical simulations showing gas enrichment on the substrate in the form of a nanobubble. (a) Reprinted with permission from ref. [182]. Copyright (2013) by the American Physical Society; (b) Reprinted from ref. [111]. © IOP Publishing. Reproduced by permission of IOP Publishing. All rights reserved.

2.6 Stability of surface nanobubbles

Once having formed, surface nanobubbles display extreme stability. However, according to the theory, nanobubbles are not in equilibrium with the liquid and should dissolve within a fraction of a second.^{1,2} The long lifetimes together with the unusually high apparent contact angles are the main topics in the current debate on nanobubbles. In this section, we present the most important experimental evidence and summarize current hypotheses that address nanobubble stability.

The long-term nanobubble stability has been an issue since first AFM images of nanobubbles were published.^{58,59} Surface nanobubbles have been found extremely stable – their lifetime can be counted in hours¹⁵⁰ or even days.⁹⁰ Interestingly, it has been reported that nanobubbles freely floating in water were stable for two weeks.¹⁸⁵ In turn, gas layers (bilayers, trilayers, pancakes) were reported to be less stable than surface nanobubbles.¹²⁹

In addition, surface nanobubbles and micropancakes displayed extreme stability while exposed to ultrasound.^{119,165} Nanobubbles grew in height after sonification but did not act as nucleation sites for cavitation. Micropancakes increased in height while their lateral size decreased after application of ultrasound. Nanobubbles were also stable under reduction of liquid pressure.^{101,119}

Several mechanisms have been proposed to explain the unusual nanobubble stability and fill the gap between theory and experimental evidence. The most often tested hypotheses will be presented and discussed in the following sections.

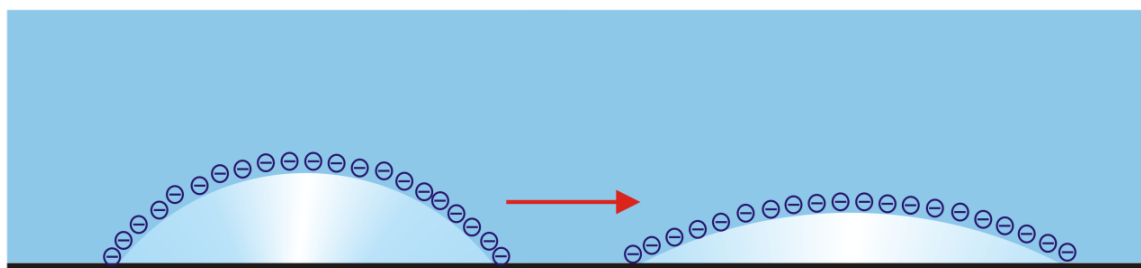


Figure 2.19. The repulsion between negative charges that possibly accumulate on the air/water interface tends to stretch out the bubble surface causing increase in nanobubble diameter and contact angle. This prevents the bubble shrinkage driven by surface tension.

2.6.1 Surface charges

An electrostatic force originating from surface charge present on the air/water interface was one of the first mechanisms of nanobubble stabilization put forward in response to the puzzling experimental evidence. Attard *et al.*¹⁸⁶ proposed that the electric double-layer repulsion between neighboring nanobubbles played role in their stabilization and limited their growth. As shown in Figure 2.19, the accumulation of negative charges on the air/water interface would decrease the surface tension and the pressure inside the bubbles slowing or preventing shrinkage of the interfacial area and bubble dissipation. The surface tension tends to reduce the surface, whilst the surface charge tends to expand it. Equilibrium will be reached when these opposing forces are equal. Any effect may be increased by the presence of additional charged materials that favor the gas/liquid interface, such as OH⁻ ions at neutral or basic pH.

The hypothesis of surface charges was supported by several authors.^{90,145,150} In addition, it has been shown that free nanobubbles in aqueous solutions were stabilized by OH⁻ ions or small organic molecules that prevented their coalescence.^{187,188,189,190} An argument against the stabilizing role of surface charges has been provided by Zhang *et al.*⁷² who compared the behavior of nanobubbles in water with and without surfactants and found no indications of decreased surface tension for nanobubbles in pure water. The authors concluded that the electrostatic forces did not play an important role in the nanobubble system.

2.6.2 Dynamic equilibrium model

A dynamic equilibrium model put forward by Brenner and Lohse¹⁰⁶ proposed that a nanobubble is stabilized by a continuous exchange of gas between the bubble interior and the surrounding liquid. The model suggests that a diffusive outflux of gas through the interface on the bubble top is balanced by the influx of gas near the three-phase contact line due to the attraction and gas enrichment at a hydrophobic substrate. The gas circulation around nanobubble is shown schematically in Figure 2.20. According to the authors of the model, a nanobubble is in metastable equilibrium (and not in thermodynamic equilibrium).

However, as pointed out by the authors, the recirculation of gas suggested by the model requires an input of energy to the system. Seddon *et al.*⁷⁶ proposed that a nanobubble contains Knudsen gas i.e. mean free path of a gas molecule is

comparable to the size of the bubble. The gas molecules inside the nanobubble hardly interact with each other, but mainly interact and exchange their energy with the gas/liquid interface. Because the nanobubble width is much larger than its height, the diffusion of gas molecules inside the bubble creates shear stresses imposed on the gas/liquid interface that induces a circulatory stream. The gas enters the bubble at the three-phase contact line and leaves it through the bubble apex. As suggested by the authors of the report, this directed gas diffusion created a vertical upward water jet above the bubble that could be detected by an AFM tip in the experiment performed in non-contact mode. However, similar jet was not detected in the subsequent experiments done on nanobubbles with different measuring techniques^{100,191} including lift mode AFM experiment described in Chapter 8. In addition, Craig¹⁹² pointed out the weakness of the Knudsen gas model proposed by Seddon *et al.* Namely, he argued that due to the fact that the model relied strongly on the presence of a solid surface breaking the symmetry of the system, it did not explain the stability of free nanobubbles in bulk water.

Thus far, the source of excess gas on the hydrophobic surface is unknown. One option assumes that it may be caused by higher density of gas dissolved in the liquid near the surface than in the bulk.^{82,84,85,173} Alternatively, the gas enrichment may result from adsorbed gas molecules in the form of micropancakes.^{112,127,131}

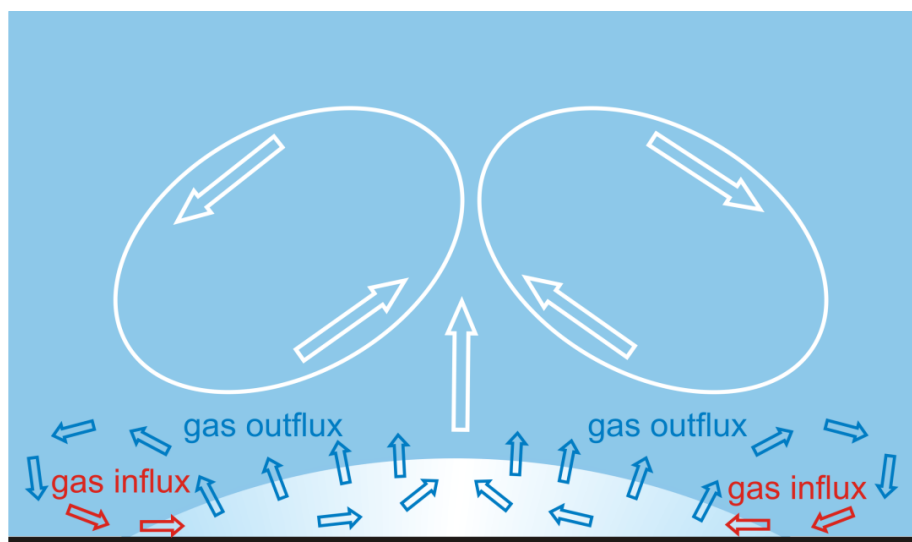


Figure 2.20. According to the dynamic equilibrium model, the circulation of gas stabilizes the nanobubble. The gas enters the bubble at the contact line near the substrate and balances the diffusive outflux of gas through the air/water interface near the bubble apex.

Despite the difficulties in defining the source of energy driving the gas circulation, the dynamic equilibrium model was supported by experimental evidence and numerical simulations.^{126,140,182} The coexistence of nanobubbles and interfacial gas enrichment areas also provides evidence of nanobubble stability by the dynamic equilibrium.^{79,176}

According to the dynamic equilibrium model, there exists a preferred equilibrium radius of the nanobubbles, which depends on gas concentration. Bubbles that have radii larger than the equilibrium radius dissolve because the outflux of gas dominates the influx; smaller bubbles shrink because the influx wins. The equilibrium radius depends on the concentration of gas in the liquid and decreases if the concentration decreases. Critical radii for nanobubble formation and growth were observed experimentally⁹⁹ and predicted numerically.¹⁷⁵ In addition, several authors reported preferential sizes and spacing of nanobubbles in their experiments.^{68,108,124,125,126}

Recently, Petsev *et al.*¹⁹³ tested the dynamic equilibrium model and found that the critical bubble radius depended not only on dissolved gas concentration but also on temperature of the liquid. According to the calculations, stable nanobubbles existed in narrow temperature and gas concentration ranges that limited maximum and minimum possible bubble size. The critical nanobubble radii monotonically decreased with temperature. Numerical results presented in the report were in good agreement with experimental evidence. In addition, the authors considered independently the effect of the perturbation in bubble radius and the perturbation in contact angle on the stability of nanobubbles, and found that bubbles with fixed contact angles could exist for a wide range of radii. Interestingly, the stable nanobubble contact angle predicted by the model was larger than 160° that was very close to the values reported in numerous experimental studies on nanobubbles.

The results presented above suggest that the dynamic equilibrium model may explain both the nucleation process of nanobubbles and their very high apparent contact angles. However, while the model is able to predict nanobubble behavior at different experimental conditions, it also has limitations. Besides the abovementioned issue with the unknown source of energy for the circulation of gas, the model cannot explain the presence of nanobubbles on hydrophilic surfaces and long-term nanobubble stability. Moreover, so far, there is no experimental evidence for the influx of gas near the three-phase contact line. If it exists, it is extremely weak and limited to the region of only few nanometers close to the substrate. Concluding, it is possible that while formed, nanobubbles might be stabilized by different mechanism than influx and outflux of gas predicted by the dynamic equilibrium model.

2.6.3 Contamination

The formation of a layer of contaminants covering the nanobubbles that alters the diffusion behavior of the enclosed gas was proposed as a stabilization mechanism by Ducker.¹¹⁸ The model was developed to offer an explanation to high apparent contact angles of nanobubbles observed experimentally. The author predicted that the existence of a contaminant layer at the air/water interface should decrease the surface tension and hinder the diffusion of gases from the bubble, increasing its lifetime. The decrease in surface tension would satisfy Young's equation and account for the increased apparent contact angle. According to the model, adsorption of contaminant molecules occurs during the growth phase of a nanobubble. The bubble grows until the gas concentration decreases and gas starts to flow out of the bubble, causing a decrease in bubble volume. As shown schematically in Figure 2.21, during the shrinking phase, the surface area of the air/water interface decreases until the contaminant molecules gathered at the bubble surface create a dense layer that serves as a diffusional barrier for gas molecules and stabilizes the bubble.

Ducker claimed that the model offered an explanation to the results of the experiment performed by Zhang *et al.*⁷² in which no change in the apparent contact angle of nanobubbles was observed after adding surfactants into solution. Since nanobubbles were already covered with contamination, addition of surfactant to the solution would not further decrease the surface tension and the contact angle of nanobubbles would not change.

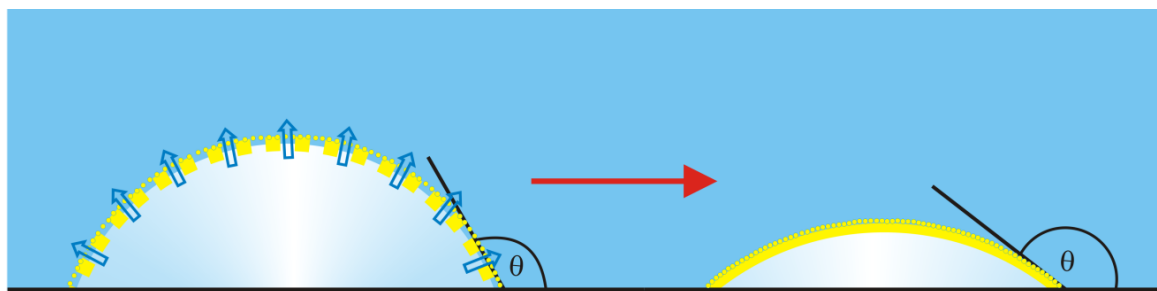


Figure 2.21. Hypothetical layer of contaminants on the air/water interface slows down the nanobubble dissolution and eventually blocks completely the outflow of gas creating a dense shell-like layer on the bubble. The presence of contaminants stabilizes the bubble and lowers the surface tension, which alters the nanobubble contact angle.

Later reports underlined the effect of surfactants on nanobubble properties such as lifetime or contact angle, but the authors stressed that the effect was not large enough to be the sole cause of the stabilization.^{120,121} Moreover, in the recent experiment, Zhang *et al.*¹⁰⁴ showed that adding surfactant to the solution during the nucleation process dramatically reduced the number of bubbles. This finding does not support the hypothesis that nanobubbles are stabilized by a layer of contaminant.

The model of contamination layer covering and stabilizing nanobubbles was revived recently by Wang *et al.*¹⁴¹ who claimed that nanobubbles measured in the experiment were stable (not affected by degassed water) and the liquid/gas interface was coated by a compact layer impermeable for gas. Berkelaar *et al.*¹⁴² showed a proof that nanobubbles on HOPG in NaCl solution were covered with a thin layer of salt that likely stabilized the nanobubbles against dissolution by blocking, or slowing down, the outward gas diffusion. However, as described in Chapter 7,¹⁵⁶ no evidence for the existence of contamination layer covering nanobubbles was found for bubbles in water.

Last but not least, in the view of recent findings showing that (supposed) surface nanobubbles were in fact polydimethylsiloxane (PDMS) nanodroplets,⁵³ the contamination model proposed by Ducker, and the whole issue of contamination in the experimental system takes on an entirely new perspective.

2.6.4 Contact line pinning and slow gas diffusion

The model of nanobubble stabilization by pinning of the three-phase contact line introduced recently by Zhang *et al.*¹¹³ and Liu *et al.*^{114,115} has received increasing attention. Pinning is crucial to the stability of nanobubbles because it causes an increase in radius of curvature when the bubble dissolves, thereby lowering the Laplace pressure inside the bubble and preventing its further shrinkage (Figure 2.22). The possibility that the contact line is pinned and that the nanobubble shrinks so that its size observed in the experiment is in fact a remain of a bigger bubble was already mentioned by Ducker¹¹⁸ in his hypothesis of nanobubble stabilization by contamination. A decrease in the heights but not in the lateral sizes of the nanobubbles was observed during their dissolution in degassed water, whereas the bubbles in supersaturated water grew in height but their widths remained constant.¹¹³ Without pinning, nanobubbles did not grow but shrank and dissolved.¹¹⁴

Nanobubbles with the pinned three-phase contact line are claimed to be in thermodynamically metastable state¹¹⁴ which supports the dynamic equilibrium model of stability¹⁰⁶ described above. Zhang *et al.*¹¹³ showed that, according to the model that assumes one-dimensional gas flow perpendicular to the nanobubble surface, the Laplace pressure decreases as the height of the bubble decreases, which decelerates bubble dissolution. A similar tendency was not observed when modelled for three-dimensional free nanobubbles in bulk water. The lifetime of a pinned one-dimensional nanobubble was many orders of magnitude longer than the lifetime of a spherical bubble of the same initial volume.

The pinning of the three-phase contact line was proposed as an explanation of the stability of nanobubbles in the acoustic field,¹⁶⁵ the nanobubble appearance on hydrophilic surfaces,^{114,115,194} and the stability to perturbations in contact angle calculated from the dynamic equilibrium model.¹⁹³ An addition of surfactant to the solution with nanobubbles reduced the number of bubbles possibly because it caused depinning of the contact line.¹⁰⁴ Finally, recent experiments comparing nanobubbles and nanodroplets showed that pinning played a crucial role for the stability of both nanobubbles and nanodroplets.^{48,172}

In addition, the pinning of the contact line of nanobubbles to the substrate is one of the assumptions of the theoretical model of slow gas diffusion proposed by Weijs *et al.*¹⁹⁵ as an alternative explanation of long lifetimes of surface nanobubbles observed experimentally. The authors suggested that a shielding effect of the neighboring bubbles, similar to the one found for free nanobubble clusters,¹⁹⁶ and slow diffusion of gas in the liquid far from the bubbles hindered the outflow of gas, increasing significantly their lifetimes from microseconds to hours or even days under normal experimental conditions.

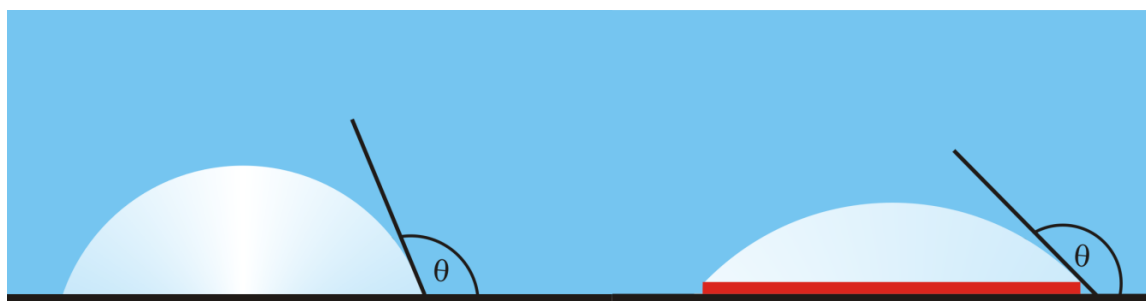


Figure 2.22. Pinning of the three-phase contact line to the substrate or e.g. a layer of adsorbate may stabilize nanobubbles and prevent their dissolution by increasing the radius of curvature and lowering the internal bubble pressure.

Even though the hypothesis of the pinning may account for the unusual stability of surface nanobubbles, the origin of pinning is unclear. It may result from the roughness of the substrate or from chemical heterogeneities of the substrate material. Again, this brings back a widely debated issue of contamination in the nanobubble system.

According to the numerical calculations performed by Liu *et al.*,^{114,115} the pinning of the contact line may account for nanobubble contact angle higher than for macroscopic bubbles. We can combine this result with the recent findings of Peng *et al.*⁷⁹ who claimed that interfacial gas enrichment covering the entire area of hydrophobic solid/water interface might be responsible for unexpected stability and anomalous contact angle of surface nanobubbles. A similar scenario was proposed by Seddon *et al.*¹¹² and Grosfils *et al.*¹¹¹ who suggested that the area between nanobubbles was covered by a thin layer of air and that nanobubbles sat on dense layer of adsorbed molecules (micropancakes). Such an additional layer of material on the sample may be a possible reason for the pinning of the contact line of nanobubbles (see Figure 2.22).

Finally, in the calculations performed by Liu *et al.*,^{114,115} a ring pattern modelling either physical or chemical heterogeneity on the sample was assumed as an initial point in the simulation of the bubble growth. In the case when the physical heterogeneity was randomly distributed on the solid surface, the nanobubble was stabilized by a contact line that had a non-circular shape. In the view of this results and knowing that pinning was most likely the mechanism responsible for irregular shapes of micropancakes,¹³¹ the question arises why most of nanobubbles observed experimentally displayed a circular three-phase contact line. Clearly, more investigation is needed to resolve this issue.

2.6.5 Dense gas aggregate

An alternative explanation to prolonged nanobubble stability is the hypothesis presented by Wang *et al.*^{183,197} that nanobubbles are composed of dense gas aggregate (gas in liquid form) rather than soft structures filled sparsely with gas molecules. The presented model, valid also for micropancakes, was based on the results of numerical simulation conducted by Fang *et al.*¹⁹⁸ for free nanobubbles in the bulk.

However, the simulation did not explain the unusually large contact angle of nanobubbles. Moreover, the hypothesis would be in contradiction with the FTIR data measured on CO₂ and butane nanobubbles.⁵⁷ The convincing experimental evidence to support the dense gas aggregate hypothesis is still lacking.

To summarize this section, none of the presented models can comprehensively and ultimately describe the formation, the long-term stability and high apparent contact angles of surface nanobubbles. Nevertheless, it is likely that the described mechanisms of nanobubble stabilization play a role at different stages of the nanobubble's lifetime, or that some or all of them contribute simultaneously to the nanobubble existence and appearance. It is also possible that nanobubbles are stabilized by another yet-to-be-discovered effect.

2.7 Applications of surface nanobubbles

Apart from being interesting for fundamental research, surface nanobubbles proved to have a practical use. The main areas where nanobubbles may be or have been useful are cleaning, micro- and nanofluidics applications and production of patterned surfaces.

Surface nanobubbles may be utilized as cleaning agents that are suitable for cleaning various materials without risk of mechanically or chemically damaging the surfaces, which may be important in many industrial processes. It has been shown that nanobubbles have implications concerning the stability of protein assemblies and protein folding³⁰ and they can be used to manipulate protein adsorption on surfaces,¹³⁹ in particular to prevent surface fouling^{136,167} or to clean surfaces already fouled with proteins.^{93,199} Similarly, it has been shown that nanobubbles influence the adsorption of nanoparticles⁹⁵ and vesicles²⁰⁰ on surfaces and that they can be used as cleaning agents for surfaces contaminated with nanoparticles.¹⁵³

Moreover, it is possible to use surface nanobubbles as masks to produce patterned surfaces by controllably depositing material (i.e. proteins) on a surface.²⁰¹ Alternatively, nanobubbles may be used to directly pattern soft surfaces¹³³ (Figure 2.23a). In addition, deliberate introduction of nanobubbles may facilitate the assembly of nanoparticles into nanoring-like structures with controllable sizes and distribution.²⁰² Furthermore, patterned surfaces may be used to nucleate nanobubbles with precisely controlled sizes, locations and even shapes.^{68,136,152,153,203} Nanobubbles may also be used as templates to produce hollow nanoparticles of different sizes¹⁶⁰ and nanoscale containers or crystals.^{204,205}

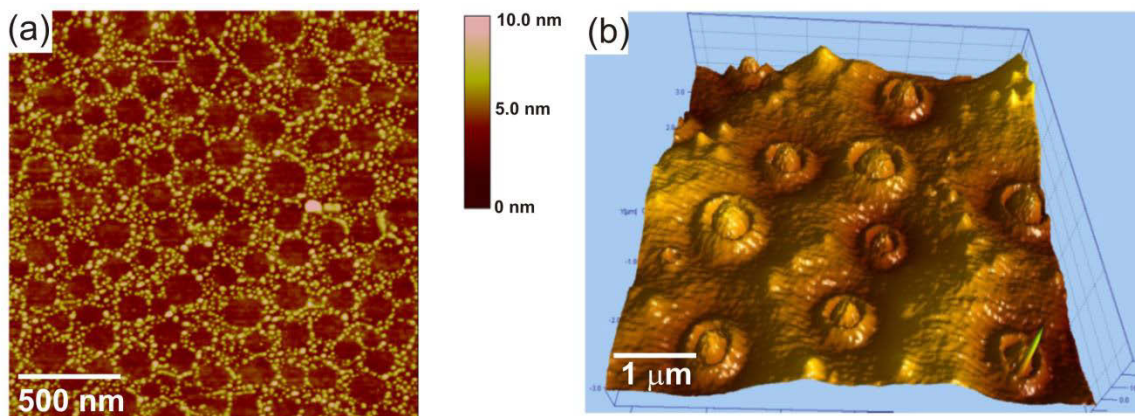


Figure 2.23. AFM image of the net-like nanopattern appearing on the polystyrene surface (Reprinted from ref. [133]. © IOP Publishing. Reproduced by permission of IOP Publishing. All rights reserved). (b) AFM image of the bubbles in the gelatin matrix, under the surface of the film, ‘pushing’ the film upwards. Vertical data scale 45 nm (Reprinted from ref. [161]. © IOP Publishing. Reproduced by permission of IOP Publishing. All rights reserved).

In addition, it has been shown that surface nanobubbles contribute to the slippage of simple fluids near the solid wall.^{181,206} They can be used to manipulate the flow conditions in microfluidic and nanofluidic devices by actively changing the wettability of the surface between non-slip and slip conditions. Moreover, nanobubbles can be used as valves in nanofluid chips.²⁰⁷

The list of actual and possible applications of surface nanobubbles is long and keeps growing. It has been shown that nanobubbles are responsible for stability, deformation and rupture of thin liquid films^{139,161,208} (Figure 2.23b) and that their presence may influence stability of emulsions of oil in water.²⁰⁹ Oxygen nanobubbles may be crucial to propel catalytic nanomotors²¹⁰ – rod-shaped nanoparticles consisting of Pt and Au that move in aqueous solutions. Nanobubbles play also an important role in flotation processes^{211,212} and in a microboiling behavior.²¹³ Furthermore, they may offer a novel hydrogen-storage method.²¹⁴ Finally, a recent study showed that nanobubbles may hinder microbubble formation and prevent the damage caused by unwanted cavitation.¹⁷¹

Besides using surface nanobubbles to our advantage, their appearance on surfaces must be prevented in the circumstances when the presence of gas is unwanted. For example, nanobubbles may inhibit protein adsorption¹³⁹ or influence the working of microsensors causing significant measurement errors.^{215,216} Some industrial processes may be hindered by the presence of nanobubbles, for example,

in the coating industry (defects or heterogeneous coatings)^{217,218} or in the semiconductor industry (lithographic systems).²¹⁹ Moreover, nanobubbles may cause hydrogen embrittlement of metals and alloys during electroplating and cathodic protection and corrosion of metals.²²⁰

Finally, with surface nanobubbles being ubiquitous, there seems to be a strong reason to suspect that they are present on hydrophobic surfaces in vivo in various biological systems. Although the mechanism of interaction with biological surfaces and possible biological impact of nanobubbles are yet unclear, it has been suggested that they may affect the functioning of living cells, regulate gas transport through membranes, and influence the aggregation of proteins or hydrophobic molecules or affect their interactions.^{221,222} Moreover, it has been considered that nanobubbles may play a role in the development of microbubbles responsible for decompression sickness.²²³ Finally, the attempts have been made to use nanobubbles in a treatment of lung diseases.²²⁴

Thus far, electrolysis, solvent exchange and use of hydrophobic surfaces proved to be the most efficient methods of nanobubble generation for practical applications. In turn, degassing the water and application of a hydrophilic coating on a surface are the two most common methods of disposing/preventing nanobubble formation. However, in order to benefit maximally from the presence of surface nanobubbles or to control their absence in the most efficient way, a deeper understanding of nanobubble properties is necessary. Intensive research and rapidly growing knowledge about the precise and reliable methods of controlling the size, location and stability of surface nanobubbles on various surfaces opens a way to create new valuable applications of nanobubbles in the future.

2.8 References

- 1 Epstein, P. S.; Plesset, M. S. On the Stability of Gas Bubbles in Liquid-Gas Solutions *J. Chem. Phys.* **1950**, *18*, 1505–1509.
- 2 Ljunggren, S.; Eriksson, J. C. The lifetime of a colloid-sized gas bubble in water and the cause of the hydrophobic attraction. *Colloids Surf. A* **1997**, *129–130*, 151–155.
- 3 Ball, P. How to keep dry in water. *Nature* **2003**, *423*, 25–26.
- 4 Hummer, G.; Rasalah, J. C.; Noworyta, J. P. Water conduction through the hydrophobic channel of a carbon nanotube. *Nature* **2001**, *414*, 188–190.

- 5 Li, T.-D.; Gao, J.; Szoszkiewicz, R.; Landman, U.; Riedo, E. Structured and viscous water in subnanometer gaps. *Phys. Rev. B* **2007**, *75*, 115415.
- 6 Braun, O. M.; Peyrard M. Dynamics and melting of a thin confined film. *Phys. Rev. E* **2003**, *68*, 011506.
- 7 Thompson, P. A.; Robbins M. O. Origin of stick-slip motion in boundary lubrication. *Science* **1990**, *250*, 792–794.
- 8 Jagla, E. A. Boundary lubrication properties of materials with expansive freezing. *Phys. Rev. Lett.* **2002**, *88*, 245504.
- 9 Odelius, M.; Bernasconi, M.; Parrinello, M. Two-dimensional ice adsorbed on mica surface. *Phys. Rev. Lett.* **1997**, *78*, 2855–2858.
- 10 Greef, R.; Frey, J. G. The water-like film on water. *Physica Status Solidi* **2008**, *5*, 1184–1186, 4th International Conference on Spectroscopic Ellipsometry (ICSE4).
- 11 Mashl, R. J.; Joseph, S.; Aluru, N. R.; Jakobsson, E. Anomalously Immobilized Water: A New Water Phase Induced by Confinement in Nanotubes. *Nano Lett.* **2003**, *3*, 589–592.
- 12 Jinesh, K. B.; Frenken, J. W. M. Capillary condensation in atomic scale friction: how water acts like a glue. *Phys. Rev. Lett.* **2006**, *96*, 166103.
- 13 Miranda, P. B.; Xu, L.; Shen, Y. R.; Salmeron, M. Icelike water monolayer adsorbed on mica at room temperature. *Phys. Rev. Lett.* **1998**, *81*, 5876–5879.
- 14 Asay, D. B.; Kim, S. H. Evolution of the adsorbed water layer structure on silicone oxide at room temperature. *J. Phys. Chem. B* **2005**, *109*, 16760–16763.
- 15 Asay, D. B.; Kim, S. H. Effects of adsorbed water layer structure on adhesion force of silicon oxide nanoasperity contact with humid ambient. *J. Chem. Phys.* **2006**, *124*, 174712.
- 16 James, M.; Darwish, T. A.; Ciampi, S.; Sylvester, S. O.; Zhang, Z.; Ng, A.; Gooding, J. J.; Hanleya, T. L. Nanoscale condensation of water on self-assembled monolayers. *Soft Matter* **2011**, *7*, 5309–5318.
- 17 Chen S.; Mallamace, F.; Mou, C.; Broccio, M.; Corsaro, C.; Faraone, A.; Liu, L. The violation of the Stokes–Einstein relation in supercooled water. *Proc. Natl. Acad. Sci. USA* **2006**, *103*, 12974–12978.
- 18 Shaw, R. A.; Durant, A. J.; Mi, Y. Heterogeneous surface crystallization observed in undercooled water. *J. Phys. Chem. B* **2005**, *109*, 9865–9868.
- 19 Christenson, H. K. Confinement effects on freezing and melting. *J. Phys.: Condens. Matt.* **2001**, *13*, R95–R133.
- 20 Tas, N. R.; Mela, P.; Kramer, T.; Berenschot, J. W.; v. d. Berg, A. Capillary induced negative pressure of water plugs in nanochannels. *Nano Lett.* **2003**, *3*, 1537–1540.
- 21 Herbert, E.; Caupin, F. The limit of metastability of water under tension: theories and experiments. *J. Phys.: Condens. Matt.* **2005**, *17*, S3597–S3602.
- 22 Yang, S.-H.; Nosonovsky, M.; Zhang, H.; Chung, K.-H. Negative pressure in water capillary bridges at nanocontacts. *Chem. Phys. Lett.* **2008**, *451*, 88–92.
- 23 Chiavazzo, E.; Fasano, M.; Asinari, P.; Decuzzi, P. Scaling behaviour for the water transport in nanoconfined geometries. *Nat. Commun.* **2014**, *5*, 4565.

- 24 Raviv, U.; Laurat, P.; Klein, J. Fluidity of water confined to subnanometre films. *Nature* **2001**, *413*, 51–54.
- 25 Zhu, Y.; Granick, S. Viscosity of Interfacial Water. *Phys. Rev. Lett.* **2001**, *87*, 096104.
- 26 Major, R. C.; Houston, J. E.; McGrath, M. J.; Siepmann, J. I.; Zhu, X.-Y. Viscous Water Meniscus under Nanoconfinement. *Phys. Rev. Lett.* **2006**, *96*, 177803.
- 27 Garofalini, S. H.; Mahadevan, T. S.; Xu, S.; Scherer, G. W. Molecular mechanisms causing anomalously high thermal expansion of nanoconfined water. *ChemPhysChem.* **2008**, *9*, 1997–2001.
- 28 Xu, S.; Scherer, G. W.; Mahadevan T. S.; Garofalini, S.H. Thermal Expansion of Confined Water. *Langmuir* **2009**, *25*, 5076–5083.
- 29 Hu, M.; Goicochea, J. V.; Michel, B.; Poulikakos, D. Water Nanoconfinement Induced Thermal Enhancement at Hydrophilic Quartz Interfaces. *Nano Lett.* **2010**, *10*, 279–285.
- 30 Lum, K.; Chandler, D.; Weeks, J. D. Hydrophobicity at Small and Large Length Scales. *J. Phys. Chem. B* **1999**, *103*, 4570–4577.
- 31 Chatterjee, J. Limiting conditions for applying the spherical section assumption in contact angle estimation. *J. Colloid Interface Sci.* **2003**, *259*, 139–147.
- 32 Marmur, A. Line Tension and the Intrinsic Contact Angle in Solid–Liquid–Fluid Systems. *J. Colloid Interface Sci.* **1997**, *186*, 462–466.
- 33 Li, D. Q. Drop size dependence of contact angles and line tensions of solid-liquid systems. *Colloids Surf. A* **1996**, *116*, 1–23.
- 34 Byakov, V. M.; Stepanov, S. V. Microscopic surface tension of liquids with curved free boundary studied by positron annihilation. *Radiat. Phys. Chem.* **2000**, *58*, 687–692.
- 35 Pethica, B. A. The contact angle equilibrium. *J. Colloid Interface Sci.* **1977**, *62*, 567–569.
- 36 Sundberg, M.; Månsson, A.; Tågerud, S. Contact angle measurements by confocal microscopy for non-destructive microscale surface characterization. *J. Colloid Interface Sci.* **2007**, *313*, 454–460.
- 37 Jung, Y. C.; Bhushan, B. Technique to Measure Contact Angle of Micro/Nanodroplets using Atomic Force Microscopy. *J. Vac. Sci. Technol., A* **2008**, *26*, 777–782.
- 38 Pompe, T.; Herminghaus S. Three-Phase Contact Line Energetics from Nanoscale Liquid Surface Topographies. *Phys. Rev. Lett.* **2000**, *85*, 1930–1933.
- 39 Checco, A.; Guenoun, P.; Daillant, J. Nonlinear Dependence of the Contact Angle of Nanodroplets on Contact Line Curvature. *Phys. Rev. Lett.* **2003**, *91*, 186101.
- 40 Checco, A.; Cai, Y.; Gang, O.; Ocko, B. M. High resolution non-contact AFM imaging of liquids condensed onto chemically nanopatterned surfaces. *Ultramicroscopy* **2006**, *106*, 703–708
- 41 Wang, R.; Takeda, M.; Kido, M. Micro pure water wettability evaluation with an AC no-contact mode of atomic force microscope. *Mater. Lett.* **2002**, *54*, 140–144.
- 42 Wang, R.; Cong, L.; Kido, M. Evaluation of the wettability of metal surfaces by micro-pure water by means of atomic force microscopy. *Appl. Surf. Sci.* **2002**, *191*, 74–84.
- 43 Weijs, J. H.; Marchand, A.; Andreotti, B.; Lohse, D.; Snoeijer, J. H. Origin of line tension for a Lennard-Jones nanodroplet. *J. Phys. Fluids* **2011**, *23*, 022001.

- 44 Cheng, Y. T.; Rodak, D. E. Is the lotus leaf superhydrophobic? *Appl. Phys. Lett.* **2005**, *86*, 144101.
- 45 Zhang, H.; Lamb, R. N.; Cookson, D. J. Nanowetting of rough superhydrophobic surfaces. *Appl. Phys. Lett.* **2007**, *91*, 254106.
- 46 Checco, A.; Schollmeyer, H.; Daillant, J.; Guenoun P.; Boukherroub, R. Nanoscale wettability of self-assembled monolayers investigated by noncontact atomic force microscopy. *Langmuir* **2006**, *22*, 116–126.
- 47 Soolaman, D. M.; Yu, H. Z. Water microdroplets on molecularly tailored surfaces: correlation between wetting hysteresis and evaporation mode switching. *J. Phys. Chem. B* **2005**, *109*, 17967–17973.
- 48 Liu, Y.; Zhang, X. Evaporation dynamics of nanodroplets and their anomalous stability on rough substrates. *Phys. Rev. E* **2013**, *88*, 012404.
- 49 Parker, J. L.; Claesson, P. M.; Attard, P. Bubbles, cavities and the long-ranged attraction between hydrophobic surfaces. *J. Phys. Chem.* **1994**, *98*, 8468–8490.
- 50 Israelachvili, J. N.; Pashley, R. M. Measurement of the Hydrophobic Interaction between Two Hydrophobic Surfaces in Aqueous Electrolyte Solutions. *J. Colloid Interface Sci.* **1984**, *98*, 500–514.
- 51 Evans, D. R.; Craig, V. S. J.; Senden, T. J. The hydrophobic force: nanobubbles or polymeric contaminant? *Physica A* **2004**, *339*, 101–105.
- 52 Häbich, A.; Ducker, W.; Dunstan, D. E.; Zhang, X. Do stable nanobubbles exist in mixtures of organic solvents and water? *J. Phys. Chem. B* **2010**, *114*, 6962–6967.
- 53 Berkelaar, R. P.; Dietrich, E.; Kip, G.; Kooij, S.; Zandvliet, H.; Lohse, D. Exposing nanobubble-like objects to a degassed environment. *Soft Matter* **2014**, *10*, 4947–4955.
- 54 No nanobubbles. *Nature* **2007**, *445*, 129–129.
- 55 Blake, T. D.; Kitchener, J. A. Stability of aqueous films on hydrophobic methylated silica. *J. Chem. Soc., Faraday Trans. 1* **1972**, *68*, 1435–1442.
- 56 Seo, Y.-S.; Satija, S. No intrinsic depletion layer on a polystyrene thin film at a water interface. *Langmuir* **2006**, *22*, 7113–7116.
- 57 Miller, J. D.; Hu, Y.; Veeramuneni, S.; Lu, Y. In-situ detection of butane gas at a hydrophobic silicon surface. *Colloids Surf. A* **1999**, *154*, 137–147.
- 58 Lou, S. T.; Ouyang, Z. Q.; Zhang, Y.; Li, X. J.; Hu, J.; Li, M. Q.; Yang, F. J. Nanobubbles on solid surface imaged by atomic force microscopy. *J. Vac. Sci. Technol., B* **2000**, *18*, 2573–2575.
- 59 Ishida, N.; Inoue, T.; Miyahara, M.; Higashitani, K. Nano bubbles on a hydrophobic surface in water observed by tapping-mode atomic force microscopy. *Langmuir* **2000**, *16*, 6377–6380.
- 60 Lou, S.; Gao, J.; Xiao, X.; Li, X.; Li, G.; Zhang, Y.; Li, M.; Sun, J.; Li, X.; Hu, J. Studies of nanobubbles produced at liquid/solid interfaces. *Mater. Charact.* **2002**, *48*, 211–214.
- 61 Tyrrell, J. W.; Attard, P. Images of Nanobubbles on Hydrophobic Surfaces and Their Interactions. *Phys. Rev. Lett.* **2001**, *87*, 176104.
- 62 Tyrrell, J. W.; Attard, P. Atomic Force Microscope Images of Nanobubbles on a Hydrophobic Surface and Corresponding Force–Separation Data. *Langmuir* **2002**, *18*, 160–167.
- 63 Binnig, G.; Quate, C. F.; Gerber, Ch. Atomic Force Microscope. *Phys. Rev. Lett.* **1986**, *56*, 930–933.

- 64 Parker, J. L.; Attard, P. Deformation of Surfaces due to Surface Forces. *J. Phys. Chem.* **1992**, *96*, 10398–10405.
- 65 Christenson, H. K. Note on Surface Deformations in Direct Force Measurements. *Langmuir* **1996**, *12*, 1404–1405.
- 66 Butt, H.-J.; Doppenschmidt, A.; Huttli, G.; Muller, E.; Vinogradova, O. I. Analysis of plastic deformation in atomic force microscopy: Application to ice. *J. Chem. Phys.* **2003**, *113*, 1194–1203.
- 67 Holmberg, M.; Kühle, A.; Garnæs, J.; Mørch, K. A.; Boisen, A. Nanobubble Trouble on Gold Surfaces. *Langmuir* **2003**, *19*, 10510–10513.
- 68 Agrawal, A.; Park, J.; Ryu, D. Y.; Hammond, P. T.; Russel, T. P.; McKinley, G. H. Controlling the Location and Spatial Extent of Nanobubbles Using Hydrophobically Nanopatterned Surface. *Nano Lett.* **2005**, *5*, 1751–1756.
- 69 Katan, A. J.; v. Es, M. H.; Oosterkamp, T. H. Quantitative force versus distance measurements in amplitude modulation AFM: a novel force inversion technique. *Nanotechnology* **2009**, *20*, 165703.
- 70 García, R.; Pérez, R. Dynamic atomic force microscopy methods. *Surf. Sci. Rep.* **2002**, *47*, 197–301.
- 71 Knoll, A.; Magerle, R.; Krausch, G. Tapping Mode Atomic Force Microscopy on Polymers: Where Is the True Sample Surface? *Macromolecules* **2001**, *34*, 4159–4165.
- 72 Zhang, X. H.; Maeda, N.; Craig, V. S. J. Physical Properties of Nanobubbles on Hydrophobic Surfaces in Water and Aqueous Solutions. *Langmuir* **2006**, *22*, 5025–5035.
- 73 Yang, S.; Dammer, S. M.; Bremond, N.; Zandvliet, H. J. W.; Kooij, E. S.; Lohse, D. Characterization of Nanobubbles on Hydrophobic Surfaces in Water. *Langmuir* **2007**, *23*, 7072–7077.
- 74 Bhushan, B.; Wang, Y.; Maali, A. Coalescence and movement of nanobubbles studied with tapping mode AFM and tip-bubble interaction analysis. *J. Phys.: Condens. Matter* **2008**, *20*, 485004.
- 75 Borkent, B. M.; de Beer, S.; Mugele, F.; Lohse, D. On the shape of surface nanobubbles. *Langmuir* **2010**, *26*, 260–268.
- 76 Seddon, J. R. T.; Zandvliet, H. J. W.; Lohse, D. Knudsen gas provides nanobubble stability. *Phys. Rev. Lett.* **2011**, *107*, 116101.
- 77 Yang, C. W.; Lu, Y. H.; Hwang, I. S. Imaging surface nanobubbles at graphite-water interfaces with different atomic force microscopy modes. *J. Phys.: Condens. Matter* **2013**, *25*, 184010.
- 78 Lu, Y. H.; Yang, C. W.; Hwang, I. S. Molecular layer of gaslike domains at a hydrophobic-water interface observed by frequency-modulation atomic force microscopy. *Langmuir* **2012**, *28*, 12691–12695.
- 79 Peng, H.; Hampton, P. A.; Nguyen, A. V. Nanobubbles Do Not Sit Alone at the Solid-Liquid Interface. *Langmuir* **2013**, *29*, 6123–6130.
- 80 Zhao, B.; Song, Y.; Wang, S.; Dai, B.; Zhang, L.; Dong, Y.; Lü, J.; Hu, J. Mechanical mapping of nanobubbles by PeakForce atomic force microscopy. *Soft Matter* **2013**, *9*, 8837–8843.
- 81 Song, Y.; Zhao, B.; Zhang, L.; Lü, J.; Wang, S.; Dong, Y.; Hu, J. The Origin of the „Snap-In” in the Force Curve between AFM Probe and the Water/Gas Interface of Nanobubbles. *ChemPhysChem* **2014**, *15*, 492–499.

- 82 Steitz, R.; Gutberlet, T.; Hauss, T.; Klosgen, B.; Krastev, R.; Schemmel, S.; Simonsen, A. C.; Findenegg, G. H. Nanobubbles and their precursor layer at the interface of water against a hydrophobic substrate. *Langmuir* **2003**, *19*, 2409–2418.
- 83 Doshi, D. A.; Watkins, E. B.; Israelachvili, J. N.; Majewski, J. Reduced water density at hydrophobic surfaces: Effect of dissolved gases. *Proc. Natl. Acad. Sci. U.S.A.* **2005**, *102*, 9458–9462.
- 84 Jensen, T. R.; Jensen, M. O.; Reitzel, N.; Balashev, K.; Peters, G. H.; Kjaer, K.; Bjørnholm, T. Water in contact with extended hydrophobic surfaces: Direct evidence of weak dewetting. *Phys. Rev. Lett.* **2003**, *90*, 086101.
- 85 Mezger, M. A.; Schöder, S. A. B.; Reichert, H. A.; Schröder, H. A.; Okasinski, J. A.; Honkimäki, V. B.; Ralston, J. C.; Bilgram, J. D.; Roth, R. A. E.; Dosch, H. Water and ice in contact with octadecyltrichlorosilane functionalized surfaces: a high resolution x-ray reflectivity study. *J. Chem. Phys.* **2008**, *128*, 244705.
- 86 Poynor, A.; Hong, L.; Robinson, I. K.; Granick, S.; Zhang, Z.; Fenter, P. A. How Water Meets a Hydrophobic Surface. *Phys. Rev. Lett.* **2006**, *97*, 266101.
- 87 Craig, V. S. J. Very small bubbles at surfaces – the nanobubble puzzle. *Soft Matter* **2011**, *7*, 40–48.
- 88 Mao, M.; Zhang, J. H.; Yoon, R. H.; Ducker, W. A. Is There a Thin Film of Air at the Interface between Water and Smooth Hydrophobic Solids? *Langmuir* **2004**, *20*, 1843–1849.
- 89 Takata, Y.; Cho, J. H. J.; Law, B. M.; Aratono, M. Ellipsometric Search for Vapor Layers at Liquid-hydrophobic Solid Surfaces *Langmuir* **2006**, *22*, 1715–1721.
- 90 Zhang, X. H.; Quinn, A.; Ducker, W. A. Nanobubbles at the interface between water and a hydrophobic solid. *Langmuir* **2008**, *24*, 4756–4764.
- 91 Zhang, X. H.; Khan, A.; Ducker, W. A. A nanoscale gas state. *Phys. Rev. Lett.* **2007**, *98*, 136101.
- 92 Zhang, L.; Zhao, B.; Xue, L.; Guo, Z.; Dong, Y.; Fang, H.; Tai, R.; Hu, J. Imaging interfacial micro- and nano-bubbles by scanning transmission soft X-ray microscopy. *J. Synchrotron Rad.* **2013**, *20*, 413–418.
- 93 Liu, G. M.; Wu, Z. H.; Craig, V. S. J. Cleaning of Protein-Coated Surfaces Using Nanobubbles - An Investigation Using a Quartz Crystal Microbalance *J. Phys. Chem. C* **2008**, *112*, 16748–16753.
- 94 Zhang, X. Quartz crystal microbalance study of the interfacial nanobubbles. *Phys. Chem. Chem. Phys.* **2008**, *10*, 6842–6848.
- 95 Seo, H.; Yoo, M.; Jeon, S. Influence of nanobubbles on the adsorption of nanoparticles. *Langmuir* **2007**, *23*, 1623–1625.
- 96 Yang, J.; Duan, J.; Fornasiero, D.; Ralston, J. Kinetics of CO₂ nanobubble formation at solid/water interface. *Phys. Chem.* **2007**, *9*, 6327–6332.
- 97 Switkes, M.; Ruberti, J. W. Rapid cryofixation/freeze fracture for the study of nanobubbles at solid-liquid interfaces. *Appl. Phys. Lett.* **2007**, *84*, 4759–4761.
- 98 Karpitschka, S.; Dietrich, E.; Seddon, J. R. T.; Zandvliet, H. J. W.; Lohse, D.; Riegler, H. Nonintrusive Optical Visualization of Surface Nanobubbles. *Phys. Rev. Lett.* **2012**, *109*, 066102.
- 99 Mirsaidov, U.; Ohl, C.-D.; Matsudaira, P. A direct observation of nanometer-size void dynamics in an ultra-thin water film. *Soft Matter* **2012**, *8*, 3108–3111.

- 100 Chan, C. U.; Ohl, C.-D. Total-Internal-Reflection-Fluorescence Microscopy for the Study of Nanobubble Dynamics. *Phys. Rev. Lett.* **2012**, *109*, 174501.
- 101 Zhang, X. H.; Li, G; Maeda, N.; Hu, J. Removal of Induced Nanobubbles from Water/Graphite Interfaces by Partial Degassing. *Langmuir* **2006**, *22*, 9238–9243.
- 102 Hampton, M. A.; Donose, B. C.; Nguyen, A. V. Effect of alcohol-water exchange and surface scanning on nanobubbles and the attraction between hydrophobic surfaces. *J Colloid Interface Sci.* **2008**; *325*, 267–274.
- 103 Zhang, L.; Zhang, X.; Zhang, Y.; Hu, J.; Fang, H. The length scales for stable gas nanobubbles at liquid/solid surfaces. *Soft Matter* **2010**, *6*, 4515–4519.
- 104 Zhang, X.; Uddin, M. H.; Yang, H.; Toikka, G.; Ducker, W.; Maeda, N. Effects of Surfactants on the Formation and the Stability of Interfacial Nanobubbles. *Langmuir* **2012**, *28*, 10471–10477.
- 105 Song, B; Walczyk, W.; Schönherr, H. Contact Angles of Surface Nanobubbles on Mixed Self-Assembled Monolayers with Systematically Varied Macroscopic Wettability by Atomic Force Microscopy. *Langmuir*, **2011**, *27*, 8223–8232.
- 106 Brenner, M. P.; Lohse, D. Dynamic Equilibrium Mechanism for Surface Nanobubble Stabilization. *Phys. Rev. Lett.* **2008**, *101*, 214505.
- 107 Yang, J.; Duan, J.; Fornasiero, D.; Ralston, J. Very Small Bubble Formation at the Solid-Water Interface. *J. Phys. Chem. B* **2003**, *107*, 6139–6147.
- 108 Kameda, N.; Nakabayashi, S. Size-induced sign inversion of line tension in nanobubbles at a solid/liquid interface. *Chem. Phys. Lett.* **2008**, *461*, 122–126.
- 109 Kameda, N; Sogoshi, N.; Nakabayashi, S. Nitrogen nanobubbles and butane nanodroplets at Si(100). *Surf. Sci.* **2008**, *602*, 1579–1584.
- 110 v. Limbeek, M. A. J.; Seddon, J. R. T. Surface Nanobubbles as a Function of Gas Type. *Langmuir* **2011**, *27*, 8694–8699.
- 111 Grosfils, P. Coarse-grained modelling of surface nanobubbles. *J. Phys. Condens. Matter* **2013**, *25*, 184006.
- 112 Seddon, J. R. T.; Lohse, D. Nanobubbles and micropancakes: Gaseous domains on immersed substrates. *J. Phys.: Condens. Matter* **2011**, *23*, 133001.
- 113 Zhang, X.; Chan, D. Y.; Wang, D.; Maeda, N. Stability of Interfacial Nanobubbles. *Langmuir* **2013**, *29*, 1017–23.
- 114 Liu, Y.; Zhang, X. Nanobubble stability induced by contact line pinning. *J Chem Phys.* **2013**, *138*, 014706.
- 115 Liu, Y.; Wang, J.; Zhang, X.; Wang, W. Contact line pinning and the relationship between nanobubbles and substrates. *J. Chem. Phys.* **2014**, *140*, 054705.
- 116 Das, S. Effect of added salt on performed surface nanobubbles: A scaling estimate. *Phys. Rev. E* **2011**, *84*, 036303.
- 117 Das, S; Mitra, S. K. Electric double-layer interactions in a wedge geometry: Change in contact angle for drops and bubbles. *Phys Rev E*, **2013**, *88*, 033021.
- 118 Ducker, W. A. Contact angle and stability of interfacial nanobubbles. *Langmuir* **2009**, *25*, 8907–8910.

- 119 Borkent, B. M.; Dammer, S. M.; Schönherr, H.; Vancso, G. J.; Lohse, D. Superstability of Surface Nanobubbles. *Phys. Rev. Lett.* **2007**, *98*, 204502.
- 120 Das, S.; Snoeijer, J. H.; Lohse, D. Effect of impurities in description of surface nanobubbles *Phys. Rev. E* **2010**, *82*, 056310.
- 121 Das, S. Effect of impurities in the description of surface nanobubbles: Role of nonidealities in the surface layer. *Phys Rev E* **2011**, *83*, 066315.
- 122 Walczyk, W.; Schönherr, H. Closer Look at the Effect of AFM Imaging Conditions on the Apparent Dimensions of Surface Nanobubbles. *Langmuir*, **2013**, *29*, 620–632.
- 123 Walczyk, W.; Schön, P.; Schönherr, H. The effect of PeakForce tapping mode AFM imaging on the apparent shape of surface nanobubbles. *J. Phys.: Condens. Matter* **2013**, *25*, 184005.
- 124 Simonsen, A. C.; Hansen, P. L.; Klösgen, B. Nanobubbles give evidence of incomplete wetting at a hydrophobic interface. *J Colloid Interface Sci.* **2004** , *273*, 291–299.
- 125 Borkent, B. M.; Schoenherr, H.; Caer, G. L.; Dollet, B.; Lohse, D. Preferred size and ordering in surface nanobubble populations. *Phys. Rev. E* **2009**, *80*, 036315.
- 126 Lhuissier, H.; Lohse, D.; Zhang, X. Spatial organization of surface nanobubbles and its implications in their formation process. *Soft Matter* **2014**, *10*, 942–946.
- 127 Zhang, X. H.; Zhang, X.; Sun, J.; Zhang, Z.; Li, G.; Fang, H.; Xiao, X.; Zeng, X.; Hu, J. Detection of Novel Gaseous States at a HOPG-Water Interface. *Langmuir* **2007**, *23*, 1778–1783.
- 128 Zhang, X. H.; Maeda, N.; Hu, J. Thermodynamic Stability of Interfacial Gaseous States. *J. Phys. Chem. B* **2008**, *112*, 13671–13675.
- 129 Zhang, L.; Zhang, X.; Fan, C.; Zhang, Y.; Hu, J. Nanoscale Multiple Gaseous Layers on a Hydrophobic Surface. *Langmuir* **2009**, *25*, 8860–8864.
- 130 Seddon, J. R. T.; Kooij, E. S.; Poelsema, B.; Zandvliet, J. W.; Lohse, D. Surface bubble nucleation stability. *Phys. Rev. Lett.* **2011**, *106*, 056101.
- 131 Seddon, J. R.; Bliznyuk, O.; Kooij, E. S.; Poelsema, B.; Zandvliet, H. J.; Lohse, D. Dynamic dewetting through micropancake growth. *Langmuir* **2010**, *26*, 9640–9644.
- 132 Guan, M.; Guo, W.; Gao, L.; Tang, Y.; Hu, J.; Dong, Y. Investigation on the Temperature Difference Method for Producing Nanobubbles and Their Physical Properties. *ChemPhysChem* **2012**, *13*, 2115–2118.
- 133 Tarábková H.; Janda, P. Nanobubble assisted nanopatterning utilized for ex situ identification of surface nanobubbles. *J. Phys.: Condens. Matter* **2013**, *25*, 184001.
- 134 Zhang, X. H.; Zhang, X. D.; Lou, S. T.; Zhang, Z. X.; Sun, J. L.; Hu, J. Degassing and Temperature Effects on the Formation of Nanobubbles at the Mica/Water Interface. *Langmuir* **2004**, *20*, 3813–3815.
- 135 Zhang, X. H.; Gang, L.; Wu, Z. H.; Zhang, X. D.; Hu, J. Effect of temperature on the morphology of nanobubbles at mica/water interface. *Chinese Phys.* **2005**, *14*, 1774–1778.
- 136 Kolivoška, V.; Gál, M.; Hromadová, M.; Lachmanová, S.; Pospíšil, L. Interactions of nanobubbles with bovine serum albumin and papain films on gold surfaces. *Biointerphases* **2011**, *6*, 164–170.

- 137 Zhang, L.; Zhang, Y.; Zhang, X.; Li, Z.; Shen, G.; Ye, M.; Fan, C.; Fang, H.; Hu, J. Electrochemically Controlled Formation and Growth of Hydrogen Nanobubbles. *Langmuir* **2006**, *22*, 8109–8113.
- 138 Yang, S.; Kooij, E. S.; Poelsema, B.; Lohse, D.; Zandvliet, H. J. W. Correlation between geometry and nanobubble distribution on HOPG surface. *EPL* **2008**, *81*, 64006.
- 139 Wu, Z. H.; Zhang, X. H.; Zhang, X. D.; Sun, J. L.; Dong, Y. M.; Hu, J. In situ AFM observation of BSA adsorption on HOPG with nanobubble *Chin. Sci. Bull.* **2007**, *52*, 1913–1919.
- 140 Yang, S.; Tsai, P.; Kooij, E. S.; Prosperetti, A.; Zandvliet, H. J. W.; Lohse, D. Electrolytically Generated Nanobubbles on HOPG Surfaces. *Langmuir* **2009**, *25*, 1466–1474.
- 141 Wang, S.; Liu, M.; Dong, Y. Understanding the stability of surface nanobubbles. *J. Phys.: Condens. Matter* **2013**, *25*, 184007.
- 142 Berkelaar, R. P.; Zandvliet, H. J. W.; Lohse, D. Covering Surface Nanobubbles with a NaCl Nanoblanket. *Langmuir* **2013**, *29*, 11337–11343.
- 143 Wang, Y.; Bhushan, B.; Zhao, X. Nanoindents produced by nanobubbles on ultrathin polystyrene films in water. *Nanotechnology* **2009**, *28*, 045301.
- 144 Wang, Y.; Bhushan, B.; Zhao, X. Improved Nanobubble Immobility Induced by Surface Structures on Hydrophobic Surfaces. *Langmuir* **2009**, *18*, 25, 9328–9336.
- 145 Mazumder, M.; Bhushan, B. Propensity and geometrical distribution of surface nanobubbles: effect of electrolyte, roughness, pH, and substrate bias. *Soft Matter* **2011**, *7*, 9184–9196.
- 146 Agrawal, A.; McKinley, G. H. Nanobubble Formation at the Solid/Liquid Interface Studied by AFM. *MRS Proceedings* **2005**, *899*, 146–151.
- 147 Nam, Y.; Ju, S. Y. Bubble nucleation on hydrophobic islands provides evidence to anomalously high contact angles of nanobubbles. *Appl. Phys. Lett.* **2008**, *93*, 103115.
- 148 Luo, L.; White, H. S. Electrogenation of Single Nanobubbles at Sub-50-nm-Radius Platinum Nanodisk Electrodes. *Langmuir* **2013**, *29*, 11169–11175.
- 149 Nakabayashi, S.; Shinozaki, R.; Senda, Y.; Yoshikawa, H. Y. Hydrogen nanobubble at normal hydrogen electrode. *J. Phys. Condens. Matter* **2013**, *25*, 184008.
- 150 Janda, P.; Frank, O.; Bastl, Z.; Klementová, M.; Tarábková, H.; Kavan, L. Nanobubble-assisted formation of carbon nanostructures on basal plane HOPG exposed to aqueous media. *Nanotechnology*. **2010**, *21*, 095707.
- 151 Py, C.; Reverdy, P.; Doppler, L.; Bico, J.; Roman, B.; Baroud, C. N. Capillary origami: spontaneous wrapping of a droplet with an elastic sheet. *Phys. Rev. Lett.* **2007**, *98*, 156103.
- 152 Checco, A.; Hofmann, T.; DiMasi, E.; Black, C. T.; Ocko, B. M. Morphology of Air Nanobubbles Trapped at Hydrophobic nanopatterned Surfaces. *Nano Lett.* **2010**, *10*, 1354–1358.
- 153 Yang, S.; Dusterwinkel, A. Removal of Nanoparticles from Plain and Patterned Surfaces Using Nanobubbles. *Langmuir* **2011**, *27*, 11430–11435.
- 154 Walczyk, W. Characterization of Surface Nanobubbles by Means of Atomic Force Microscopy. *Master Thesis*, University of Twente, Enschede, The Netherlands **2009**.
- 155 Hui, F.; Li, B.; He, P.; Hu, J.; Fang, Y. Electrochemical fabrication of nanoporous polypyrrole film on HOPG using nanobubbles as templates. *Electrochem. Commun.* **2009**, *11*, 639–642.

- 156 Walczyk, W.; Schönherr, H. Characterization of the Interaction between AFM Tips and Surface Nanobubbles. *Langmuir*, **2014**, *30*, 7112–7126.
- 157 Walczyk, W.; Schönherr, H. Hydrodynamic effects of the tip movement on surface nanobubbles: A combined tapping mode, lift mode and force volume mode AFM study. *Soft Matter* **2014**, DOI: 10.1039/C4SM01024H.
- 158 Enríquez, O. R.; Sun, C.; Lohse, D.; Prosperetti, A.; v. d. Meer, D. The quasi-static growth of CO₂ bubbles. *J. Fluid Mech.* **2014**, *741*, R1–9.
- 159 Yang, S.; Tsai, P.; Kooij, E. S.; Prosperetti, A.; Zandvliet, H. J. W.; Lohse, D. Correction to Electrolytically Generated Nanobubbles on Highly Orientated Pyrolytic Graphite Surfaces *Langmuir* **2013**, *29*, 5937–5937.
- 160 Huang, C.; Jiang, J.; Lu, M.; Sun, L.; Meletis, E. L.; Hao, Y. Capturing electrochemically evolved nanobubbles by electroless deposition. A facile route to the synthesis of hollow nanoparticles. *Nano Lett.* **2009**, *9*, 4297–4301.
- 161 Alsawafta, M.; Badilescu, S.; Truong, V. V.; Packikisamy, M. The effect of hydrogen nanobubbles on the morphology of gold–gelatin bionanocomposite films and their optical properties. *Nanotechnology* **2012**, *23*, 065305.
- 162 Svetovoy, V. B.; Sanders, R. G. P.; Elwenspoek, M. C. Transient nanobubbles in short-time electrolysis. *J. Phys.: Condens. Matter* **2013**, *25*, 184002.
- 163 Zhang, X. H.; Wu, Z. H.; Zhang, X. D.; Li, G.; Hu, J. Addendum to ‘Nanobubbles at the interface of HOPG and ethanol solution’. *Int. J. Nanosci.* **2010**, *9*, 383–384.
- 164 Henry, W. Experiments on the quantity of gases absorbed by water, at different temperature, and under different pressures. *Phil. Trans. R. Soc.* **1803**, *93*, 29–42.
- 165 Brotchie, A.; Zhang, X. H. Response of interfacial nanobubbles to ultrasound radiation. *Soft Matter* **2011**, *7*, 265–269.
- 166 Liu, M.; Zhao, W.; Wang, S.; Guo, W.; Tang, Y.; Dong, Y. Study on nanobubble generation: saline solution/water exchange method. *ChemPhysChem* **2013**, *14*, 2589–2593.
- 167 Wu, Z. H.; Chen, H. B.; Dong, Y. M.; Mao, H. L.; Sun, J. L.; Chen, S. F.; Craig, V. S. J.; Hu, J. Cleaning using Nanobubbles: defouling by electrochemical generation of bubbles *J. Colloid Interface Sci.* **2008**, *328*, 10–14.
- 168 Christenson, H. K.; Claesson, P. M. Cavitation and the Interaction Between Macroscopic Hydrophobic Surfaces *Science* **1988**, *239*, 390–392.
- 169 Palmer, L. A.; Cookson, D.; Lamb, R. N. The Relationship Between Nanobubbles and the Hydrophobic Force. *Langmuir*, **2011**, *27*, 144–147.
- 170 Berkelaar, R. P.; Seddon, J. R. T.; Zandvliet, H. J. W.; Lohse, D. Temperature Dependence of Surface Nanobubbles. *ChemPhysChem* **2012**, *13*, 2213–2217.
- 171 Zhang, X.; Lhuissier, H. E.; Enríquez, O. R.; Sun, C.; Lohse, D. Deactivation of microbubble nucleation sites by alcohol–water exchange. *Langmuir* **2013**, *29*, 9979–9984.
- 172 Zhang, X.; Lhuissier, H. E.; Sun, C.; Lohse, D. Surface Nanobubbles Nucleate Microdroplets. *Phys. Rev. Lett.* **2014**, *112*, 144503.

- 173 Martinez, J.; Stroeve, P. Transient behavior of the hydrophobic surface/water interface: from nanobubbles to organic layer. *J. Phys. Chem. B* **2007**, *111*, 14069–14072.
- 174 Zhou, D.; Mi, J.; Zhong, C. Theoretical Study of Dissolved Gas at a Hydrophobic Interface. *J. Phys. Chem. C* **2012**, *116*, 3042–3049.
- 175 Zhou, D.; Haque Ansari, Z.; Mi, J. Modeling of bubble nucleation of an air–water mixture near hydrophobic walls. *J. Phys. Condens. Matter* **2013**, *25*, 184004.
- 176 Peng, H.; Birkett, G. R.; Nguyen, A. V. Origin of Interfacial Nanoscopic Gaseous Domains and Formation of Dense Gas Layer at Hydrophobic Solid–Water Interface. *Langmuir* **2013**, *29*, 15266–15274.
- 177 Dammer, S. M.; Lohse, D. Gas enrichment at liquid–wall interfaces. *Phys. Rev. Lett.* **2006**, *96*, 206101.
- 178 d. Gennes, P. G. On fluid/wall slippage. *Langmuir*, **2002**, *18*, 3413–3414.
- 179 Maali, A.; Cohen-Bouhacina, T.; Kellay, H. Measurement of the slip length of water flow on graphite surface. *Appl. Phys. Lett.* **2008**, *92*, 053101.
- 180 Maali, A.; Bhushan, B. Nanobubbles and their role in slip and drag. *J Phys Condens Matter.* **2013**, *25*, 184003.
- 181 Wang, Y. L.; Bhushan, B.; Maali, A. AFM measurement of boundary slip on hydrophilic, hydrophobic, and superhydrophobic surfaces. *J. Vac. Sci. Technol., A* **2010**, *27*, 754–760.
- 182 Weijs, J. H.; Snoeijer, J. H.; Lohse, D. Formation of Surface Nanobubbles and the Universality of Their Contact Angles - A Molecular Dynamics Approach. *Phys. Rev. Lett.* **2012**, *108*, 104501.
- 183 Wang, C.; Li, Z.; Li, J.; Peng, X.; Hu, J.; Fang, H. High density gas state at water/graphite interface studied by molecular dynamics simulation. *Chin. Phys. B* **2008**, *17*, 2646–2654.
- 184 Koishi, T.; Yoo, S.; Yasuoka, K.; Zeng, X. C.; Narumi, T.; Susukita, R.; Kawai, A.; Furusawa, H.; Suenaga, A.; Okimoto, N.; Futatsugi, N.; Ebisuzaki T. Nanoscale Hydrophobic Interaction and Nanobubble Nucleation. *Phys. Rev. Lett.* **2004**, *93*, 185701.
- 185 Ohgaki, K.; Khanh, N. Q.; Joden, Y.; Tsuji, A.; Nakagawa, T. Physicochemical approach to nanobubble solutions. *Chem. Eng. Sci.* **2010**, *65*, 1296–1300.
- 186 Attard, P.; Moody, M. P.; Tyrrell, J. W. G. Nanobubbles: The Big Picture. *Physica A* **2002**, *314*, 696–705.
- 187 Jin, F.; Li, J.; Ye, X.; Wu, C. Effects of pH and ionic strength on the stability of nanobubbles in aqueous solutions of α -cyclodextrin. *J. Phys. Chem. B* **2007**, *111*, 11745–11749.
- 188 Jin, F.; Ye, J.; Hong, L.; Lam, H.; Wu, C. Slow Relaxation Mode in Mixtures of Water and Organic Molecules: Supramolecular Structures or Nanobubbles? *J. Phys. Chem. B.* **2007**, *111*, 2255–2261.
- 189 Bunkin, N. F.; Shkirin, A. V.; Ignatiev, P. S.; Chaikov, L. L.; Burkhanov, I. S.; Starosvetskij A. V. Nanobubble clusters of dissolved gas in aqueous solutions of electrolyte. I. Experimental proof. *J. Chem. Phys.* **2012**, *137*, 054706.
- 190 Bunkin, N. F.; Shkirin, A.V. Nanobubble clusters of dissolved gas in aqueous solutions of electrolyte. II. Theoretical interpretation. *J. Chem. Phys.* **2012**, *137*, 054707.
- 191 Dietrich, E.; Zandvliet, H. J. W.; Lohse, D.; Seddon, J. R. T. Particle tracking around surface nanobubbles. *J. Phys.: Condens. Matter* **2013**, *25*, 184009.

- 192 Craig, V. S. J. Surface nanobubbles of Knudsen bubbles? *Physics* **2011**, *4*, 70.
- 193 Petsev, N. D.; Shell, M. S.; Leal, L. G. Dynamic equilibrium explanation for nanobubbles' unusual temperature and saturation dependence. *Phys. Rev. Lett. E* **2013**, *88*, 10402.
- 194 Colaco, R.; Serro, A. P.; Saramago, B. On the stability of bubbles trapped at a solid-liquid interface: A thermodynamical approach. *Surf. Sci.* **2009**, *603*, 2870–2873.
- 195 Weijjs, J. H.; Lohse, D. Why surface nanobubbles live for hours. *Phys. Rev. Lett.* **2013**, *110*, 054501.
- 196 Weijjs, J. H.; Seddon, J. R.; Lohse, D. Diffusive Shielding Stabilizes Bulk Nanobubble Clusters. *ChemPhysChem* **2012**, *13*, 2197–2204.
- 197 Zhang, L.; Wang, C.; Tai, R.; Hu, J.; Fang, H. The Morphology and Stability of Nanoscopic Gas States at Water/Solid Interfaces. *ChemPhysChem* **2012**, *13*, 2188–2195.
- 198 Fang, H.-P.; Hu, J. Molecular dynamics simulation studies on some topics of water molecules on hydrophobic surface. *J. Nucl. Sci. Technol.* **2006**, *17*, 71–77.
- 199 Liu, G. M.; Craig, V. S. J. Improved Cleaning of Hydrophilic Protein-Coated Surfaces using the Combination of Nanobubbles and SDS *ACS Appl. Mater. Interfaces* **2009**, *1*, 481–487.
- 200 Seo, H.; Ko, W.; Jeon, S. Influence of dissolved air on the adsorption properties and stability of vesicles on various surfaces. *Appl. Phys. Lett.* **2012**, *101*, 153703.
- 201 Kolivoška, V.; Gál, M.; Hromadová, M.; Lachmanová, S.; Tarábková, H. Janda, P.; Pospíšil, L.; Turoňová, A. M. Bovine serum albumin film as a template for controlled nanopancake and nanobubble formation: In situ atomic force microscopy and nanolithography study. *Colloids. Surf. B, Biointerfaces* **2012**, *94*, 213–219.
- 202 Darwich, S.; Mougín, K.; Vidal, L.; Gnecco, E.; Haidara, H. Nanobubble and nanodroplet template growth of particle nanorings versus nanoholes in drying nanofluids and polymer films. *Nanoscale* **2011**, *3*, 1211–1217.
- 203 Hansson, P. M.; Swerin, A.; Scheolkopf, J.; Gane, P. A.; Thormann, E. Influence of Surface Topography on the Interactions between Nanostructured Hydrophobic Surfaces. *Langmuir* **2012**, *28*, 8026–8034.
- 204 Fan, Y.; Wang, R. Submicrometer-Sized Vaterite Tubes Formed Through Nanobubble-Templated Crystal Growth. *Adv. Mater.* **2005**, *17*, 2384–2388.
- 205 Bajpai, V.; He, P. G.; Dai, L. M. Conducting-Polymer Microcontainers: Controlled Syntheses and Potential Applications. *Adv. Funct. Mater.* **2004**, *14*, 145–151.
- 206 Vinogradova, O. I. Drainage of a thin liquid-film confined between hydrophobic surfaces *Langmuir* **1995**, *11*, 2213–2220.
- 207 Hua, S. Z.; Sachs, F.; Yang, D. X.; Chopra, H. D. Microfluidic actuation using electrochemically generated bubbles. *Anal. Chem.* **2002**, *74*, 6392–6396.
- 208 Stöckelhuber, K. W.; Radoev, B.; Wenger, A.; Schulzet, H. J. Rupture of Wetting Films Caused by Nanobubbles. *Langmuir* **2004**, *20*, 164–168.
- 209 Pashley, R. M. Effect of degassing on the formation and stability of surfactant-free emulsions and fine teflon dispersions. *J Phys. Chem. B* **2003**, *107*, 1714–1720.

- 210 Paxton, W. F.; Kistler, K. C.; Olmeda, C. C.; Sen, A.; St. Angelo, S. K.; Cao, Y.; Mallouk, T. E.; Lammert, P. E.; Crespi, V. H. Catalytic Nanomotors: Autonomous Movement of Striped Nanorods. *J. Am. Chem. Soc.* **2004**, *126*, 13424–13431.
- 211 Mishchuk, N.; Ralston, J.; Fornasiero, D. Influence of very Small Bubbles on particle/bubble Heterocoagulation. *J. Colloid Interface Sci.* **2006**, *301*, 168–175.
- 212 Schubert, H. Nanobubbles, hydrophobic effect, heterocoagulation and hydrodynamics in flotation. *Int. J. Miner. Process.* **2005**, *78*, 11–21.
- 213 Thomas, O. C.; Cavicchi, R. E.; Tarlov, M. J. Effect of Surface Wettability on Fast Transient Microboiling Behavior. *Langmuir* **2003**, *19*, 6168–6177.
- 214 Chambers, A.; Park, C.; Baker, R. T. K.; Rodriguez, N. M. Hydrogen storage in graphite nanofibers. *J. Phys. Chem. B* **1998**, *102*, 4253–4256.
- 215 Jeon, S.; Desikan, R.; Tian, F.; Thundat, T. Influence of nanobubbles on the bending of microcantilevers. *Appl. Phys. Lett.* **2006**, *88*, 103118–103123.
- 216 Feng, X.; Roy, S. C.; Grimes, C. A. Eliminating unwanted nanobubbles from hydrophobic solid/liquid interfaces: a case study using magnetoelastic sensors. *Langmuir* **2008**, *24*, 3918–3921.
- 217 Allongue, P.; Devilleneuve, C. H.; Pinsard, L.; Bernard, M. C. Evidence for hydrogen incorporation during porous silicon formation. *Appl. Phys. Lett.* **1995**, *67*, 941–943.
- 218 Tsai, W. L.; Hsu, P. C.; Hwu, Y.; Chen, C. H.; Chang, L. W.; Je, J. H.; Lin, H. M.; Groso, A.; Margaritondo, G. Building on bubbles in metal electrodeposition. *Nature* **2002**, *417*, 139–139.
- 219 Wei, Y.; Brandl, S.; Goodwin, F.; Back, D. 193nm Immersion-Related Defects and Strategies of Defect Reduction. *Future Fab. Intl.* **2007**, *22*, 65–68.
- 220 Coleman, D. H.; Popov, B. N.; White, R. E. Hydrogen permeation inhibition by thin layer Zn–Ni alloy electrodeposition. *J. Appl. Electrochem.* **1998**, *28*, 889–894.
- 221 Ball, P. Nanobubbles are not a Superficial Matter. *ChemPhysChem* **2012**, *13*, 2173–2177.
- 222 Seddon, J. R.; Lohse, D.; Ducker, W. A.; Craig, V. S. A Deliberation on Nanobubbles at Surfaces and in Bulk. *ChemPhysChem* **2012**, *13*, 2179–2187.
- 223 Craig, V. S. J. Formation of Micronuclei Responsible for Decompression Sickness. *J. Colloid Interface. Sci.* **1996**, *183*, 260–268.
- 224 Revalerio Corporation, US patent application 20100008997: Compositions and methods for treating asthma and other lung disorders. **2010**.

3

Motivation and research objectives

Two decades after the discovery of surface nanobubbles, the explanation and control of their existence and physical properties still pose major scientific challenges. This thesis focuses on the analysis of surface nanobubbles with Atomic Force Microscopy (AFM), which is the most common technique employed to study nanobubbles so far. The knowledge of nanobubble dimensions is essential to estimate correctly various nanobubble properties and parameters that are necessary to formulate correct theories on their formation and stability. It is known that AFM is an invasive technique to study soft samples. Even though much AFM evidence on nanobubbles has been published, it was not clear how the AFM method influenced the apparent shape of nanobubbles in AFM topographic images. The work presented in this thesis systematically addresses this issue for various relevant AFM imaging modes. This chapter describes the motivation behind the research and the main research objectives of the thesis, setting the framework for the experimental evidence presented in the following chapters.

3.1 Motivation

The idea behind the work presented in the following chapters was born after a long struggle to image surface nanobubbles with Atomic Force Microscopy (AFM). Despite the best efforts to create similar experimental conditions in each experiment and to keep them stable during several hours of the measurement, a substantial collection of different-looking AFM images was gathered. As an example, several of these AFM images are shown in Figure 3.1. Nanobubbles, if present in the images, looked differently in different experiments. They were big or small, circular, elongated or with irregular shapes, densely covering the sample surface or very sparse and difficult to localize. On some days, bubbles in images were perfectly round and the sample surface was smooth. On other days, bubbles were distorted, flat or doughnut-like shaped and images were blurred. On some days, bubbles were staying at their locations for hours. On other days, bubbles were “smeared” over the sample surface and the imaging was unstable. On some days, bubbles appeared in the images while on other days, even when “they were there”, for unknown reason, it was difficult to obtain a single stable image. Finally, there were days when nanobubbles did not appear on the sample in spite of using, what seemed, similar experimental conditions as in the days when they did appear.

Faced with these inconsistent results of AFM imaging, it was a natural reaction to ask: Why do surface nanobubbles look and “behave” so differently in different experiments? In order to answer this question it was necessary to look critically at the experimental technique, i.e. AFM and to investigate in detail the entire process of imaging nanobubbles.

In the previous chapter, an extensive comparison and discussion of past experimental and theoretical work on surface nanobubbles has been presented. Special attention has been paid to several remaining uncertainties considering the nanobubbles’ composition, curvature, contact angle, internal pressure and lifetime. From this description, it has become clear that AFM, which is the most commonly used technique to investigate surface nanobubbles, is far from ideal as an analytical tool. For example, the poor temporal resolution is often mentioned as a main drawback of the AFM, as compared to other techniques utilized – capturing a single AFM image usually requires several minutes. However, the benefit provided by the high spatial resolution of AFM outweighed this limitation and made AFM the main source of evidence on surface nanobubbles for the last 15 years.

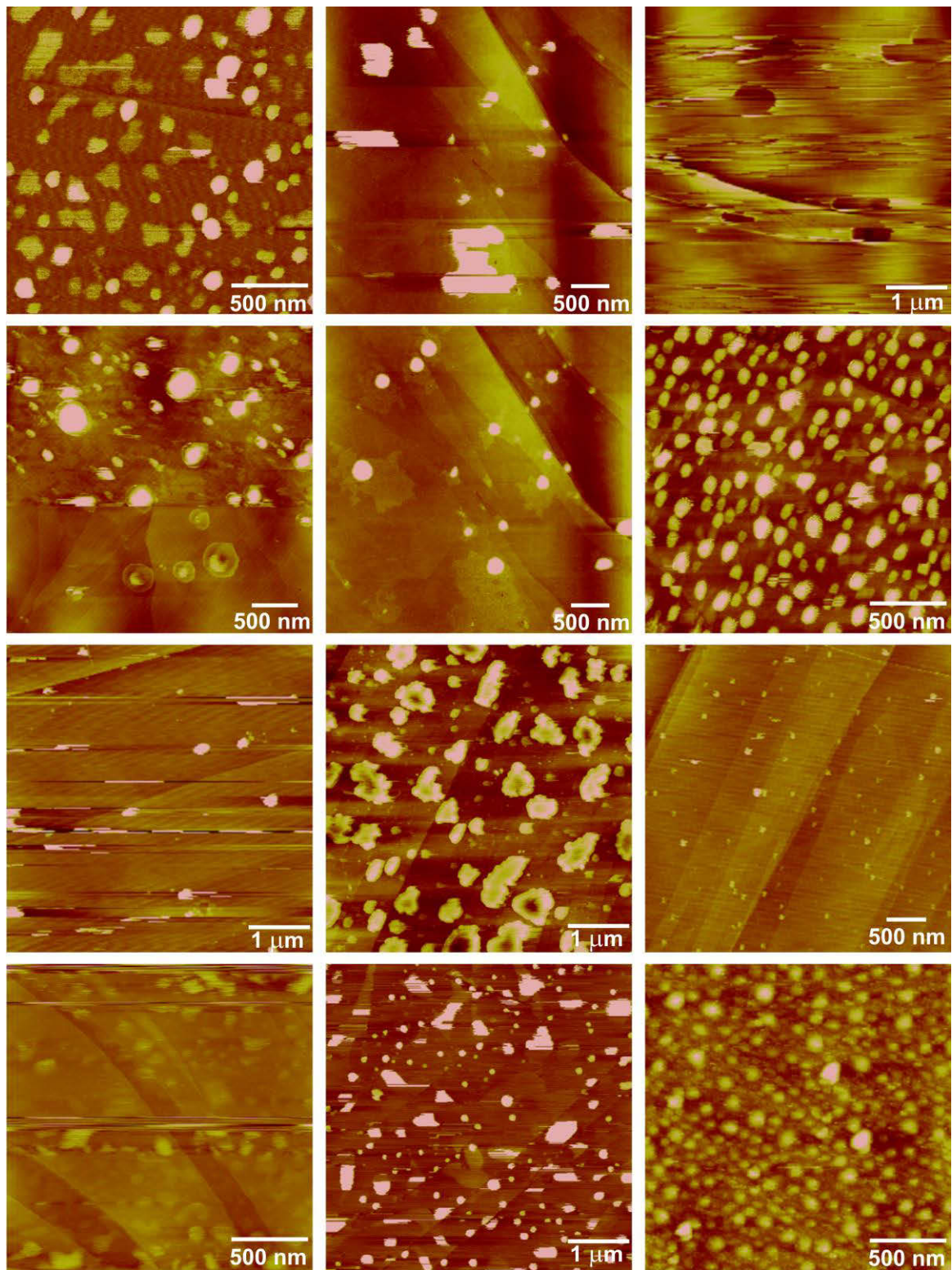


Figure 3.1. TM AFM topographic images of surface nanobubbles on highly oriented pyrolytic graphite (HOPG) acquired under supposedly similar (but in fact: various) experimental conditions. Vertical color scale of all images is 20 nm. Images reprinted from ref. [1].

While confronted with the ubiquity of AFM images of nanobubbles in the literature, it is easy to forget that the “predominance” of AFM in the nanobubble research does not automatically imply that all information provided by the machine is correct. Nor is the abundance of “similarly looking” data a guarantee that one always deals with similar “nanobubble-like” objects.²

Unfortunately, in addition to the “inconvenience” caused by the poor temporal resolution in most commercial AFM for measurements in liquid, AFM on surface nanobubbles suffers from several other issues. Often, they are not readily noticeable because they do not disturb the working of the microscope and the scanning protocol. Nevertheless, they may greatly influence the data in AFM images and hence all information about the sample that can be extracted from the images.

The AFM is invasive and, as the name indicates, it involves *force*. During scanning, a non-zero force must be exerted on the sample in order to produce an image or a force-displacement curve. If one deals with a sample containing very soft material, exerting force may change the shape and/or the properties of the sample, affect its functioning or even damage or destroy the sample.^{3,4,5,6} Even relatively soft cantilevers, although minimize the chance of damage, do not prevent the sample deformation completely, especially in the case of extremely soft materials. It has been shown that AFM imaging may lead to the height underestimation of soft surfaces such as polymers,^{7,8,9,10} lipid layers,¹¹ biological samples,¹² and droplets^{13,14,15,16,17} that in many cases is caused by sample deformation. In particular, the apparent topography of the sample may be influenced by several scanning parameters such TM AFM amplitude setpoint¹⁸ or approach speed of the tip.¹⁹

Bubbles, including surface nanobubbles, are very soft and fragile structures.^{20,21,22|23} This feature makes them extremely prone to deformation in response to any external force applied, which includes forces involved in the AFM scanning. The consequences for the apparent shape and dimensions might be crucial to several issues that have been discussed in the previous chapter, in particular nanobubble stability.

Although many authors agree that nanobubbles are possibly deformed during the AFM imaging, this issue was not mentioned explicitly in the reports describing experiments on nanobubbles, but for only few exceptions.^{24,25,26,27,28,29} This was probably caused by overmuch confidence put in the AFM, combined with a lack of detailed technical knowledge over how the imaging is performed. In a typical AFM device, a user is only required to set up the sample and the cantilever and to adjust few parameters before the software carries on and does the scanning automatically.

In many experiments on nanobubbles, with no external method to verify the correctness of displayed data, the shapes and the sizes of the features in AFM images were considered correct, or at least acceptable, as long as they resembled nanobubbles (without any serious deviations or obvious artefacts visible). Only few times the discussion was raised, if the features in the AFM images were indeed surface nanobubbles and not a sort of contaminations or liquid droplets.^{2,30,31} Apart from that, a large majority of AFM results was accepted as ‘nanobubbles’ without much pondering. Interestingly, as shown in the previous chapter, similar approaches did not necessarily apply to all sort of information derived based on the data measured from the AFM images of nanobubbles. This includes several hypotheses trying to explain the unusually long-term stability of nanobubbles observed experimentally.^{32,33} In defense of the widespread acceptance of the qualitative and the quantitative data provided by AFM images of nanobubbles one must say that, until recently, very little was known about the mechanism and extent of the nanobubble deformation during AFM scanning and their possible consequences for the sample topography displayed in an AFM image.

In short, despite several years of nanobubble research, the effects of AFM imaging on the appearance of nanobubbles in a particular experiment and a particular AFM image were unknown. Without that particular knowledge, maintaining constant experimental conditions during the scanning was virtually impossible. Lack of control over the imaging process resulted in unreliable experimental data and very likely led to a large diversity of AFM images of nanobubbles and caused problems during the imaging similar to the ones described at the beginning of this chapter.

With AFM being and, in the nearest future, remaining the main source of information on surface nanobubbles, there was a great need to learn about the influence of the scanning procedure on the quantitative information provided by AFM. A great number of imaging modes that have been employed to image nanobubbles, each of them having several parameters involved in the scanning, made this a challenging task. In addition, one must keep in mind that an AFM experiment on surface nanobubbles involves a procedure consisting of several steps including preparing the sample, assembling the setup, scanning and post-processing the image, and interpreting information derived from the image. In sum, it is a complex experimental system ruled by many factors. Dealing with a multidimensional parameter space required a series of carefully designed and executed AFM experiments carried on surface nanobubbles described in the following chapters of this thesis.

3.2 Research objectives

The central research hypothesis addressed in this thesis is that apparent dimensions of surface nanobubbles in AFM images do not reflect their actual dimensions, but are distorted because of the imaging.

The main objective of the work described in the following chapters is the determination of the factors that influenced the appearance of nanobubbles in AFM images and description of their actual impact on the bubble dimensions in order to reveal the actual bubble shape, size and mechanical properties. In particular, it was important to determine if the unusually flat profile of nanobubbles reported in numerous experiments was merely a consequence of AFM imaging or had its source in some independent mechanism. As already mentioned in Chapter 2, this information is of great importance to the theories concerning nanobubble formation and stability.

In the work, four AFM imaging modes were employed: TM, Peak Force Tapping, Force Volume and lift mode AFM. Each of these modes involves different parameters and protocol of imaging, and provides different information about the sample. Comparing the results obtained independently on nanobubbles in these four scanning modes made it possible to extract several principles that apply to AFM imaging of surface nanobubbles in general, and to separate them from the results inherent to a particular scanning mode.

First, in order to determine the influence of substrate wettability on the apparent nanobubble shape, nanobubbles have been tested in TM AFM on specially designed samples with similar physical properties (roughness) but different macroscopic contact angles. Apart from providing information on the bubble shape and nanoscopic contact angle, the experiment offered an opportunity to study the effect of tip convolution, i.e. the influence of non-zero AFM tip apex size on the apparent nanobubble dimensions, and to discuss the limitations it imposes on the imaging of nanobubbles on different substrates with real AFM tips. In addition, in the experiment, a protocol of the nanobubble analysis has been established.

In order to design a method to determine the unperturbed nanobubble shape, the next two experiments focused on the effects of non-zero force AFM scanning conditions employed during imaging on the apparent dimensions of surface nanobubbles. The aim of these experiments was to establish quantitatively the relation between the values of various scanning parameters and the change in the apparent nanobubble

sizes in AFM images in order to use the discovered relation to estimate the actual bubble dimensions.

Because to date most of the experiments on nanobubbles were done in TM AFM, the first step was to analyze the influence of two parameters that define the scanning force applied on the sample during the imaging performed in this mode, namely the amplitude of the cantilever oscillation and the amplitude setpoint ratio on the apparent nanobubble size. In the complementary Peak Force AFM experiment, the results obtained in TM AFM have been verified by investigating the effect of varying maximum scanning force on the apparent nanobubble dimensions. This mode allowed not only to control directly the force that was exerted on nanobubbles during imaging but also to obtain more straightforward information on the nanobubble deformation in response to the scanning force, which confirmed that deformation of nanobubbles is not unique to a specific imaging mode, but is a general phenomenon in the AFM experiments.

Next, the nanobubble deformation in the AFM has been investigated in detail. First, it was necessary to investigate the stiffness of nanobubble interface, in order to determine what kind of material nanobubbles are made of: gas, liquid or solid. Another interesting issue was the nature of interaction between an AFM tip and a nanobubble during imaging. For these purposes, the experiments in Force Volume and in combined Force Volume and lift mode AFM were performed.

Finally, a detailed analysis of the experimental results and comparing the AFM data with the numerical results of the modeling of tip-nanobubble interaction provided detailed information on the apparent and actual nanobubble shape.

3.3 References

- 1 Walczyk, W. Characterization of Surface Nanobubbles by Means of Atomic Force Microscopy. *Master Thesis*, University of Twente, Enschede, The Netherlands **2009**.
- 2 Berkelaar, R. P.; Dietrich, E.; Kip, G.; Kooij, S.; Zandvliet, H.; Lohse, D. Exposing nanobubble-like objects to a degassed environment. *Soft Matter* **2014**, *10*, 4947–4955.
- 3 Butt, H.-J.; Doppenschmidt, A.; Huttli, G.; Muller, E.; Vinogradova, O. I. Analysis of plastic deformation in atomic force microscopy: Application to ice. *J. Chem. Phys.* **2003**, *113*, 1194–1203.
- 4 Christenson, H. K. Note on Surface Deformations in Direct Force Measurements. *Langmuir* **1996**, *12*, 1404–1405.

- 5 Parker, J. L.; Attard, P. Deformation of Surfaces due to Surface Forces. *J. Phys. Chem.* **1992**, *96*, 10398–10405.
- 6 Weisenhorn, A. L.; Khorsandi, M.; Kasas, S.; Gotzos, V.; Butt, H.-J. Deformation and height anomaly of soft surfaces studied with an AFM. *Nanotechnology* **1993**, *4*, 106–113.
- 7 Zhong, Q.; Inniss, D. Fractured polymer/silica fiber surface studied by tapping mode atomic force microscopy. *Surf. Sci. Lett.* **1993**, *290*, 688–692.
- 8 Schönherr, H.; Frank, C. W. Ultrathin films of poly(ethylene oxides) on oxidized silicon. 2. In situ study of crystallization and melting by hot stage AFM. *Macromolecules* **2003**, *36*, 1199–1208.
- 9 Vancso, G. J.; Schönherr, H. Scanning Force Microscopy of Polymers. *Springer: Berlin*, **2010**.
- 10 Knoll, A.; Magerle, R.; Krausch, G. Tapping Mode Atomic Force Microscopy on Polymers: Where Is the True Sample Surface? *Macromolecules* **2001**, *34*, 4159–4165.
- 11 Kumar, B.; Pifer, P. M.; Giovengo, A.; Legleiter, J. The effect of set point ratio and surface Young's modulus on maximum tapping forces in fluid tapping mode atomic force microscopy. *Journ. Appl. Phys.* **2010**, *107*, 044508.
- 12 Morris, V. J.; Kirby, A. R.; Gunning, A. P. Atomic Force Microscopy for Biologists. *Imperial College Press: London*, **2010**.
- 13 Tamayo, J.; Garcia, R. Deformation, contact time, and phase contrast in tapping mode scanning force microscopy. *Langmuir*, **1996**, *12*, 4430–4435.
- 14 Herminghaus, S.; Fary, A.; Reim, D. Imaging of droplets of aqueous solutions by tapping-mode scanning force microscopy. *Ultramicroscopy* **1997**, *69*, 211–217.
- 15 Pompe, T.; Fery, A.; Herminghaus S. Imaging liquid structures on inhomogeneous surfaces by scanning force microscopy. *Langmuir* **1998**, *14*, 2585–2588.
- 16 Connell, S. D. A.; Allen, S.; Roberts, C. J.; Davies, J.; Davies, M. C.; Tandler, S. J. B.; Williams, P. M. Investigating the Interfacial properties of single-liquid nanodroplets by atomic force microscopy. *Langmuir* **2002**, *18*, 1719–1728.
- 17 Zhang, X.; Ducker, W. Interfacial oil droplets. *Langmuir* **2008**, *24*, 110–115.
- 18 Tamayo, J. ; García, R. Deformation, Contact Time, and Phase Contrast in Tapping Mode Scanning Force Microscopy. *Langmuir* **1996**, *12*, 4430–4435.
- 19 Rutland, M. W.; Tyrrell, J. W. G.; Attard, P. Analysis of atomic force microscopy data for deformable materials. *J. Adhesion Sci. Technol.* **2004**, *18*, 1199–1215.
- 20 Attard, P.; Miklavcic, S. J. Effective Spring Constant of Bubbles and Droplets. *Langmuir* **2001**, *17*, 8217–8223.
- 21 Attard, P.; Miklavcic, S. J. Effective Spring Constant of Bubbles and Droplets. *Langmuir* **2003**, *19*, 2532–2532.
- 22 Attard, P.; Miklavcic, S. J. Effective Spring Description of a Bubble or a Droplet Interacting with a Particle. *J Colloid Interface Sci.* **2002**, *247*, 255–257.
- 23 Zhao, B.; Song, Y.; Wang, S.; Dai, B.; Zhang, L.; Dong, Y.; Lü, J.; Hu, J. Mechanical mapping of nanobubbles by PeakForce atomic force microscopy. *Soft Matter* **2013**, *9*, 8837–8843.
- 24 Ishida, N.; Inoue, T.; Miyahara, M.; Higashitani, K. Nano bubbles on a hydrophobic surface in water observed by tapping-mode atomic force microscopy. *Langmuir* **2000**, *16*, 6377–6380.

- 25 Lou, S. T.; Ouyang, Z. Q.; Zhang, Y.; Li, X. J.; Hu, J.; Li, M. Q.; Yang, F. J. Nanobubbles on solid surface imaged by atomic force microscopy. *J. Vac. Sci. Technol., B* **2000**, *18*, 2573–2575.
- 26 Zhang, X. H.; Maeda, N.; Craig, V. S. J. Physical properties of nanobubbles on hydrophobic surfaces in water and aqueous solutions. *Langmuir* **2006**, *22*, 5025–5035.
- 27 Bhushan, B.; Wang, Y.; Maali, A. Coalescence and movement of nanobubbles studied with tapping mode AFM and tip-bubble interaction analysis. *J. Phys.: Condens. Matter* **2008**, *20*, 485004.
- 28 Yang, S.; Kooij, E. S.; Poelsema, B.; Lohse, D.; Zandvliet, H. J. W. Correlation between geometry and nanobubble distribution on HOPG surface. *Europhys. Lett.* **2008**, *81*, 64006.
- 29 Craig, V. S. J. Very small bubbles at surfaces – the nanobubble puzzle. *Soft Matter* **2011**, *7*, 40–48.
- 30 Evans, D. R.; Craig, V. S. J.; Senden, T. J. The hydrophobic force: nanobubbles or polymeric contaminant? *Physica A* **2004**, *339*, 101–105.
- 31 Häbich, A.; Ducker, W.; Dunstan, D. E.; Zhang, X. Do stable nanobubbles exist in mixtures of organic solvents and water? *J. Phys. Chem. B* **2010**, *114*, 6962–6967.
- 32 Lou, S. T.; Ouyang, Z. Q.; Zhang, Y.; Li, X. J.; Hu, J.; Li, M. Q.; Yang, F. J. Nanobubbles on solid surface imaged by atomic force microscopy. *J. Vac. Sci. Technol., B* **2000**, *18*, 2573–2575.
- 33 Ishida, N.; Inoue, T.; Miyahara, M.; Higashitani, K. Nano bubbles on a hydrophobic surface in water observed by tapping-mode atomic force microscopy. *Langmuir* **2000**, *16*, 6377–6380.

4

Surface nanobubbles on defined substrates

This chapter describes an atomic force microscopy (AFM) study of surface nanobubbles on surfaces with varied wettability. First, we compared two methods of preparation of molecular mixed self-assembled monolayers (SAMs) of octadecanethiol (ODT) and 16-mercaptohexadecanoic acid (MHDA) on template-stripped gold – coadsorption from solution and microcontact printing, in order to find the optimal conditions to prepare surfaces with well-defined contact angles. Next, with a set of substrates with systematically varied wettability, we investigated the effect of varying macroscopic contact angle of the sample on the apparent shape of surface nanobubbles in AFM height images by performing a series of experiments in tapping mode (TM) AFM. We found that for all tested samples, the nanoscopic contact angle θ_{nano} of the bubbles was higher than the corresponding macroscopic contact angle θ_{macro} . The values of θ_{nano} decreased with decreased θ_{macro} and the discrepancy between them became less pronounced for more hydrophilic surfaces. Very low $\theta_{nano} < 86^\circ$ were observed for the first time for nanobubbles on hydrophilic surfaces.

The chapter consists of the following publications:

Binary Self-Assembled Monolayers of Alkanethiols on Gold: Deposition from Solution versus Microcontact Printing and the Study of Surface Nanobubbles

Haider Bayat, Davide Tranchida, Bo Song, Wiktorja Walczyk, Elena Sperotto and Holger Schönherr

Langmuir **2011**, *27*, 1353–1358

Reprinted with permission. Copyright (2011) American Chemical Society.

Contribution in the article:

Haider Bayat: surface modification and analysis;

Dr. Davide Tranchida: surface modification and analysis, data analysis (spectra);

Dr. Bo Song: data analysis (spectra), AFM measurements;

Wiktorja Walczyk: AFM measurements and data analysis;

Dr. Elena Sperotto: synthesis of deuterated thiol, data analysis (spectra).

The experiment was designed and supervised, and the manuscript was written and perfected by **Prof. Dr. Holger Schönherr**.

Supporting Information directly follows the article.

Contact Angles of Surface Nanobubbles on Mixed Self-Assembled Monolayers with Systematically Varied Macroscopic Wettability by Atomic Force Microscopy

Bo Song, Wiktorja Walczyk and Holger Schönherr

Langmuir **2011**, *27*, 8223–8232

Reprinted with permission. Copyright (2011) American Chemical Society.

Contribution in the article:

Dr. Bo Song: surface modification and analysis, AFM measurements, contact angle measurements of macroscopic bubbles, Scanning Electron Microscopy imaging of AFM tips;

Wiktoria Walczyk: AFM measurements, AFM data analysis and calculations including: measurements of AFM tips, modification and application of a 3-dimensional spherical-cap fit model of nanobubble, error calculation, calculation of geometrical dependences, modelling and calculation of tip convolution.

The experiment was designed by **Prof. Dr. Holger Schönherr**. Based on discussions and guidance from **Prof. Dr. Holger Schönherr**, the manuscript was drafted by **Dr. Bo Song** and **Wiktoria Walczyk**, and perfected by **Prof. Dr. Holger Schönherr**.

Supporting Information directly follows the article.

Binary Self-Assembled Monolayers of Alkanethiols on Gold: Deposition from Solution versus Microcontact Printing and the Study of Surface Nanobubbles[†]

Haider Bayat,[‡] Davide Tranchida, Bo Song, Wiktoria Walczyk, Elena Sperotto, and Holger Schönherr*

Department of Physical Chemistry I, University of Siegen, Adolf-Reichwein-Strasse 2, 57076 Siegen, Germany.

[‡]Current address: University of Kabul, Science Faculty, Physical Chemistry Department, Kabul, Afghanistan.

Received October 1, 2010. Revised Manuscript Received November 11, 2010

The coadsorption of alkanethiols on noble metals has been recognized for a long time as a suitable means of affording surfaces with systematically varied wettability and other properties. In this article, we report on a comparative study of the composition of the mixed self-assembled monolayers (SAMs) obtained (i) by the coadsorption of octadecanethiol (ODT) and 16-mercaptohexadecanoic acid (MHDA) from ethanol and chloroform onto gold substrates and (ii) by microcontact printing using poly(dimethyl siloxane) (PDMS) stamps. SAMs prepared by coadsorption from solution showed a preferential adsorption of ODT for both solvents, but this trend was reversed in microcontact-printed SAMs when using chloroform as a solvent, as evidenced by contact angle and Fourier transform infrared (FTIR) spectroscopy measurements. An approximately linear relationship between the static contact angle and the degree of swelling with different solvents was observed, which suggests that the surface composition can be controlled by the interaction of the solvent and the PDMS elastomer. The altered preference is attributed to the different partitioning of the two thiols into solvent-swelled PDMS, as shown by ¹H NMR spectroscopy. Finally, molecularly mixed binary SAMs on ODT and MHDA on template-stripped gold were applied to study the effect of surface nanobubbles on wettability by atomic force microscopy (AFM). With a decreasing macroscopic contact angle measured through water, the nanoscopic contact angle was found to decrease as well.

Introduction

Self-assembled monolayers (SAMs) not only have been regarded as sometimes ideal model systems for studying fundamental aspects of surfaces and interfaces but also have quickly found application in various surface-based technologies.^{1,2} Application areas range from wettability control,³ sensor surface modification,⁴ and nanoparticle synthesis⁵ to surfaces with actively switchable properties,⁶ to name just a few areas of interest. Soon after starting in the 1980s with the first systematic studies of monolayer formation and properties (e.g., in thiol- and disulfide-based SAMs on gold^{7,8} or trichloroalkanesilane- or triethoxyalkanesilane-based monolayers on oxidized silicon⁹), it was realized that surface properties can be varied systematically between two limiting situations by assembling binary two-component SAMs.¹⁰ This feature among others predestines binary SAMs to be a platform for surface-based supramolecular chemistry.⁴

Initial studies focused, for instance, on an improved understanding of the fundamentals of wetting.¹¹ Wettability, as probed in contact angle measurements of a probe liquid (often water) was successfully varied in binary SAMs that were either molecularly mixed or phase separated into domains. Such wettability control may also provide a means to address a controversial phenomenon that has received increasing attention recently. The so-called surface nanobubbles,^{12–16} originally inferred as the potential origin of long-range forces observed in various force measurements on hydrophobic surfaces,¹⁷ have been observed by many groups worldwide. Their formation and extreme stability,¹⁸ which is in conflict with the curved interface and corresponding pressure difference, and the anomalously high contact angles¹⁹ are among the many unsolved questions in this area. The investigation of surface nanobubbles on ultraflat surfaces with systematically varied molecular composition may provide additional insight to clarify and demystify this phenomenon.

For alkanethiol SAMs on gold, it was realized that the coadsorption of two different thiols from a mixed solution often leads to fractional surface coverages that differ from the molar fraction of the thiols in solution.^{20,21} This altered surface composition

[†] Part of the Supramolecular Chemistry at Interfaces special issue.

*Corresponding author. Tel: +49 (0) 271 740 2806. Fax: +49 (0) 271 740 2805. E-mail: schoenherr@chemie.uni-siegen.de.

(1) Love, J. C.; Estroff, L. A.; Kriebel, J. K.; Nuzzo, R. G.; Whitesides, G. M. *Chem. Rev.* **2005**, *105*, 1103.

(2) Schreiber, F. *Prog. Surf. Sci.* **2000**, *65*, 151.

(3) Laibinis, P. E.; Whitesides, G. M. *J. Am. Chem. Soc.* **1992**, *114*, 1990.

(4) Spinke, J.; Liley, M.; Schmitt, F. J.; Guder, H. J.; Angermaier, L.; Knoll, W. *J. Chem. Phys.* **1993**, *99*, 7012.

(5) Brust, M.; Walker, M.; Bethell, D.; Schiffrin, D. J. *Chem. Commun.* **1994**, 801.

(6) Lahann, J.; Mitragotri, S.; Tran, T. N.; Kaido, H.; Sundaram, J.; Choi, I. S.; Hoffer, S.; Somorjai, G. A.; Langer, R. *Science* **2003**, *299*, 371.

(7) Nuzzo, R. G.; Allara, D. L. *J. Am. Chem. Soc.* **1983**, *105*, 4481.

(8) Porter, M. D.; Bright, T. B.; Allara, D. L.; Chidsey, C. E. D. *J. Am. Chem. Soc.* **1987**, *109*, 3559.

(9) Sagiv, J. *Israel. J. Chem.* **1979**, *18*, 339.

(10) Yang, J. Y. M.; Frank, C. W. In *Organic Thin Films: Structure and Applications*; Frank, C. W., Ed.; ACS Symposium Series 695; American Chemical Society: Washington, DC, 1998.

(11) Ulman, A.; Evans, S. D.; Shnidman, Y.; Sharma, R.; Eilers, J. E.; Chang, J. C. *J. Am. Chem. Soc.* **1991**, *113*, 1499.

(12) Hampton, M. A.; Nguyen, A. V. *Adv. Colloid Interface Sci.* **2010**, *154*, 30.

(13) Carambassis, A.; Jonker, L. C.; Attard, P.; Rutland, M. W. *Phys. Rev. Lett.* **1998**, *80*, 5357.

(14) Simonsen, A. C.; Hansen, P. L.; Klosgen, B. *J. Colloid Interface Sci.* **2004**, *273*, 291.

(15) Zhang, X. H.; Quinn, A.; Ducker, W. A. *Langmuir* **2008**, *24*, 4756.

(16) Brenner, M. P.; Lohse, D. *Phys. Rev. Lett.* **2008**, *101*, 214505.

(17) Parker, J. L.; Claesson, P. M.; Attard, P. *J. Phys. Chem.* **1994**, *98*, 34.

(18) Borkent, B. M.; Dammer, S. M.; Schönherr, H.; Vancso, G. J.; Lohse, D. *Phys. Rev. Lett.* **2007**, *98*, 204502.

(19) Borkent, B. M.; de Beer, S.; Mugele, F.; Lohse, D. *Langmuir* **2010**, *26*, 260.

has been attributed to kinetic effects because a SAM of one of the components is expected to be thermodynamically more stable, hence in the thermodynamic equilibrium only one type of thiol should comprise the SAM. Despite the kinetic control of the surface composition and hence surface properties and the concomitant need to determine the actual surface composition experimentally, binary self-assembled monolayers of alkanethiols on gold have found widespread application, as mentioned above.

Another important breakthrough in the area of surface modification was certainly the introduction of microcontact printing (μ CP) as a versatile, cost-efficient patterning methodology.^{22–24} As reported originally for alkanethiols on gold, this method has been expanded to other SAM systems and has found its way into industrial patterning. Surprisingly few reports address μ CP involving binary thiol mixtures. Salaita et al. reported on the deposition of a binary mixture of alkanethiols on a gold μ CP and dip pen nanolithography (DPN).²⁵ These authors observed intriguing phase-separation behavior via friction-mode atomic force microscopy (AFM). In particular, nearly complete phase-separation behavior was observed for microcontact-printed 16-mercaptohexadecanoic acid (MHDA) and 1-octadecanethiol (ODT) mixtures with inner hydrophilic and outer hydrophobic regions. This behavior was attributed to the different transport properties of the two thiols. Considering the different solubilities of the thiols in water, the formation of menisci by capillary condensation, especially for DPN, and the resulting different transport pathways, this observed phase separation can indeed be rationalized.

Obviously, the fabrication of molecularly thin patterns of adsorbate molecules is a central application of μ CP. However, μ CP also possesses the advantage that the formation of SAMs by contact printing exploiting conformal contact is much more rapid than assembly from solution. μ CP may also be the method of choice in situations in which the immersion of a composite substrate in an organic solvent must be avoided to prevent the extraction of potential contaminants and the deposition of these trace compounds on the desired surface. One example is template-stripped gold, which is prepared by peeling an epoxy-backed gold layer from an atomically smooth substrate.²⁶ Depending on the solvent used to deposit the thiols, the epoxy glue may become unstable or trace amounts of the components may be extracted and deposited on the actual gold surface, thereby compromising the SAM quality.

This potential drawback of solution deposition and potential cross-contamination was the motivation for the current study. As we report in this article, we investigated the coadsorption behavior of binary solutions of MHDA and ODT on gold surfaces and compared the possibly altered fractional surface coverage of the thiols in the resulting SAMs with SAMs prepared by μ CP using a featureless stamp. In addition to the identification of a novel means to control SAM composition in binary self-assembled monolayers of alkanethiols on gold, we applied binary SAMs with systematically varied wettability in a preliminary study of surface nanobubbles. This work forms the basis for a broadened scope of mixed SAMs as a supramolecular platform for studies on surfaces.

Experimental Section

Materials. 16-Mercaptohexadecanoic acid (MHDA, $\text{HS}(\text{CH}_2)_{15}\text{COOH}$, 90%) and 1-octadecanethiol (ODT, $\text{HS}(\text{CH}_2)_{17}\text{CH}_3$, 98%) were obtained from Aldrich and used without further purification. Ethanol and chloroform, used as solvents for the thiols, were purchased from J. T. Backer (ethanol was 97% with 1% petroleum ether, chloroform was stabilized with about 0.75% ethanol). Further experiments were carried out with other solvents including dichloromethane (DCM, 99.99%, Fisher), diethyl ether (99.98%, Fisher), ethyl acetate (99.99%, Fisher), acetonitrile (99.99%, Fisher), and methanol (99.8%, J. T. Baker). Glass substrates for gold evaporation were obtained from Menzel-Glaser. The substrates, cut to a size of 60 mm \times 26 mm, were immersed in a solution of Nochromix (Aldrich, 2.0 g Nochromix in 18 mL of concentrated sulfuric acid) overnight at room temperature. Water (Werner Reinstwasser, E-pure) with a resistivity higher than 17.9 M Ω cm was used in the experiments to clean glass substrates before and after gold evaporation.

Sample Preparation. A thermal evaporator (MED 010/Balzers Union) operating at 10⁻⁶ mbar was used to deposit approximately 2 nm of chromium and 150 nm of gold (99.99%, Allgemeine Gold und Silberscheideanstalt AG) onto the glass substrates. Evaporated gold substrates (Au/Cr/glass) were cleaned by exposure to chloroform, followed by rinsing with ethanol and water. Afterwards, the substrates were further cleaned with piranha solution, a sulfuric acid/hydrogen peroxide solution (3:1 v/v), for 15 s. (**Caution!** Piranha solution is very reactive and may explode on coming into contact with organic solvents. Extreme precautions must be taken at all times.) After piranha treatment, the substrates were immersed immediately in water and then rinsed thoroughly with water and ethanol, followed by drying in a stream of nitrogen. Stock solutions of ODT and MHDA in ethanol and chloroform, respectively, were prepared at a concentration of 1.0 mM, followed by mixing in the appropriate ratios to obtain mixed solutions with a known composition of each thiol and a constant total concentration of adsorbate. Gold substrates were immersed for 20 h in these solutions that were saturated with argon. After the formation of the self-assembled monolayers, the substrates were rinsed with pure solvent and dried in a stream of nitrogen.

Microcontact Printing. The stamp material Sylgard-184 PDMS, obtained from Dow Corning, was mixed in a polystyrene Petri dish in a 1:10 curing agent/prepolymer ratio. After the two components were mixed, PDMS was degassed in a vacuum chamber and then cured overnight at 60 °C. Thin PDMS slabs were cut with a scalpel and used as stamps to provide unpatterned homogeneous SAMs. Each stamp was immersed in ethanol and sonicated for 2 min prior to use to remove dust and impurities on the PDMS. The PDMS slab was dried in a stream of nitrogen and then immersed for 4 min in the corresponding solution. Afterwards, the slab was rinsed with the corresponding pure solvent and briefly dried in a stream of nitrogen. Then the stamp was brought into contact with the cleaned gold surfaces. A mass of 500 g was placed on the PDMS stamp for 10 min in order to achieve conformal contact. After this time, the gold surfaces were rinsed with ethanol and dried with nitrogen.

Contact Angle Measurements. Contact angles were measured with minimal delay on a contact angle microscope (Dataphysics OCA-15) with water as the probe liquid. Static, advancing, and receding contact angles were measured at room temperature.

Fourier Transform Infrared Spectroscopy. The FTIR spectra in grazing incidence reflection mode were obtained using a Bruker IFS 66v FTIR spectrometer equipped with a VEE MAX II grazing-angle accessory (Pike Technologies) and a liquid-nitrogen-cooled cryogenic mercury cadmium telluride (MCT) detector. The spectral resolution was maintained at 2 cm⁻¹ with 1000 scans. Background spectra were obtained from a gold substrate modified with a SAM of 1-decanthiol-*d*₂₁.

Template-Stripped Gold. Silicon wafers were cut into 1 cm² pieces, pretreated with piranha solution until no gas bubbles

(20) Laibinis, P. E.; Fox, M. A.; Folkers, J. P.; Whitesides, G. M. *Langmuir* **1991**, *7*, 3167.

(21) Laibinis, P. E.; Nuzzo, R. G.; Whitesides, G. M. *J. Phys. Chem.* **1992**, *96*, 5097.

(22) Kumar, A.; Biebuyck, H. A.; Whitesides, G. M. *Langmuir* **1994**, *10*, 1498.

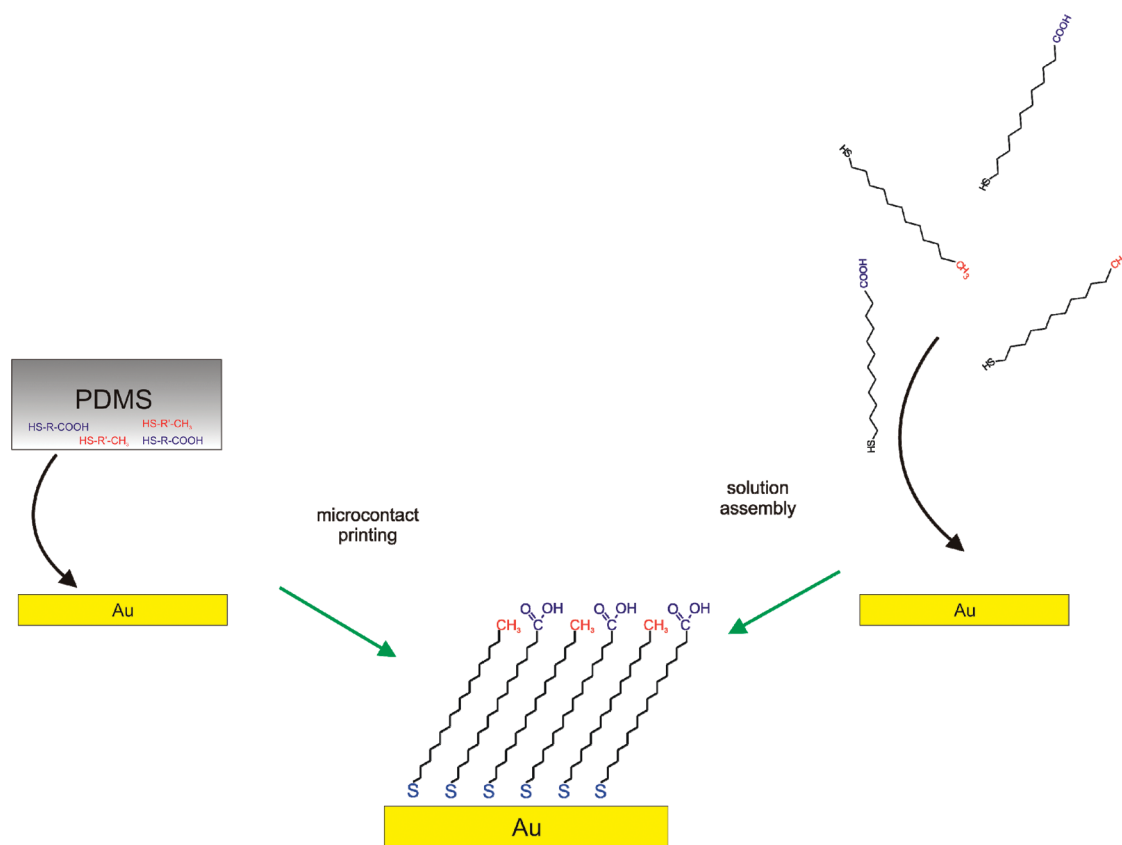
(23) Smith, R. K.; Lewis, P. A.; Weiss, P. S. *Prog. Surf. Sci.* **2004**, *75*, 1.

(24) Kaufmann, T.; Ravoo, B. J. *Polym. Chem.* **2010**, *1*, 371.

(25) Salaita, K.; Amarnath, A.; Maspoeh, D.; Higgins, T. B.; Mirkin, C. A. *J. Am. Chem. Soc.* **2005**, *127*, 11283.

(26) Hegner, M.; Wagner, P.; Semenza, G. *Surf. Sci.* **1993**, *291*, 39.

Scheme 1. Schematic of Solution Assembly and Microcontact Printing of Binary Thiol Mixtures on Gold



? : composition, phase separation, wettability etc.

evolved, and then thoroughly washed with water and blown dry with nitrogen. The dried, dust-free pieces of the wafer were directly placed into the vacuum chamber for the evaporation of gold. Vacuum was held at approximately 10^{-6} to 10^{-5} mbar, and the evaporation rate was less than 0.1 nm/s for the first 15 nm and was then increased to 0.4 nm/s to yield a final gold thickness of between 100 and 150 nm. The samples were allowed to cool for 15 min in the vacuum chamber and after venting were immediately glued onto the clean glass slides (EPO-TEK 377) and cured at 150 °C for 2 h. The glass substrate was separated from the silicon wafer using tweezers. Special care was taken not to glue the glass directly to the bare silicon wafer surface. The flat gold surfaces that were obtained were used without any further treatment.

Atomic Force Microscopy (AFM) Measurement. A Multi-Mode IIIa AFM (Veeco, Santa Barbara, California) equipped with a tapping-mode liquid cell was used. The cantilever-tip assemblies (Veeco type MLCT, nominal resonance frequency of 15 Hz and spring constant of 0.03 N/m) were cleaned in oxygen plasma (30% power for 1 min on a SPI Plasma Prep II) prior to use. After the substrate was mounted on the scanner, a drop of purified water was placed on the substrate and then the liquid cell with a mounted tip was put on the top of substrate. All experiments were conducted in tapping mode at room temperature after an equilibration time of 60 min.

Results and Discussion

The assembly of the two alkanethiols from ethanol and chloroform solution onto clean gold substrates was investigated first to establish the relationship between the molar fraction in solution and the fractional surface coverage in the SAM after an assembly

time of 20 h. The compositional analysis is based on the measurement of the water contact angles and the application of the Cassie (eq 1)²⁷ and Israelachvili equations (eq 2).²⁸ It is well known that contact angle data on heterogeneous surfaces can be modeled successfully by the Cassie equation. The equation is particularly applicable when the surface is composed of separate, chemically distinct patches. By contrast, when the size of the patches approaches molecular dimensions, the Israelachvili equation is used.

$$\cos \theta_{\text{expt}} = x_A \cos \theta_A + x_B \cos \theta_B \quad (1)$$

$$(1 + \cos \theta_{\text{expt}})^2 = x_A (1 + \cos \theta_A)^2 + x_B (1 + \cos \theta_B)^2 \quad (2)$$

where θ_{expt} , θ_A , and θ_B denote the contact angles of the mixed SAM, a SAM of pure thiol A, and a SAM of pure thiol B, respectively, and x_A and x_B denote the fractional surface coverages of the corresponding components.

In addition to the contact angle data analysis, the grazing-angle reflection FTIR spectra were recorded and analyzed after deconvolution. From the contact angle data shown in the Supporting Information and the FTIR spectra shown in Figure 1, it is obvious that the type of solvent in this case has a marginal influence on the composition of the mixed SAMs. A preferred adsorption of ODT is obvious. The FTIR spectra show the well known absorbances attributed to the C–H stretching vibrations of the methyl and

(27) Cassie, A. B. D.; Baxter, S. *Trans. Faraday Soc.* **1944**, *40*, 546.

(28) Israelachvili, J. N.; Gee, M. L. *Langmuir* **1989**, *5*, 288.

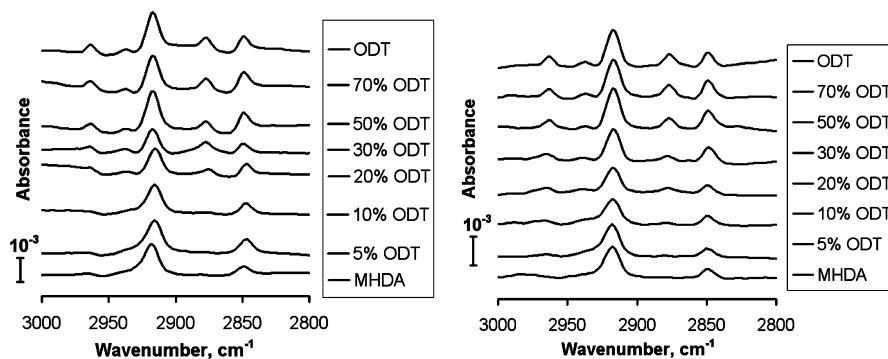


Figure 1. Grazing-angle FTIR spectra of mixed SAMs assembled from ethanol solutions (left) and chloroform solutions (right).

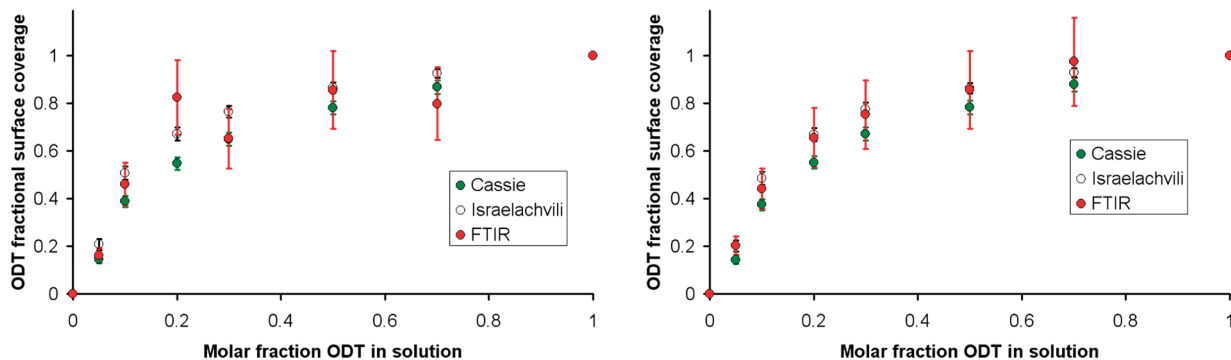


Figure 2. Fractional surface coverage of mixed SAMs assembled from ethanol solutions (left) and chloroform solutions (right) as determined from contact angle measurements and the application of the Cassie and Israelachvili equations, as well as from FTIR data.

methylene groups of the thiols comprising the SAMs.⁸ The C–H stretching region of the FTIR spectra of ODT is different from that of MHDA because ODT shows C–H stretching bands of the methyl group ($\nu_a \text{CH}_3$, $\sim 2964 \text{ cm}^{-1}$), an asymmetric methylene stretching band ($\nu_a \text{CH}_2$, $\sim 2919 \text{ cm}^{-1}$), a symmetric methyl stretching band ($\nu_s \text{CH}_3$, $\sim 2879 \text{ cm}^{-1}$), and a symmetric methylene stretching band ($\nu_s \text{CH}_2$, $\sim 2850 \text{ cm}^{-1}$), and MHDA shows only two peaks related to the methylene stretches. In the spectra, it can be noted that the peaks at ~ 2879 and $\sim 2964 \text{ cm}^{-1}$ decrease gradually from the pure ODT to mixed SAMs obtained from solutions of mixed thiols, finally vanishing for the pure MHDA.

The area under the peaks was deconvoluted, and the ratio of the two thiols was hence estimated. The data are summarized and compared to the fractional surface coverages calculated on the basis of the Cassie and Israelachvili equations, respectively, in Figure 2. Despite the scatter in the data, it becomes evident that mixed SAMs of ODT and MHDA show a preferential adsorption of the hydrophobic long-chain thiol and irrespective of the solvent used for assembly do not exhibit significant differences.

These data can be compared to data by Bain and Whitesides, who analyzed binary SAMs of undecanethiol and mercaptoundecanoic acid,²⁹ and work by Lee et al.,³⁰ who compared the coadsorption of hexadecanethiol and MHDA. In both cases, a much less pronounced preference for the adsorption of the methyl-group-terminated thiol was observed. This effect can be attributed to the practically negligible difference in chain length for those systems. Consequently, our measurements are in agreement with literature data, which show that an increase in the

chain-length difference between the two thiols favors the adsorption of the long-chain thiol.³¹ Thus far, the data are in full agreement with the available literature.

In general, we observed that the Israelachvili equation describes the compositional data obtained from the analysis of the FTIR data better than the Cassie equation. This may indicate that the binary SAMs are mixed on very small length scales. Independent confirmation of this assertion was obtained by time-of-flight secondary ion mass spectrometry (ToF-SIMS, Supporting Information) and lateral force microscopy measurements (Supporting Information).³²

When binary SAMs were prepared by μCP , a pronounced effect of the solvent used to apply the thiols to the stamp was observed. For stamping, a featureless stamp was used to avoid possible effects of capillary condensation and differential solubility of the two thiols in the water meniscus.²⁵ SAMs prepared using ethanol showed an enhanced preference for the adsorption of ODT, whereas for chloroform the opposite trend was observed (Figures 3 and 4, contact angle data in Supporting Information). In the latter case, MHDA adsorption was preferentially adsorbed.

In principle, this pronounced effect can be attributed to the differential uptake or differential release (or both) of the corresponding thiols into the PDMS stamp. A striking difference between the two solvents used thus far is the degree of swelling of PDMS. Although ethanol possesses only a marginal, if any, effect on PDMS and thus represents a solvent of choice for inking stamps in μCP , chloroform swells the stamp to a significant extent. The swelling of the stamp will certainly alter the partitioning of low-molar-mass compounds in the stamp. Thus, the degree of swelling was measured for a range of different solvents for a

(29) Bain, C. D.; Whitesides, G. M. *Langmuir* **1989**, *5*, 1370.

(30) Lee, G. S.; Kim, T. Y.; Choi, H.; Ahn, D. J. *Korean J. Chem. Eng.* **2009**, *26*, 691.

(31) Bain, C. D.; Whitesides, G. M. *J. Am. Chem. Soc.* **1989**, *111*, 7164.

(32) Wilbur, J. L.; Biebuyck, H. A.; MacDonald, J. C.; Whitesides, G. M. *Langmuir* **1995**, *11*, 825.

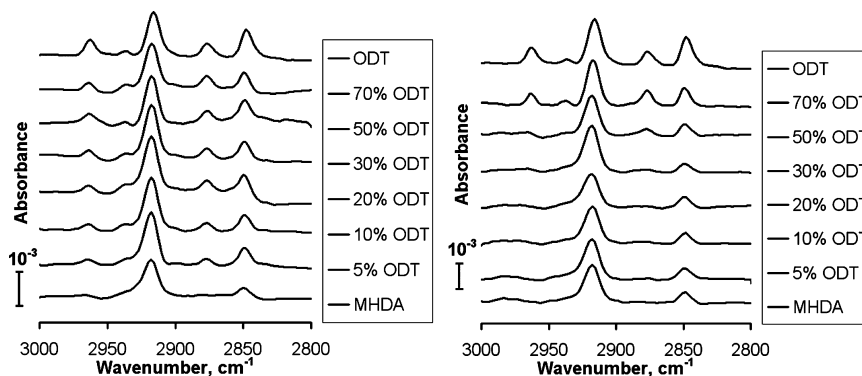


Figure 3. Grazing-angle FTIR spectra of mixed SAMs prepared by μ CP using ethanol solutions (left) and chloroform solutions (right).

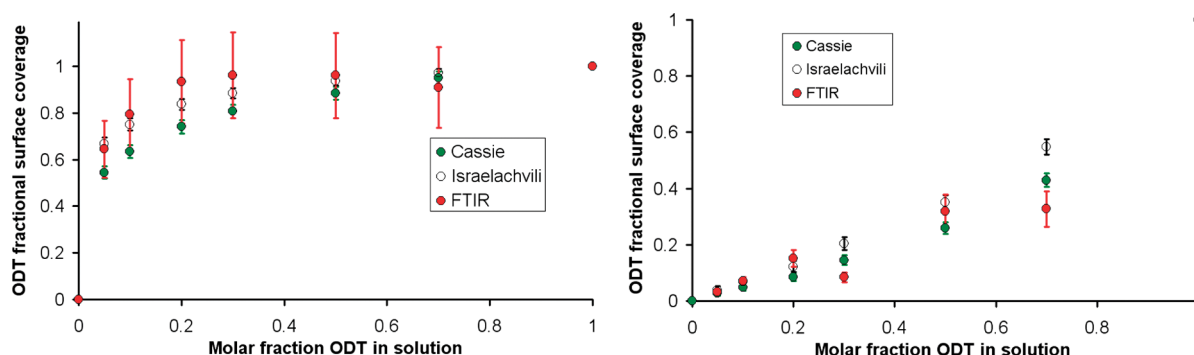


Figure 4. Fractional surface coverage of mixed SAMs prepared by μ CP using ethanol solutions (left) and chloroform solutions (right) as determined from contact angle measurements and the application of the Cassie and Israelachvili equations as well as from FTIR data.

constant immersion time of 10 min in a solution of $x_{\text{ODT}}(\text{solution}) = 0.5$ (Table 1). If we compare the degree of swelling and the resulting surface composition of the binary SAM, then a clear correspondence is observed (Figure 5). The higher the degree of swelling, the lower the contact angle and hence the higher the fraction of MHDA in the binary SAM at constant $x_{\text{ODT}}(\text{solution})$. It is noted that the measured contact angle data cannot be rationalized on the basis of the dielectric constants of the solvents or the polarity or H-bonding capability (Supporting Information).

From these data, one can conclude that the partitioning of the two thiols into the stamp and the release indeed depends on the degree of swelling of the stamp. We postulate that an increase in the degree of swelling of the stamp results in a higher fraction of the more hydrophilic thiol in the apolar PDMS matrix. This postulate is supported by extraction experiments carried out by placing PDMS slabs into solutions with $x_{\text{ODT}} = 0.7$ in chloroform. The ratio of the two thiols was determined by solution ^1H NMR after bringing the solutions to dryness and taking up the solid with deuterated chloroform. An increase in the MHDA fraction of up to 15% was thus observed.

These data show that the composition of practically molecularly mixed binary SAMs can be conveniently adjusted via the selection of the appropriate ratios of the two thiols as well as the choice of the solvent and the mode of SAM formation. In particular, μ CP of binary mixtures with complementary preferential adsorption compared to solution assembly has been established here as a very rapid method for depositing mixed SAM. Most notably, the method can be expanded to situations in which liquid organic solvent must be excluded.

The binary SAMs described above were applied to interrogate the recently controversially discussed gas cavities (called surface

Table 1. Degree of Swelling of the PDMS Stamps Determined Gravimetrically

solvent	% weight difference
chloroform	56 ± 1.0
dichloromethane	60 ± 1.0
diethyl ether	52 ± 1.0
ethyl acetate	20 ± 1.0
acetonitrile	1.0 ± 0.2
ethanol	0 ± 0.2
methanol	1.0 ± 0.2

nanobubbles) at the solid–liquid interface.^{12–19} By systematic variations of the SAM composition, the wettability of the surface can be varied over a broad range and the anomalously high contact angle observed thus far for the nanobubbles can be addressed.¹⁹ As shown in Figure 6, elevated features with the appearance of spherical caps were observed by tapping AFM in water at SAM surfaces on template-stripped gold for SAMs with different macroscopic contact angles. The observed features resemble those reported in the recent literature and can be faithfully assigned to nanobubbles because the consistency checks, including imaging the underlying substrate at higher forces in contact mode and observing the nanobubbles at low forces (or tapping mode) afterwards, were successfully carried out.

Nanobubbles were detected on SAMs of ODT (Supporting Information) and binary SAMs with static contact angles as low as 15° . Because all substrates possess identical roughness values of the underlying template-stripped gold substrate, any roughness effect can be neglected. In all measurements, the amplitude set point was adjusted to be as high as possible and the rms amplitude was adjusted to be as low as possible to ensure the minimum impact of the tip oscillation on the measured bubble dimensions. The dimensions of these nanobubbles were found to be, depending

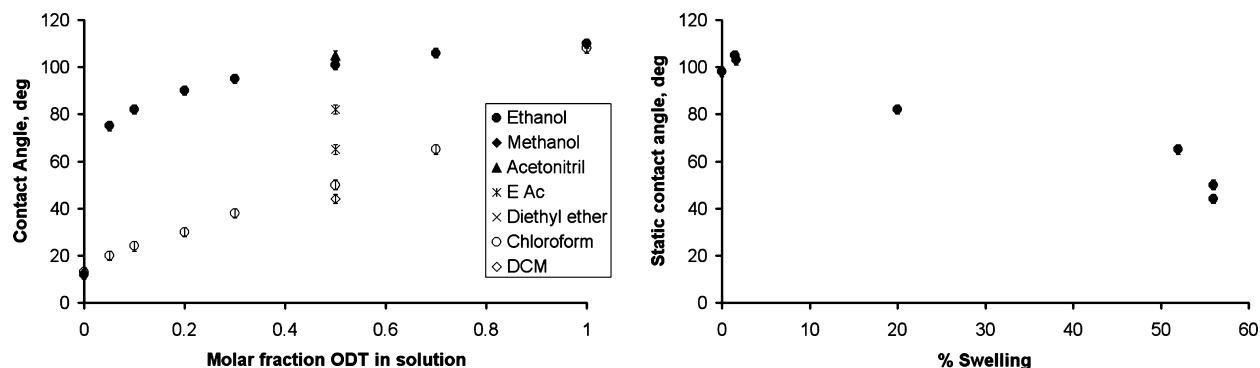


Figure 5. Contact angles of mixed SAMs prepared by μ CP using different solvents (left) and plot of static contact angles vs degree of swelling (right). A molar fraction of ODT in the solution of 0.5 was used for all experiments.

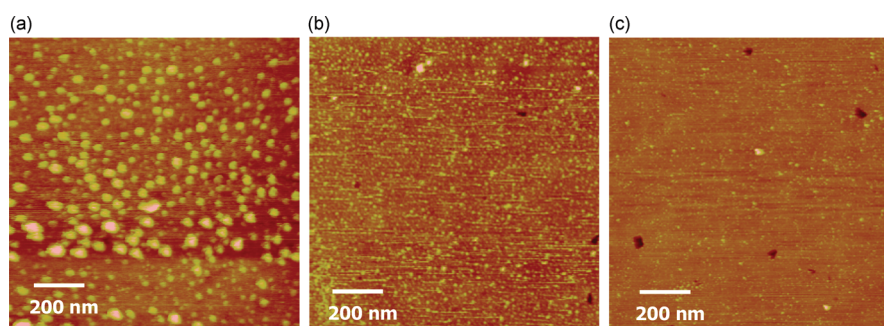


Figure 6. Tapping-mode AFM height images acquired in water on binary SAMs with macroscopic contact angles of (a) 50, (b) 30, and (c) 15° (the height scale covers 20 nm). The depressions observed in panels b and c are isolated imperfections in the template-stripped gold substrate that were found to have no impact on the AFM data observed.

on the wettability of the SAM, approximately between 5 and 20 nm in height and between 20 and 50 nm in apparent radius. It is striking that nanobubbles on the more hydrophilic SAMs appear to be very small, thus increasing the uncertainty in the quantitative determination of the bubbles' dimensions. In addition, the data is heavily convoluted because the AFM tip can track only the top part of the bubble.

A truly quantitative analysis of these data is beyond scope of this article because not only the impact of the AFM tip and the force exerted on the cavities on the height data but also an accurate deconvolution (to correct for tip-broadening effects) and the errors in the fitting procedure (fit of the observed profile to a spherical cap) must be considered. A complete account of this ongoing work will be reported elsewhere.

Conclusions

The composition of binary self-assembled monolayers of MHDA and ODT assembled from ethanol and chloroform solution was compared for the first time to that of mixed SAMs prepared by microcontact printing using featureless stamps. Although the solution assembly data was found to be in agreement with literature data on the coadsorption of methyl- and carboxylic acid-terminated thiols with identical chain length and preferential adsorption for longer-chain thiols, the composition of microcontact-printed binary SAMs was found to depend on the degree of swelling of the PDMS stamp. Compared to ethanol that

does not swell the elastomer and hence led to the preferred adsorption of ODT, chloroform showed the opposite trend. Therefore, the composition of mixed monolayers can be tuned by using an appropriate solvent at constant molar fractions of thiols. Molecularly mixed binary SAMs were further investigated at the solid–liquid interface by in situ tapping-mode AFM. Nanobubbles were observed for all SAMs, even when the macroscopic contact angle was as low as 15°. This work forms the basis for a systematic and quantitative analysis of surface nanobubbles on SAMs with systematically altered wettability.

Acknowledgment. We thank M.Sc. Igor Aronov (analytical chemistry) for the acquisition of the ToF-SIMS data and Dipl. Ing. Gregor Schulte and Brigitte Niesenhaus for excellent technical assistance. H.B. gratefully acknowledges financial support from the German Academic Exchange Service (Deutscher Akademischer Austauschdienst, DAAD). D.T. and B.S. gratefully acknowledge financial support from the Alexander von Humboldt Foundation. W.W. gratefully acknowledges the University of Siegen for a stipend for female doctorate students.

Supporting Information Available: Contact angle data for coadsorbed SAMs, microcontact-printed SAMs, lateral force microscopy, ToF-SIMS data of binary SAMs on template-stripped gold, AFM data of nanobubbles on SAMs of ODT, and solvent characteristics. This material is available free of charge via the Internet at <http://pubs.acs.org>.

Binary self-assembled monolayers of alkanethiols on gold: Deposition from solution versus microcontact printing and the study of surface nanobubbles

Haider Bayat,[#] Davide Tranchida, Bo Song, Wiktoria Walczyk, Elena Sperotto,

and Holger Schönherr*

Supporting Information

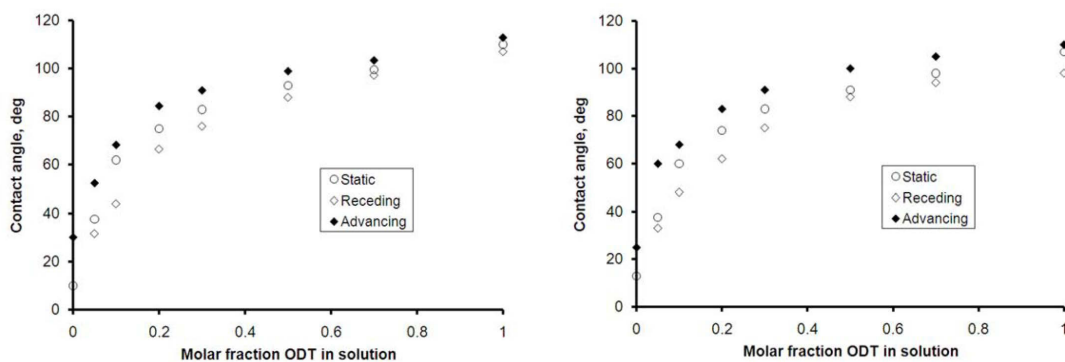


Figure S-1. Contact angle data of mixed SAMs assembled from ethanol solutions (left) and chloroform solutions (right)

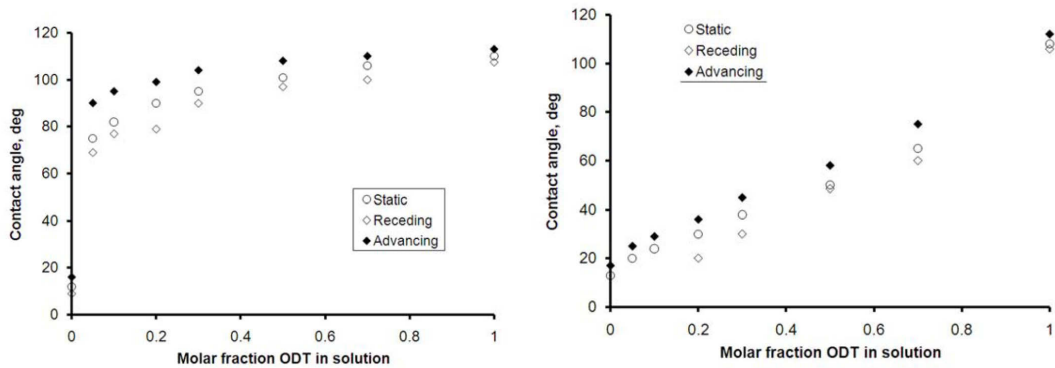


Figure S-2. Contact angle data of mixed SAMs prepared by μ CP using ethanol solutions (left) and chloroform solutions (right)

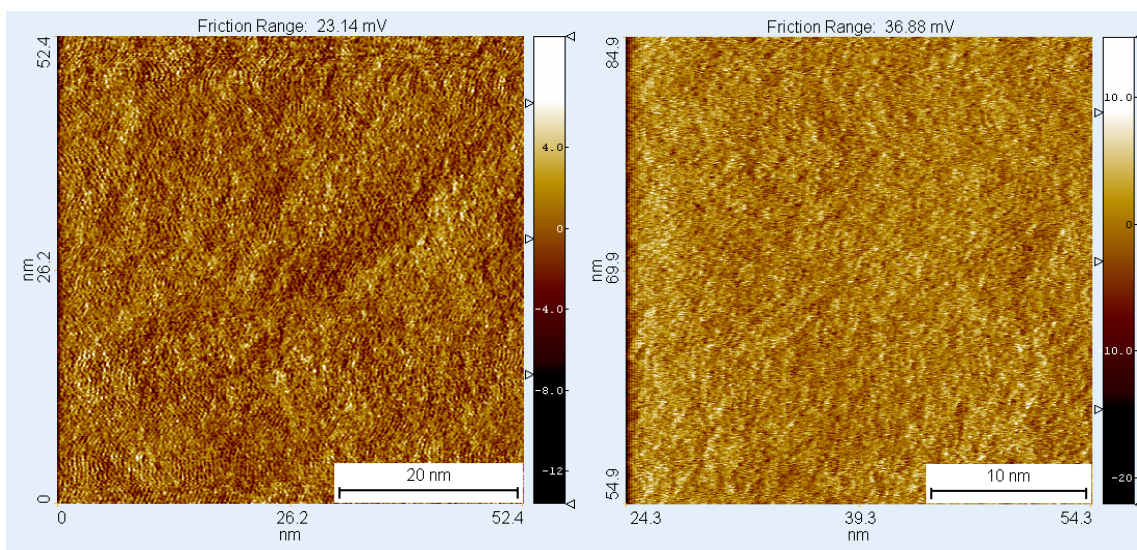


Figure S-3. LFM data of $x_{ODT} = 0.75$ and $x_{ODT} = 0.50$. Also on small scan sizes no domains were observed, which indicates that the two thiols are mixed down to molecular length scales (NB: The friction contrast between pure ODT and MHDA SAMs is known to be very pronounced^{Error! Bookmark not defined.}).

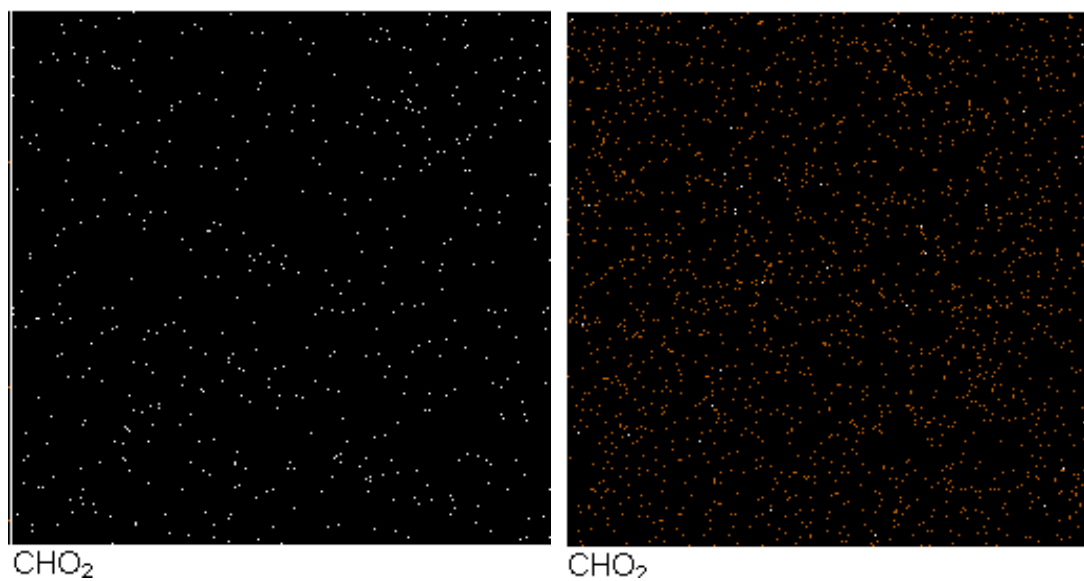


Figure S-4. ToF-SIMS data for the CHO₂ ion (left: positive mode; right: negative mode; image size 100 μm x 100 μm) for a binary SAM prepared from a solution with $x_{\text{ODT}} = 0.5$.

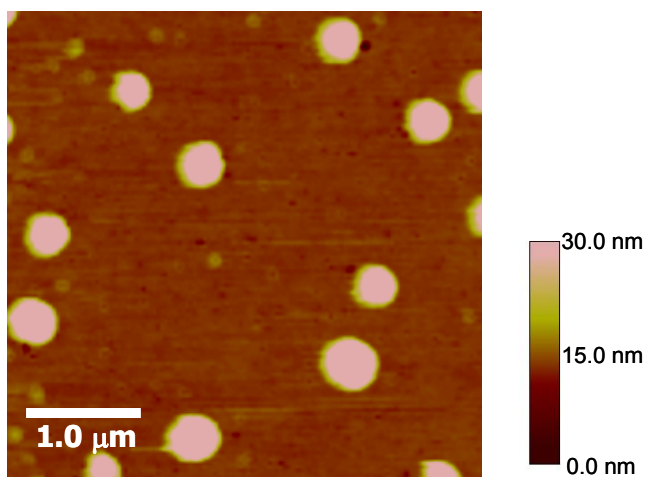


Figure S-5. Tapping mode AFM images acquired in water on SAM of ODT.

Table S-1. *Solvents characteristic properties and corresponding contact angle*

Solvents	Polarity	H-bond	Dielectric constant	Contact angle	
				50% ^(solvent-ODT)	50% ^(solvent-MHDA)
Chloroform	-	-	4.8		50
DCM	-	-	9.1		44
Diethyl ether	-	+	4.3		65
Ethyl acetate	+	+	6		82
Acetonitril	+	+	37		105
Ethanol	+	+	33		98
Methanol	+	+	30		103

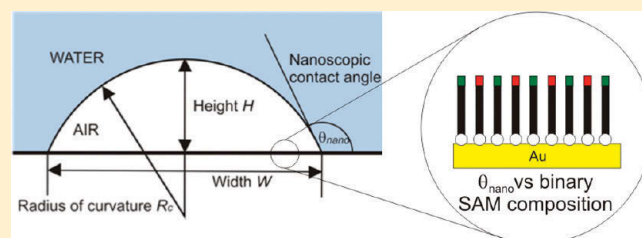
Contact Angles of Surface Nanobubbles on Mixed Self-Assembled Monolayers with Systematically Varied Macroscopic Wettability by Atomic Force Microscopy

Bo Song, Wiktoria Walczyk, and Holger Schönherr*

Physical Chemistry I, Department of Chemistry and Biology, Science & Technology, University of Siegen, Adolf-Reichwein-Straße 2, 57076 Siegen, Germany

S Supporting Information

ABSTRACT: The dependence of the properties of so-called “surface nanobubbles” at the interface of binary self-assembled monolayers (SAMs) of octadecanethiol (ODT) and 16-mercaptohexadecanoic acid (MHDA) on ultraflat template-stripped gold and water on the surface composition was studied systematically by in situ atomic force microscopy (AFM). The macroscopic water contact angle (θ_{macro}) of the SAMs spanned the range between $107^\circ \pm 1^\circ$ and $15^\circ \pm 3^\circ$. Surface nanobubbles were observed on all SAMs by intermittent contact-mode AFM; their size and contact angle were found to depend on the composition of the SAM. In particular, nanoscopic contact angles $\theta_{\text{nano}} < 86^\circ$ were observed for the first time for hydrophilic surfaces. From fits of the top of the bubble profile to a spherical cap in three dimensions, quantitative estimates of nanobubble height, width, and radius of curvature were obtained. Values of θ_{nano} calculated from these data were found to change from $167^\circ \pm 3^\circ$ to $33^\circ \pm 58^\circ$, when θ_{macro} decreased from $107^\circ \pm 1^\circ$ to $37^\circ \pm 3^\circ$. While the values for θ_{nano} significantly exceeded those of θ_{macro} for hydrophobic SAMs, which is fully in line with previous reports, this discrepancy became less pronounced and finally vanished for more hydrophilic surfaces.



INTRODUCTION

Nanometer-scale gas-filled cavities observed at the solid–liquid interface, the so-called “surface nanobubbles”, have attracted considerable attention recently. This interest stems, among others, from the meanwhile confirmed role of these bubbles in the long-range hydrophobic interactions originally observed in the 1980s.¹ In addition to the still unclear mechanism of nanobubble formation and the origin of their surprising stability, there are a number of potentially interesting applications that capture the interest of many groups worldwide. These include froth flotation,² hydrodynamic boundary slip,³ or manipulation of protein adsorption.⁴

Surface nanobubbles were first observed in atomic force microscopy (AFM) measurements reported independently in 2000 by Lou et al.⁵ and Ishida et al.⁶ As has been reviewed recently,^{7–9} the conditions under which nanobubbles form, their gas content, and many other details, including some characteristics of micropancakes, have been reported.¹⁰ However, it is fair to state that several issues remain far from being understood. These include, among others, nanobubble stability and their unexpectedly high values for the nanoscopic contact angles (measured through water).

The Laplace pressure, which is a consequence of the curved interface, and the gas transport through the interface can be modeled quantitatively.^{11,12} Depending on the radius of curvature, the predicted lifetimes for nanobubbles are far below a

second,^{7–9,12} which is in contradiction with the long lifetimes observed experimentally. Several models have been put forward to explain the stability. Brenner and Lohse¹³ proposed a dynamic model with an inward and outward flux of gas, while Ducker¹⁴ attributed the stability to a stabilizing contamination layer at the air–water interface, which alters the diffusion behavior of the enclosed gas. Recent reports underline the effect of surfactants on bubble properties; however, the effect is not large enough to be the sole cause of the stabilization.¹⁵

Another yet unexplained feature is the very high (compared to macroscopic contact angles) *apparent* contact angle of surface nanobubbles (Figure 1).¹⁶ Most studies have targeted hydrophobic surfaces [silane-modified silicon wafers, highly oriented pyrolytic graphite (HOPG), polystyrene, etc.], while studies on hydrophilic surfaces are limited to mica¹⁷ and metals, such as platinum.¹⁸ Surprisingly, all nanoscopic contact angles reported to date in the literature are higher than the macroscopic contact angles. Even for surfaces, such as mica, that are macroscopically completely wetted by water, nanoscopic contact angles of $>120^\circ$ were reported,¹⁷ while hydrophobic surfaces show contact angles between $>160^\circ$ and 119° .¹⁶

Received: April 23, 2011

Revised: May 25, 2011

Published: June 13, 2011

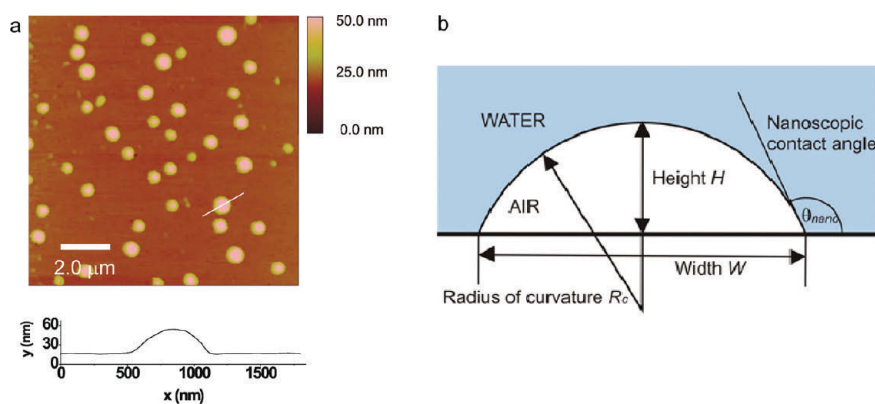


Figure 1. (a) AFM height image of surface nanobubbles on a mixed SAM and cross-sectional plot of one nanobubble. (b) Schematic cross-section of a nanobubble.

It is obvious that there is considerable interest to address this substantial discrepancy. All studies reported to date were either confined to a single type of substrate and hence macroscopic wettability or focused on different substrates with unique wetting properties but also considerably differing nanoscale surface topographies.^{17b,19,20} This renders any comparison difficult.

To obtain insight into the relation of surface nanobubble properties in dependence of the surface wettability (at constant topography) and hence to clarify and demystify some of the phenomena mentioned above, we investigated how nanobubble shape and nanoscopic contact angles depend on the composition of binary self-assembled monolayers (SAMs)²¹ on ultraflat gold surfaces. The template-stripped gold²² ensures the absence of differences in substrate topography, and the molecularly mixed two-component SAM allowed us to systematically vary the macroscopic substrate wettability. In addition, recent hypotheses that assigned the disparity between nanoscopic and macroscopic contact angles to contamination effects are critically addressed.

EXPERIMENTAL SECTION

Materials. 16-Mercaptohexadecanoic acid [MHDA; HS-(CH₂)₁₅COOH, 90%] and 1-octadecanethiol [ODT; HS-(CH₂)₁₇-CH₃, 98%] were purchased from Aldrich and used without further purification. Ethanol (97% with 1% petrol ether) was purchased from J.T. Baker. Milli-Q water from a Direct-Q 8 system (Millipore) with resistivity of 18.0 MΩ/cm was used in all experiments. EPO-TEK 377 epoxy glue was purchased from Polytec PT GmbH Polymere Technologien, Germany. This two-component glue contains no solvent and is resistant to many solvents, in particular alcohols.

Substrates and Self-Assembled Monolayer Preparation. The ultraflat gold surface was prepared by the method reported by Stamou et al.²² Silicon wafers [CZ-silicon wafer, type P/boron/(100), manufactured by Okmetic, Finland] were cut into 1 cm × 1 cm square pieces and pretreated with piranha [a sulfuric acid/hydrogen peroxide solution (3:1 v/v)] until gas bubbles stopped evolving, followed by a thorough wash with Milli-Q water and drying in a stream of nitrogen. *Warning: Piranha solution is highly reactive and may explode upon contact with organic material, such as solvents. Extreme precautions must be taken at all times.* The dried and dust-free wafers were directly placed into the vacuum chamber of a thermal evaporator (MED 010, Balzers Union) for evaporation of gold (pressure 1 × 10⁻⁶ mbar; evaporation rate ~0.1 nm/s for the first 15 nm and then

~0.4 nm/s to yield a final gold thickness around 150 nm). The samples were allowed to cool down for 15 min in the vacuum chamber and were then quickly glued onto the clean glass slides (which were pretreated with piranha for 10 min, rinsed with water and ethanol, and blown dry with nitrogen) and cured at 150 °C for 2 h. Before use, the silicon wafer was carefully separated from the glass substrate by use of a scalpel knife. Immediately afterward, the substrate with the ultraflat gold surface was immersed in a 1 × 10⁻³ mol/L ethanolic solution of thiols (MHDA, ODT, or a binary mixture) for SAM formation. After 2 h, the substrate was taken out, rinsed with ethanol, and blown dry with nitrogen. Contact angles were measured with minimal delay. Specimens for AFM experiments were again rinsed with ethanol and dried with nitrogen and then introduced into the AFM for nanobubble investigations.

Contact Angle Measurements. The contact angles of the modified surfaces were measured with an OCA 15plus instrument (Data Physics Instruments GmbH, Germany). Contact angle data based on both the sessile drop method and the captive bubble method were acquired. For the captive bubble measurements, the substrates were put upside down in a glass cell (GC20, Data Physics Instruments GmbH, Germany) and air was injected by a syringe from below. The volume of the air bubble was calculated on the basis of recorded optical images, calibrated via the known diameter of the syringe needle.

Fourier Transform Infrared Spectroscopy. Fourier transform infrared (FTIR) spectra were obtained in grazing-angle reflection mode on a Bruker IFS 66v FTIR spectrometer equipped with a liquid nitrogen-cooled mercury–cadmium–telluride (MCT) detector and a VEEMAX-II grazing-angle accessory (Pike Technologies). In total, 1024 scans with a spectral resolution of 2 cm⁻¹ were recorded. Background spectra were obtained with a bare gold substrate. Peak deconvolution, as reported previously,²³ was applied to separately integrate the areas of the peaks at approximately 2850 cm⁻¹ (vibration of -CH₂) and 2880 cm⁻¹ (vibration of -CH₃) to determine the surface composition of the binary SAM.

AFM Measurement and Image Analysis. Nanobubble imaging was carried on two different AFM instruments: a Multi-Mode IIIa (Veeco, Santa Barbara, CA; substrates with $\theta_{\text{macro}} = 117^\circ, 86^\circ, 60^\circ, 50^\circ,$ and 37°) and a BioScope I (Veeco, Santa Barbara, CA; substrate with $\theta_{\text{macro}} = 15^\circ$). Two types of probe tips were used: Veeco MLCT V-shaped Si₃N₄ (cantilever with nominal spring constant of 0.03 N/m) and Veeco DNP-S V-shaped Si₃N₄ (cantilever with nominal spring constant of

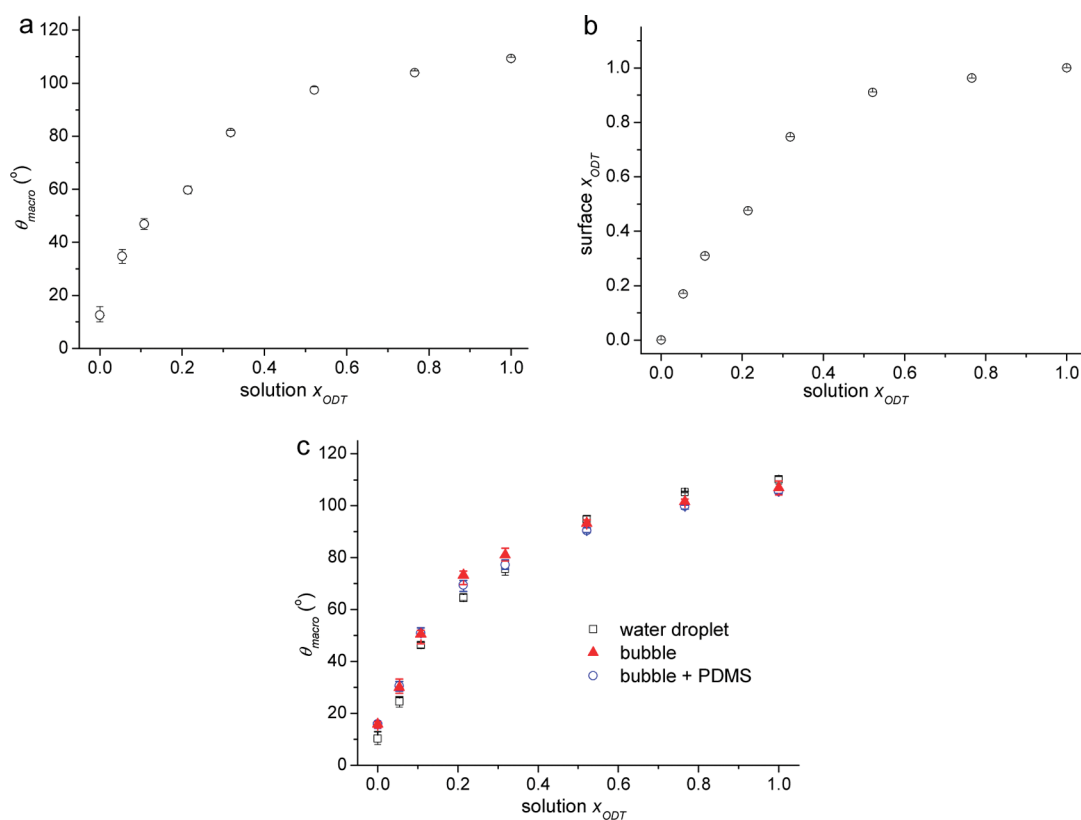


Figure 2. (a) Macroscopic contact angles (θ_{macro}) determined by the sessile drop method vs molar fraction of ODT (x_{ODT}) in the assembly solution. (b) Surface x_{ODT} calculated from FTIR vs solution x_{ODT} . (c) Macroscopic contact angles measured by sessile drop and captive bubble methods vs solution x_{ODT} . Data for captive bubble experiments in the presence of siloxane contamination are also shown.

0.32 N/m). All cantilevers were cleaned immediately prior to use by oxygen plasma for 60 s (PlasmaPrep2, GaLa Instrumente). Measurements were conducted in an open liquid cell configuration (without rubber O-ring). Before use, the liquid cell was rinsed with ethanol and dried in a stream of nitrogen. A drop of Milli-Q water was placed directly on the sample by use of a syringe. Another drop was placed on the liquid cell and then the cell was mounted into the optical head of the microscope. Upon lowering the optical head, the two droplets coalesced and were squeezed such that a meniscus formed between the sample and the liquid cell. The system was left for about 30 min to thermally equilibrate before the measurements were started. All the experiments were conducted at room temperature.

After recording of the AFM images, the raw data were processed with a first-order plane fit and a first-order flattening (here the nanobubbles were excluded). These images were exported to ASCII format and further analyzed with MATLAB 7.10.0.499 (R2010a) software.

Tip Correction. The tip radii were evaluated by two methods: section profiles of scanning electron microscopy (SEM) images of the tips used (acquired on a FESEM Ultra 55 produced by Carl Zeiss SMT GmbH, Germany) and blind reconstruction by use of images obtained on a standard sample (TGT1, NT-MDT Co., Russia). The radii of curvature of the tips were determined by fitting a circle to the SEM images of the apex of the tips. The blind reconstruction was carried out with SPIP software, purchased from Image Metrology A/S, Denmark.

RESULTS AND DISCUSSION

As the central objective of this study was to unravel the relation between macroscopic and nanoscopic contact angles for surface nanobubbles, we start with a thorough analysis of the composition and wettability of the binary SAM substrates on ultraflat gold. Subsequently, the imaging of nanobubbles on substrates with systematically varied wettability by AFM is discussed.

Prior to the liquid cell AFM work, the surface roughness of the ultraflat template-stripped gold surface was examined by intermittent contact (tapping) mode AFM in air. While gold surfaces prepared by conventional thermal evaporation possess a typical root-mean-square (rms) roughness of approximately 4–5 nm covering height differences of over 20 nm, the ultraflat gold showed rms roughness of 0.2 nm and height differences of <1.0 nm. In addition to the low number of pinhole-type defects, the low roughness and small surface corrugation ensure that nanobubbles on SAMs on close to atomically smooth surface were studied.

By changing the molar fraction of ODT (x_{ODT}) in the assembly solution, binary SAMs of ODT and MHDA with different surface wettabilities, ranging from $107^\circ \pm 1^\circ$ to $15^\circ \pm 3^\circ$, were obtained. As shown in Figure 2a, the static contact angles of the mixed SAMs increased with increasing x_{ODT} in the assembly solution. In line with reports in the literature and also our previous work,²³ the relationship was found to be nonlinear. The surface compositions of the mixed SAMs were calculated by use of the Israelachvili–Gee equation (eq 1)²⁴ that was independently shown to agree more favorably than the Cassie–Baxter equation²⁵ with grazing angle reflection FTIR spectroscopy data

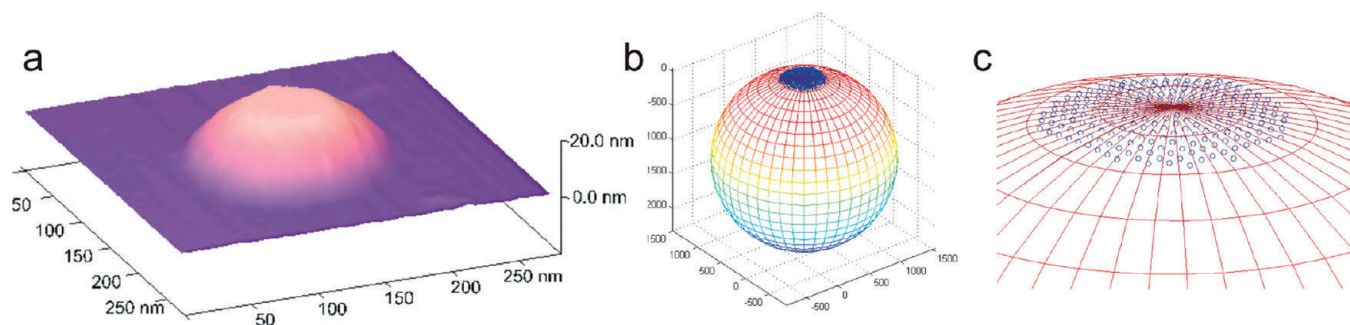


Figure 3. (a) Three-dimensional representation of AFM height image of a nanobubble acquired on a binary SAM. (b, c) Three-dimensional spherical fits (mesh) of the AFM data points (data points are indicated as circles). For bubbles with low contact angles, only the top part of the bubble could be fitted.

(Figure 2b).²³ Independent lateral force microscopy and time-of-flight secondary ion mass spectrometry data underline the conclusion from this observation that the binary SAMs are practically molecularly mixed with no discernible phase separation.²⁶

For the mixed SAMs, the surface x_{ODT} was always larger than the solution x_{ODT} , which indicates that ODT adsorbs preferentially under the same conditions (concentration, temperature, adsorption time, etc)

$$(1 + \cos \theta)^2 = f_1(1 + \cos \theta_1)^2 + f_2(1 + \cos \theta_2)^2 \quad (1)$$

Here, f_1 and f_2 are the fractional surface coverages of the two components in the mixed monolayer, respectively; θ_1 and θ_2 are the contact angles of the pure monolayers ($\theta_1 = 12.5^\circ \pm 3.2^\circ$ and $\theta_2 = 109.3^\circ \pm 0.5^\circ$); and θ is the contact angle of the mixed monolayer.

The macroscopic contact angles (denoted θ_{macro}) were evaluated by the sessile drop and also by the captive bubble method, as an analogous method. In these experiments the same series of samples were used. As shown in Figure 2c, the contact angles measured by the sessile drop method (\square) and by the captive bubble method (\blacktriangle) show a very similar trend for the various surfaces. The captive bubble data showed consistently $\sim 5^\circ$ higher readings. To be able to compare our data to the literature, we use from here on the macroscopic contact angle data determined according to the sessile drop method. This choice has no significant impact on our conclusions.

Using a separate set of samples, the contact angles were determined by the captive bubble method with Milli-Q water that was intentionally brought into contact with the siloxane-containing packaging material. This material was believed to contribute to the anomalously high nanoscopic contact angles observed before, for example, on HOPG.¹⁶ Here a piece of poly(dimethylsiloxane) (PDMS) material ($10.0 \times 10.0 \times 1.5 \text{ mm}^3$) that was cut from the Gel Pack AFM tip storage box was immersed in 20 mL of Milli-Q water for 24 h. The data in Figure 2c (\circ) show that there was no significant change in θ_{macro} compared to the values measured in pure Milli-Q water, which means that the gel pack tested yielded, if at all, a contamination level that was too low to influence the contact angles.

To further underscore the above interpretation, two sets of experiments were carried out. First, the thus presumably contaminated water was evaporated in vacuum and the “contamination” was dissolved in deuterated chloroform (without tetramethylsilane). ^1H NMR spectroscopic data (Supporting Information,

Figure S-1a) confirmed that *no* PDMS contamination in the water was detectable. A certain amount of heptane had been added as internal standard.

A second control experiment was performed by adding an oligomeric PDMS precursor (silicone prepolymer type Sylgard 184, Dow Coming GmbH, Germany) as contaminant to the water. ^1H NMR spectroscopic data (Supporting Information, Figure S-1b) showed a peak attributed to the protons of a dimethylsiloxane unit. This means that the PDMS precursor may indeed contaminate the water and, by adsorption on the substrate surface, this may potentially result in changes of the surface wettability. However, under the conditions tested, θ_{macro} reached a maximum value of 110° (Supporting Information, Figure S-2), which does not satisfactorily explain the anomalously high nanoscopic contact angles of 160° .¹⁶

Intermittent contact (tapping) mode AFM data of the surface nanobubbles were acquired under conditions of minimized forces in the surface normal direction to avoid the potential deformation of the nanobubbles.^{27–29} Typical AFM data are shown, for example, in Figures 1 and 3. In agreement with numerous reports in the literature, the surface nanobubbles exhibit a spherical cap-like topography with a circumference that is, in the absence of asymmetric tip shapes, circular.

For further analysis of the AFM data, we assume that the nanobubbles can indeed be described by a spherical cap. The small residuals in the corresponding fits (see below) support this choice. For a spherical cap, the bubble height H and width W (compare Figure 1b) are related to the radius of curvature R_c via

$$R_c = \frac{(W/2)^2 + H^2}{2H} \quad (2)$$

The contact angle θ_{nano} of the nanobubbles is defined as contact angle through the liquid (compare Figure 1b):

$$\sin \theta_{\text{nano}} = \frac{W}{2R_c} \quad (3)$$

For the quantitative analysis, a method developed and described by Borkent et al.^{16,30} was applied. The AFM height images were leveled such that the sample surface was set to zero height (0.0 nm). All data points higher than a given threshold value (typically 2 nm), which constituted the bubble profile, were analyzed.³¹ For bubbles with low contact angles, the top part of the profile was fitted. For each bubble that was analyzed, a three-dimensional spherical-cap fit was applied. First, the center of the fitted sphere and its apparent radius of curvature R_c^{app} were

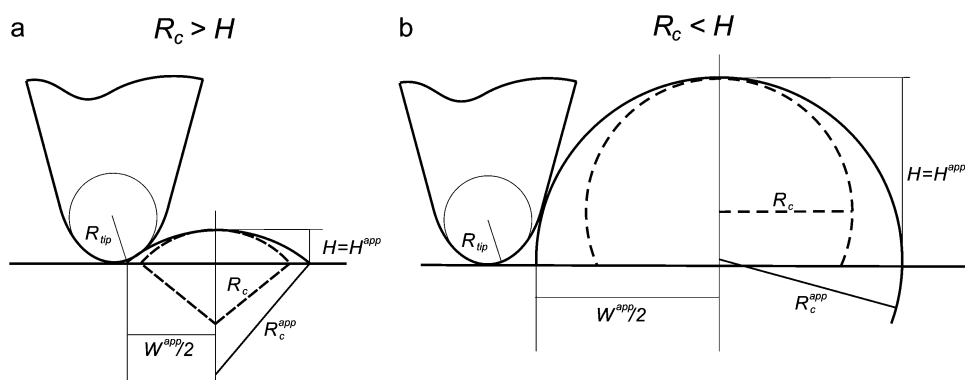


Figure 4. Schematic of AFM tip convolution in the measurement of a nanobubble. (a) In the case of $R_c > H$ ($\theta_{\text{nano}}^{\text{app}} > 90^\circ$), only the spherical end of the tip is used to obtain the image. (b) For bubbles with $R_c < H$ ($\theta_{\text{nano}}^{\text{app}} < 90^\circ$), the tip's side walls interact with the bubble. In both cases the apparent radius of curvature R_c^{app} is larger than its true value R_c . However, the height H remains unchanged. We note that the tip correction does not affect the conclusions of this paper qualitatively.

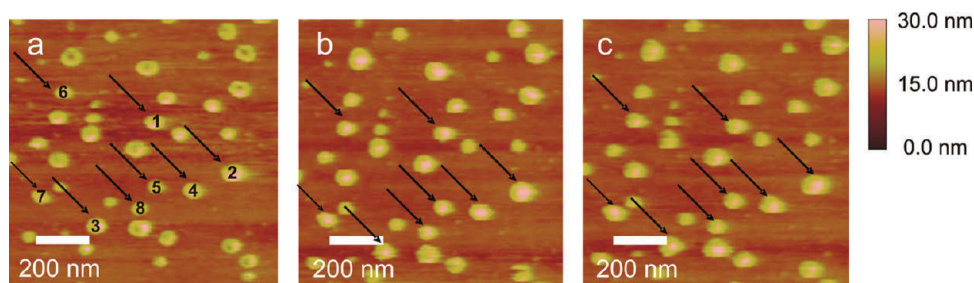


Figure 5. Sequence of tapping-mode AFM height images of nanobubbles on the same scan area of an ODT/MHDA sample ($\theta_{\text{macro}} = 60^\circ$) in water after scanning (a) one time, (b) 7 times, and (c) 13 times with approximately the same amplitude set point ratios. It can be observed that the nanobubbles remain essentially unchanged. The dimensions of the eight bubbles marked with arrows were analyzed quantitatively; the results are plotted in Figure 6.

determined. Then the height of the bubble H^{app} was calculated as the difference between R_c^{app} and the distance from the center of the sphere to the zero (sample) level. Finally, by transforming eqs 2 and 3, the apparent width W^{app} and the contact angle $\theta_{\text{nano}}^{\text{app}}$ of the fitted bubble were calculated:

$$W^{\text{app}} = 2\sqrt{2H^{\text{app}}R_c^{\text{app}} - (H^{\text{app}})^2} \quad (4)$$

$$\theta_{\text{nano}}^{\text{app}} = 180 - \frac{180}{\pi} \cos^{-1} \left(1 - \frac{H^{\text{app}}}{R_c^{\text{app}}} \right) \quad (5)$$

Figure 3 shows an example of a three-dimensional AFM image of a nanobubble and the corresponding nanobubble data points (blue circles) fitted to a sphere (mesh). Small rms errors (typically on the order of 0.1% to several percent) show that the fit provides a reasonable estimate of the bubble shape and dimensions.

The apparent (uncorrected) values of R_c^{app} , W^{app} , and $\theta_{\text{nano}}^{\text{app}}$ obtained from this analysis represent overestimates due to the well-known effect of AFM tip convolution. Since the sizes of the tip and nanobubbles are of the same order of magnitude, this effect becomes significant and an appropriate correction is necessary. The end of the tip was assumed to be spherical with a radius of curvature R_{tip} . We employed two methods to confirm this assumption and to determine R_{tip} : (i) blind reconstruction and (ii) direct metrology of the very tip apex by use of SEM data (see Supporting Information, Figure S-3). Both methods provided, within experimental error, very similar values for the radius of curvature of the very tip apex, which we

consider underestimates of the true tip radius. Therefore we also estimated for which arbitrarily assumed value of the tip radius the radius of curvature of the nanobubbles became imaginary. This provided an upper bound for the true tip radius, which we estimated from these data as the median.

In the simplified correction model shown schematically in Figure 4, we assumed that the apparent width W^{app} and radius of curvature R_c^{app} of the bubble are overestimated and the apparent height H^{app} remains unchanged ($H = H^{\text{app}}$). This assumption is valid for bubbles with $\theta_{\text{nano}}^{\text{app}} > 90^\circ$ (thus for $R_c > H$), provided that only the tip apex is used to acquire the image and not its side walls. In the case of bubbles with $\theta_{\text{nano}}^{\text{app}} < 90^\circ$ ($R_c < H$) it is likely that also the tip's side walls interacted with the bubble surface. With the corresponding tip radii, the deconvoluted radii of curvature R_c of the nanobubbles were obtained by subtracting the tip radius R_{tip} from R_c^{app} :

$$R_c = R_c^{\text{app}} - R_{\text{tip}} \quad (6)$$

The deconvoluted width W and the contact angle θ_{nano} were calculated analogously to the apparent values W^{app} and $\theta_{\text{nano}}^{\text{app}}$, as described above.

The experimental errors were calculated as follows. Three possible error sources were considered: (1) AFM measurement errors (piezo positioning errors) ΔR_c^{app} were assumed to amount to a maximum of 1% of the measured value in each of the three spatial directions. (2) The error in the fit of the spherical cap $\Delta^{\text{rms}} R_c^{\text{app}}$ (i.e., the rms values of the radial distances between the data points and the ideal sphere that was fitted)

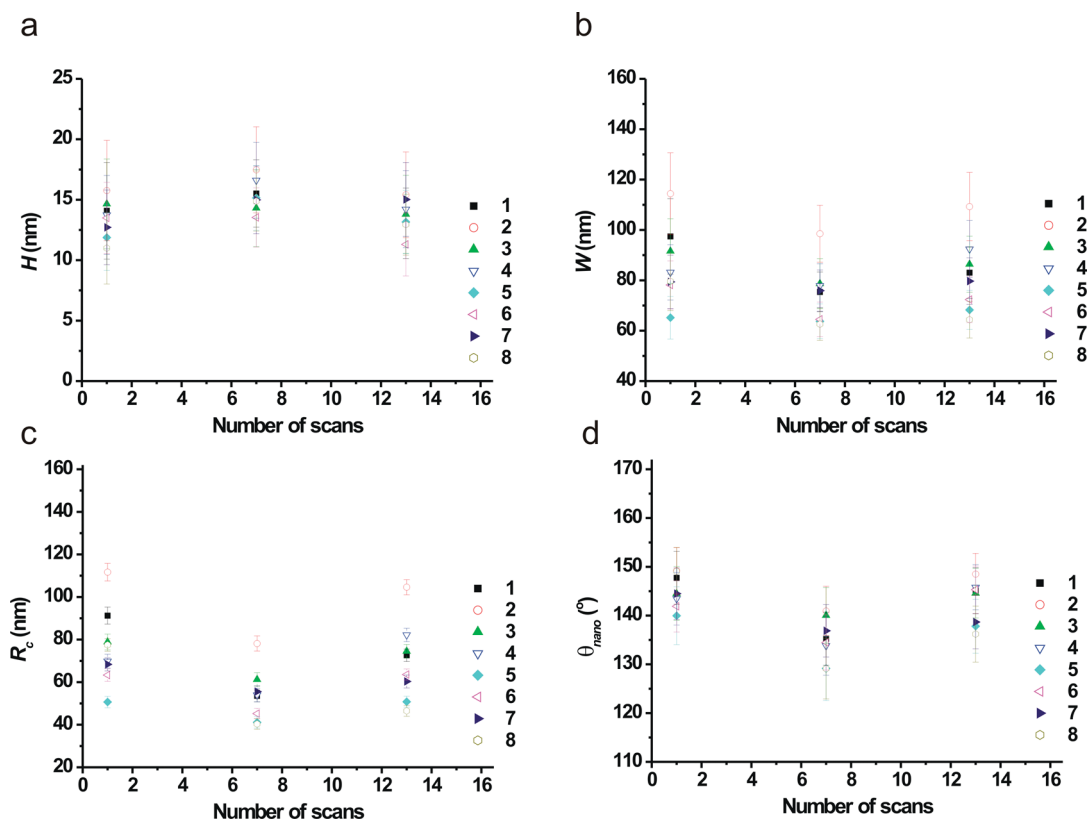


Figure 6. Plots of tip-corrected (a) height, (b) width, (c) radius of curvature, and (d) nanoscopic contact angle of the nanobubbles as a function of number of scans. Each symbol represents a single nanobubble as marked in Figure 5.

represent an error in radius of curvature. Finally, (3) a relative error ΔR_{tip} of $\sim 10\%$ resulted from the uncertainty in the true values of R_{tip} used in the deconvolution.

Since the surface nanobubbles are composed of gas and may be considered as soft, delicate objects, we first established the stability of the surface nanobubbles during subsequent AFM scans. Figure 5 shows a set of AFM images captured with practically identical amplitude set point ratios.

For the 13 images captured subsequently (~ 8 min/frame; here we show the first, seventh, and 13th scan), most of the bubbles maintained their position and size. The nanobubble dimensions were analyzed and are compared in Figure 6. Eight bubbles (marked with arrows in Figure 5) were selected for this quantitative analysis, in which H , W , R_c , and θ_{nano} were determined according to the procedures detailed above. From this analysis it can be concluded that (i) the bubbles are stable over time and (ii) they do not appear to change their size significantly. Hence the enclosed gas volume appears to be constant in time and is not markedly affected by the interactions between scanning tip and nanobubble.

Having established the composition of the mixed SAMs and confirmed the stability of the nanobubbles, we employed tapping-mode AFM to observe the surface nanobubbles on surfaces with different contact angles in situ in Milli-Q water. The rms amplitudes were minimized and the set point ratio values were kept as high as possible to capture images of the surface nanobubbles under minimally invasive conditions.

Figure 7 shows six typical AFM height images of surface nanobubbles on mixed SAMs with θ_{macro} of 107° , 86° , 60° , 50° , 37° , and 15° , respectively. On the basis of our AFM data, it is not possible to decide how far the observed number densities of

surface nanobubbles (or preferred sizes,³⁰ see below) depend on the surface composition of the SAM. A possible trend of increasing number densities with increasing fraction of MHDA may be present. However, with decreasing contact angle (increasing fraction of MHDA), the apparent bubble size was found to decrease. In addition, we observed in some cases mixed nanobubble populations (for example, Figure 7b). Due to the limited size of the smaller bubbles, a quantitative analysis was not possible in all cases (see also below).

In addition, when the surface becomes hydrophilic, the surface nanobubbles become more susceptible to displacement by the AFM tips during scanning. For example, the nanobubbles on the sample with θ_{macro} of 37° were readily merged together, and after the first round of scanning most of the small bubbles were fused into isolated larger bubbles. In line with data reported in the literature,³² we found evidence for this explanation by zooming out and scanning a larger area. The previously not scanned area still contained smaller bubbles, which again merged while the image was captured (see Supporting Information, Figure S-4). The AFM image shown in Figure 7e was taken after the merging of the smaller bubbles. On the surface with θ_{macro} of 15° , the apparent size of the bubbles was too small to allow us to perform a meaningful analysis.

The apparent widths of the bubbles observed varied, depending on the composition of the binary SAM, from tens to hundreds of nanometers, and the heights covered a range of 10 nm to ~ 130 nm. Both parameters are related according to eq 7; hence we plotted H versus W for each bubble analyzed in Figure 8.

$$\theta_{\text{nano}} = 180 - \frac{360}{\pi} \tan^{-1} \left(\frac{H}{W/2} \right) \quad (7)$$

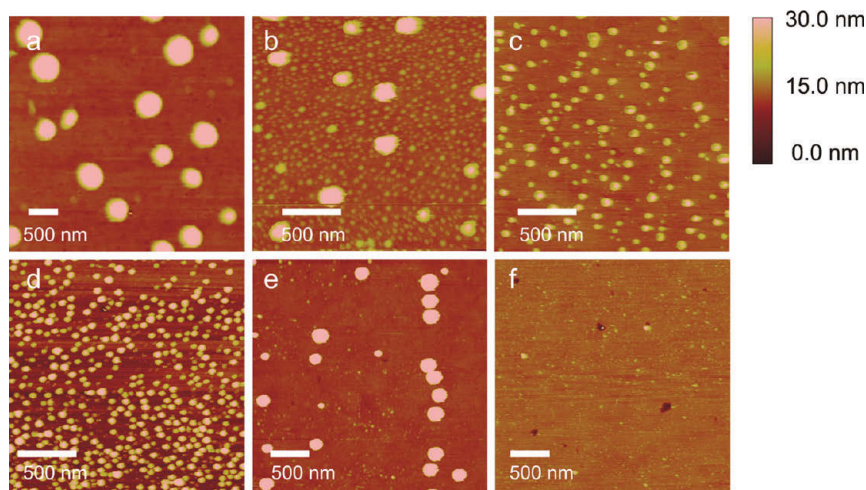


Figure 7. Tapping-mode AFM height images of nanobubbles on mixed SAM surfaces with macroscopic contact angles of water of (a) 107°, (b) 86°, (c) 60°, (d) 50°, (e) 37°, and (f) 15°.

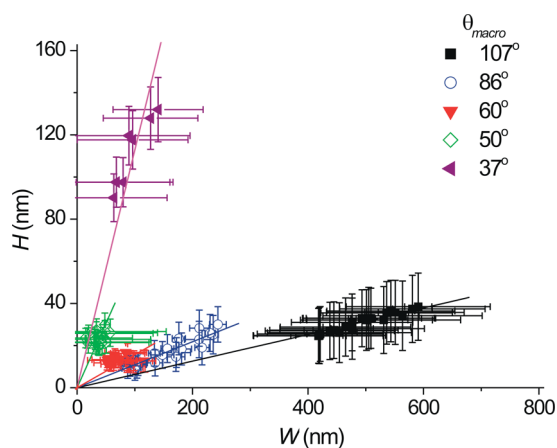


Figure 8. Nanobubble height vs width (tip-corrected) for SAMs with different θ_{macro} .

For each data set, the height of the bubble was found, within experimental error, to increase linearly with the width. This linear relationship implies that the nanoscopic contact angle is constant for each substrate. The data lead via eq 7 and a linear least-squares fit [bound to (0,0)] directly to an estimate of the mean θ_{nano} of the surface nanobubbles (Table 1).

Subsequently, we analyzed whether there was any dependence of θ_{nano} on the radius of curvature. To clarify this question, the individually determined values of θ_{nano} were plotted as a function of the corresponding radius of curvature R_c (Figure 9a). These data were compared with macroscopic contact angle data acquired by the captive bubble method (Figure 9b).

On substrates with θ_{macro} of 107° and 86°, the surface nanobubbles possessed values of θ_{nano} of $\sim 165^\circ$, which were clearly independent of R_c . On the other substrates, the values of θ_{nano} showed some scatter; however, due to the significant errors and hence uncertainty of the values, we cannot decide conclusively whether there is a dependence of θ_{nano} on R_c . If there is a dependence, it must be very weak. The nanoscopic contact angles for the most hydrophilic sample is the smallest value reported thus far and corresponds, within experimental error, to

Table 1. Mean θ_{nano} of Surface Nanobubbles Obtained from Figure 8

θ_{macro} (°)	$H/(2W)$	$\Delta H/(2W)$	θ_{nano} (°)	$\Delta\theta_{\text{nano}}$ (°)
107	0.13	0.01	165.6	0.1
86	0.22	0.01	155.4	0.7
60	0.31	0.02	145.2	1.9
50	1.22	0.09	78.5	4.0
37	2.56	0.11	47.8	2.1

the macroscopic contact angle. On the basis of the tip-corrected values for the radius of curvature, we estimated Laplace pressures (i.e., the pressure difference between the inside and outside of the nanobubbles) between 2.53 and 3.53 MPa for the sample with $\theta_{\text{nano}} = 50^\circ$ and between 1.28 and 2.81 MPa for the sample with $\theta_{\text{nano}} = 37^\circ$.

As a control experiment, the dependence of the macroscopic contact angle on the size of the captive bubbles was also determined (Figure 9b). The radius of curvature was calculated from the measured height and width of the bubbles, such as those shown as insets in Figure 9b. The data shown indicate that θ_{macro} did not change significantly for a range in the radius of curvature of the captive bubble between 3700 and 300 μm , which corresponds to Laplace pressures for these bubbles between 39 and 480 Pa. By combining the results of surface nanobubbles and captive bubbles, we can conclude that the contact angle of the bubbles has no marked dependence on the radius of curvature.

If both θ_{macro} and θ_{nano} possess constant values for a given binary SAM, which are independent from R_c , we can plot θ_{macro} versus θ_{nano} . In Figure 10 we compare this dependence for the raw (not tip-corrected) data (Figure 10a) and for the deconvoluted data (Figure 10b).

Figure 10a shows that the values for $\theta_{\text{nano}}^{\text{app}}$ (uncorrected and hence overestimated) are $<90^\circ$ only for the sample with $\theta_{\text{macro}} = 37^\circ$, while Figure 10b indicates that (except for data on the two more hydrophilic SAMs) the values for θ_{nano} remain (much) larger than the values for θ_{macro} even after correction for the hydrophobic SAMs. This trend was already obvious from the analysis summarized in Table 1. In the literature, surface

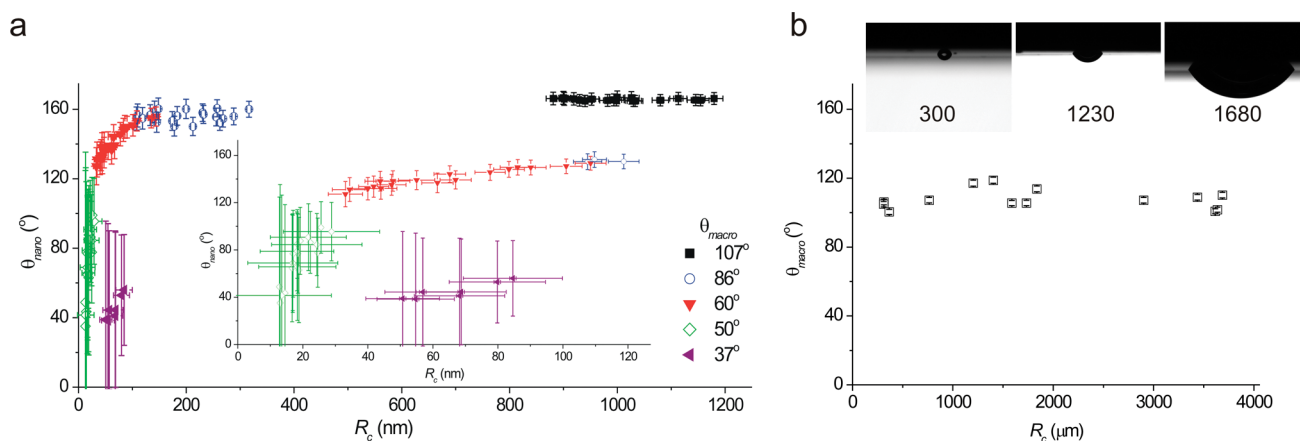


Figure 9. (a) Nanoscopic contact angles of individually analyzed nanobubbles as a function of their radii of curvature (tip-corrected). (Inset) Enlarged part of the plot. (b) Macroscopic contact angles of captive bubbles in water as a function of their radii of curvature. (Insets) Optical images of captive bubbles with different radii of curvature.

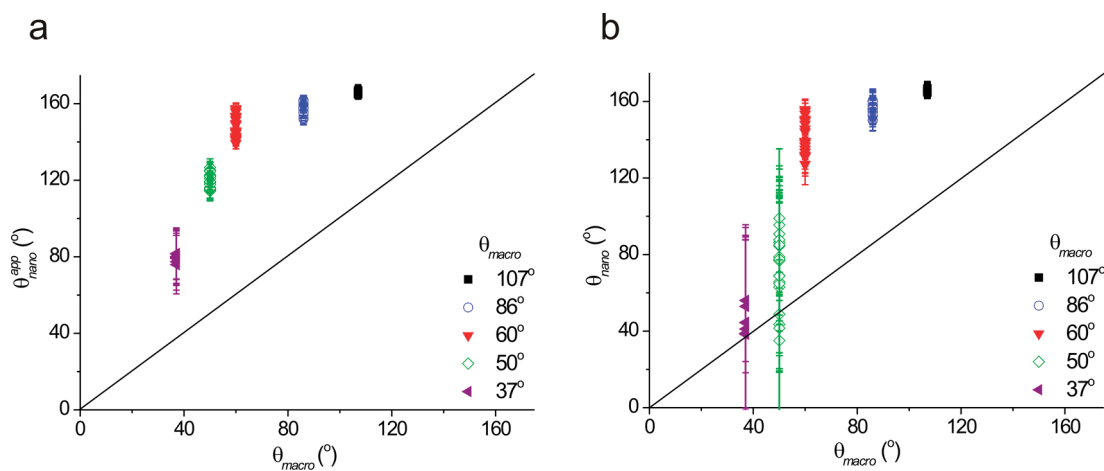


Figure 10. Nanoscopic versus macroscopic contact angles of bubbles on SAMs with different compositions: (a) before and (b) after tip correction. The solid line representing $\theta_{\text{nano}} = \theta_{\text{macro}}$ has been added as a guide to the eye.

nanobubbles were reported to always show higher than expected contact angles.

What could be the reason for this discrepancy for the more hydrophobic SAMs? In principle, three possible contributions can be considered: (i) an erroneous tip radius correction, (ii) the presence of a contamination layer that would mask the true contact angle, or (iii) force-induced bubble deformation and hence a too-high apparent θ_{nano} .

From a closer look at the data in Figure 10, it becomes obvious that the tip radius correction has indeed a pronounced effect on θ_{nano} for the more hydrophilic SAMs. The error in θ_{nano} in Figure 10b is dominated by the uncertainties of the tip radius. Despite the use of two complementary methods to determine the tip radius, the corresponding error could not be reduced to a level that would significantly reduce the error in θ_{nano} for the hydrophilic SAMs. The correction is probably not fully adequate for the data set obtained on the SAM with $\theta_{\text{nano}} = 37^{\circ}$, since the values for bubble height were much larger than $2R_c$. However, when we consider the opening angle of the tip, the data would be expected to reside even closer to the line with a slope of unity.

It is also clear that the data for the hydrophobic SAM with a contact angle of 107° are much less affected by the correction and

correspondingly the errors in R_c . If one calculates the tip radius from the acquired AFM data, assuming that $\theta_{\text{macro}} = \theta_{\text{nano}}$ (compare also Figure 10) and that the discrepancy is *exclusively* due to the tip convolution of a spherical tip, then tip radii in excess of $1 \mu\text{m}$ would be required (see Supporting Information, Figure S-5). These values are clearly unreasonable.

The unusually high values for contact angles on HOPG, among others, have been attributed by Borkent et al.¹⁶ in part to tip-borne contamination, namely, oligomeric siloxanes that may be liberated from the AFM cantilever packaging (Gel Pack), as has been shown in a different context.³³ In general, polysiloxanes possess a low solubility in water, and if they are surface-active, they are expected to adsorb at the air–liquid interface to lower the interfacial energy; adsorption of (hydrophobic) siloxanes on a hydrophilic surface immersed in water would increase the interfacial free energy, hence this is, in contrast to experiment at the solid–air interface, energetically unfavorable. In our study we have found no experimental evidence for adsorbed siloxanes in the contact angle data as well as in the analysis data of the aqueous imaging solutions (by ^1H NMR). We can therefore exclude this source of potential contamination for our experiments and as the

origin for the too-large nanoscopic contact angles observed in this study. Contamination of the solid–gas interface with hydrophobic adsorbates prior to the AFM experiment, however, could explain the unreasonable contact angle reported in the literature for mica.¹⁷

It could also be argued that surface nanobubbles may be soft and are deformed by the AFM tip during scanning. In intermittent contact mode AFM we used minimized amplitude and the highest possible set point ratio.^{27–29} The data acquired on different AFMs and also via a fundamentally different imaging mode (Peak Force) did not lead to an altered trend.³⁴ Furthermore, in an independent systematic study of nanobubbles formed on HOPG, we extrapolated the forces in both intermittent contact mode and peak force AFM to zero interactions and observed that the smallest nanoscopic contact angles were around 120–130°. While the values correspond to the lowest values reported thus far (by Borkent et al.),¹⁶ there is still a discrepancy that is certainly beyond any experimental error. These observations imply that nanobubble deformation can also be excluded as single reason for the observed discrepancy in the present study. On the basis of the currently available evidence, we cannot identify the origin of the clear discrepancy with certainty.

CONCLUSIONS

We have investigated systematically how the shape and dimensions of surface nanobubbles change with the composition and hence macroscopic wettability of binary methyl/carboxyl-terminated SAMs on template-stripped gold. While the literature-known deviations for hydrophobic samples, on which nanobubbles are apparently very flat and laterally expanded, were confirmed for hydrophobic binary SAMs, we observed, within experimental error, a good match of θ_{macro} to θ_{nano} on hydrophilic samples. In particular, this report represents to the best of our knowledge the first experimental determination of radii of curvature and contact angles of nanobubble with $\theta_{\text{nano}} < 90^\circ$. The alleged role of oligo- or poly(dimethylsiloxane) contamination in the mismatch of the macroscopic and (apparent) nanoscopic contact angles could not be substantiated in our experiments and appeared to be negligible. This study complements recent efforts to understand these important, but far too little understood, features of solid–liquid interfaces.

ASSOCIATED CONTENT

S Supporting Information. Additional text, five figures, and one table showing ¹H NMR spectroscopic data, contact angle data of contaminated surfaces, AFM blind reconstruction and SEM image of AFM tip, AFM micrograph of nanobubbles, calculated tip radii, and fit parameters. This material is available free of charge via the Internet at <http://pubs.acs.org>.

AUTHOR INFORMATION

Corresponding Author

*E-mail schoenherr@chemie.uni-siegen.de; fax (+49) 271/740-2805.

ACKNOWLEDGMENT

We gratefully acknowledge generous financial support by the Alexander von Humboldt Foundation (Germany) (B.S.) and the

University of Siegen for a stipend for female doctorate students (W.W.). We are further indebted to M.Sc. H. Zhang and Professor Dr. X. Jiang (University of Siegen) for the SEM measurements and to Dipl. Ing. G. Schulte, Dr. D. Tranchida (both University of Siegen) and Professor Dr. D. Lohse (University of Twente) for stimulating discussions.

REFERENCES

- (a) Israelachvili, J. N.; Pashley, R. M. *Nature* **1982**, *300*, 341–342.
- (b) Christenson, H. K.; Claesson, P. M. *Science* **1988**, *239*, 390–392.
- (c) Parker, J. L.; Claesson, P. M.; Attard, P. J. *Phys. Chem.* **1994**, *98*, 8468–8480.
- (d) Carambassis, A.; Jonker, L. C.; Attard, P.; Rutland, M. W. *Phys. Rev. Lett.* **1998**, *80*, 5357–5360.
- (e) Attard, P. *Adv. Colloid Interface Sci.* **2003**, *104*, 75–91.
- Mishchuk, N.; Ralston, J.; Fornasiero, D. *J. Colloid Interface Sci.* **2006**, *301*, 168–175.
- Vinogradova, O. I. *Langmuir* **1995**, *11*, 2213–2220.
- (a) Wu, Z. H.; Chen, H. B.; Dong, Y. M.; Mao, H. L.; Sun, J. L.; Chen, S. F.; Craig, V. S. J.; Hu, J. J. *Colloid Interface Sci.* **2008**, *328*, 10–14.
- (b) Liu, G. M.; Wu, Z. H.; Craig, V. S. J. *J. Phys. Chem. C* **2008**, *112*, 16748–16753.
- (c) Liu, G. M.; Craig, V. S. J. *ACS Appl. Mater. Interfaces* **2009**, *1*, 481–487.
- Lou, S. T.; Ouyang, Z. Q.; Zhang, Y.; Li, X. J.; Hu, J.; Li, M. Q.; Yang, F. J. *J. Vac. Sci. Technol., B* **2000**, *18*, 2573–2575.
- Ishida, N.; Inoue, T.; Miyahara, M.; Higashitani, K. *Langmuir* **2000**, *16*, 6377–6380.
- Hampton, M. A.; Nguyen, A. V. *Adv. Colloid Interface Sci.* **2010**, *154*, 30–55.
- Craig, V. S. J. *Soft Matter* **2011**, *7*, 40–48.
- Seddon, J. R. T.; Lohse, D. *J. Phys.: Condens. Matter* **2011**, *23*, 133001.
- Seddon, J. R. T.; Kooij, E. S.; Poelsema, B.; Zandvliet, H. J. W.; Lohse, D. *Phys. Rev. Lett.* **2011**, *106*, No. 056101.
- (a) Epstein, P. S.; Plesset, M. S. *J. Chem. Phys.* **1950**, *18*, 1505–1509.
- (b) Ljunggren, S.; Eriksson, J. C. *Colloids Surf., A* **1997**, *129–130*, 151–155.
- Borkent, B. M.; Dammer, S. M.; Schönherr, H.; Vancso, G. J.; Lohse, D. *Phys. Rev. Lett.* **2007**, *98*, No. 204502.
- Brenner, M. P.; Lohse, D. *Phys. Rev. Lett.* **2008**, *101*, No. 214505.
- Ducker, W. A. *Langmuir* **2009**, *25*, 8907–8910.
- Das, S.; Snoeijer, J. H.; Lohse, D. *Phys. Rev. E* **2010**, *82*, No. 056310.
- Borkent, B. M.; de Beer, S.; Mugele, F.; Lohse, D. *Langmuir* **2010**, *26*, 260–268.
- (a) Zhang, L.; Zhang, X.; Zhang, Y.; Hu, J.; Fang, H. *Soft Matter* **2010**, *6*, 4515–4519.
- (b) Colaço, R.; Serro, A. P.; Saramago, B. *Surf. Sci.* **2009**, *603*, 2870–2873.
- Cavicchi, R. E.; Avedisian, C. T. *Phys. Rev. Lett.* **2007**, *98*, No. 124501.
- (a) Zhang, X. H.; Quinn, A.; Ducker, W. *Langmuir* **2008**, *24*, 4756–4764.
- (b) Yang, J.; Duan, J.; Fornasiero, D.; Ralston, J. J. *Phys. Chem. B* **2003**, *107*, 6139–6147.
- Seddon, J. R. T.; Zandvliet, H. J. W. *Surf. Sci.* **2010**, *604*, 476–477.
- Love, J. C.; Estroff, L. A.; Kriebel, J. K.; Nuzzo, R. G.; Whitesides, G. M. *Chem. Rev.* **2005**, *105*, 1103–1169.
- Stamou, D.; Gourdon, D.; Liley, M.; Burnham, N. A.; Kulik, A.; Vogel, H.; Duschl, C. *Langmuir* **1997**, *13*, 2425–2428.
- Bayat, H.; Tranchida, D.; Song, B.; Walczyk, W.; Sperotto, E.; Schönherr, H. *Langmuir* **2011**, *27*, 1353–1358.
- Israelachvili, J. N.; Gee, M. L. *Langmuir* **1989**, *5*, 288–289.
- Cassie, A. B. D.; Baxter, S. *Trans. Faraday Soc.* **1944**, *40*, 546–551.
- Song, B.; Zhou, Y.; Schönherr, H. Manuscript in preparation.
- Schönherr, H.; Vancso, G. J. *Scanning Force Microscopy of Polymers*; Springer: Vienna, 2010.
- Garcia, R. *Amplitude Modulation Atomic Force Microscopy*, Wiley–VCH: Weinheim, Germany, 2010.
- Garcia, R.; Perez, R. *Surf. Sci. Rep.* **2002**, *47*, 197–301.

- (30) Borkent, B. M.; Schönherr, H.; Le Caër, G.; Dollet, B.; Lohse, D. *Phys. Rev. E* **2009**, *80*, 036315.
- (31) If a higher threshold value was chosen, the data did not change significantly up to 50% of the maximum height of the bubble (see Supporting Information, Table S-1).
- (32) Simonsen, A. C.; Hansen, P. L.; Klösgen, B. *J. Colloid Interface Sci.* **2004**, *273*, 291–299.
- (33) Lo, Y. S.; Huefner, N. D.; Chan, W. S.; Dryden, P.; Hagenhoff, B.; Beebe, T. P. *Langmuir* **1999**, *15*, 6522–6526.
- (34) Walczyk, W.; Schönherr, H.; et al. Unpublished data.

**Contact Angles of Surface Nanobubbles on Mixed
Self-Assembled Monolayers with Systematically Varied
Macroscopic Wettability by Atomic Force Microscopy**

Bo Song, Wiktoria Walczyk, and Holger Schönherr*

Supporting Information

Siloxane contamination of aqueous phase

$^1\text{H-NMR}$ spectroscopic data confirmed that no PDMS contamination that may have leached from PDMS based Gel pack material was detectable in water. In a first experiment oligomeric PDMS precursor (Silicone prepolymer of type Sylgard 184, Dow Coming GmbH, Germany) was added as contaminant to the water. $^1\text{H-NMR}$ spectroscopic data of the residual material isolated from the aqueous phase after evaporation of the water (Figure S-1a) showed a peak attributed to the protons of a *dimethylsiloxane* unit at 0.07 ppm. The concentration in water calculated according to the siloxane unit was around 2.14 mM. For the further test experiments, a 1 cm \times 1 cm piece of the PDMS based adhesive layer of the tip storage package was cut and immersed into 20 mL of Milli-Q water for 12h. After taking the PDMS out, the water was removed under vacuum. The alleged residual material was taken up with CDCl_3 and a certain amount of heptane was added as internal standard for $^1\text{H-NMR}$ characterization. No traces of PDMS were detected (absence of peak attributed to the protons of a *dimethylsiloxane* unit at ~ 0.07 ppm, see Figure S-1b)

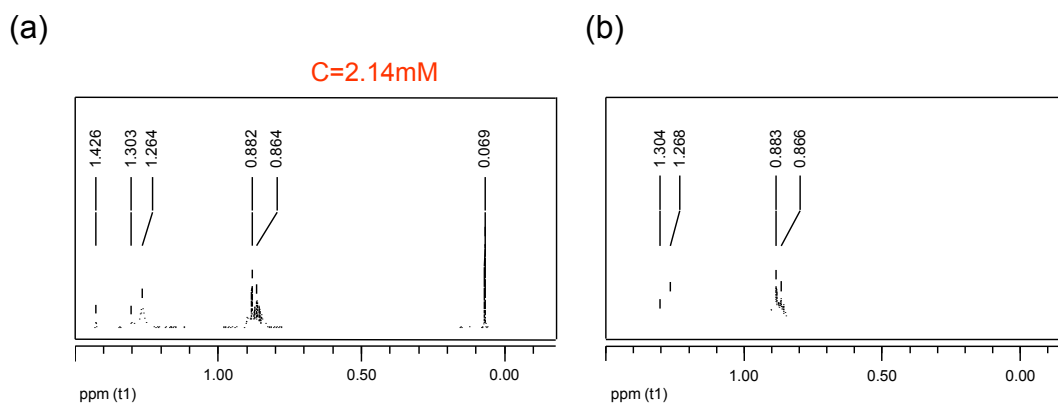


Figure S-1. NMR spectra of the possible “contamination” in water originating (a) from a PDMS precursor and (b) from a PDMS-based Gel pack material. A certain amount of heptane was added for reference. The concentration of the PDMS precursor was 2.14 mM as deduced from the known concentration of heptane.

Siloxane contamination of substrates

The contact angles θ_{macro} of binary SAMs that were contaminated with siloxanes by repeated transfer through the air - water interface were determined according to the captive bubble method. Here one drop of the liquid PDMS precursor prepolymer was added into Milli-Q water. The separated aqueous phase of this solution was used for contact angle measurements. The substrates functionalized with a binary SAMs of certain composition were repeatedly taken out and immersed in the water to measure the contact angle. With increasing number of passages through the air - water interface, the contact angle increased until a maximum value of 110° was reached (Figure S-2). Although the PDMS gel pack does not have influence the contact angle (as shown in Figure 2C), the PDMS precursor was thus shown to contaminate the substrate. These results were also confirmed by the thickness measured by ellipsometry. After the captive bubble experiment, the substrate was covered with a tens of nanometers thick of PDMS precursor.

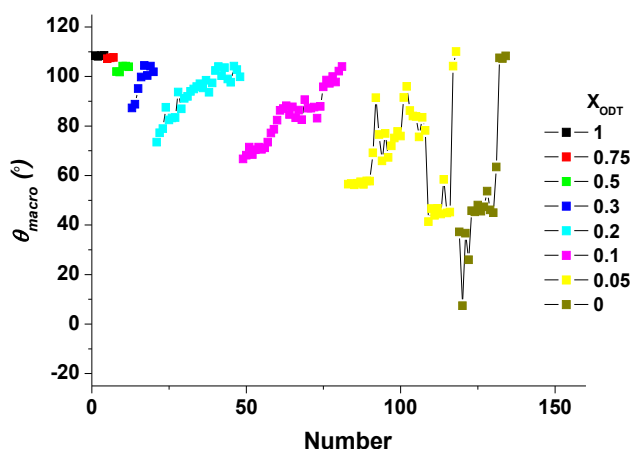


Figure S-2. Contact angles of captive bubbles measured for repeated passages through the air-water interface in the presence of PDMS precursor in the solution; the contact angles increased after immersion in the contaminated water and reached a very similar limiting value of $108 \pm 3^\circ$.

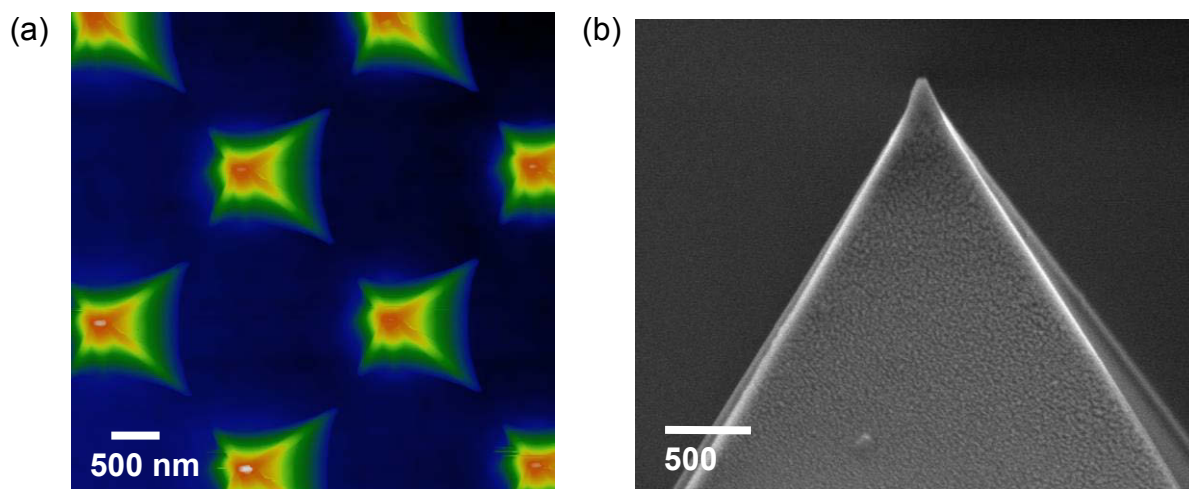
AFM tip radius calibration

Figure S-3. (a) AFM image acquired on a TGT1 calibration standard for blind construction and (b) SEM image of a used AFM tip in side view.

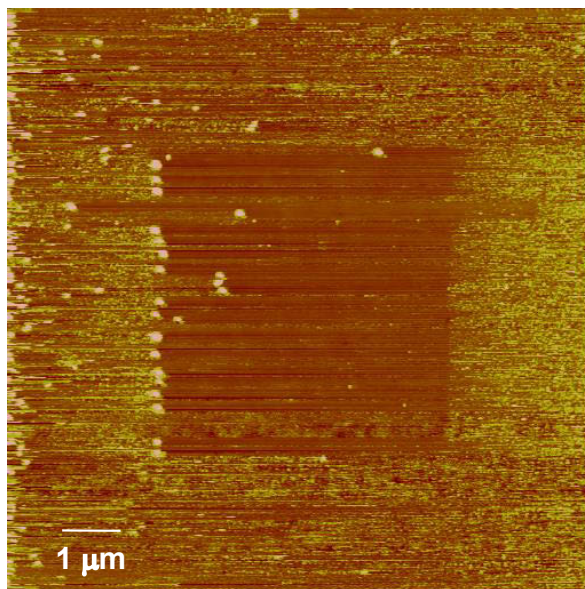
Merging of nanobubbles

Figure S-4. AFM image of surface nanobubbles on substrate with contact angle of 37° (the height scale covers 50 nm). The scanning in the central area resulted in the merging of many of the originally small bubbles and the concomitant formation of larger bubbles located predominantly close to the edge on the scanned square. Figure 7e shows the surface nanobubbles after merging.

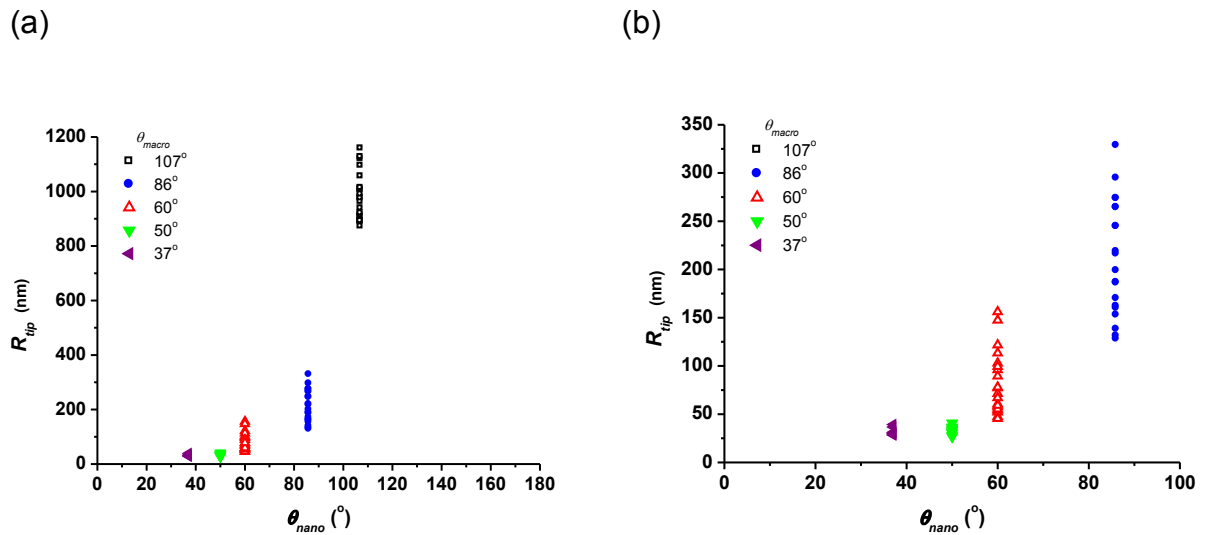
AFM tip radius

Figure S-5. AFM tip radius R_{tip} calculated back from the tip correction model under the assumption that the contact angles of the nanobubbles are equal to the macroscopic contact angles and that the observed deviation is solely due to tip convolution. The data for nanobubbles on the samples with $\theta_{macro} = 37^\circ$, 50° , 60° and 86° are enlarged (plot on the right hand side).

*Nanobubble parameters***Table S-1.** Fitted parameters of an exemplary nanobubble on the sample with $\theta_{macro} = 37^\circ$ for fitting with different threshold values.

threshold (nm)	2	10	20	30	40	50	60	70	80	90	100	110
H (nm)	127.7	127.7	127.9	128.0	128.7	128.6	129.8	131.0	131.6	131.6	134.9	136.9
$W/2$ (nm)	106.5	106.5	106.0	105.5	103.7	103.7	100.0	95.5	93.0	93.0	77.5	60.2
R_c (nm)	108.2	108.2	107.9	107.5	106.1	106.1	103.4	100.3	98.7	98.7	89.7	81.7
θ_{nano} ($^\circ$)	79.6	79.6	79.3	79.0	77.8	77.7	75.2	72.2	70.5	70.4	59.8	47.5
RMS error (nm)	10.9	11.0	11.0	10.8	10.6	10.6	10.1	9.8	9.7	9.7	8.9	8.6

5

The apparent shape of surface nanobubbles in tapping mode AFM

The issue with the unusually high apparent nanoscopic contact angles of surface nanobubbles, which are in clear contradiction with the theoretical predictions, originates from the evidence provided by numerous experiments performed in tapping mode (TM) AFM. In this chapter, we addressed the question how the TM scanning conditions influence the apparent dimensions of nanobubbles in AFM height images. In particular, by systematically varying the free amplitude of the cantilever oscillations and the amplitude setpoint ratio, we analyzed the effect on the apparent nanobubble height, width and contact angle. We found that even in nearly zero-interaction-force imaging conditions, nanobubbles in the AFM images appeared smaller, both in the height and the width, than their actual sizes, and that the underestimation of bubble sizes depended in a systematic way on the values of the scanning parameters employed. Based on our findings, we developed a method to estimate the actual bubble size.

The chapter consists of the following publication:

Closer Look at the Effect of AFM Imaging Conditions on the Apparent Dimensions of Surface Nanobubbles

Wiktorja Walczyk and Holger Schönherr

Langmuir **2013**, *29*, 620–632

Reprinted with permission. Copyright (2013) American Chemical Society.

Supporting Information directly follows the article.

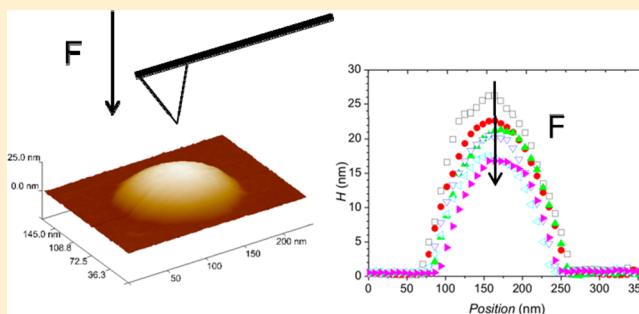
Closer Look at the Effect of AFM Imaging Conditions on the Apparent Dimensions of Surface Nanobubbles

Wiktoria Walczyk and Holger Schönherr*

Department of Chemistry and Biology, Science & Technology, Physical Chemistry I, University of Siegen, Adolf-Reichwein-Str. 2, 57076 Siegen, Germany

Supporting Information

ABSTRACT: To date, TM AFM (tapping mode or intermittent contact mode atomic force microscopy) is the most frequently applied direct imaging technique to visualize surface nanobubbles at the solid–aqueous interface. On one hand, AFM is the only profilometric technique that provides estimates of the bubbles' nanoscopic dimensions. On the other hand, the nanoscopic contact angles of surface nanobubbles estimated from their apparent dimensions that are deduced from AFM “height” images of nanobubbles differ markedly from the macroscopic water contact angles on the identical substrates. Here we show in detail how the apparent bubble height and width of surface nanobubbles on highly oriented pyrolytic graphite (HOPG) depend on the free amplitude of the cantilever oscillations and the amplitude setpoint ratio. (The role of these two AFM imaging parameters and their interdependence has not been studied so far for nanobubbles in a systematic way.) In all experiments, even with optimal scanning parameters, nanobubbles at the HOPG–water interface appeared to be smaller in the AFM images than their true size, which was estimated using a method presented herein. It was also observed that the severity of the underestimate increased with increasing bubble height and radius of curvature. The nanoscopic contact angle of $>130^\circ$ for nanobubbles on HOPG extrapolated to zero interaction force was only slightly overestimated and hence significantly higher than the macroscopic contact angle of water on HOPG ($63 \pm 2^\circ$). Thus, the widely reported contact angle discrepancy cannot be solely attributed to inappropriate AFM imaging conditions.



INTRODUCTION

Surface nanobubbles have been controversially discussed in the literature for several years. Since the observation of a long-range attractive force between hydrophobic surfaces and the hypothesis of nanobubbles as a possible reason for this interaction,^{1–3} much progress has been made. Following the first direct observation of surface nanobubbles by atomic force microscopy (AFM)^{4,5} and conflicting X-ray and neutron reflectometry experiments^{6,7} that suggested the absence of nanobubbles under the sample preparation conditions employed, their existence has been confirmed in the meantime by various noninvasive techniques such as attenuated total internal reflection Fourier transform infrared (FTIR) spectroscopy^{8–11} and the quartz crystal microbalance.^{12,13} Very recently, interference microscopy,¹⁴ transmission electron microscopy,¹⁵ and total internal reflection fluorescence microscopy¹⁶ proved to be the first noninvasive microscopy methods for visualizing surface nanobubbles. We have been able very recently to confirm the report by Ohl's group¹⁶ and show additionally optically that there is indeed a gas–liquid interface.

In the past few years, many important issues in this area have been addressed, including mechanisms of nanobubble formation^{17,18} and possible stabilization,^{17–21} the alleged role of

contamination,^{21–24} the role of temperature, gas type, and concentration,^{9,11,17,25–28} their apparent contact angles, which are markedly higher than the macroscopic ones,^{18,29} the coexistence of nanobubbles with so-called micropancakes,^{9,27,29} and possible applications (e.g., for surface cleaning^{30–33}). All descriptions and hypotheses put forward in this field are based on at least two assumptions: (1) the bubbles possess uniform curvature along the contact line and therefore a spherical cap shape similar to macroscopic bubbles and (2) as suggested by their name, nanobubbles are soft gaseous structures, which, depending on the experimental details, may be covered with a layer of contamination at the gas–water interface. Among the open questions concerning nanobubbles are their very pronounced stability¹⁰ and high contact angles.³⁴ The answers to all of these questions are intimately linked to the accurate and precise knowledge of the nanobubbles' dimensions.

Starting from the pioneering experiments of Christenson et al. in 1988,² for many years, only AFM provided access to the nanobubble profile in 3D (i.e., it could be operated in the liquid medium and had sufficient spatial resolution). In these terms,

Received: October 23, 2012

Revised: December 4, 2012

Published: December 5, 2012

AFM still represents a unique approach. Strikingly, AFM, as the only family of techniques employed to determine the dimensions of surface nanobubbles directly, is invasive in nature, and knowledge on the height and width of nanobubbles (and the radius of curvature and nanoscopic contact angle derived from these data) is crucial for an adequate description and analysis.

Many important observations have been made by means of TM AFM^{4,5,25–27,34–47} and CM (contact mode) AFM.^{43,48–50} Unfortunately, many results published to date lack the appropriate description of the exact experimental conditions used. This renders, as will be shown in this article, comparisons among the different published data sets and experiments difficult, if not impossible. Moreover, it must be taken into consideration that AFM is not an invasive technique and, as a microscopy technique, is not free of imaging artifacts. It is already known that TM imaging may underestimate the height of soft surfaces such as polymers, biological structures, and nanodroplets.^{51–57} In addition, Banin and co-workers demonstrated systematic errors in the assessment of nanoparticle heights for AFM in air depending on the tip–sample interaction.⁵⁹ In the recent nanobubble literature, one can find some suggestions that the nanobubble height is underestimated in TM AFM and that the bubble deforms because of the scanning.^{4,5,35,42,44,45} However, many authors do not take this effect into account in the discussion of their own results on nanobubbles, even though the evidence is clear.^{35,50}

In view of the urgent need to clarify the remaining uncertainties about the nanobubbles, we ask a simple question: what are the actual dimensions of surface nanobubbles in the absence of forces? The answer to this question has fundamental relevance because any other information about the bubble properties, such as internal pressure, bubble lifetime, calculated contact angles, and all proposed stability mechanisms and many other parameters rely on two assumptions mentioned above and/or on the determination of the accurate bubble shape and dimensions obtained from AFM height images.

In our work, we investigated nanobubbles at the HOPG–water interface using constant-amplitude TM AFM and systematically studied the role of the free amplitude of the cantilever oscillation A_0 controlled via the dithering piezo's driving amplitude and the amplitude setpoint ratio (related to the damping), respectively. This choice was motivated by two facts: (1) these two parameters can be set and modified freely by the user in each AFM experiment and (2) the free amplitude and the setpoint amplitude are related to each other to control the level of interaction between the sample and surface and cannot be treated independently.

The influence of A_0 on the apparent dimensions of nanobubbles in AFM height images has not been studied so far. Even worse, the value of A_0 is typically not quantitatively determined, calibrated, or even reported. In isolated reports, its values have been stated, but surprisingly, the dependence of the results obtained on the amplitude value used was not discussed.^{40,42,49} By contrast, the role of the amplitude setpoint ratio has already been investigated, albeit not in a systematic manner. The results are scarce and often inconsistent. Some authors did not observe any influence of the setpoint ratio on the bubble shape,³⁵ but others observed a clear dependence.^{35,40,44,45} Unfortunately, all of the publications lack a conclusive explanation of why the apparent bubble shape depends (or does not depend) on the setpoint ratio in a particular way. The change in the apparent bubble shape caused

by scanning with the TM AFM was suggested to be a possible reason for the discrepancy between the macroscopic and nanoscopic contact angles.^{4,34,35} However, this hypothesis has not yet been tested experimentally. The only suggestion coming from the reports is that, in order to minimize the force applied to the bubble but without losing scanning resolution, one should use high setpoint ratio values (90–95%).

Therefore, in this article we report on our systematic study that addressed how changes in the free oscillation amplitude of the cantilever and the amplitude setpoint ratio influence the apparent shape of surface nanobubbles in TM AFM height images. In addition, we show a method to estimate the actual unperturbed sizes of nanobubbles, discuss the influence of the bubble size on the obtained results, and address the issue of the high apparent contact angles of nanobubbles on HOPG.

■ EXPERIMENTAL SECTION

Nanobubbles were measured on highly oriented pyrolytic graphite (HOPG) (Veeco, grade ZYH) with a macroscopic water contact angle of $63^\circ \pm 2$. The water contact angle of freshly cleaved HOPG was measured with the sessile drop method with an OCA 15 Plus instrument (Data Physics Instruments GmbH, Filderstadt, Germany) using Milli-Q water from a Direct-Q 8 system (Millipore) with a resistivity of 18.0 M Ω /cm.

The AFM experiments were carried on a MultiMode IIIa (Veeco, Santa Barbara, CA) in an open liquid cell configuration (without a rubber O-ring) and on an Asylum Research MFP-3D Bio (Asylum Research, Santa Barbara, CA). The liquid cell was rinsed with ethanol and dried in a stream of nitrogen before use. A drop of Milli-Q water was put on the liquid cell using a sterile disposable plastic syringe and sterile needle so that it filled the groove and covered the cantilever. Another drop was placed directly on the sample. As the last step, the liquid cell was inserted into the optical head of the microscope and the optical head was lowered such that the two droplets coalesced and formed a meniscus between the liquid cell and the sample.⁵⁴ AFM measurements were performed by TM AFM in Milli-Q water with V-shaped Bruker MLCT Si₃N₄ cantilevers (cantilever nominal spring constant of 0.6 N/m). All cantilevers were cleaned immediately prior to use with oxygen plasma for 60 s at a power of ~ 60 W (PlasmaPrep2, GaLa Instrumente, Bad Schwalbach, Germany).

The drive frequencies used for those cantilevers were 25–27 kHz. The drive amplitude and the amplitude setpoint ratio were changed according to the description below. After the AFM images were recorded, the raw data were processed using a first-order plane fit and a zeroth-order flattening (with nanobubbles excluded). Subsequently, the images were exported to ASCII format and analyzed with MATLAB software according to the procedure described elsewhere.³⁴ No tip correction was applied.

The free amplitude A_0 (V) was calculated from amplitude-displacement curves recorded before and after each captured image as an average of 30–50 points. Using the deflection sensitivity, it was converted into A_0 in nm. The amplitude setpoint ratio was calculated as the ratio of the setpoint value set during the measurements and A_0 calculated from the corresponding A – Z curve. All setpoint ratio values given in this article are mean values of two setpoint ratios calculated using curves recorded before and after scanning the corresponding image.

The error in the measured data includes (1) an experimental error of 1% for all spatial directions and (2) the error from fitting the data to a spherical cap shape. The detailed error calculation is described in the Supporting Information.

■ RESULTS AND DISCUSSION

We assume that the surface nanobubbles adopt a spherical cap shape with a radius of curvature R_c , base width W , and height H above the surface as defined in the schematic bubble cross section shown in Figure 1a. The nanoscopic contact angle θ_{nano}

is defined through the water phase. Typically, the bubble height is comparable to the size of the AFM tip apex (Figure 1b).

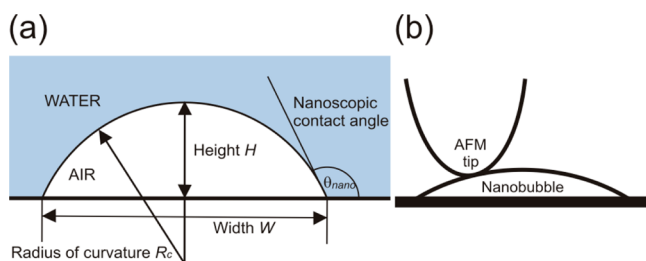


Figure 1. (a) Schematic cross section of a surface nanobubble. We define the contact angle through the condensed (i.e., the aqueous) phase. (b) Schematic (approximately to scale) of the AFM tip apex and surface nanobubble. The nanobubble height is much smaller than its width and approximately the same order of magnitude as the radius of curvature of the tip end.

Relevance of Setpoint Ratio and Amplitude in Studying Surface Nanobubbles. In TM AFM imaging, the cantilever is oscillated at (or close to) its resonance frequency f_0 of several tens of kilohertz with an amplitude A ,

which is proportional to the drive amplitude of a dithering piezo that excites the forced oscillation of the cantilever. When the tip is far from the surface, A equals the free (maximum) amplitude A_0 . During a topographic scan, A_0 is decreased (damped) by the interaction forces between the tip and the surface in the vicinity of the surface. In a particular constant-amplitude-mode experiment, one chooses to which extent the oscillations are damped by defining a setpoint amplitude for the feedback loop to track the surface topography. The setpoint ratio is defined as the ratio between the setpoint amplitude and free amplitude (i.e., $(A/A_0) \times 100\%$). Operating the AFM at a setpoint ratio of 100% is physically impossible because one needs an interaction with the surface to be able to detect it. High setpoint ratios (\geq ca. 90%) ensure relatively small damping of the oscillation and hence weak interaction with the surface. However, this relative damping involves different energies depending on the absolute value of the free amplitude A_0 used in the measurement.

Initially, we examined how the amplitude A changes during the approach of the AFM tip to the surface for small and large amplitudes A_0 . Figure 2 shows AFM amplitude–piezo displacement (A – Z) curves measured on a HOPG sample in water for two different free amplitudes $A_0 = 4.9$ nm (small amplitude,

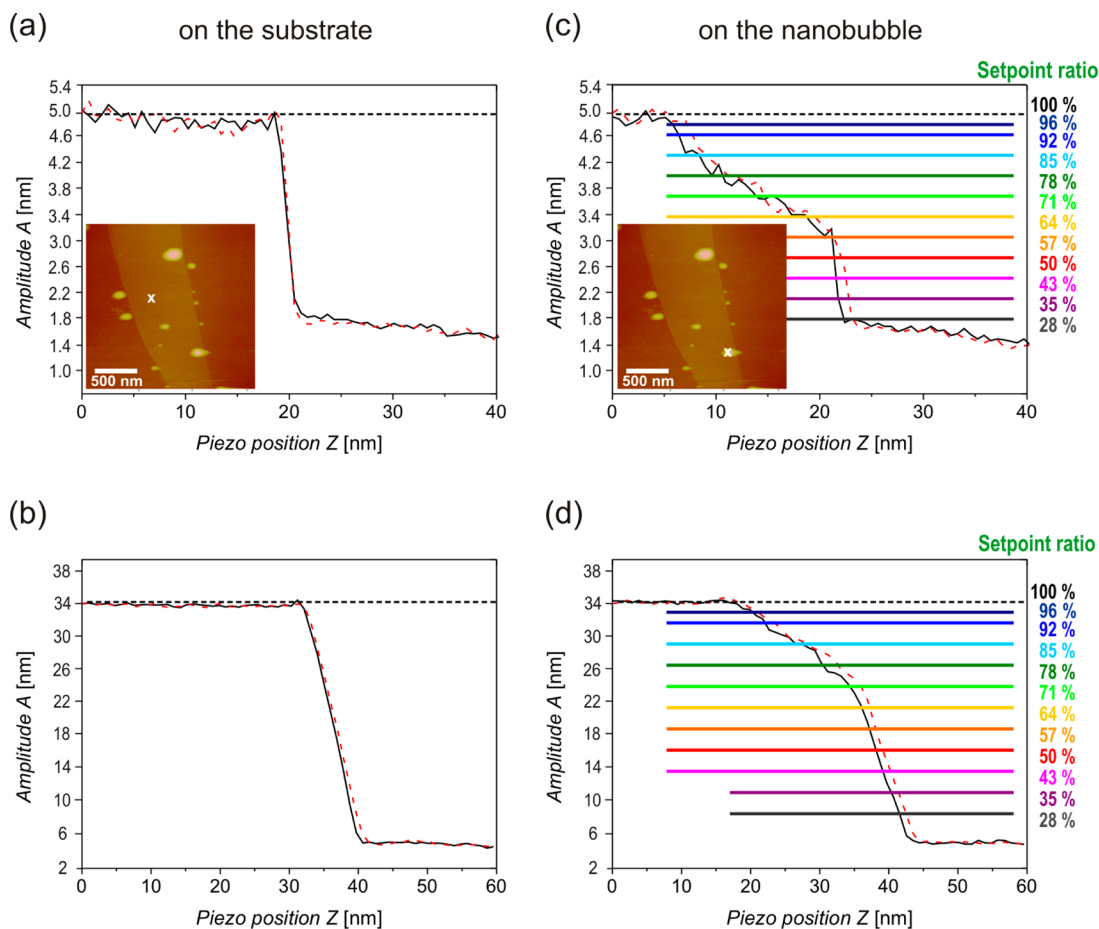


Figure 2. AFM amplitude–displacement curves (black solid, approach; red dashed, retraction) measured in water on the HOPG (a) for free amplitude $A_0 = 4.9$ nm on the substrate, (b) for $A_0 = 34$ nm on the substrate, (c) for $A_0 = 4.9$ nm on the nanobubble, and (d) for $A_0 = 34$ nm on the nanobubble. The positions of data acquisition are marked with crosses in the topographic TM AFM images shown as insets (measured for $A_0 = 40$ nm and a 95% setpoint ratio, pixel size $3.9 \text{ nm} \times 3.9 \text{ nm}$, height scale 30 nm). In the plots in panels a and b, the amplitude decreases when the tip interacts with the hard substrate. In the plots in panels c and d, the initial less-steep slope indicates damping of the oscillations by interactions with the bubble, which is followed by a steeper slope when the oscillations are damped by interaction with the sample surface.

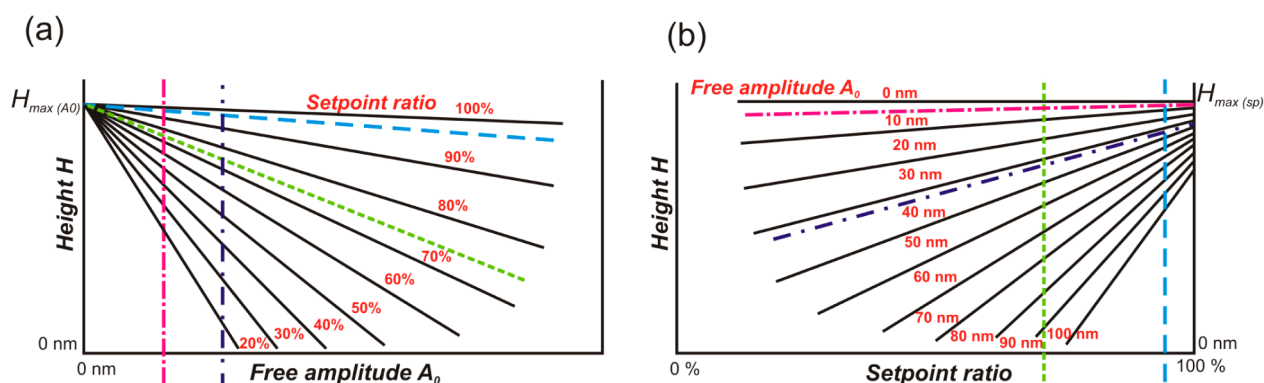


Figure 3. (a) Schematic plot of the height–amplitude dependence for a single nanobubble for different setpoint ratios. The slope $\Delta H/\Delta A_0$ becomes steeper as the setpoint ratio decreases. The actual bubble height $H_{\max(A_0)}$, which is the bubble height in the extrapolated unperturbed state, is reached at $A_0 = 0$ nm. The apparent bubble height measured with a fixed value of the setpoint ratio decreases with increasing amplitude and is always lower than $H_{\max(A_0)}$. (b) Schematic plot of the height–setpoint ratio dependence for different free amplitudes A_0 for a single nanobubble. The slope $\Delta H/\Delta(\text{setpoint ratio})$ increases for larger amplitudes.

upper plots) and $A_0 = 34$ nm (large amplitude, lower plots) at two locations: (1) on the atomically flat substrate and (2) on the nanobubble. All plots show both approach and retraction curves. The exact locations of the data acquisition are marked with crosses in the TM AFM height images shown as insets in the upper plots. The AFM images were measured with $A_0 = 40$ nm and a setpoint ratio of 95%. The A – Z curves in Figure 2a,b measured on the substrate possess qualitatively similar shapes for both sets of data, and hysteresis between consecutively captured approach and retract cycles was absent. When the tip was far away from the surface, the amplitude was constant and equal to the free amplitude A_0 . It decreased when the tip approached closer to the surface. One difference between these two data sets is the vertical scale: the absolute drop in the amplitude is larger for larger A_0 . Likewise, the A – Z curves measured on the nanobubble possess different shapes. When the bubble was approached, the amplitude first decreased slightly (apparent slope approximately -0.12 nm/nm for $A_0 = 4.9$ nm and approximately -0.36 nm/nm for $A_0 = 34$ nm), indicating damping of the cantilever oscillations primarily by the bubble, which was followed by a rapid decrease in A (apparent slope approximately -1.0 nm/nm for $A_0 = 4.9$ nm and approximately -2.2 nm/nm for $A_0 = 34$ nm), when the tip interacted with the underlying stiff substrate. This rapid decrease was similar to that in the plots measured on the bare substrate (Figure 2a,b). The presence of two different slopes in the A – Z curves was observed both for data captured on the bubble with small and large A_0 . However, for the small amplitude a less-steep (-0.12 nm/nm) apparent slope prevailed, whereas for large amplitudes this part of the curve constituted only a small part of the total amplitude drop. This means that most of the oscillation was damped by the bubble for small A_0 whereas for large A_0 most of the oscillation was damped by the substrate. In all curves, the total distance covered by the piezo, until the oscillations were damped effectively, was longer for $A_0 = 34$ nm ($\Delta Z \approx 30$ nm) than for $A_0 = 4.9$ nm ($\Delta Z > 20$ nm). This behavior was again similar for the curves measured on the substrate and on the nanobubble.

These results, which show different shapes of amplitude–displacement curves measured on the bubble and on the substrate, are similar to the results reported by Bhushan et al.⁴² but are in contradiction to the results of Zhang et al.,³⁵ who did not observe any slope change on the bubble.

For the two curves in Figure 2c,d measured on the bubble, the ranges of the less-steep slopes (-0.12 nm/nm for small and -0.36 nm/nm for large amplitude) were approximately ~ 16 nm for both values of A_0 . From the length of these slopes, we could roughly judge the height of the bubble. (To get the actual height of the bubble, we should take also the deflection of the cantilever into account, which might be up to a few nanometers.) The estimated value of ~ 16 nm is comparable to 15 nm for the bubble height as measured from the AFM image shown in the inset of the upper plot (scanned with $A_0 = 40$ nm and a 95% setpoint ratio). The consequence of these differences becomes apparent when different amplitude setpoint ratios are compared. In Figure 2c,d, different values of the setpoint ratio are represented by horizontal lines drawn in the A – Z curves. During scanning with a particular setpoint ratio, the distance ΔZ measured from the point where the corresponding line crosses the A – Z curve (i.e., contact with the bubble surface) to the point where the slope of the curve becomes steeper (i.e., interaction with the substrate beneath the bubble) is transferred to the apparent height and displayed in the AFM topographic image. Because the lines for different setpoint ratios cross the A – Z curve at different points, the distance ΔZ and thus the apparent height of the bubble must depend on the choice of the setpoint ratio. It is thus expected to decrease markedly with decreasing setpoint ratio (thus increasing damping). Moreover, if one compares the plots in Figure 2c,d, then the distance ΔZ also depends on A_0 ; for the same setpoint ratio, ΔZ is larger for small A_0 than for large A_0 . In other words, measurements of the same bubble with the same value of the setpoint ratio but with different free amplitudes A_0 result in different apparent bubble heights in the AFM image. It is also obvious that the apparent height is expected to decrease faster with decreasing setpoint ratio for larger amplitudes and is always smaller than the actual “true” height of the bubble. Hence, it is clear that the amplitude A_0 and the setpoint ratio A/A_0 are two parameters that cannot be treated independently because they both influence the result of TM AFM measurements of surface nanobubbles.

As mentioned above, the apparent height of the bubble in the AFM images depends both on A_0 and the setpoint ratio. Because the slopes in Figure 2c,d are constant in the range of the bubble height, we may assume a linear dependence of the height on the setpoint ratio. Consequently, the dependence of

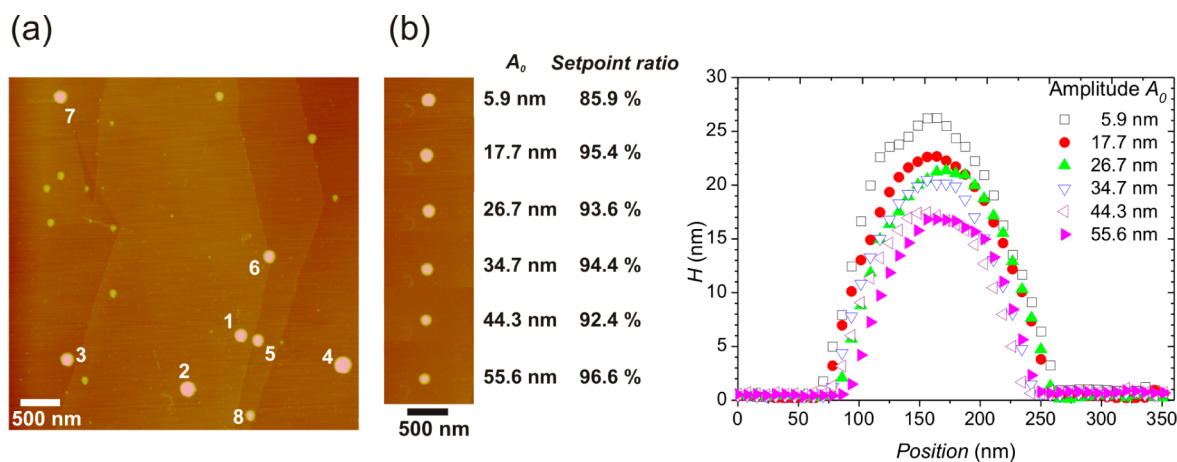


Figure 4. (a) TM AFM height image of nanobubbles on HOPG in water scanned with $A_0 = 10.2$ nm and a setpoint ratio of 91.9%. The dimensions of eight bubbles marked with numbers were analyzed and are plotted in Figure 5. (b) Sequence of AFM images (left) and corresponding cross sections of a single nanobubble (no. 2 in panel a) scanned with different free amplitudes A_0 (right). The apparent size of the bubble decreases with increasing amplitude. The height scale of all AFM images is 30 nm, and the pixel size is $7.8 \text{ nm} \times 7.8 \text{ nm}$.

the height on the amplitude should also be linear. The plots in Figure 3 schematically show these dependences for an exemplary nanobubble. Lines with different slopes are labeled with different setpoint ratios in Figure 3a and different A_0 values in Figure 3b. In this way, we are able to describe all possible experimental conditions in a single plot. A fixed value of the free amplitude is represented by a dotted–dashed vertical line in Figure 3a. A change in A_0 means shifting the line to lower (left) or higher (right) values of the apparent bubble height. The change in the setpoint ratio is represented by moving up and down along the fixed amplitude line and also results in a different apparent height of the bubble. The apparent height always decreases with decreasing setpoint ratio, but the absolute decrease is less pronounced for small amplitudes and more pronounced for large amplitudes A_0 .

This behavior is also shown in the corresponding plot in Figure 3b that displays the dependence of the apparent bubble height on the setpoint ratio for different amplitudes A_0 . Points for 0 and 100% setpoint ratio on the horizontal axis correspond to maximum and minimum (zero) damping, respectively. The apparent height decreases linearly with decreasing setpoint ratio, and the slope of the functions becomes steeper for larger amplitudes. For $A_0 = 0$ nm, the slope is zero, and for all setpoint ratios, the apparent bubble height H equals the maximum height $H_{\max(A_0)}$ (the convergence point in Figure 3a, which represents the bubble height in the extrapolated unperturbed state⁶⁰). However, for the 100% setpoint ratio the apparent height reaches its maximum value $H_{\max(\text{sp})}$, which still depends on the amplitude A_0 and is smaller than $H_{\max(A_0)}$ for $A_0 > 0$ nm. Accordingly, the line in Figure 3a labeled with 100% setpoint ratio possesses a nonzero slope. This means that even if one was able to increase the setpoint ratio to 100% the bubble height shown in the AFM image would still depend on the free amplitude used. By minimizing A_0 , one gets closer to the actual value of the bubble height $H_{\max(A_0)}$ (the one reached for 0 nm free amplitude and 100% setpoint ratio). This height cannot be measured by TM AFM because of the nonzero amplitude and nonzero damping conditions necessary to make any measurement possible. Therefore, the apparent bubble height in AFM images is always underestimated and smaller than $H_{\max(A_0)}$. Moreover, the apparent height may vary in different experi-

ments for bubbles of the same sizes depending on the scanning parameters used.

To experimentally test and verify the dependence of the nanobubble size on the free amplitude A_0 and the setpoint ratio obtained from the A – Z curves above, we conducted two further series of experiments described in the next two sections.

Constant Setpoint Ratio and Different Amplitudes. In the first series of experiments, we studied the influence of the free amplitude A_0 on the apparent size of the nanobubbles. We kept the setpoint ratio constant and systematically changed A_0 . Figure 4a shows a typical TM AFM image of nanobubbles on HOPG in water. The nanobubbles resembled spherical caps, were approximately 10–30 nm high and 50–230 nm wide (the size also depended on the scanning conditions, vide infra), and $\sim 50\%$ of the bubbles imaged were located near atomic steps. No micropancakes or apparent impurities were observed on the surface during these experiments.

We scanned the bubbles at the same location on the HOPG sample with systematically varying amplitudes, starting from $A_0 = 5.9 \text{ nm} \pm 0.5 \text{ nm}$ and gradually increasing up to $A_0 = 55.6 \pm 3.4 \text{ nm}$. In total, a series of 19 images was taken. For each image, after the AFM tip was engaged, the setpoint ratio was adjusted to the highest possible value at which the contact with the surface was still established/kept, and force–displacement and amplitude–displacement curves were recorded (on top of the bubbles). Subsequently, a constant-amplitude (height) image was acquired using identical scan rate and gain settings. After the scan was completed, F – Z and A – Z curves were recorded again on the substrate and the AFM tip was withdrawn. Immediately afterward, A_0 was increased to a new value and the tip was engaged again in the same place to capture the next image. The entire procedure took approximately 25 min per image (20 min of scanning + 5 min of other operations).

To minimize the interactions with the AFM tip, the setpoint ratio was kept at the highest possible level during the entire experiment. For each individual image, the value of the setpoint ratio was determined as the mean value of setpoint ratios measured in the A – Z curves recorded before and after scanning the frame, as described in the Experimental Section. The measured values showed some fluctuations for different frames (Figure S-1 in the Supporting Information). For all images

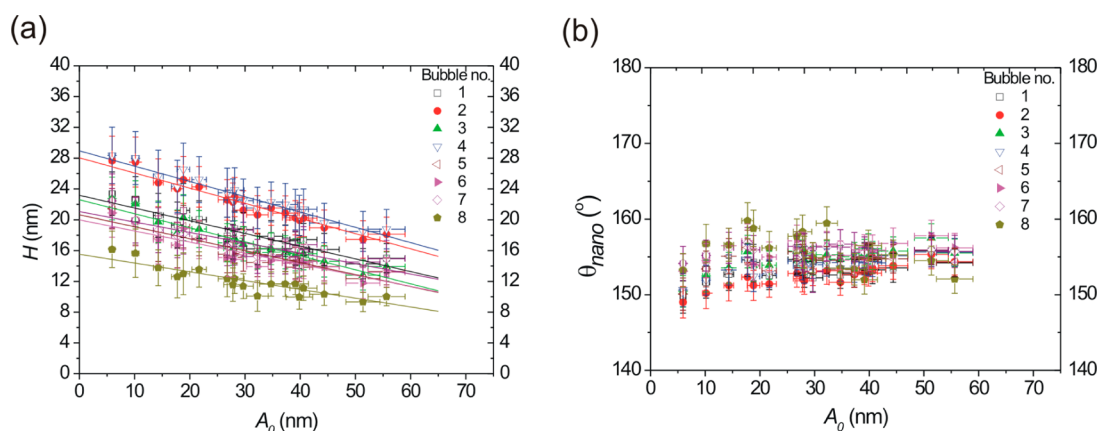


Figure 5. Apparent nanobubble (a) height H and (b) contact angle θ_{nano} as functions of the free amplitude A_0 measured with setpoint ratios $>85.9\%$ for the eight bubbles marked in Figure 4a. The apparent height decreases, and the contact angle slightly increases with increasing amplitude. θ_{nano} is greater than the macroscopic contact angle. Even if the data are corrected by taking the AFM tip radius into account, the discrepancy between macroscopic and nanoscopic contact angles is $>80^\circ$.

except the first one, the setpoint ratio was hence kept between 91 and 97%. As will be shown below, even those variations in the setpoint ratio may influence the results; however, they do not change the overall trend. The variations in the setpoint ratio observed were caused by fluctuations of the amplitude signal over time (the actual scan of each image took approximately 20 min). This effect was more pronounced for low A_0 because then the signal was closer to the noise level and more unstable. For $A_0 = 5.9$ nm, the maximum setpoint ratio was 85.9%; for $A_0 = 4.2$ nm, no height data could be obtained for setpoint ratios higher than 64.8%. Because of the large deviation in the setpoint ratio, these data were not included in the series.

In general, nanobubbles apparently become smaller in the AFM image as the free amplitude A_0 increases. As an example, a series of six AFM images and cross sections of one bubble (bubble no. 2 in Figure 4a) scanned with different amplitudes are shown in Figure 4b. Both the apparent height and width of the bubble decrease with increasing A_0 .

In total, eight bubbles marked with numbers in Figure 4a were measured and analyzed. Their apparent heights H and nanoscopic contact angles θ_{nano} are plotted as functions of the free amplitude A_0 in Figure 5. The corresponding dependences for their widths W and radii of curvature R_c are shown in Figure S-2 in the Supporting Information. To within the error, the apparent height H decreases linearly with increasing amplitude for all measured nanobubbles. This result is in agreement with the dependence shown schematically in Figure 3. The extrapolation of the fits to the free amplitude $A_0 = 0$ nm yields an estimate of the maximum (actual) heights of the measured nanobubbles, denoted as $H_{\text{max}(A_0)}$. $H_{\text{max}(A_0)}$ for a particular bubble is always larger than any apparent value measured in AFM images for this bubble.

In contrast to the height, the apparent contact angle of nanobubbles θ_{nano} does not show a strong dependence on the amplitude A_0 . After the initial small increase for small amplitudes, which can be attributed to the actual small variations of the setpoint ratio, θ_{nano} is scattered over the range between 150 and 160°. Variations for individual bubbles did not exceed 10°. All measured θ_{nano} significantly ($>80^\circ$) exceed the independently determined macroscopic contact angle ($63 \pm 2^\circ$) of water on HOPG.

None of the data shown in the plots were corrected for the AFM tip size. The correction was not applied because the apparent heights of nanobubbles were not constant during the experiment and the tip deconvolution introduces a systematic error into all measurements, which can be neglected as long as one does not compare data from experiments done with different tips. As mentioned, the correction does not lower the contact angle so much that it will reach the macroscopic value.³⁴

According to the scheme in Figure 3a, the slope $\Delta H/\Delta A_0$ is steeper for lower setpoint ratios. In our experiment with relatively high setpoint ratios, the apparent height decreased by approximately 30% when the amplitude A_0 was increased by 50 nm. This is a significant decrease; therefore, the role of amplitude in imaging nanobubbles cannot be neglected. Typical values of amplitudes used in AFM experiments for scanning under optimal conditions range from several to several tens of nanometers. This variation in amplitude causes a significant difference in apparent bubble shape in the AFM images even if the setpoint ratio is kept high ($>90\%$). We believe that although A_0 may vary depending on the cantilever type and the microscope model used, this range represents the amplitudes used in many experiments on nanobubbles reported in the literature so far.

Constant Amplitudes and Different Setpoint Ratios.

In the next set of experiments, we studied the influence of the setpoint ratio on the apparent size of the nanobubbles. This time, we kept the amplitude A_0 constant and systematically changed the setpoint ratios. The bubbles were scanned with setpoint ratios from $98.5 \pm 0.1\%$ down to $30.0 \pm 0.2\%$ and mean amplitudes $A_{0,\text{mean}}$ from 4.5 ± 0.2 to 120.7 ± 0.1 nm. In total, we conducted three experiments and tested six amplitudes. In Figure 6, TM AFM height images of nanobubbles from three different experiments are shown. The bubbles in Figure 6a were scanned with $A_{0,\text{mean}} = 4.5 \pm 0.2$ nm (one series). The bubbles in Figure 6b were successively scanned with amplitudes $A_{0,\text{mean}}$ of 43.1 ± 0.4 , 65.3 ± 1.3 , and 120.7 ± 0.1 nm (three series). The bubbles in Figure 6c were scanned with $A_{0,\text{mean}} = 90.5 \pm 0.6$ nm and subsequently with $A_{0,\text{mean}} = 11.0 \pm 0.1$ nm (two series). For each amplitude value, a series of 15–21 constant-amplitude (height) images were

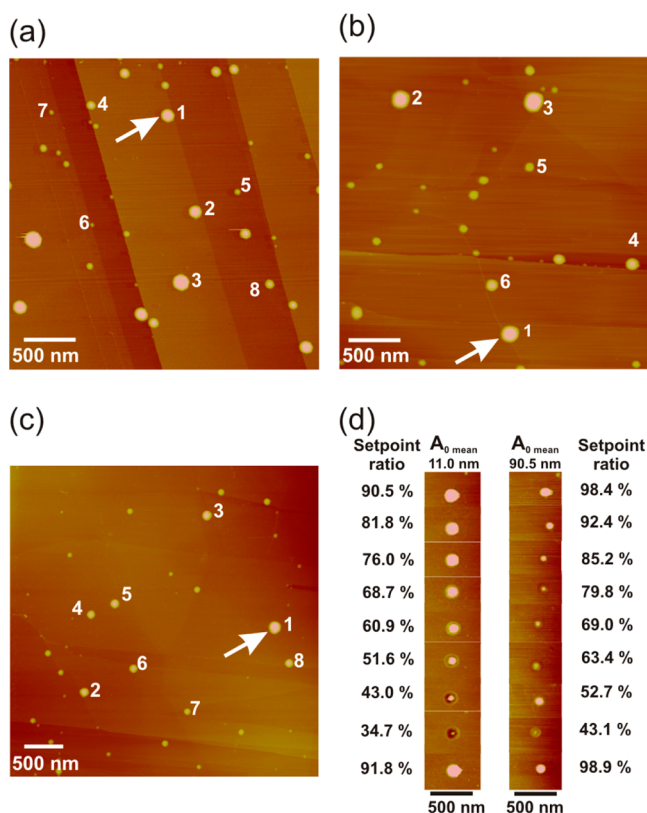


Figure 6. TM AFM height images of nanobubbles on HOPG in water measured with different free amplitudes $A_{0,\text{mean}}$: (a) 4.5 ± 0.2 , (b) 43.1 ± 0.4 , 65.3 ± 1.3 , and 120.7 ± 0.1 nm, and (c) 11.0 ± 0.1 and 90.5 ± 0.6 nm. For each amplitude, a series of images was scanned with different setpoint ratios. The dimensions of three bubbles marked with arrows were measured and plotted in Figure 7. The heights of bubbles marked with numbers are plotted in Figures 8 and 9. (d) Sequence of AFM images of a single bubble (no. 1 in panel c) scanned with $A_{0,\text{mean}} = 11.0 \pm 0.1$ nm and $A_{0,\text{mean}} = 90.5 \pm 0.6$ nm with various setpoint ratios. The apparent size of the bubble depends on the amplitude and decreases with decreasing setpoint ratio. The height scale of all images is 30 nm, and the pixel size is $5.9 \text{ nm} \times 5.9 \text{ nm}$ in panels a and b and $7.8 \text{ nm} \times 7.8 \text{ nm}$ in panels c and d.

recorded. The first image in each series was scanned with the highest possible setpoint ratio (usually higher than 94%), and then the setpoint ratio was gradually decreased to the minimum possible value (usually around 35%). Finally, the setpoint ratio was reset to the highest possible value, and one more image was scanned in order to determine whether the bubbles changed their size (volume) or position during scanning the series. For setpoint ratios lower than 30%, imaging was possible, but the signal became very noisy. The recording of each image took approximately 15 min. In all three experiments, the nanobubbles possessed similar sizes, with apparent heights H ranging from 10 to 36 nm and widths W between 50 and 200 nm (as measured for setpoint ratios $>90\%$).

For each image, the amplitude was measured from the A - Z curves recorded before and after scanning the image as described in the Experimental Section. Afterward the mean amplitude was calculated for each image and finally for the whole series. The amplitudes were held constant during each series in order to minimize their influence on the bubble size (Figure S-4 in the Supporting Information). The only exception was the series acquired for $A_{0,\text{mean}} = 90.5 \pm 0.6$ nm, for which the amplitude first decreased with changing setpoint ratio at a gradient of approximately $0.5 \text{ nm}/\%$ and then increased again. This decrease affected the results (Figures 7 and 8).

Figure 6d shows two series of AFM images obtained for a single bubble scanned with different setpoint ratios (the bubble is marked with an arrow in Figure 6c). The first series was made for small amplitudes ($A_{0,\text{mean}} = 11.0 \pm 0.1$ nm), and the second series was made for large amplitudes ($A_{0,\text{mean}} = 90.5 \pm 0.6$ nm). In both cases, the bubble gradually decreased in size for decreasing setpoint ratios. Its apparent shape changed dramatically from a typical spherical cap shape for high setpoint ratios through a hatlike structure for intermediate setpoint ratios to complete disappearance in images for low setpoint ratios. After the set point was reset to high values, the bubble reappeared on the surface in its original location and size. The bubble size depended on the amplitude and was smaller for larger $A_{0,\text{mean}}$ for comparable setpoint ratios. This is in line with the results described in the previous sections. Similar behavior was observed for all measured bubbles. They remained

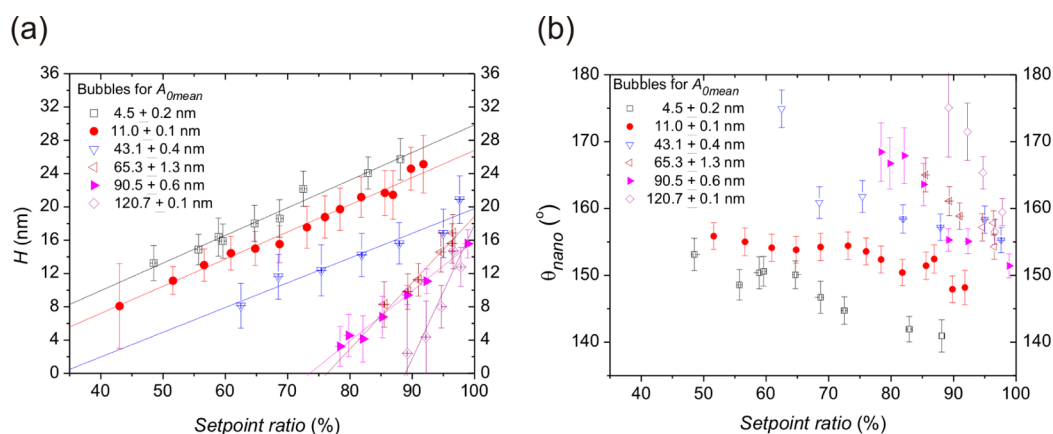


Figure 7. Apparent nanobubble (a) height H and (b) contact angle θ_{nano} as functions of the setpoint ratio measured for three bubbles marked with arrows in Figure 6 for six different free amplitudes $A_{0,\text{mean}}$. Data for $A_{0,\text{mean}} = 11.0 \pm 0.1$ and 90.5 ± 0.6 nm concern the same bubble measured during the same experiment but with different scanning parameters. Similarly, data points for $A_{0,\text{mean}} = 43.1 \pm 0.4$, 65.3 ± 1.3 , and 120.7 ± 0.1 nm refer to the same bubble. The apparent height decreases and the contact angle increases with decreasing setpoint ratio. The slopes increase with increasing amplitude.

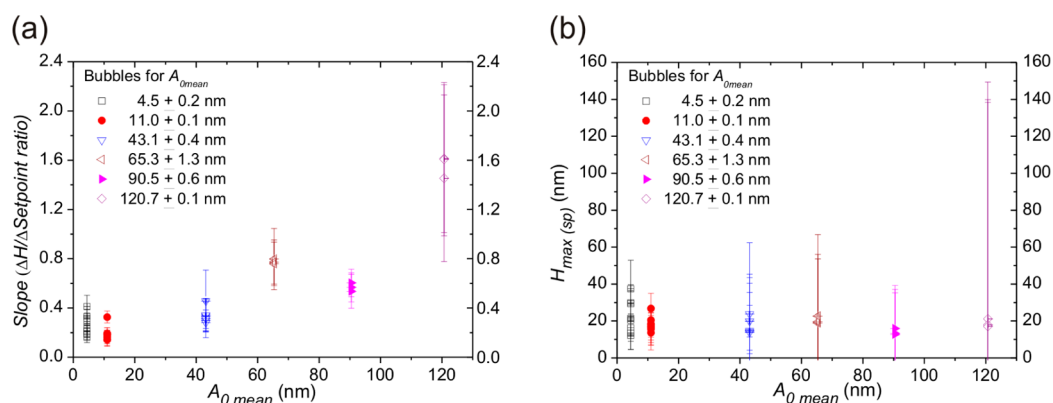


Figure 8. Change of (a) the slope $\Delta H/\Delta \text{setpoint ratio}$ and (b) the maximum height $H_{\text{max}(sp)}$ (apparent bubble height extrapolated to 100% setpoint ratio) as functions of the mean amplitude $A_{0,mean}$ for different bubbles. Each data point corresponds to a single bubble marked with numbers in Figure 6. The slope increases with the amplitude; the maximum height shows no clear trend.

unchanged as long as the setpoint ratio and amplitude were held constant but changed their apparent shape in response to changes in one of these parameters. In all experiments, smaller bubbles disappeared from the AFM image faster (i.e., for higher setpoint ratios) than large bubbles, but all bubbles reappeared unchanged for high setpoint ratios. This observation indicates that nanobubbles do survive the tip–bubble interaction not only without being destroyed but also without any change in their apparent shape or size. Therefore, they proved their extreme stability over a long time (several hours) and under harsh scanning conditions.

As explained in the previous section, the disappearance of nanobubbles in the AFM images for lower setpoint ratios is caused by the fact that the bubble does not damp oscillations sufficiently and the AFM tip approaches and eventually interacts with the hard substrate. Moreover, because bubbles are lower at the edges, this effect is more pronounced at the rim than in the center and visible in the image as a circular depression around the bubble. In addition, for large amplitudes, after the initial bubble disappearance, if we further lower the setpoint ratio, the bubble reappears and disappears again (Figure 6d). The reason for this is a repulsive force between the tip and the sample that becomes more significant for lower setpoint ratios and causes a much faster damping of the oscillations. As a consequence, the piezo moves less toward the tip (retracts the sample) and that is seen as an elevation in the height image. For larger amplitudes, this artifact is visible for even higher setpoint ratios, where relatively more damping of A_0 is needed to establish contact with the surface and repulsive forces play a role in the earlier stage.

The underestimation of the nanobubble height as a result of TM AFM scanning has already been observed by several authors. For instance, the real bubble height estimated from the force–displacement curves measured on the bubble by Zhang et al.³⁵ was found to be more than 2 times larger than the apparent height measured in TM AFM height images. Also, Holmberg et al.⁵⁰ reported that the real bubble height deduced from force–displacement curves was larger than the one measured via CM AFM. Interestingly, Bhushan et al.⁴² obtained approximately the same bubble height in TM AFM height images (setpoint ratio 95% and free amplitude 7 nm) as compared to an estimate from the amplitude–displacement and phase shift–displacement curves measured on the same bubble.

The apparent shrinkage of bubble heights and widths as a result of decreased setpoint ratios is in agreement with most of

the data reported in the literature. Wang et al.⁴⁴ studied nanobubbles on spin-coated PS films and observed the apparent bubble disappearance from the height image for a low setpoint ratio (80%) and the reappearance for a high (95%) setpoint ratio. Yang et al.⁴⁵ measured nanobubbles on HOPG in water for five values of the setpoint ratio between 89 and 44%. They observed the decrease in the apparent bubble height and width for decreased setpoint ratios. For an example bubble, the apparent bubble height decreased from ~ 11 to ~ 1 nm and the bubble became nearly flat. The gradient of shrinkage was relatively small for setpoint ratios of 89–67% and increased for setpoint ratios of 67–44%. No tip correction was applied in this report. Borkent et al.⁴⁰ also investigated nanobubbles on HOPG in water and measured them with different cantilevers for free amplitudes that were as low as 1 to 2 nm and several setpoint ratios ranging from 98 to 50%. In some cases, no change in the apparent shape was observed down to a setpoint ratio of 50%, and in other cases, the bubble size decreased for setpoint ratios $< 90\%$ and showed a plateau for setpoint ratios $> 90\%$. Finally, in a few cases, a decrease was observed for the whole range of setpoint ratios used. According to the authors' claims, these differences could not be assigned to different cantilever stiffnesses (a stiffer cantilever presumably caused a weaker dependence), but were the result of the contamination of the cantilever of unknown origin (all cantilevers were plasma cleaned prior to use and investigated with high-resolution SEM after use). This contamination might cause pinning of the contact line and was argued to form a layer on the nanobubble's air–water interface, increasing its stiffness and weakening its response to the force applied by the AFM tip, which resulted in a plateau in the plots. Clean cantilevers (also plasma cleaned and investigated with SEM) gave reproducible results; however, the different slopes in the setpoint ratio dependences could not be explained by the varying cantilever stiffness.

In experiments on nanobubbles on OTS-covered silicon in water carried out by Zhang et al.,³⁵ the setpoint ratio was changed from 92.6 to 74.1% (only two values examined). The bubbles were found to be insensitive to the setpoint ratio and kept their apparent height and width constant, which is similar to the plateau effect observed by Yang et al. and Borkent et al. but in contradiction with our results. Interestingly, the same authors also measured nanobubbles on OTS in 0.5 CMC Tween 20 solutions and observed a strong setpoint ratio dependence in the range of 96.8 to 74.4%. The apparent bubble size decreased with lowering the setpoint ratio and increased

with increasing the setpoint ratio (no plateau observed). The strong response to the variation in the setpoint ratio was explained by the authors as a consequence of a decreased surface tension and hence a decreased stiffness of the bubble due to the presence of the surfactant.

As shown in the present work, unfortunately, the values of setpoint ratios given by different authors cannot be compared directly because of other unknown scanning parameters and different cantilevers, substrates, and solutions used. Moreover, in some experiments the cantilevers were precleaned, and in others they were not. In our opinion, the inconsistency in the measured setpoint values and therefore the extent to which the apparent bubble size changed as a result of the tip action may be mainly ascribed to the variations in the free amplitude in different experiments. (Unfortunately, in most cases the values of A_0 were not reported.) The origin of the plateau effect reported by some authors, although also observed by us in other experiments, is still unclear. Finally, moving, coalescence with neighboring bubbles, or even the removal of nanobubbles from the image for low setpoint ratios reported by Agrawal et al.⁴³ and Wang et al.⁴⁶ can be attributed to large lateral forces due to the contamination of (nonprecleaned) AFM tips used in the experiments. It should be noted that such effects may also occur for hydrophobic AFM probe tips at the highest possible setpoint ratios.^{34,40} Similar effects of tip operation on the bubble height were also observed in contact-mode AFM.^{5,48–50}

Throughout all of our experiments, we assumed that nanobubbles possess a spherical cap shape and that they kept this shape over the whole course of the experiment, also for low setpoint ratios. Therefore, as long as the bubbles were visible in the AFM images, we applied the spherical cap fit and measured their apparent dimensions. The apparent heights H and contact angles θ_{nano} of three example bubbles marked with arrows in Figure 6a–c are plotted as functions of the setpoint ratio in Figure 7. Different data points refer to six series of measurements made for different amplitudes in three experiments. Series for $A_{0,\text{mean}} = 11.0 \pm 0.1$ and 90.5 ± 0.6 nm describe the same bubble. (They were measured during the same experiment at the same location on the sample.) Similarly, data points for $A_{0,\text{mean}} = 43.1 \pm 0.4$, 65.3 ± 1.3 , and 120.7 ± 0.1 nm refer to the same bubble. The apparent widths W and radii of curvature R_c of the bubbles as functions of the setpoint ratio are shown in Figure S-5 in the Supporting Information.

For all bubbles, the apparent bubble height H decreased with decreasing setpoint ratio. Similar trends were observed in independent PeakForce TM AFM measurements of surface nanobubbles, where the apparent height decreased for increased maximum scanning force.⁶¹ In the current TM AFM experiments reported here, we assumed a linear dependence of H on the setpoint ratio in Figure 7a, and we applied a linear fit to the data points. For each series, the data points followed the trend and the slope $\Delta H/\Delta \text{setpoint}$ ratio of the fit increased for increasing A_0 . This observation is in agreement with the schematic plot in Figure 3b. To confirm this, we calculated the slopes $\Delta H/\Delta \text{setpoint}$ ratio for several bubbles marked with numbers in Figure 6: eight bubbles from the series measured with amplitudes of $A_{0,\text{mean}} = 4.5 \pm 0.2$ and 11.0 ± 0.1 nm (bubble no. 1–8 in Figure 6a,c, respectively), six bubbles from the series for $A_{0,\text{mean}} = 43.1 \pm 0.4$ nm (bubbles no. 1–6 in Figure 6b), and three bubbles from the series for amplitudes $A_{0,\text{mean}} = 90.5 \pm 0.6$ nm (bubbles no. 1–3 in Figure

6c) and $A_{0,\text{mean}} = 65.3 \pm 1.3$ and 120.7 ± 0.1 nm (bubbles no. 1–3 in Figure 6b). The results are plotted as functions of the mean amplitude in Figure 8a. Each data point in this plot corresponds to a single bubble in Figure 6. The slope increases for increasing amplitude, which is again in line with the dependence shown in the scheme in Figure 3b. The line is constant for $A_0 = 0$ nm in the scheme; therefore, no dependence of the size on the setpoint ratio is represented in Figure 8a as the (0, 0) point. However, it is difficult to judge whether there is a linear dependence of the slope on the amplitude because of (1) the deviation of $A_{0,\text{mean}} = 4.5 \pm 0.2$ nm data, (2) the deviation of $A_{0,\text{mean}} = 90.5 \pm 0.6$ nm data, and (3) the possible dependence of the slope on the bubble size discussed in detail in the next section (where we compare three bubbles of different sizes measured in three different experiments). The deviation of $A_{0,\text{mean}} = 4.5 \pm 0.2$ nm data (slopes steeper than for $A_{0,\text{mean}} = 11.0 \pm 0.1$ nm) can be explained by the lack of points available for fitting for high setpoint ratios (the highest setpoint ratio was <90%) and by presumably different AFM tip sizes/shapes. The slope of the bubbles measured with $A_{0,\text{mean}} = 90.5 \pm 0.6$ nm deviates from the linear trend (is less steep) most likely because the amplitude decreased during the experiment (Figure S-4 in the Supporting Information). This decrease affected (increased) the apparent bubble heights measured for lower setpoint ratios and consequently resulted in a less-steep slope.

The extrapolation of the fitted lines in Figure 7a to a 100% setpoint ratio yields an estimate of $H_{\text{max(sp)}}$. The estimated values were larger than the apparent values of H measured from the AFM images. Importantly, the same bubble measured with the same setpoint but a larger amplitude displayed both lower apparent and maximum heights (cf. the series for $A_{0,\text{mean}} = 11.0 \pm 0.1$ nm (red circles) and for $A_{0,\text{mean}} = 90.5 \pm 0.6$ nm (magenta right-facing triangles) in Figure 7a). This observation is in agreement with the schemes in Figure 3 in which $H_{\text{max(sp)}}$ depends on the amplitude. However, when we extrapolated the data for the rest of the bubbles to the 100% setpoint ratio, the estimated maximum apparent heights $H_{\text{max(sp)}}$ did not show a clear dependence on the amplitude (Figure 8b). This was caused by the large error bars, which in turn resulted from the accumulation of the errors in the linear fitting.

The additional evidence of the dependence of the nanobubble height on the setpoint ratio and amplitude comes from the experiment described in the previous section concerning the nanobubbles measured with high setpoint ratios and different amplitudes A_0 . This time, if one focuses on only one bubble, then one can see that the apparent heights measured with different amplitudes A_0 were all smaller than the actual height of this bubble estimated from the linear fit in Figure 5a and that the apparent heights measured for comparable setpoint ratios decrease with increased free amplitudes. This is similar to the behavior shown in Figures 3b and 7a. An example plot of the apparent height versus setpoint ratio for a single bubble (no. 2 in Figure 4a) is shown in Figure S-3 in the Supporting Information.

The apparent contact angles θ_{nano} of the bubbles plotted in Figure 7b increased with decreasing setpoint ratios. The increase was more pronounced for larger amplitudes. In addition, for a single bubble θ_{nano} was larger when measured with the same setpoint ratio but a larger amplitude. All measured values were in the range of 140–180° and hence significantly greater than the macroscopic contact angle of 63 ±

2°. As mentioned in the previous section, such high contact angles decrease by a maximum of 10–15° when they are corrected for the tip size and are hence still much higher than the macroscopic value. Contrary to nanobubbles, nanodroplets display a nanoscopic contact angle close to the macroscopic contact angle.^{56–58} Interestingly, a setpoint dependence of the contact angle similar to the one observed by us (but of course with different values of the contact angle) was observed by Zhang et al.⁵⁷ for decane nanodroplets studied with TM AFM. The apparent contact angle (measured on the decane side) was found to be decreased with a decreased setpoint ratio, and the droplets appeared to be more flat in the topographic images.

Some authors suggested that bubble deformation due to the scanning in TM AFM can serve as an explanation of the unusually high contact angle of surface nanobubbles.^{4,34,35} However, the difference in the nanoscopic contact angles calculated by Zhang et al.³⁵ using the real bubble height estimated from the force–displacement curves and the apparent height measured in the TM AFM height image was only 7° (the bubble width did not change). This value is smaller than the range of variations of the contact angle caused by using a nonzero free amplitude and a setpoint ratio <100%. In our experiments, the smallest value of $\theta_{\text{nano(sp)}}$ that could be estimated from the plot (for a 100% setpoint ratio) does not exceed 135° and is hence $\sim 70^\circ$ higher than the macroscopic value.

The apparent bubble widths W followed the same trend as the apparent heights H and decreased with decreasing setpoint ratios. This change was more pronounced for larger $A_{0\text{mean}}$ (details in Figure S-5 in the Supporting Information). Again, the same bubble measured with comparable setpoint ratios had different apparent widths in the TM AFM height images, depending on the free amplitude. The larger the amplitude, the smaller the bubble appeared.

Contrary to the heights and the widths, the apparent bubble radii of curvature R_c did not display any particular trend in the tested setpoint ratio range. They had values of 100–300 nm, and for a single bubble, they remained approximately equal independent of the amplitude. However, for large amplitudes, data points became more scattered and the error increased. This is likely caused by an inferior fit to the spherical cap model for severely deformed bubbles measured for large amplitudes.

At this point, one may ask how serious the height underestimation caused by the scanning conditions actually is. As an example, the relative change in the bubble height $(H_{\text{max(sp)}} - H)/H_{\text{max(sp)}}$ is plotted as a function of the setpoint ratio for eight bubbles scanned with the amplitude $A_{0\text{mean}} = 4.5 \pm 0.2$ nm (Figure 6a). The small amplitude was chosen to investigate the effect of the setpoint ratio for the most optimal experimental conditions that we could obtain. The results are plotted in Figure 9. Despite the large error bars attributed to the error in the estimation of $H_{\text{max(sp)}}$ from the linear fits, the trend for the data points is clear: the underestimation of the height is as high as 10% even for high setpoint ratios ($\sim 90\%$) and increases with decreasing setpoint ratio by approximately 10% for each 10% decrease in the setpoint ratio. Therefore, it is clear that even for optimal scanning conditions the apparent sizes of the nanobubbles deviate significantly from their actual sizes. Moreover, one must keep in mind that this underestimation becomes even larger for higher amplitudes because the slope $\Delta H/\Delta \text{setpoint ratio}$ increases. Even more evidence showing that TM AFM scanning is an invasive technique comes

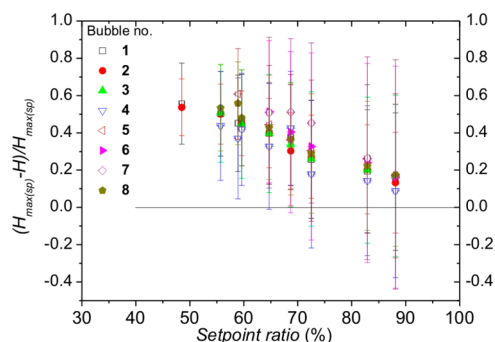


Figure 9. Relative underestimation of the apparent height $(H_{\text{max(sp)}} - H)/H_{\text{max(sp)}}$ as a function of the setpoint ratio for eight nanobubbles marked with numbers in Figure 6a, measured with amplitude $A_{0\text{mean}} = 4.5 \pm 0.2$ nm. $H_{\text{max(sp)}}$ values for the 100% setpoint ratio were estimated from the linear fits of data points similar to those shown in Figure 6a.

from the work of Zhang et al.,⁶² who showed that even scanning with setpoint ratios close to 100% (free amplitude unknown) caused the shape transformation of pancakelike gaseous layers into regular nanobubbles of unchanged volume.

Size Dependence. In this section, the above-mentioned influence of the bubble size on the dependence of the height on the setpoint ratio and the amplitude is addressed for two series of images: (1) for eight bubbles measured with different amplitudes and high setpoint ratios (bubbles 1–8 in Figure 4a) and (2) for eight bubbles measured with the smallest amplitude $A_{0\text{mean}} = 4.5 \pm 0.2$ nm and setpoint ratios varying from 95 to 40% (bubbles 1–8 in Figure 6a). The choice of the small-amplitude conditions ensured the most optimal conditions for measuring nanobubbles and provided the longest series of AFM images. The apparent heights of the bubbles were plotted in Figure 10a,c as functions of the setpoint ratio for different A_0 values and different setpoint ratios, respectively. Although measured in different experiments, bubbles in both series had comparable heights of 10–35 nm. To estimate the maximum height $H_{\text{max}(A_0)}$ and $H_{\text{max(sp)}}$ of the bubbles, as before, we applied a linear fit to the data points and extrapolated the functions to 0 nm free amplitude in Figure 10a and 100% setpoint ratio in Figure 10c. In both cases, the estimated maximum heights served as an indication of the bubbles' actual sizes. As the next step, we plotted calculated slopes $\Delta H/\Delta A_0$ and $\Delta H/\Delta \text{setpoint ratio}$ as functions of the corresponding maximum heights, as shown in Figure 10b,d, respectively. In both plots, the slopes depend on the bubble size and become steeper for larger bubbles. Therefore, we conclude that the apparent height of a nanobubble in the TM AFM height image decreases more drastically for larger bubbles with a decreasing setpoint ratio or with an increasing free amplitude. Hence, the underestimation of the height that is always present for setpoint ratios <100% and free amplitudes > 0 nm also depends on the bubble size and is larger for bigger bubbles. This observation is in line with the reasoning presented by Bhushan et al.⁴² and also confirms the suggestion made by Borkent et al.⁴⁰ that larger bubbles are more easily deformable/penetrable than smaller ones. The difference is caused presumably by the difference in the Laplace pressure for bubbles of different sizes. For the bubbles considered in Figure 10, the Laplace pressure varied from 0.64 MPa for the largest bubble to 1.16 MPa for the smallest one. Clearly, the larger bubbles were softer and the tip

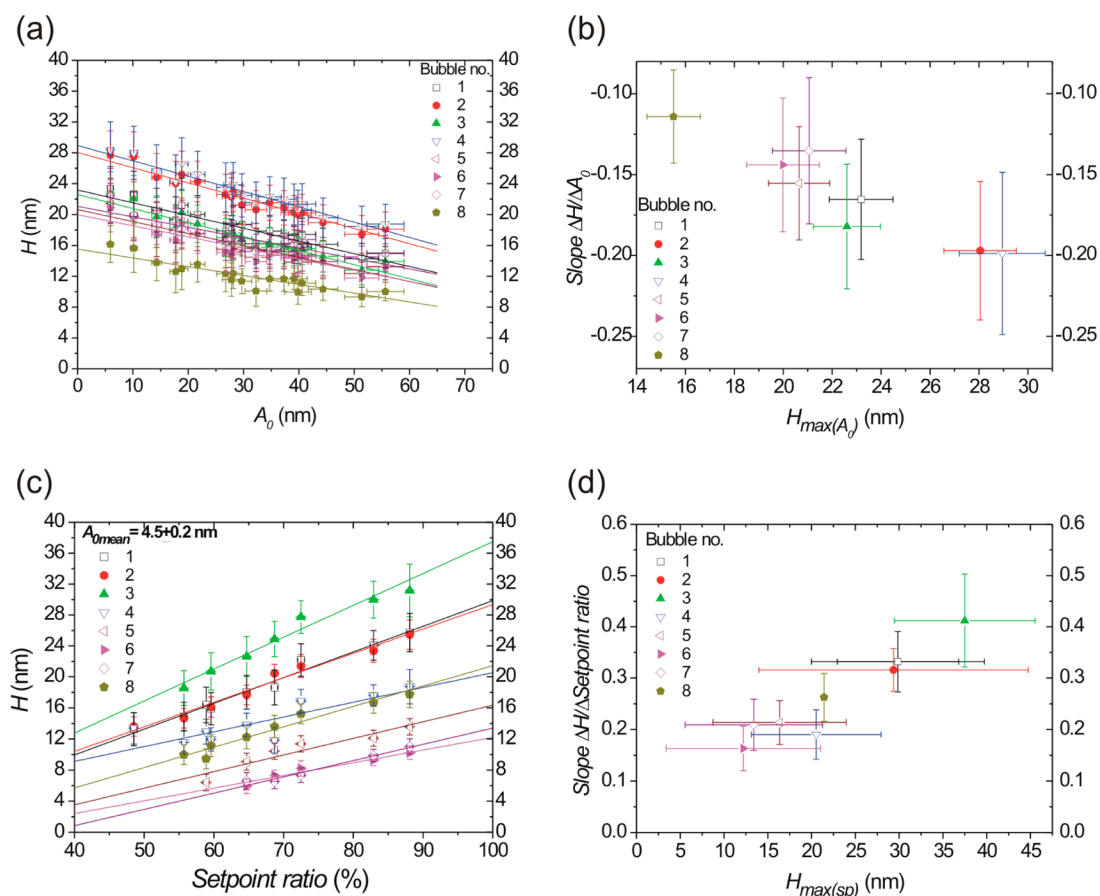


Figure 10. (a) Apparent nanobubble height vs free amplitude A_0 for eight bubbles indicated with numbers in Figure 4a as measured for high setpoint ratios ($>89.5\%$) and (b) corresponding slopes $\Delta H/\Delta A_0$ as a function of the bubble size $H_{\max(A_0)}$ (apparent bubble height extrapolated to $A_0 = 0$ nm). (c) Apparent nanobubble height vs setpoint ratio measured for $A_{0\text{mean}} = 4.5 \pm 0.2$ nm for eight bubbles indicated with numbers in Figure 6a and (d) corresponding slopes $\Delta H/\Delta \text{setpoint ratio}$ as a function of the bubble size $H_{\max(\text{sp})}$ (apparent bubble height extrapolated to 100% setpoint ratio). Both slopes increase with increasing bubble size, and hence the height underestimation is larger for larger bubbles.

deformed them more easily than smaller bubbles. These results indicate that the bubble size (radius of curvature) is an additional parameter that influences the appearance of nanobubbles in TM AFM height images.

CONCLUSIONS

We addressed the influence of the two central intermittent contact (tapping)-mode AFM scanning parameters, namely, the free amplitude of the cantilever oscillations A_0 and the setpoint ratio, on the size and shape of surface nanobubbles on HOPG in water, as seen in TM AFM height images. In general, the apparent height of nanobubbles was found to decrease with decreasing setpoint ratio and with increasing amplitude. When the amplitude was large compared to the bubble height (several tens of nanometers), the AFM tip deformed the bubble to a larger extent, and the same holds for lower setpoint ratios. In turn, if the amplitude was low (a few nanometers), then the bubble size was less affected even for relatively low setpoint ratios. We showed that nanobubbles were stable for a long time and under severe scanning conditions. Independent of the scanning conditions, the apparent size of nanobubbles measured with TM AFM was always underestimated and thus smaller than their actual size and depended both on the amplitude and on the setpoint ratio. In addition, this dependence was shown to be more pronounced for bubbles

with larger radii of curvature and hence smaller Laplace pressure. The actual heights of the bubbles could be estimated from the extrapolation to the 100% setpoint ratio and $A_0 = 0$ nm (ideal noninvasive scanning conditions). Importantly, the change in the apparent bubble shape due to imaging with nonzero amplitude and nonzero setpoint ratios did not explain the discrepancy between nanoscopic and macroscopic contact angles. The apparent nanoscopic contact angles of nanobubbles on HOPG extrapolated to the 100% setpoint ratio and $A_0 = 0$ nm were $>130^\circ$ and hence significantly higher than the macroscopic contact angle in water (63°). Therefore, it is not the AFM scanning itself that causes the high apparent contact angle of nanobubbles. As a final remark, we want to emphasize that (1) maximizing the setpoint ratio and minimizing the free amplitude is crucial to obtaining optimal and reliable results of TM AFM measurements of surface nanobubbles and (2) both parameters must be controlled during the course of the experiment and carefully reported. Only this will enable one to compare the results within a single experiment and, more importantly, with data from different experiments.

ASSOCIATED CONTENT

Supporting Information

Error calculation, AFM data for setpoint fluctuation, amplitudes A_0 used, and various nanobubble widths and R_c data. This

material is available free of charge via the Internet at <http://pubs.acs.org>.

AUTHOR INFORMATION

Corresponding Author

*E-mail: schoenherr@chemie.uni-siegen.de. Tel: (+49) 271/740-2806. Fax (+49) 271/740-2805.

Notes

The authors declare no competing financial interest.

ACKNOWLEDGMENTS

We thank Dr. Bo Song for inspiring discussions and useful comments and gratefully acknowledge the financial support from the Deutsche Forschungsgemeinschaft (DFG grant no. INST 221/87-1 FUGG) and the University of Siegen.

REFERENCES

- Israelachvili, J. N.; Pashley, R. M. The hydrophobic interaction is long range, decaying exponentially with distance. *Nature* **1982**, *300*, 341–342.
- Christenson, H. K.; Claesson, P. M. Cavitation and the interaction between macroscopic hydrophobic surfaces. *Science* **1988**, *239*, 390–392.
- Parker, J. L.; Claesson, P. M.; Attard, P. Bubbles, cavities and the long-ranged attraction between hydrophobic surfaces. *J. Phys. Chem.* **1994**, *98*, 8468–90.
- Ishida, N.; Inoue, T.; Miyahara, M.; Higashitani, K. Nano bubbles on a hydrophobic surface in water observed by tapping-mode atomic force microscopy. *Langmuir* **2000**, *16*, 6377–6380.
- Lou, S. T.; Ouyang, Z. Q.; Zhang, Y.; Li, X. J.; Hu, J.; Li, M. Q.; Yang, F. J. Nanobubbles on solid surface imaged by atomic force microscopy. *J. Vac. Sci. Technol., B* **2000**, *18*, 2573–2575.
- Jensen, T. R.; Jensen, M. O.; Reitzel, N.; Balashev, K.; Peters, G. H.; Kjaer, K.; Bjørnholm, T. Water in contact with extended hydrophobic surfaces: direct evidence of weak dewetting. *Phys. Rev. Lett.* **2003**, *90*, 086101.
- Steitz, R.; Gutberlet, T.; Hauss, T.; Klösgen, B.; Krastev, R.; Schemmel, S.; Simonsen, A. C.; Findenegg, G. H. Nanobubbles and their precursor layer at the interface of water against a hydrophobic substrate. *Langmuir* **2003**, *19*, 2409–2418.
- Miller, J. D.; Hu, Y.; Veeramasuneni, S.; Lu, Y. In-situ detection of butane gas at a hydrophobic silicon surface. *Colloids Surf., A* **1999**, *154*, 137–147.
- Zhang, X. H.; Zhang, X.; Sun, J.; Zhang, Z.; Li, G.; Fang, H.; Xiao, X.; Zeng, X.; Hu, J. Detection of novel gaseous states at the highly oriented pyrolytic graphite-water interface. *Langmuir* **2007**, *23*, 1778–1783.
- Zhang, X. H.; Khan, A.; Ducker, W. A. A nanoscale gas state. *Phys. Rev. Lett.* **2007**, *98*, 136101.
- Zhang, X. H.; Quinn, A.; Ducker, W. A. Nanobubbles at the interface between water and a hydrophobic solid. *Langmuir* **2008**, *24*, 4756–4764.
- Zhang, X. H. Quartz crystal microbalance study of the interfacial nanobubbles. *Phys. Chem. Chem. Phys.* **2008**, *10*, 6842–6848.
- Yang, J.; Duan, J.; Fornasiero, D.; Ralston, J. Kinetics of CO₂ nanobubble formation at the solid/water interface. *Phys. Chem. Chem. Phys.* **2007**, *9*, 6327–6332.
- Karpitschka, S.; Dietrich, E.; Seddon, J. R. T.; Zandvliet, H. J. W.; Lohse, D.; Riegler, H. Nonintrusive optical visualization of surface nanobubbles. *Phys. Rev. Lett.* **2012**, *109*, 066102.
- Mirsaidov, U.; Ohl, C.-D.; Matsudaira, P. A direct observation of nanometer-size void dynamics in an ultra-thin water film. *Soft Matter* **2012**, *8*, 3108–3111.
- Chan, Ch. U.; Ohl, C.-D. Total-internal-reflection-fluorescence microscopy for the study of nanobubble dynamics. *Phys. Rev. Lett.* **2012**, *109*, 174501.
- Seddon, J. R. T.; Kooij, E. S.; Poelsema, B.; Zandvliet, H. J. W.; Lohse, D. Surface bubble nucleation stability. *Phys. Rev. Lett.* **2011**, *106*, 056101.
- Weijs, J. H.; Snoeijer, J. H.; Lohse, D. Formation of surface nanobubbles and the universality of their contact angles: a molecular dynamics approach. *Phys. Rev. Lett.* **2012**, *108*, 104501.
- Brenner, M. P.; Lohse, D. Dynamic equilibrium mechanism for surface nanobubble stabilization. *Phys. Rev. Lett.* **2008**, *101*, 214505.
- Seddon, J. R. T.; Zandvliet, H. J. W.; Lohse, D. Knudsen gas provides nanobubble stability. *Phys. Rev. Lett.* **2011**, *107*, 116101.
- Ducker, W. A. Contact angle and stability of interface nanobubbles. *Langmuir* **2009**, *25*, 8907–8910.
- Das, S. Effect of added salt on performed surface nanobubbles: A scaling estimate. *Phys. Rev. E* **2011**, *84*, 036303.
- Das, S. Effect of impurities in the description of surface nanobubbles: role of nonidealities in the surface layer. *Phys. Rev. E* **2011**, *83*, 066315.
- Das, S.; Snoeijer, J. H.; Lohse, D. Effect of impurities in description of surface nanobubbles. *Phys. Rev. E* **2010**, *82*, 056310.
- van Limbeek, M. A. J.; Seddon, J. R. T. Surface nanobubbles as a function of gas type. *Langmuir* **2011**, *27*, 8694–8699.
- Berkelaar, R. P.; Seddon, J. R. T.; Zandvliet, H. J. W.; Lohse, D. Temperature dependence of surface nanobubbles. *ChemPhysChem* **2012**, *13*, 2213–2217.
- Guan, M.; Guo, W.; Gao, L.; Tang, Y.; Hu, Y.; Dong, Y. Investigation of the temperature difference method for producing nanobubbles and their physical properties. *ChemPhysChem* **2012**, *13*, 2115–2118.
- Mezger, M. A.; Schöder, S. A. B.; Reichert, H. A.; Schröder, H. A.; Okasinski, J. A.; Honkimäki, V. B.; Ralston, J. C.; Bilgram, J. D.; Roth, R. A. E.; Dosch, H. Water and ice in contact with octadecyl-trichlorosilane functionalized surfaces: a high resolution X-ray reflectivity study. *J. Chem. Phys.* **2008**, *128*, 244705.
- Seddon, J. R. T.; Lohse, D. Nanobubbles and micropancakes: gaseous domains on immersed substrates. *J. Phys.: Condens. Matter* **2011**, *23*, 133001.
- Wu, Z.; Chen, H.; Dong, Y.; Mao, H.; Sun, J.; Chen, Sh.; Craig, V. S. J.; Hu, J. Cleaning using nanobubbles: defouling by electrochemical generation of bubbles. *J. Colloid Interface Sci.* **2006**, *328*, 10–14.
- Chen, H.; Mao, H.; Wu, L.; Zhang, J.; Dong, Y.; Wu, Z.; Hu, J. Defouling and cleaning using nanobubbles on stainless steel. *Biofouling* **2009**, *25*, 353–357.
- Liu, G.; Craig, V. S. J. Improved cleaning of hydrophilic protein-coated surfaces using the combination of nanobubbles and SDS. *ACS Appl. Mater Interfaces* **2009**, *1*, 481–487.
- Yang, S.; Dusterwinkel, A. Removal of nanoparticles from plain and patterned surfaces using nanobubbles. *Langmuir* **2011**, *27*, 11430–11435.
- Song, B.; Walczyk, W.; Schönherr, H. Contact angles of surface nanobubbles on mixed self-assembled monolayers with systematically varied macroscopic wettability by atomic force microscopy. *Langmuir* **2011**, *27*, 8223–8232.
- Zhang, X. H.; Maeda, N.; Craig, V. S. J. Physical properties of nanobubbles on hydrophobic surfaces in water and aqueous solutions. *Langmuir* **2006**, *22*, 5025–5035.
- Zhang, X. H.; Li, X. J.; Maeda, N.; Hu, J. Removal of induced nanobubbles from water/graphite interfaces by partial degassing. *Langmuir* **2006**, *22*, 9238–9243.
- Yang, S.; Dammer, S. M.; Bremond, N.; Zandvliet, H. J. W.; Kooij, E. S.; Lohse, D. Characterization of nanobubbles on hydrophobic surfaces in water. *Langmuir* **2007**, *23*, 7072–7077.
- Hampton, M. A.; Donose, B. C.; Nguyen, A. V. Effect of alcohol-water exchange and surface scanning on nanobubbles and the attraction between hydrophobic surfaces. *J. Colloid Interface Sci.* **2008**, *325*, 267–274.
- Zhang, X. H.; Maeda, N.; Hu, J. Thermodynamic stability of interfacial gaseous states. *J. Phys. Chem. B* **2008**, *112*, 13671–13675.

(40) Borkent, B. M.; de Beer, S.; Mugele, F.; Lohse, D. On the shape of surface nanobubbles. *Langmuir* **2010**, *26*, 260–268.

(41) Zhang, L.; Zhang, X.; Zhang, Y.; Hu, J.; Fang, H. The length scales for stable gas nanobubbles at liquid/solid surfaces. *Soft Matter* **2010**, *6*, 4515–4519.

(42) Bhushan, B.; Wang, Y.; Maali, A. Coalescence and movement of nanobubbles studied with tapping mode AFM and tip-bubble interaction analysis. *J. Phys.: Condens. Matter* **2008**, *20*, 485004.

(43) Agrawal, A.; Park, J.; Ryu, D. Y.; Hammond, P. T.; Russell, T. P.; McKinley, G. H. Controlling the location and spatial extent of nanobubbles using hydrophobically nanopatterned surfaces. *Nano Lett.* **2005**, *5*, 1751–1756.

(44) Wang, Y.; Bhushan, B. Boundary slip and nanobubble study in micro/nanofluidics using atomic force microscopy. *Soft Matter* **2010**, *6*, 29–66.

(45) Yang, S.; Kooij, E. S.; Poelsema, B.; Lohse, D.; Zandvliet, H. J. W. Correlation between geometry and nanobubble distribution on HOPG surface. *Europhys. Lett.* **2008**, *81*, 64006.

(46) Wang, Y.; Bhushan, B.; Maali, A. Atomic force microscopy measurement of boundary slip on hydrophilic, hydrophobic and superhydrophobic surfaces. *J. Vac. Sci. Technol., A* **2009**, *27*, 754–760.

(47) Craig, V. S. J. Very small bubbles at surfaces – the nanobubble puzzle. *Soft Matter* **2011**, *7*, 40–48.

(48) Tyrrell, J. W. G.; Attard, P. Images of nanobubbles on hydrophobic surfaces and their interactions. *Phys. Rev. Lett.* **2001**, *87*, 176104.

(49) Tyrrell, J. W. G.; Attard, P. Atomic force microscope images of nanobubbles on a hydrophobic surface and corresponding force-separation data. *Langmuir* **2002**, *18*, 160–167.

(50) Holmberg, M.; Kühle, A.; Garnæs, J.; Mørch, K. A.; Boisen, A. Nanobubble trouble on gold surfaces. *Langmuir* **2003**, *19*, 10510–10513.

(51) van Noort, S. J. T.; van der Werf, K. O.; de Groot, B. G.; van Hulst, N. F.; Greve, J. Height anomalies in tapping mode atomic force microscopy in air caused by adhesion. *Ultramicroscopy* **1997**, *69*, 117–127.

(52) Chen, X.; Davies, M. C.; Roberts, C. J.; Tendler, S. J. B.; Williams, P. M.; Davies, J.; Dawkes, A. C.; Edwards, J. C. Interpretation of tapping mode atomic force microscopy data using amplitude-phase-distance measurements. *Ultramicroscopy* **1998**, *75*, 171–181.

(53) Schönherr, H.; Frank, C. W. Ultrathin films of poly(ethylene oxides) on oxidized silicon. 2. In situ study of crystallization and melting by hot stage AFM. *Macromolecules* **2003**, *36*, 1199–1208.

(54) Vancso, G. J.; Schönherr, H. *Scanning Force Microscopy of Polymers*; Springer: Berlin, 2010.

(55) Morris, V. J.; Kirby, A. R.; Gunning, A. P. *Atomic Force Microscopy for Biologists*; Imperial College Press: London, 2010.

(56) Connell, S. D. A.; Allen, S.; Roberts, C. J.; Davies, J.; Davies, M. C.; Tendler, S. J. B.; Williams, P. M. Investigating the Interfacial properties of single-liquid nanodroplets by atomic force microscopy. *Langmuir* **2002**, *18*, 1719–1728.

(57) Zhang, X.; Ducker, W. Interfacial oil droplets. *Langmuir* **2008**, *24*, 110–115.

(58) Kameda, N.; Sogoshi, N.; Nakabayashi, S. Nitrogen nanobubbles and butane nanodroplets at Si(100). *Surf. Sci.* **2008**, *602*, 1579–1584.

(59) Ebenstein, Y.; Nahum, E.; Banin, U. Tapping mode atomic force microscopy for nanoparticle sizing: tip-sample interaction effects. *Nano Lett.* **2002**, *2*, 945–950.

(60) This reasoning is valid only if the bubble does not deform toward the tip in the early stage of approach and thus appears in the TM AFM image larger than its actual size.

(61) Walczyk, W.; Schön, P.; Schönherr, H. The effect of peak force tapping mode AFM imaging on the apparent shape of surface nanobubbles. *J. Phys.: Condens. Matter* **2012**, submitted for publication.

(62) Zhang, L.; Zhang, X.; Fan, C.; Zhang, Y.; Hu, J. Nanoscale multiple gaseous layers on a hydrophobic surface. *Langmuir* **2009**, *25*, 8860–8864.

Closer Look at the Effect of AFM Imaging Conditions on the Apparent Dimensions of Surface Nanobubbles

Wiktoria Walczyk and Holger Schönherr

Supporting information

Error calculation

The error calculation included:

- 1) AFM measurements – experimental error of 1% for all spatial directions (also 1% of radius of curvature R_c)
- 2) MATLAB fitting procedure – rms error for R_c and consequently for H , W and θ_{nano} .
- 3) Free amplitude – rms amplitude A_0 [V] was measured as a mean value of $n = 30-50$ points from the amplitude-displacement plots:

$$A_o = \frac{1}{n} \sum_{i=1}^n A_{0i}$$

Error in A_0 = mean squared error (standard deviation of the mean) was calculated as

$$\Delta A_0 [V] = \sqrt{\frac{\sum_{i=1}^n (A_{0i} - A_0)^2}{n(n-1)}}$$

The amplitude A_0 [nm] = A_0 [V] * *deflection sensitivity of the cantilever*

Error in A_0 [nm]: dA_0 [nm] = ΔA_0 [V] * *deflection sensitivity of the cantilever*

- 4) Averaging of A_0 [nm] (from two curves for one image – recorded before and after the scan):
 $(dA_{0 \text{ before}} [\text{nm}] + dA_{0 \text{ after}} [\text{nm}])/2$
- 5) Setpoint ratio – error in the setpoint amplitude was equal to ΔA_0 [V]
 Error in setpoint ratio ($A / A_0 * 100\%$) was calculated by the partial derivatives method
 Error of the averaging of setpoint ratio from two curves for one image – analogous as for the free amplitude in point 4)

Constant setpoint ratio, different amplitudes experiment

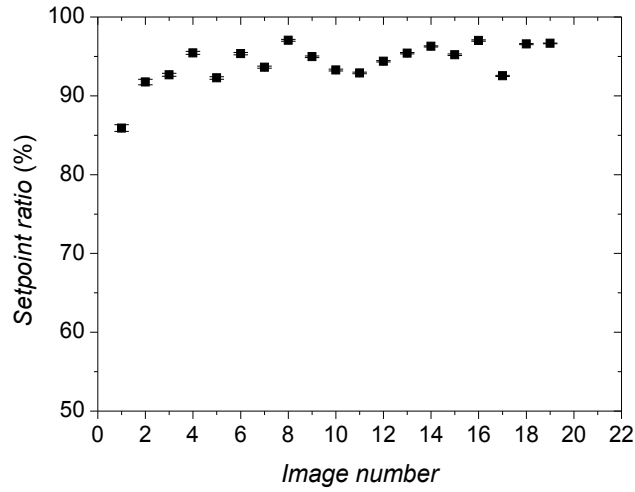


Figure S-1. Setpoint ratios measured for nominally identical AFM settings. The setpoint ratio was kept high ($> 90\%$) for all images beside the first one taken at $A_0 = 5.9$ nm, for which the setpoint ratio 85.9 % was the highest value at which imaging was possible. Variations in the setpoint ratio were caused by the fluctuations of the free amplitude during the imaging.

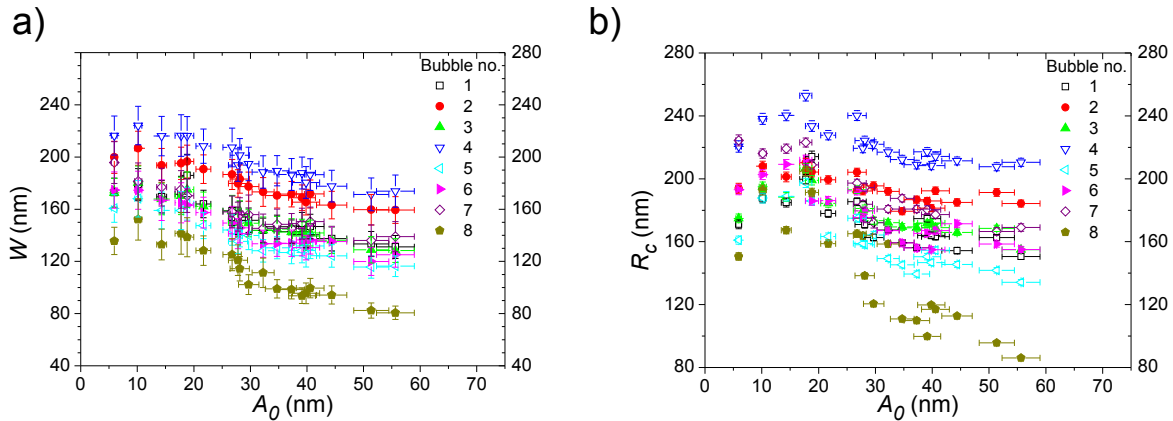


Figure S-2. Apparent nanobubble (a) width W , (b) radius of curvature R_c as function of the free amplitude A_0 measured with setpoint ratios $> 85.9\%$ for eight bubbles marked in Figure 4a. Both parameters decrease with increasing amplitude.

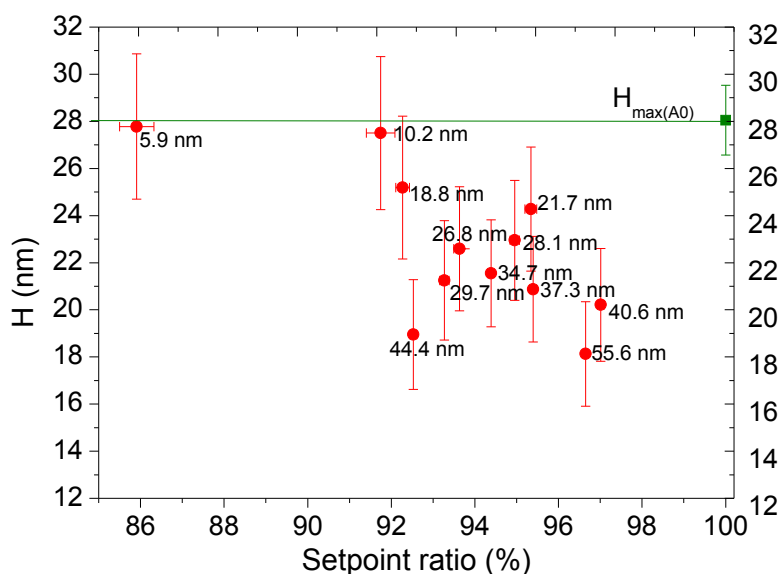


Figure S-3. Apparent nanobubble height as a function of the setpoint ratio measured for different free amplitudes A_0 (see labels) for bubble no. 2 in Figure 4. The height $H_{max(A_0)}$ (green square) was estimated for 100 % setpoint ratio from the linear fit for this bubble as shown in Figure 5a. The $H_{max(A_0)}$ level is marked in the plot with the horizontal line. All other data points marking the individual apparent heights are smaller than $H_{max(A_0)}$ and lay below this line and thus are all smaller than $H_{max(A_0)}$. The apparent heights of the bubble decrease for increasing free amplitude when measured with comparable setpoint ratio. Compare this plot with the plots in Figures 3b and 7a.

Constant amplitudes, different setpoint ratios experiment

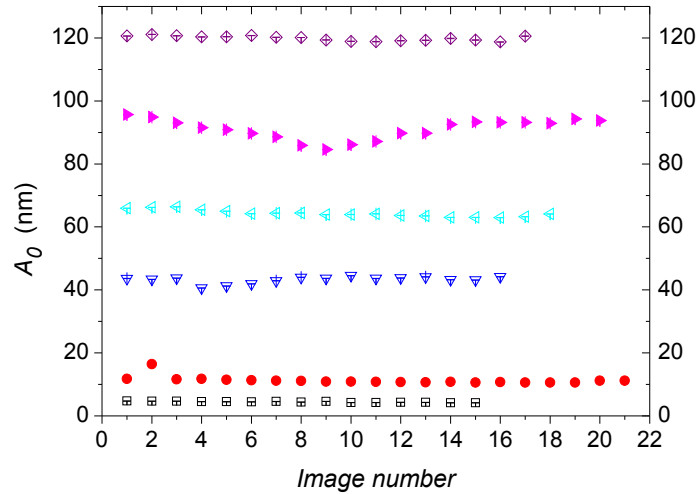


Figure S-4. Free amplitudes A_0 as a function of the image number for six series of measurements marked with different symbols. For each series except $A_{0\text{mean}} = 90.5 \pm 0.6$ nm the amplitude was held constant.

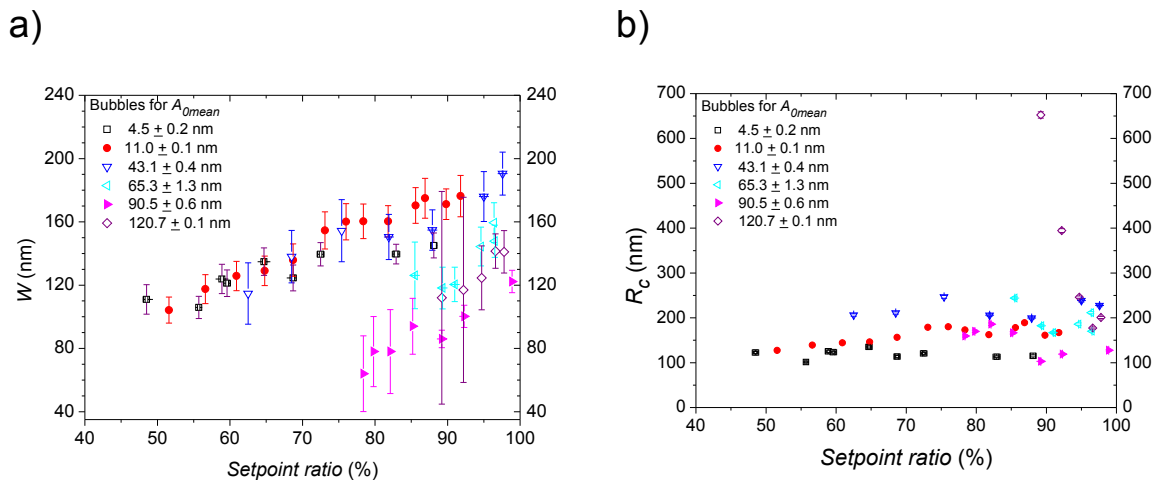


Figure S-5. Apparent nanobubble (a) width W , and (b) radius of curvature R_c as function of the setpoint ratio, measured for three bubbles marked in Figure 6 for six different free amplitudes $A_{0\text{mean}}$. Data for $A_{0\text{mean}} = 11.0 \pm 0.1$ nm and 90.5 ± 0.6 nm concern the same bubble measured during the same experiment, but with different scanning parameters. Similarly, data points for $A_{0\text{mean}} = 43.1 \pm 0.4$ nm, 65.3 ± 1.3 nm and 120.7 ± 0.1 nm refer to the same bubble. The apparent width decreases and the radius of curvature remains constant for decreasing setpoint ratio.

6

The apparent shape of surface nanobubbles in Peak Force Tapping AFM

This chapter expands on the material presented in Chapter 5 and deals with the effect of AFM scanning parameters on the apparent shapes and dimensions of surface nanobubbles. Here, we describe the results of experiments on nanobubbles performed in peak force tapping (PFT) AFM mode, which allows a more precise control of the force exerted by a tip on the sample than TM AFM. We analyzed how the apparent dimensions of nanobubbles in AFM height images depended on the maximum applied force (“peak force”) in PFT AFM. We found that bubbles appeared smaller than their actual sizes even for very small forces and that the magnitude of the size underestimation increased for increased peak force. The strength of this effect depended in addition on the bubble size. The actual nanobubble contact angles, estimated from an extrapolation of the apparent contact angles to zero scanning force conditions, were larger than 140° and larger than the macroscopic contact angle. This result was comparable to the result obtained for nanobubbles in TM AFM.

The chapter consists of the following publication:

The effect of PeakForce tapping mode AFM imaging on the apparent shape of surface nanobubbles

Wiktoria Walczyk, Peter Schön and Holger Schönherr

J. Phys.: Condens. Matter **2013**, *25*, 184005

© IOP Publishing. Reproduced by permission of IOP Publishing. All rights reserved.

Contribution in the article:

Wiktoria Walczyk: AFM measurements, AFM data analysis and calculations;

Dr. Peter Schön: assistance in the PeakForce tapping mode AFM measurements.

The experiment was designed by **Prof. Dr. Holger Schönherr**. Based on discussions and guidance from **Prof. Dr. Holger Schönherr**, the manuscript was drafted by **Wiktoria Walczyk**, and perfected by **Prof. Dr. Holger Schönherr**.

Supporting Information directly follows the article.

The effect of PeakForce tapping mode AFM imaging on the apparent shape of surface nanobubbles

Wiktorja Walczyk¹, Peter M Schön² and Holger Schönherr¹

¹ Physical Chemistry I, University of Siegen, Adolf-Reichwein-Straße 2, D-57076 Siegen, Germany

² Materials Science and Technology of Polymers, MESA⁺ Institute for Nanotechnology, University of Twente, Postbus 217, 7500 AE Enschede, The Netherlands

E-mail: schoenherr@chemie.uni-siegen.de


Received 23 October 2012, in final form 31 January 2013

Published 18 April 2013

Online at stacks.iop.org/JPhysCM/25/184005

Abstract

Until now, TM AFM (tapping mode or intermittent contact mode atomic force microscopy) has been the most often applied direct imaging technique to analyze surface nanobubbles at the solid–aqueous interface. While the presence and number density of nanobubbles can be unequivocally detected and estimated, it remains unclear how much the *a priori* invasive nature of AFM affects the apparent shapes and dimensions of the nanobubbles. To be able to successfully address the unsolved questions in this field, the accurate knowledge of the nanobubbles' dimensions, radii of curvature etc is necessary. In this contribution we present a comparative study of surface nanobubbles on HOPG (highly oriented pyrolytic graphite) in water acquired with (i) TM AFM and (ii) the recently introduced PFT (PeakForce tapping) mode, in which the force exerted on the nanobubbles rather than the amplitude of the resonating cantilever is used as the AFM feedback parameter during imaging. In particular, we analyzed how the apparent size and shape of nanobubbles depend on the maximum applied force in PFT AFM. Even for forces as small as 73 pN, the nanobubbles appeared smaller than their true size, which was estimated from an extrapolation of the bubble height to zero applied force. In addition, the size underestimation was found to be more pronounced for larger bubbles. The extrapolated true nanoscopic contact angles for nanobubbles on HOPG, measured in PFT AFM, ranged from 145° to 175° and were only slightly underestimated by scanning with non-zero forces. This result was comparable to the nanoscopic contact angles of 160°–175° measured using TM AFM in the same set of experiments. Both values disagree, in accordance with the literature, with the macroscopic contact angle of water on HOPG, measured here to be 63° ± 2°.

 Online supplementary data available from stacks.iop.org/JPhysCM/25/184005/mmedia

(Some figures may appear in colour only in the online journal)

1. Introduction

Over two decades ago, the first hypotheses of surface nanobubbles were put forward as a possible explanation for the long-range attractive interaction observed between hydrophobic surfaces immersed in water [1–3]. Since the first observation of spherical cap shaped domains at the solid–aqueous interface by atomic force microscopy

(AFM) [4, 5], many attempts have been made to interrogate these gas-filled cavities. The intrinsic features of nanobubbles, namely their nanoscopic size and their liquid environment, limit the number of techniques that can be applied. Among others, data from neutron reflectivity [6–8], attenuated total internal reflection Fourier transform infrared (FTIR) spectroscopy [9–11], rapid cryofixation [12], x-ray reflectivity [13, 14], quartz crystal microbalance [15, 16], and, very recently,

interference microscopy [17] and total internal reflection fluorescence microscopy [18, 19] have been reported. Compared to these techniques, AFM has become the standard technique for measuring surface nanobubbles [20–35]. This is mainly due to its ability to investigate simultaneously the shape and size of nanoscale objects, even in liquids, with nanometer scale resolution.

Over the years, many important issues of surface nanobubbles have been addressed by AFM, including the methods of nanobubble formation [22, 23], their stability [19, 23–26], the role of the substrate [27–29], the liquid [30, 31], temperature [32, 33], gas type and concentration [34, 35], and the coexistence of nanobubbles with so-called micropancakes [9, 21, 34, 36]. So far, it has been shown that nanobubbles contribute to the attraction between hydrophobic surfaces in water [1–3], rupture of thin liquid films [37, 38], and hydrodynamic slip [29]. Moreover, they play a role in froth-flotation [39], immersion lithography [40], and are a useful tool for cleaning surfaces fouled with proteins or nanoparticles [41, 42].

The large body of AFM data collected over the years has been the starting point for all existing theories and explanations that have been put forward to rationalize the unexpected lifetimes, stability and nanoscopic contact angles of surface nanobubbles (as measured through the condensed phase), which are all much higher than for macroscopic bubbles [23–25]. However, a consensus has not been achieved yet. To be able to successfully address the unsolved questions in this field, an accurate and precise knowledge of the nanobubbles' dimensions, radii of curvature etc is a mandatory prerequisite. The exact information about surface nanobubble properties is crucial because it may enable one to predict the existence of nanobubbles in various systems and to avoid them in those situations when the complete wetting of surfaces by water is essential.

Since AFM is *a priori* an invasive technique and is prone to provide apparently quantitative data even if the measurement conditions preclude this, great care has to be taken to (i) perform AFM experiments adequately and (ii) to analyze the data appropriately. For instance, it is well established that AFM images comprise a convolution of the geometry of the scanning probe and of the sample surface topology. In addition, AFM may under- or overestimate the absolute height of sample surface features, especially in the case of soft structures such as polymers, biological structures, or nanodroplets, but also in the case of solid nanoparticles and nanotubes [43–50].

Most experiments on surface nanobubbles were conducted in TM (tapping mode) AFM [4, 5, 27–29, 32–35, 51–58], which is considered less invasive than CM (contact mode) and therefore more suitable for imaging soft and delicate structures. The pronounced lateral forces involved in the scanning in CM AFM are the main reason that only a few researchers have reported successful imaging of surface nanobubbles in this mode [57, 59]. Some other authors observed the removal of the bubbles from the AFM image during the scanning, presumably caused by the action of the AFM probe [5, 59–61].

However, even for TM AFM several authors reported that the nanobubble height may be underestimated and that the bubbles may deform due to the force exerted by the AFM tip [4, 5, 28, 51, 56, 58, 62]. Our recent experiments fully confirm these earlier observations and show that the apparent sizes and shapes of nanobubbles in TM AFM height images are altered even when scanning with the lowest possible amplitude and highest possible setpoint ratio. The force exerted by the tip alters the apparent nanobubble dimensions to such an extent that it cannot be neglected [62]. The true bubble size in the absence of an applied force can be obtained by extrapolating the AFM height data to conditions of zero amplitude of the cantilever's oscillations and 100% amplitude setpoint ratio. These conditions are physically impossible to obtain during the TM scanning and require laborious experiments that render the mentioned extrapolation feasible.

Obviously, the magnitude of the forces, which play a role in the scanning process, influences the apparent image of the surface nanobubbles. Unfortunately, TM mode does not allow direct control of the force exerted. To address this shortcoming, we present here the first study employing a novel imaging approach to analyze surface nanobubbles by means of AFM, namely PeakForce tapping (PFT) mode. PFT has been recently used to study the properties of very delicate samples such as polymer films, polymer brushes, nanoparticles, various biological structures, nanotubes and liquid films [63–65]. In this mode the force is controlled directly by using the peak force (maximum force exerted) as a feedback parameter. This mode allows one to control and minimize the interactions between the tip and the nanobubble. This, in turn, makes it possible to approach experimentally the dimensions of surface nanobubbles in the absence of forces. The knowledge about the unperturbed size of the bubbles is, as mentioned above, crucial because all derived bubble properties, such as its internal pressure and contact angles rely on the accurate bubble shape and dimensions, which, in turn, is required to explain the observed bubble lifetime and stability.

Thus, here we present the first results of surface nanobubbles analyzed at the HOPG–water interface using PFT mode AFM. In particular, we investigated how the apparent shape of surface nanobubbles in height images depends on the applied force. In addition, we compared PFT and TM AFM data on nanobubbles and analyzed as to how far the bubble dimensions and derived parameters depend on the imaging mode chosen.

2. Experimental details

Nanobubbles were measured in fresh Milli-Q water (from an Advantage A 10 system (Millipore) with a resistivity of $18.0 \text{ M}\Omega \text{ cm}^{-1}$) on freshly cleaved highly oriented pyrolytic graphite (HOPG) (VEECO, grade ZYH) with a water contact angle of $63^\circ \pm 2^\circ$. The contact angle was measured by means of the sessile drop method with an OCA 15plus instrument (Data Physics Instruments GmbH, Filderstadt, Germany) using Milli-Q water.

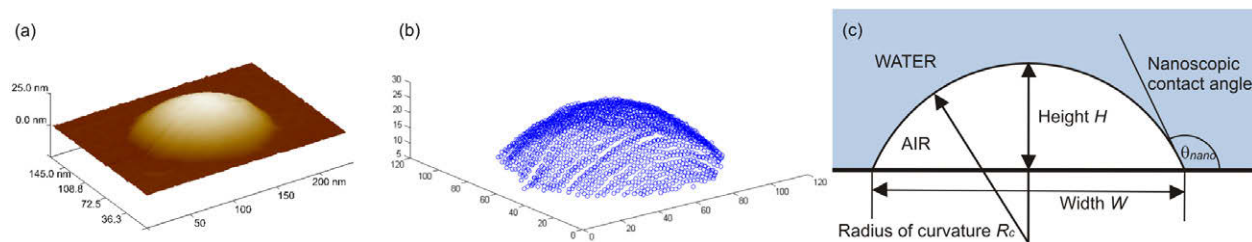


Figure 1. (a) Three-dimensional topographic PFT mode AFM image of a nanobubble. (b) Three-dimensional representation of the nanobubble; each data point represents one pixel in the AFM topographic image. (c) Schematic cross-section of a surface nanobubble. We define the contact angle through the condensed, i.e. the aqueous phase.

PeakForce TM and TM AFM measurements were carried out on a Multimode 8 AFM instrument equipped with a NanoScope V controller, a vertical engage E-scanner and NanoScope version 8.10 software (Bruker AXS, Santa Barbara, CA). An open liquid cell configuration (without rubber O-ring) was used [44]. The liquid cell was rinsed with ethanol (99.9%, Merck KGaA, Darmstadt, Germany), dried in a stream of nitrogen and inserted into the optical head of the microscope. Immediately, a drop of Milli-Q water was put in the groove of the liquid cell and on the cantilever using a sterile disposable plastic syringe and a sterile needle. Another drop was placed directly on the sample and when the optical head was lowered, the two droplets coalesced and formed a meniscus between the liquid cell and the sample [44]. AFM measurements were performed with V-shaped MLTC Si_3N_4 cantilevers (Bruker AXS, Camarillo, CA, spring constant $k_c = 0.7 \pm 0.07 \text{ N m}^{-1}$). The cantilever spring constant was independently calibrated also on an Asylum Research MFP-3D Bio (Asylum Research, Santa Barbara, California). The cantilevers were cleaned prior to the measurements for 60 s by oxygen plasma (Plasma PrepII, SPI Supplies, West Chester, USA). The nanobubbles were scanned first in TM AFM and subsequently in PFT mode AFM without changing the cantilever and the tip. The drive frequency used for imaging in TM AFM was 27 kHz. The free amplitude (in volts) was calculated from amplitude–displacement curves recorded before and after recording of the image, as an average of 50 points. Using the appropriate value of the deflection sensitivity, it was recalculated into a free amplitude in nm. The amplitude setpoint ratio (ratio of the setpoint amplitude value set during the measurements and the free amplitude calculated from the corresponding curve) was calculated as the mean value of two setpoint ratios calculated using curves recorded before and after scanning the image. In PFT mode the sample was oscillating at 2 kHz (off resonance). The peak force tapping amplitude was set to 110 nm and the peak force threshold was varied for each image. The deformation fit region was set on 85%.

The raw PFT and TM height images were processed using a first-order plane fit and a zero-order flattening (with nanobubbles excluded) [44]. The data analysis, the reconstruction of the bubble shape, the fit of the profile obtained to the spherical cap and the calculation of the bubble dimensions, as displayed in figure 1, were performed with

MATLAB software according to the procedure described elsewhere [27]. No tip size correction was applied. Adhesion, deformation and dissipation PFT images were not processed except for a normalization of the data, as mentioned in the text.

3. Results and discussion

3.1. PeakForce TM AFM on surface nanobubbles

PeakForce tapping mode has been recently introduced as an atomic force microscopy imaging mode [64]. Apart from topographic images, it provides maps of stiffness, deformation, adhesion (pull-off force) and dissipation of the sample with nanoscale resolution. In the work presented here, nanobubbles at the solid–liquid interface were investigated by PFT AFM.

In PeakForce tapping mode, the AFM tip is brought intermittently into contact with the sample surface, which minimizes lateral forces, similar to tapping mode. The main differences between the two modes are: (1) the working frequency—in PFT, the tip (or the sample) is oscillated out of resonance at a frequency of 1–10 kHz, which is lower than in standard TM in liquid, and (2) in PFT, the parameter maintained constant in the feedback loop is the peak (maximum) load force, not the amplitude of the cantilever oscillations. Imaging speeds and resolution in both modes are comparable. The amplitude of the cantilever oscillations in PFT may be varied between 0.1 nm and 3 μm peak-to-peak.

In the PFT mode, the cantilever is constantly moving in the surface normal direction and in each oscillation cycle a force–displacement curve is measured. The force is zero (baseline force), which corresponds to the deflection of the free hanging cantilever, when the probe is not contacting the surface. The value of the peak force threshold (the difference between maximum force and baseline force) is held constant by the feedback loop so that at each point (each pixel of the image) the force exerted on the sample is the same. In our experiment, a modulation rate of 2 kHz was used, therefore each curve consisted of 250 points.

The interaction forces measured at different distances between the tip and the sample constitute the shape of the force–distance curve. In the approach phase, when the tip

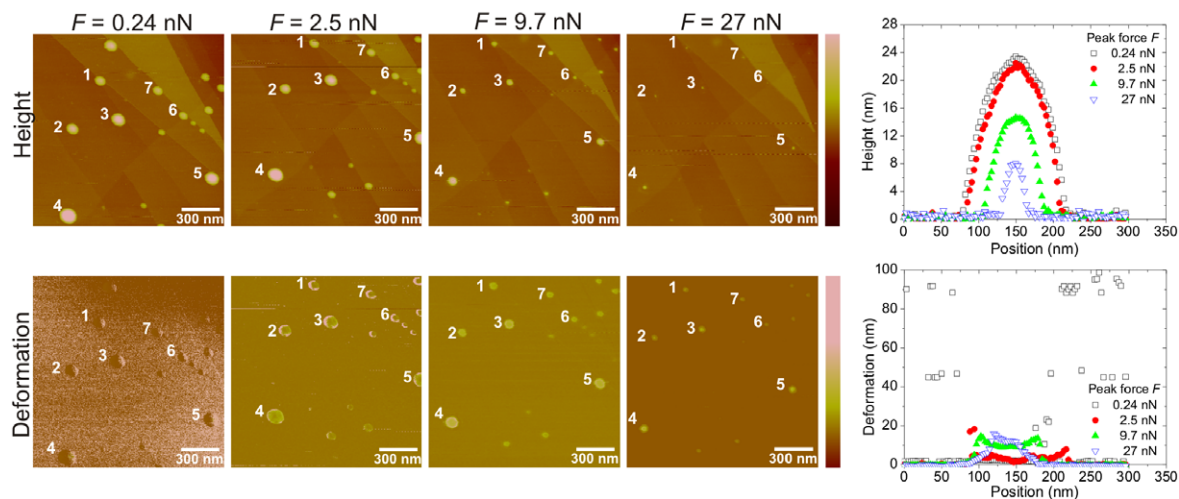


Figure 2. PFT AFM height and deformation images of surface nanobubbles on HOPG in water scanned with peak forces of $F = 0.24, 2.5, 9.7$ and 27 nN. The dimensions of the bubbles marked with numbers were quantitatively analyzed and are plotted in figure 3. Vertical scale of the images: height: 30 nm, deformation: 40 nm. Pixel size: $2.9 \text{ nm} \times 2.9 \text{ nm}$. In the last column, the cross-sections of bubble no. 4 are shown.

is far from the sample, the force is zero (initial zero force line). Close to the sample the tip may experience van der Waals attraction, snapping into contact with the surface and subsequently bending up due to strong repulsive forces until it reaches the peak force threshold (usually repulsive). After that, the tip is retracted and instantly brought back to the baseline (zero) reference force. During the retraction, the cantilever may stick to the sample and bend down due to adhesive forces (the force drops below the zero force line) until it eventually snaps off and returns to the baseline deflection position. Next, the tip is moved to the next position on the sample and the whole procedure is repeated. Different behavior of the cantilever during the approach and the retraction action results in the hysteresis in the force–displacement curve.

In addition to direct measured data i.e. adhesive forces, in PFT, a number of derived data may be calculated from the force–displacement curve. The derived quantities—deformation and dissipation—can be plotted according the x – y position of the AFM tip or can be used in a feedback loop and maintained constant during the measurements. ‘Adhesion’ (pull-off force) data is calculated as the largest negative force detected during the retraction curve. The area enclosed between the approach force curve and the retract force curve accounts for the dissipation of the energy per oscillation cycle. Finally, the maximum deformation of the sample is calculated as the difference in the piezo-displacement between the points of maximum (peak) and zero (baseline) force, measured along the approach curve, and corrected for the change in the deflection of the cantilever. The calculated value includes both elastic and plastic contributions and reaches its maximum at the peak force. There may be some error in the determining the deformation value due to the fact that the tip first contacts the sample at the snap-in point (when the force is attractive before it becomes repulsive) and not at the zero crossing point.

3.2. Dependence of the apparent nanobubble size on the scanning force in PFT AFM

In our experiments, we systematically investigated surface nanobubbles on HOPG in water with PFT AFM. During the course of the experiment, at a fixed location on the sample, an area of $1.5 \times 1.5 \mu\text{m}^2$ was scanned several times with gradually increasing peak force. The peak force threshold was varied between 73 pN and 27 nN, so the forces used in our experiment ranged over several orders of magnitude. The smallest force was limited by the minimum interaction required for the imaging to occur, which was proportional to the cantilever stiffness (a relatively stiff cantilever of $k_c = 0.7 \text{ N m}^{-1}$ was used). The largest force was limited by the apparent disappearance of (most of) the bubbles from the height image. During the scan, the maximum force (measured at the tip apex) exerted at each point of the sample was stable and constant, i.e. it did not exceed a predefined threshold value. However, the effective force varied from zero (close to the moment of first contact) to the threshold value (at the point of acquiring the data).

In order to minimize the interactions between the AFM tip and the sample, the first scan was done with the lowest possible force, i.e. with the force for which any features were visible in the image. After the scanning of each image was completed, we immediately increased the force and continued the scanning. The last image in the series was scanned again with the lowest possible force and was used as a control image in order to verify that the nanobubbles’ positions and sizes did not change due to the scanning. In total, we obtained a series of 10 images. The so-called adhesion, dissipation and deformation images were acquired simultaneously with the height images. Exemplary images no. 2, 4, 6 and 10 from the series, scanned with peak forces 0.24 nN, 2.5 nN, 9.7 nN and 27 nN, respectively are shown in figure 2 (height and deformation) and in figure S1 (available at stacks.iop.org/

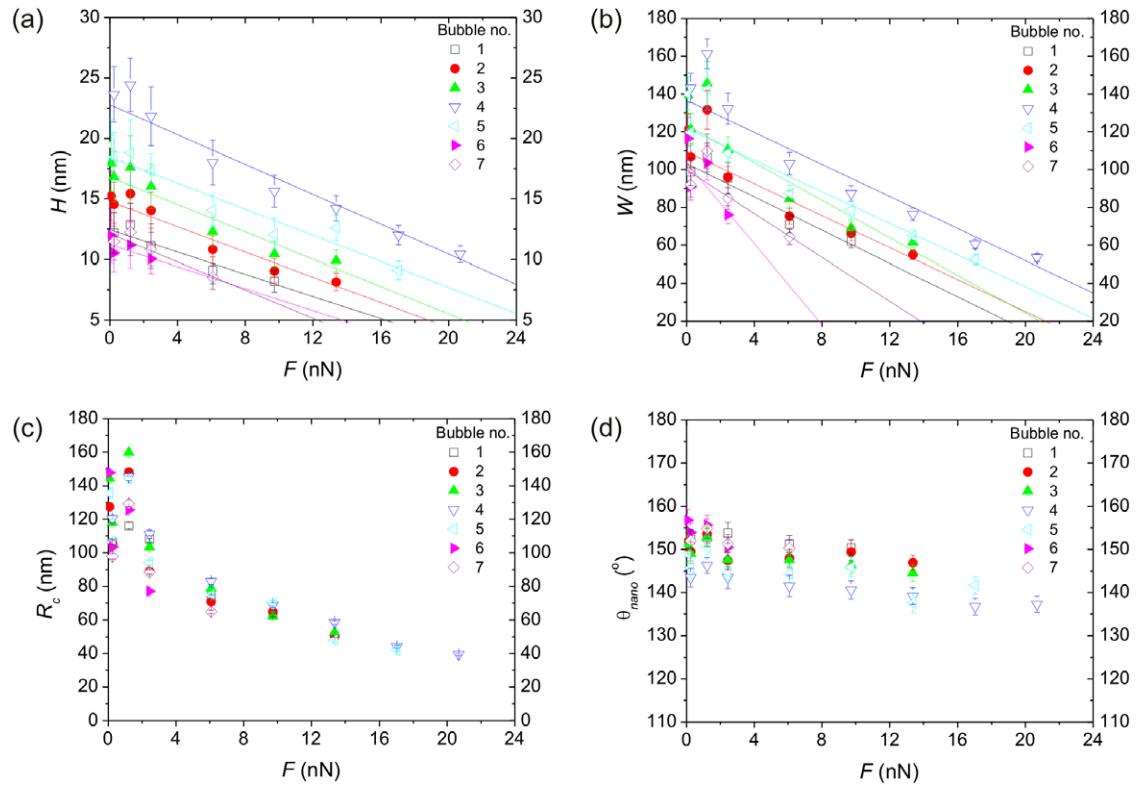


Figure 3. Nanobubble (a) height H , (b) width W , (c) radius of curvature R_c and (d) nanoscopic contact angle θ_{nano} as functions of scanning force measured for seven bubbles marked in figure 2.

JPhysCM/25/184005/mmedia) in the supporting information (adhesion and dissipation). In addition, the cross-sections of one bubble (no. 4) are shown as an example in figure 2. In total the apparent dimensions of seven bubbles (as indicated with numbers in figure 2) were measured. If not noted differently, all data discussed in this paper is apparent, i.e. as stated by the software.

We succeeded in imaging surface nanobubbles on HOPG for a large range of scanning peak forces. In general, nanobubble sizes were observed to decrease with increasing scanning peak force and to gradually disappear from the height images with higher forces. The smallest bubbles completely disappeared already for relatively small scanning forces (compare the height images in figure 2), whereas larger bubbles remained visible and could be measured for forces up to $F = 21$ nN. After resetting the peak force threshold to a small value ($F = 0.73$ nN), all bubbles reappeared in the height image in their initial sizes and locations. Therefore, their disappearance from the height image for high peak forces was only apparent, and was certainly not caused by the physical action of the AFM tip.

Adhesion, deformation and dissipation images corresponding to the topographic images shown in figure 2 and figure S1 in the supporting information (available at stacks.iop.org/JPhysCM/25/184005/mmedia) confirm that the bubbles were extremely stable and did not change their sizes, shape or locations during the whole experiment, even for the highest peak force used. The footprint of the nanobubbles (i.e. the outer perimeter of the three phase line) did not

depend on the peak force in the images of these channels. The substrate below the bubbles that became visible in the height images scanned with high forces did not display any features such as defects, impurities or micropancakes that could cause the bubble pinning. No further evidence for contamination was found in the course of the entire experiment.

For forces $F > 24$ nN all nanobubbles became too small to be measured (i.e. fitted with the spherical cap); therefore, only bubbles from a maximum of 8 of a total of 10 images in the series could be analyzed (for small bubbles the number of images was smaller). The apparent heights H , widths W , radii of curvature R_c and nanoscopic contact angles θ_{nano} of seven bubbles from figure 2 are plotted in figure 3 as a function of the peak force F . The bubbles measured for low forces < 1 nN possessed heights of 10–25 nm, widths of 90–160 nm, and radii of curvature of 100–160 nm. The nanoscopic contact angles θ_{nano} were within the range 140°–160° and were smaller for larger bubbles. The values of $\theta_{\text{nano}} > 140^\circ$ are in agreement with the data obtained so far for nanobubbles on HOPG in water scanned in TM AFM [31, 35, 51, 54, 55, 62]. When the peak force increased from ~ 1.0 to ~ 20 nN, the apparent heights, widths and radii of curvature of all bubbles decreased by approximately 50%. At the same time, the apparent contact angle decreased only by less than 10% (approximately 10° per bubble). Regardless of scanning conditions, all measured values of θ_{nano} were much higher than the macroscopic contact angle of $63^\circ \pm 2^\circ$ for water on HOPG. Although the correction for the tip size was not applied in this work, it has been shown elsewhere that the

correction does not lower the contact angle so much that it will reach the macroscopic value [27].

To within the error, the apparent height and width of seven measured bubbles decreased linearly with increasing peak force. We applied a linear least squares fit to the data points and extrapolated this fit to zero force conditions. These extrapolations provide a good estimation of the unperturbed bubble heights and widths. The values denoted as $H_{\max}(F=0)$ and $W_{\max}(F=0)$ may be treated as the actual and not apparent values and therefore are used as a reference point in our further considerations.

In the second row of figure 2 four deformation images and bubble profiles are shown. For the smallest force the deformation on the bubble was zero and hence comparable to the deformation measured on the substrate. The signal on the substrate (but not on the bubble) was very noisy, and at some points a very large apparent deformation was measured. The HOPG surface is very stiff, and certainly could not become deformed by several tens of nm by the cantilever of much lower stiffness, especially not for very low applied forces. Therefore, we concluded that the noise was an artifact caused presumably by the irregular shape of the force–distance curve obtained for very low peak force threshold. Moreover, as can be seen in the cross-sectional plot, this artificial noise effect was absent on the bubble, and disappeared completely from the signal for larger peak forces used. For intermediate forces (second and third deformation image in figure 2) the deformation on the bubbles increased, while it remained zero at the substrate. Interestingly, the deformations of the bubble centers were smaller than the deformations on their edges, mirroring the spatial variation in pull-off forces (figure S1, supporting information available at stacks.iop.org/JPhysCM/25/184005/mmedia). In the AFM images a higher deformation was visible as a bright ring along the bubble rim. Finally, for large forces (fourth image) the deformation increased even more, but its range became limited only to the bubble centers. This effect was more pronounced for larger bubbles.

The deformation measured on the bubbles was <20 nm and was always smaller than the corresponding maximum apparent bubble height measured. Thus, the bubble was not deformed more (in the vertical direction) than indicated by its apparent physical size. This means that the maximum apparent bubble heights in the images, though underestimated, were close to the actual dimensions of the bubbles. Moreover, the decrease in the apparent bubble height corresponded well to the increase in the deformation signal. In fact, adding up the signals from the height and deformation channels should provide the actual bubble shape. As an example in two dimensions, the profiles of bubble no. 4 constructed as the sum of the height and the deformation signals measured for different peak forces are shown in figure 4. Because of the very noisy deformation signal on the substrate and practically zero deformation on the bubble for the smallest force $F = 0.24$ nN, only the apparent height profile was plotted (black open squares) and used as a reference. For the intermediate forces, the combined bubble profiles fall onto each other and resemble very well the reference bubble profile. Only for very

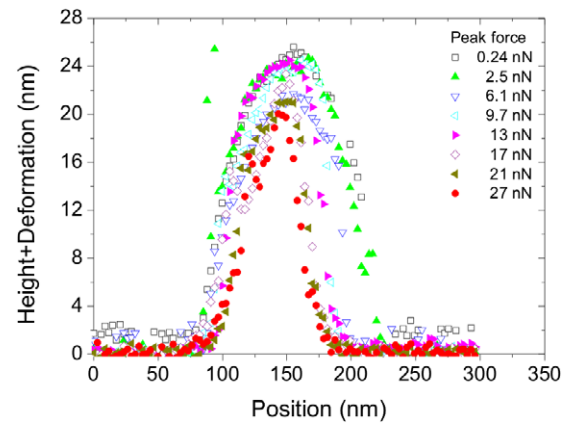


Figure 4. Topographic profiles of bubble no. 4 in figure 2 constructed as the sum of the apparent nanobubble height and the maximum deformation calculated for different scanning peak forces. The sum provides a good estimate of the actual unperturbed bubble height.

large forces $F > 20$ nN does the reconstructed bubble profile become less high and narrower, but it is still significantly higher and wider than the original apparent height profile (compare with figure 2). This may be caused partly by the fact that the deformation fit region in the force–displacement curves was set for 85% and not 100%. In general, by means of adding topography and deformation signals, the bubble shape, especially the height, is reconstructed successfully. For example: for $F = 0.24$ nN the apparent height of the bubble in figure 4 was 23.8 nm and the deformation signal was nearly zero. The same bubble measured with $F = 9.7$ nN displayed a height of 14.9 nm with a deformation of 8.8 nm. The sum of the decrease in the apparent height and the deformation gives the value of 23.7 nm, which is close to the apparent height measured for $F = 0.24$ nN. For larger forces, the sum of the apparent height and deformation decreases, most likely due to a non-linear dependence between the height and the deformation. However, we have shown that, in the regime of low forces, the true bubble height can be estimated by combining the information from height and deformation images.

In addition, in figure S1 in the supporting information (available at stacks.iop.org/JPhysCM/25/184005/mmedia), four force maps of nanobubbles measured for different peak forces are shown together with exemplary cross-sections of bubble no. 4. The signals on the substrate for all profiles were treated as a reference and were brought to the same level. For a small peak force of $F = 0.24$ nN the adhesion signal on the nanobubble was equal to the signal on the substrate. This result indicates a minimum interaction of the tip with the bubble surface for such a small force. With the increase of the peak force, adhesion on the bubble changed and reflected the different contact geometry of tip and bubble. The center of the bubble showed different adhesion compared to the rim.

Finally, energy dissipation images displayed in the second row of figure S1 in the supporting information (available at stacks.iop.org/JPhysCM/25/184005/mmedia) show an increase of energy dissipated on the bubble with increasing

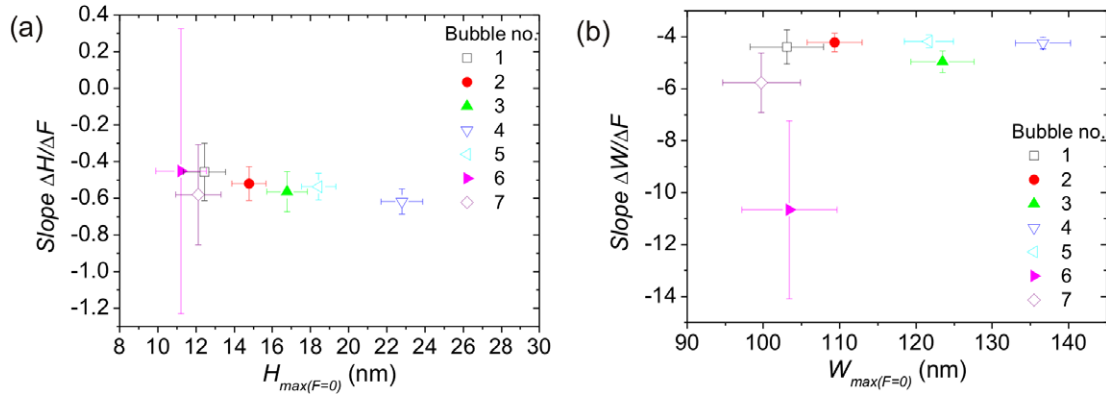


Figure 5. Slopes $\Delta H/\Delta F$ of the linear fits from figure 3(a) as a function of bubble size $H_{\max(F)}$ (apparent bubble height extrapolated to $F = 0$ N), (b) Slopes $\Delta W/\Delta F$ of the linear fits from figure 3(a) as a function of the bubble size $W_{\max(F)}$ (apparent bubble width extrapolated to $F = 0$ N). Both slopes increase with increasing bubble size.

peak force (here shown only qualitatively). This behavior mirrors the spatial variation in adhesion (see figure S2 in the supporting information available at stacks.iop.org/JPhysCM/25/184005/mmedia) and deformation observed on the bubble scanned with larger forces. Initially, for small forces, the dissipation was small and uniform on the bubble and on the substrate. For larger forces, the dissipation increased first more along the edges of the bubbles and later it spread toward the bubble center. Such rings are visible in the dissipation image for bubbles scanned with $F = 27$ nN. Practically zero energy dissipation on the bubbles measured for very small forces indicates that PFT AFM is an almost non-invasive technique for imaging surface nanobubbles, provided that the low threshold force is used.

In order to better interpret the images of the additional channels, we measured the apparent widths of bubble no. 4 as visible in the profiles for height and deformation images in figure 2. The results are collected in table 1. The measured values of the apparent width are compared to the value of $W_{\max(F=0)}$ estimated from the linear fit of the data points in figure 3(b). Strikingly, all apparent widths are similar, except for the ones measured for large forces (this estimation is an approximation with an error of at least a few nm). In addition, the apparent lateral bubble sizes remained unchanged also in the adhesion and dissipation images, regardless of the scanning peak force conditions (see table S1 in the supporting information available at stacks.iop.org/JPhysCM/25/184005/mmedia). Therefore, we conclude that, although nanobubbles change their apparent width in the height images depending on the scanning conditions, in all cases their real widths can be estimated from the adhesion or dissipation images. In addition, the absence of a difference between the maximum bubble width measured from the adhesion images and the apparent width measured from the height image measured for $F = 0.24$ nN confirms practically non-invasive scanning conditions of imaging surface nanobubbles in PFT AFM.

3.3. Dependence of the apparent nanobubble size on the force in PeakForce TM as a function of the bubble size

To determine how the dependence of the apparent nanobubble size on force ($\Delta H/\Delta F$ and $\Delta W/\Delta F$) depends on the applied

Table 1. Apparent widths measured from the cross-sections of nanobubble no. 4 as seen in the height and deformation images shown in figure 2.

Force F (nN)	Height $W_{\text{app}(h)}$ (nm)	Deformation $W_{\text{app}(de)}$ (nm)	$W_{\max(F=0)}$ (nm)
0.24	144	n.a.	138
2.5	133	144	
9.7	88	117	
27	35	114	

imaging force, we analyzed the data plotted in figures 3(a) and (b). As mentioned above, we applied a linear regression to the data sets for $H(F)$ and $W(F)$ for seven bubbles marked with numbers in figure 2. The real (maximum) bubble heights and widths were estimated for $F = 0$ N and denoted as $H_{\max(F=0)}$ and $W_{\max(F=0)}$, respectively. Subsequently, we plotted the slopes $\Delta H/\Delta F$ and $\Delta W/\Delta F$ as functions of the corresponding sizes $H_{\max(F=0)}$ and $W_{\max(F=0)}$. The results are shown in figure 5. For the apparent height, the slopes depend on the bubble size and increase for larger bubbles (become more negative). This means that the bubbles' apparent sizes, as observed in AFM height images, depend on the scanning peak force in a different way for small and for large bubbles. Larger bubbles display steeper slopes, which means that they are deformed to a higher extent by the AFM tip than small bubbles for comparable forces. All height data points in figure 5(a) follow this trend. In the case of the apparent bubble width, the data points in the plot in figure 5(b) are more scattered and show no clear trend. In addition, the point for bubble no. 6 falls out of the data set. This fact, as well as the large vertical error bars for this small bubble, are the consequences of the fitting made for only few points. The apparent bubble sizes were only big enough to be measured in images obtained for the lowest peak forces $F < 4.0$ nN. For larger forces, although visible in the images, the bubble was too small (i.e. consisted of too few pixels) for the spherical cap fitting procedure to work properly.

The tendency of larger bubbles to be deformed more than small bubbles during the scanning (at least in the vertical direction) may be explained by the differences in the Laplace

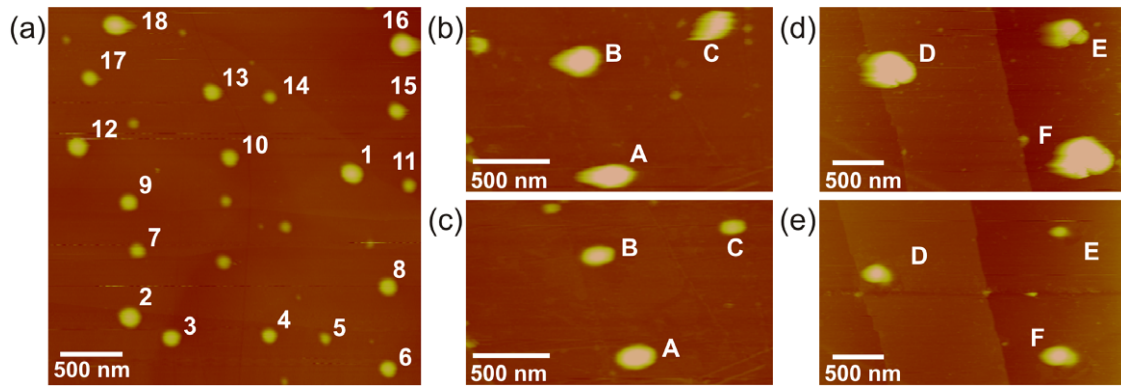


Figure 6. Height images of surface nanobubbles on HOPG in water scanned in (a) TM AFM with free amplitude $A_0 = 35.4$ nm and 96.1% setpoint ratio, (b) TM AFM with free amplitude $A_0 = 3.9$ nm and 88.6% setpoint ratio, (c) PFT AFM with peak force 3.14 nN, (d) TM AFM with free amplitude $A_0 = 6.2$ nm and 93.5% setpoint ratio, (e) PFT AFM with peak force 0.93 nN. The dimensions of bubbles marked with numbers are listed in table S2 in the supporting information (available at stacks.iop.org/JPhysCM/25/184005/mmedia). The dimensions of bubbles marked with letters are plotted in figure 7. The vertical scale of the height images is 30 nm. Pixel sizes in (a), (c), (d) and (e) are $5.9 \text{ nm} \times 5.9 \text{ nm}$ and in (b) are $7.8 \text{ nm} \times 7.8 \text{ nm}$.

pressure (excess pressure inside the bubble) $L_p = 2\gamma/R_c$, with γ being the surface tension. This explanation was already suggested by some authors [54, 55] and confirmed in our previous TM AFM experiments [62]. Here we confirm this result independently in PFT AFM. Table 2 lists the estimated true bubble heights $H_{\max(F=0)}$ and compares them with the slopes $\Delta H/\Delta F$ and Laplace pressure values calculated for $F = 0.24$ nN for all seven measured bubbles. One can see that indeed the slope $\Delta H/\Delta F$ increases (becomes more negative) and the Laplace pressure decreases with the bubble size. In other words, larger bubbles are softer and therefore they are deformed more. The range of pressures measured for those bubbles is from 1.2 MPa for the largest ones to 1.5 MPa for the smallest ones. All these values are much larger than the atmospheric pressure. The different response to the scanning action in PFT AFM observed for the bubbles of different sizes resembles the results obtained by us for bubbles scanned in TM AFM [62]. Large bubbles with lower Laplace pressure were deformed to a more significantly increasing extent than small bubbles with decreasing TM amplitude setpoint ratio. The detailed comparison of nanobubbles measured with PFT and TM AFM is discussed in section 3.4.

3.4. Comparison of PeakForce tapping mode and tapping mode AFM

As stated in section 1, TM has so far been the most common AFM mode to investigate surface nanobubbles. Therefore, in this section, we briefly compare our results obtained on surface nanobubbles on HOPG in PFT with data acquired using TM AFM. In the experiments, scanning in TM mode had been performed before the PFT mode was launched. The same AFM tip was used later in both modes. The free TM amplitude was set to $A_0 = 35.4$ nm and a setpoint ratio of 96.1% was chosen. Figure 6(a) shows a $3 \times 3 \mu\text{m}^2$ TM AFM height image of nanobubbles. Eighteen nanobubbles marked with numbers have been analyzed and their apparent heights, widths, radii of curvature, contact angles and Laplace

Table 2. Estimated maximum height $H_{\max(F=0)}$, slope $\Delta H/\Delta F$, and Laplace pressure L_p calculated for peak force $F = 0.24$ nN, for the seven bubbles measured in PeakForce TM AFM and marked in figure 2. The slope increases and L_p decreases with increasing bubble size.

Bubble no.	$H_{\max(F=0)}$ (nm)	Slope $\Delta H/\Delta F$ (m N^{-1})	L_p (MPa)
6	11.2	-0.45	1.4
7	12.1	-0.58	1.5
1	12.4	-0.45	1.4
2	14.8	-0.52	1.4
5	16.8	-0.53	1.2
3	18.4	-0.56	1.4
4	22.8	-0.61	1.2

pressures are summarized in the supporting information (table S2 available at stacks.iop.org/JPhysCM/25/184005/mmedia). These bubbles are not the same bubbles that were scanned later with PFT AFM, but their sizes were of the same range as the sizes of bubbles discussed in sections 3.2 and 3.3, which allows a comparison. In addition, figures 6(b)–(e) compare three nanobubbles that were subsequently scanned in the two imaging modes. The radii of curvature and contact angles estimated from these images are shown in figure 7 (height and width data is provided in figure S3, supporting information available at stacks.iop.org/JPhysCM/25/184005/mmedia). The non-circular bubble shape in the AFM images represents a well-established effect that results from the non-spherical probe tip shape and poor contact with the sample during scanning with very high setpoint ratios, resulting in poor tracking of the surface contour once the tip has traversed the bubble [44].

The bubbles in figure 6(a) had apparent heights and widths between 7–15 nm and 130–240 nm, respectively. Both height and width are underestimated because of non-zero interaction scanning conditions [62]. The nanoscopic contact angles were in the range of 160° – 170° . A rough correction (without error calculation) for $A_0 = 35.4$ nm yields the

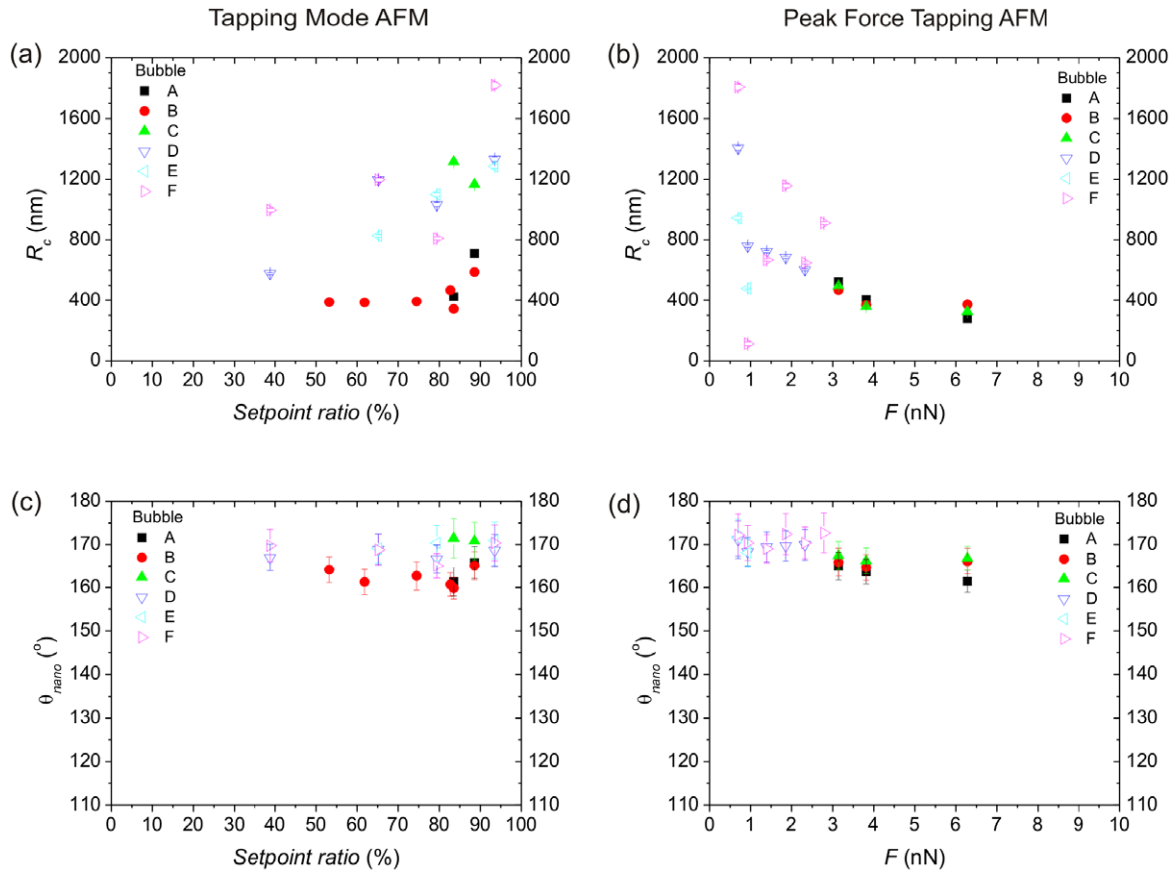


Figure 7. Apparent nanobubble radii of curvature R_c ((a), (b)) and nanoscopic contact angles θ_{nano} ((c), (d)) scanned in TM and in PFT AFM as functions of the setpoint ratio and scanning force, respectively, measured for the six bubbles marked with letters in figure 6.

estimated true heights of the bubbles in the range of 10–18 nm, true widths in the range of 180–280 nm, and true contact angles of 160° – 164° . These TM results are comparable to the results obtained in PFT AFM (*vide supra*) and to the values typically reported for nanobubbles on HOPG in water [31, 35, 51, 54–56, 62]. In addition, we observed that $\theta_{\text{nano app}}$ was smaller for larger bubbles, which is a similar dependence to the one for bubbles in PFT AFM described above.

Very similar data were recorded for the experiment shown in figures 6(b)–(e). These data were also not corrected for the tip size, which results in a negligible error due to the limited height and large contact angle observed. It is clear that, in accordance with a companion TM AFM study, the high nanoscopic contact angle could not be explained by the underestimation of the bubble size due to the scanning with the non-zero amplitude and setpoint ratio less than 100% [62]. In this work, we confirmed that the size underestimation was not caused by using non-zero scanning force. Because we obtained similar results using two independent AFM approaches, we can generalize our statement and say that, although AFM is an invasive measuring technique, it is not the reason for the observed discrepancy between the macroscopic and nanoscopic contact angles.

The high nanoscopic contact angles estimated from the data observed in figure 6 suggest a lower Laplace pressure for those bubbles than for bubbles in some previous studies, where the radii of curvature were significantly smaller. Due

to the relatively small number of nanobubbles analyzed we cannot conclude that the Laplace pressure is as low as $\sim 80 \times 10^3$ Pa with certainty. However, such a low value in conjunction with omnipresent trace contaminations that may adsorb at the gas–liquid interface and hence slow down the gas transport [24, 25] may in parts explain the long nanobubble lifetimes.

The data shown above clearly demonstrate the potential of PeakForce tapping mode AFM in analyzing surface nanobubbles under carefully controlled force conditions. However, the imaging conditions are not *a priori* comparable and more work has to be done to fully understand the nanobubble profiles. For instance, a comparison of the data shown here and independent force–displacement measurements (compare also data in the literature [51, 59, 61, 65]) shows that while the force required to completely compress a typical nanobubble in force–displacement experiments with a vertical scan rate of 1 Hz is on the order of 2 nN. By contrast, nanobubbles apparently withstand >10 nN in PFT (at a frequency of 2 kHz) and presumably similarly high or higher normal forces in TM AFM (at a frequency of ~ 20 kHz). If we may assume that interfacial or nanobubble viscoelasticity effects play a role in the deformation and imaging of nanobubbles, the imaging and hence our understanding of the behavior of nanobubbles can further be improved.

4. Conclusions

We have shown that PeakForce™ AFM is an alternative mode of imaging surface nanobubbles and enables one to assess the apparent dimensions of nanobubbles in a more controlled way than in TM AFM. The apparent size of the bubbles on HOPG, as recorded in AFM height images obtained in PFT, gradually decreased with increased scanning force. The adhesion, deformation and dissipation channels, however, display clearly the unaltered footprint area of the bubble also in those cases, when the height image shows a significantly reduced bubble width. Bubbles with larger radii of curvature, which possess smaller Laplace pressures, show this force-induced apparent size reduction in a more pronounced manner. After resetting the force to a lower value, all bubbles reappeared unchanged in size, shape or location. The actual bubble size can be estimated by extrapolation of the height data to zero force or by combining the information from height, deformation and adhesion images. The apparent decrease in nanobubble size for the increased peak force in PFT was similar to the decrease observed for bubbles scanned in TM AFM with decreased setpoint ratio. Hence, the contact angle discrepancy is independent of the scanning mode and does not originate from a force-induced bubble compression.

Acknowledgments

The authors would like to thank G J Vancso and H Knepe for enlightening discussions and helpful suggestions, C J Padberg for technical support, and gratefully acknowledge financial support from the Deutsche Forschungsgemeinschaft (DFG grant no. INST 221/87-1 FUGG), the University of Siegen, and the MESA⁺ Institute for Nanotechnology.

References

- [1] Israelachvili J N and Pashley R M 1982 The hydrophobic interaction is long range, decaying exponentially with distance *Nature* **300** 341–2
- [2] Christenson H K and Claesson P M 1988 Cavitation and the interaction between macroscopic hydrophobic surfaces *Science* **239** 390–2
- [3] Parker J L, Claesson P M and Attard P 1994 Bubbles, cavities and the long-ranged attraction between hydrophobic surfaces *J. Phys. Chem.* **98** 8468–90
- [4] Ishida N, Inoue T, Miyahara M and Higashitani K 2000 Nano bubbles on a hydrophobic surface in water observed by tapping-mode atomic force microscopy *Langmuir* **16** 6377–80
- [5] Lou S T, Ouyang Z Q, Zhang Y, Li X J, Hu J, Li M Q and Yang F J 2000 Nanobubbles on solid surface imaged by atomic force microscopy *J. Vac. Sci. Technol. B* **18** 2573–5
- [6] Steitz R, Gutberlet T, Hauss T, Klösgen B, Krastev R, Schemmel S, Simonsen A C and Findenegg G H 2003 Nanobubbles and their precursor layer at the interface of water against a hydrophobic substrate *Langmuir* **19** 2409–18
- [7] Doshi D A, Watkins E B, Israelachvili J N and Majewski J 2005 Reduced water density at hydrophobic surfaces: effect of dissolved gases *Proc. Natl Acad. Sci. USA* **102** 9458–62
- [8] Seo Y S and Satija S 2006 No intrinsic depletion layer on a polystyrene thin film at a water interface *Langmuir* **22** 7113–6
- [9] Zhang X H, Zhang X, Sun J, Zhang Z, Li G, Fang H, Xiao X, Zeng X and Hu J 2007 Detection of novel gaseous states at the highly oriented pyrolytic graphite–water interface *Langmuir* **23** 1778–83
- [10] Zhang X H, Khan A and Ducker W A 2007 A nanoscale gas state *Phys. Rev. Lett.* **98** 136101
- [11] Zhang X H, Quinn A and Ducker W A 2008 Nanobubbles at the interface between water and a hydrophobic solid *Langmuir* **24** 4756–64
- [12] Switkes M and Ruberti J W 2004 Rapid cryofixation/freeze fracture for the study of nanobubbles at solid–liquid interfaces *Appl. Phys. Lett.* **84** 4759–61
- [13] Jensen T R, Jensen M O, Reitzel N, Balashev K, Peters G H, Kjaer K and Bjørnholm T 2003 Water in contact with extended hydrophobic surfaces: direct evidence of weak dewetting *Phys. Rev. Lett.* **90** 086101
- [14] Mezger M A, Schöder S A B, Reichert H A, Schröder H A, Okasinski J A, Honkimäki V B, Ralston J C, Bilgram J D, Roth R A E and Dösch H 2008 Water and ice in contact with octadecyl-trichlorosilane functionalized surfaces: a high resolution x-ray reflectivity study *J. Chem. Phys.* **128** 244705
- [15] Zhang X H 2008 Quartz crystal microbalance study of the interfacial nanobubbles *Phys. Chem. Chem. Phys.* **10** 6842–8
- [16] Yang J, Duan J, Fornasiero D and Ralston J 2007 Kinetics of CO₂ nanobubble formation at the solid/water interface *Phys. Chem. Chem. Phys.* **9** 6327–32
- [17] Karpitschka S, Dietrich E, Seddon J R T, Zandvliet H J W, Lohse D and Riegler H 2012 Nonintrusive optical visualization of surface nanobubbles *Phys. Rev. Lett.* **109** 066102
- [18] Mirsaidov U, Ohl C-D and Matsudaira P 2012 A direct observation of nanometer-size void dynamics in an ultra-thin water film *Soft Matter* **8** 3108–11
- [19] Chan C U and Ohl C-D 2012 Total-internal-reflection-fluorescence microscopy for the study of nanobubble dynamics *Phys. Rev. Lett.* **109** 174501
- [20] Craig V S J 2011 Very small bubbles at surfaces—the nanobubble puzzle *Soft Matter* **7** 40–8
- [21] Seddon J R T and Lohse D 2011 Nanobubbles and micropancakes: gaseous domains on immersed substrates *J. Phys.: Condens. Matter* **23** 133001
- [22] Seddon J R T, Kooij E S, Poelsema B, Zandvliet H J W and Lohse D 2011 Surface bubble nucleation stability *Phys. Rev. Lett.* **106** 056101
- [23] Weijs J H, Snoeijer J H and Lohse D 2012 Formation of surface nanobubbles and the universality of their contact angles: a molecular dynamics approach *Phys. Rev. Lett.* **108** 104501
- [24] Ducker W A 2009 Contact angle and stability of interface nanobubbles *Langmuir* **25** 8907–10
- [25] Brenner M P and Lohse D 2008 Dynamic equilibrium mechanism for surface nanobubble stabilization *Phys. Rev. Lett.* **101** 214505
- [26] Seddon J R T, Zandvliet H J W and Lohse D 2011 Knudsen gas provides nanobubble stability *Phys. Rev. Lett.* **107** 116101
- [27] Song B, Walczyk W and Schönherr H 2011 Contact angles of surface nanobubbles on mixed self-assembled monolayers with systematically varied macroscopic wettability by atomic force microscopy *Langmuir* **27** 8223–32
- [28] Yang S, Kooij E S, Poelsema B, Lohse D and Zandvliet H J W 2008 Correlation between geometry and nanobubble distribution on HOPG surface *Europhys. Lett.* **81** 64006

- [29] Wang Y, Bhushan B and Maali A 2009 Atomic force microscopy measurement of boundary slip on hydrophilic, hydrophobic and superhydrophobic surfaces *J. Vac. Sci. Technol. A* **27** 754–60
- [30] Yang S, Dammer S M, Bremond N, Zandvliet H J W, Kooij E S and Lhose D 2007 Characterization of nanobubbles on hydrophobic surfaces in water *Langmuir* **23** 7072–7
- [31] Zhang X, Uddin M H, Yang H, Toikka G, Ducker W and Maeda N 2012 Effects of surfactants on the formation and the stability of interfacial nanobubbles *Langmuir* **28** 10471–7
- [32] Berkelaar R P, Seddon J R T, Zandvliet H J W and Lohse D 2012 Temperature dependence of surface nanobubbles *ChemPhysChem* **13** 2213–7
- [33] Guan M, Guo W, Gao L, Tang Y, Hu Y and Dong Y 2012 Investigation of the temperature difference method for producing nanobubbles and their physical properties *ChemPhysChem* **13** 2115–8
- [34] van Limbeek M A J and Seddon J R T 2011 Surface nanobubbles as a function of gas type *Langmuir* **27** 8694–9
- [35] Zhang X H, Li X J, Maeda N and Hu J 2006 Removal of induced nanobubbles from water/graphite interfaces by partial degassing *Langmuir* **22** 9238–43
- [36] Zhang L, Zhang X, Fan C, Zhang Y and Hu J 2009 Nanoscale multiple gaseous layers on a hydrophobic surface *Langmuir* **25** 8860–4
- [37] Stockelhuber K W, Radoev B, Wenger A and Schulze H J 2004 Rupture of wetting films caused by nanobubbles *Langmuir* **20** 164–8
- [38] Wu Z, Zhang X, Zhang X, Sun J, Dong Y and Hu J 2007 *In situ* AFM observation of BSA adsorption on HOPG with nanobubble *Chin. Sci. Bull.* **52** 1913–9
- [39] Schubert H 2005 Nanobubbles, hydrophobic effect, heterocoagulation and hydrodynamics in flotation *Int. J. Miner. Process.* **78** 11–21
- [40] Wei Y, Brandl S and Goodwin F 2008 Formation mechanism of 193nm immersion defects and defect reduction strategies *Advances in Resist Materials and Processing Technology XXV; Proc. SPIE* **6923** 69231Y
- [41] Liu G and Craig V S J 2009 Improved cleaning of hydrophilic protein-coated surfaces using the combination of nanobubbles and SDS *ACS Appl. Mater. Interfaces* **1** 481–7
- [42] Yang S and Dusterwinkel A 2011 Removal of nanoparticles from plain and patterned surfaces using nanobubbles *Langmuir* **27** 11430–5
- [43] Schönherr H and Frank C W 2003 Ultrathin films of poly(ethylene oxides) on oxidized silicon. 2. *In situ* study of crystallization and melting by hot stage AFM *Macromolecules* **36** 1199–208
- [44] Schönherr H and Vancso G J 2010 *Scanning Force Microscopy of Polymers* (Berlin: Springer)
- [45] Morris V J, Kirby A R and Gunning A P 2010 *Atomic Force Microscopy for Biologists* (London: Imperial College Press)
- [46] Connell S D A, Allen S, Roberts C J, Davies J, Davies M C, Tendler S J B and Williams P M 2002 Investigating the interfacial properties of single-liquid nanodroplets by atomic force microscopy *Langmuir* **18** 1719–28
- [47] Zhang X and Ducker W 2008 Interfacial oil droplets *Langmuir* **24** 110–5
- [48] Kameda N, Sogoshi N and Nakabayashi S 2008 Nitrogen nanobubbles and butane nanodroplets at Si(100) *Surf. Sci.* **602** 1579–84
- [49] Ebenstein Y, Nahum E and Banin U 2002 Tapping mode atomic force microscopy for nanoparticle sizing: tip–sample interaction effects *Nano Lett.* **2** 945–50
- [50] Alizadegan R, Liao A D, Xiong F, Pop E and Hsia K J 2012 Effects of tip–nanotube interactions on atomic force microscopy imaging of carbon nanotubes *Nano Res.* **5** 235–47
- [51] Zhang X H, Maeda N and Craig V S J 2006 Physical properties of nanobubbles on hydrophobic surfaces in water and aqueous solutions *Langmuir* **22** 5025–35
- [52] Hampton M A, Donose B C and Nguyen A V 2008 Effect of alcohol–water exchange and surface scanning on nanobubbles and the attraction between hydrophobic surfaces *J. Colloid Interface Sci.* **325** 267–74
- [53] Zhang X H, Maeda N and Hu J 2008 Thermodynamic stability of interfacial gaseous states *J. Phys. Chem. B* **112** 13671–5
- [54] Borkent B M, de Beer S, Mugele F and Lohse D 2010 On the shape of surface nanobubbles *Langmuir* **26** 260–8
- [55] Zhang L, Zhang X, Zhang Y, Hu J and Fang H 2010 The length scales for stable gas nanobubbles at liquid/solid surfaces *Soft Matter* **6** 4515–9
- [56] Bhushan B, Wang Y and Maali A 2008 Coalescence and movement of nanobubbles studied with tapping mode AFM and tip–bubble interaction analysis *J. Phys.: Condens. Matter* **20** 485004
- [57] Agrawal A, Park J, Ryu D Y, Hammond P T, Russell T P and McKinley G H 2005 Controlling the location and spatial extent of nanobubbles using hydrophobically nanopatterned surfaces *Nano Lett.* **5** 1751–6
- [58] Wang Y and Bhushan B 2010 Boundary slip and nanobubble study in micro/nanofluidics using atomic force microscopy *Soft Matter* **6** 29–66
- [59] Holmberg M, Kühle A, Garnæs J, Mørch K A and Boisen A 2003 Nanobubble trouble on gold surfaces *Langmuir* **19** 10510–3
- [60] Tyrrell J W G and Attard P 2001 Images of nanobubbles on hydrophobic surfaces and their interactions *Phys. Rev. Lett.* **87** 176104
- [61] Tyrrell J W G and Attard P 2002 Atomic force microscope images of nanobubbles on a hydrophobic surface and corresponding force-separation data *Langmuir* **18** 160–7
- [62] Walczyk W and Schönherr H 2013 A closer look at the effect of AFM imaging conditions on the apparent dimensions of surface nanobubbles *Langmuir* **29** 620–32
- [63] Schön P M, Bagdi K, Molnar K, Markus P, Pukanszky B and Vancso G J 2011 Quantitative mapping of elastic moduli at the nanoscale in phase separated polyurethanes by AFM *Eur. Polym. J.* **47** 692–8
- [64] Shi J, Hu Y, Hu S, Ma J and Su C 2011 Method and apparatus of using peak force tapping mode to measure physical properties of a sample *Patent* 306867
- [65] Hansson P M, Swerin A, Schoelkopf J, Gane P A C and Thormann E 2012 Influence of surface topography on the interactions between nanostructured hydrophobic surfaces *Langmuir* **28** 8026–34

The effect of PeakForce Tapping Mode AFM imaging on the apparent shape of surface nanobubbles

Wiktorja Walczyk, Peter Schön, and Holger Schönherr

Supporting information

1) Dependence of the apparent nanobubble size on the scanning force in PFT AFM

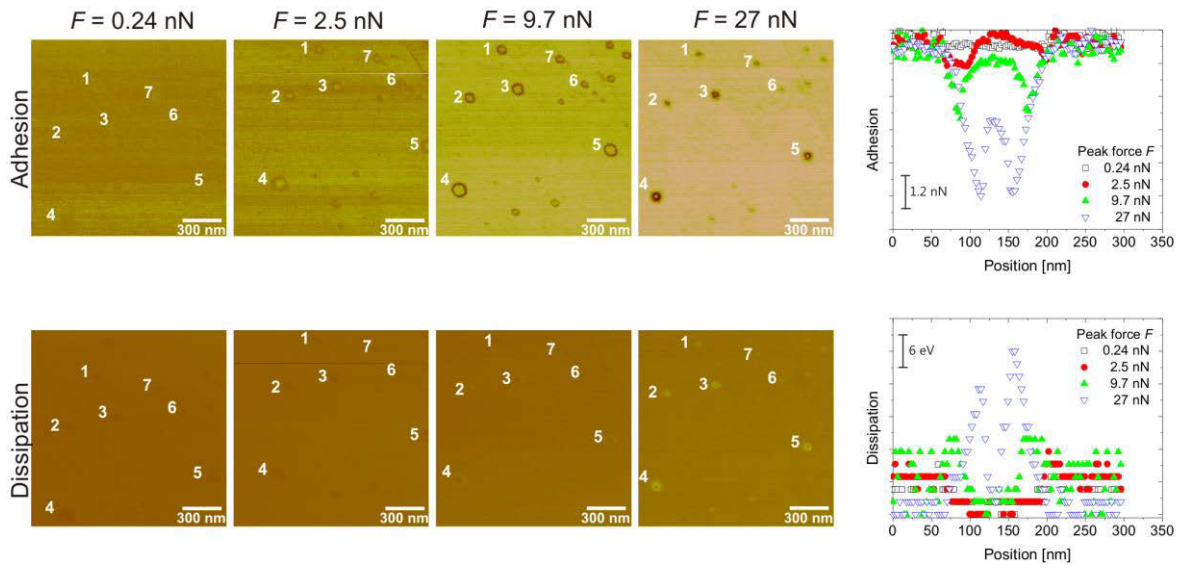


Figure S-1: PeakForce Tapping AFM adhesion and dissipation images of surface nanobubbles on HOPG in water scanned with peak forces $F = 0.24$ nN, $F = 2.5$ nN, $F = 9.7$ nN and $F = 27$ nN. The dimensions of the bubbles marked with number were quantitatively analyzed and are plotted in figure 4. Vertical scale of the images: adhesion: 9.7 nN, dissipation: 300 eV. Pixel size: 2.9 nm \times 2.9 nm. In the last column, the cross-sections of bubble no. 4 are shown. The functions were normalized to the value of the parameter measured for the bare substrate

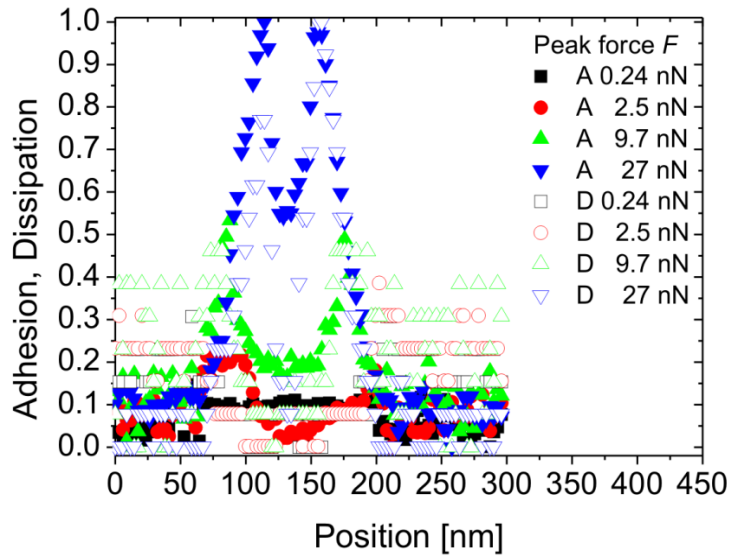


Figure S-2: Normalized profiles of adhesion (A, solid symbols) and dissipation (D, open symbols) on bubble no. 4 in figure S-1 plotted together for different scanning peak forces. The profiles on the bubble overlap. One unit for the adhesion is equal to 0.58 nN and for the dissipation is 3 eV.

Table S-1. Apparent widths measured from the cross-sections of nanobubble no. 4 as seen in the adhesion and dissipation images shown in figure S-1.

Force F (nN)	Adhesion $W_{app(ad)}$ (nm)	Dissipation $W_{app(di)}$ (nm)
0.24	144	150
2.5	144	147
9.7	138	144
27	150	147

2) Comparison of PeakForce Tapping Mode and Tapping Mode AFM

Table S-2. Apparent heights, widths, radii of curvature, contact angles of eighteen nanobubbles measured in TM AFM and marked with numbers in figure 7.

#	H_{app} [nm]	W_{app} [nm]	$R_{c\ app}$ [nm]	$\theta_{nano\ app}$ [°]	L_p [MPa]
1	13.6	203	286	165	0.51
2	12.1	203	433	167	0.34
3	11.0	170	334	165	0.44
4	10.3	152	286	165	0.51
5	7.45	161	437	169	0.33
6	11.3	158	282	164	0.52
7	8.51	169	423	169	0.34
8	10.3	183	411	167	0.35
9	10.0	170	365	167	0.40
10	9.26	178	460	168	0.32
11	7.82	129	270	166	0.54
12	11.4	194	415	167	0.35
13	10.3	179	398	167	0.37
14	7.75	141	324	167	0.45
15	10.4	155	293	165	0.50
16	14.7	229	454	165	0.32
17	9.58	163	351	167	0.41
18	13.7	241	537	167	0.27

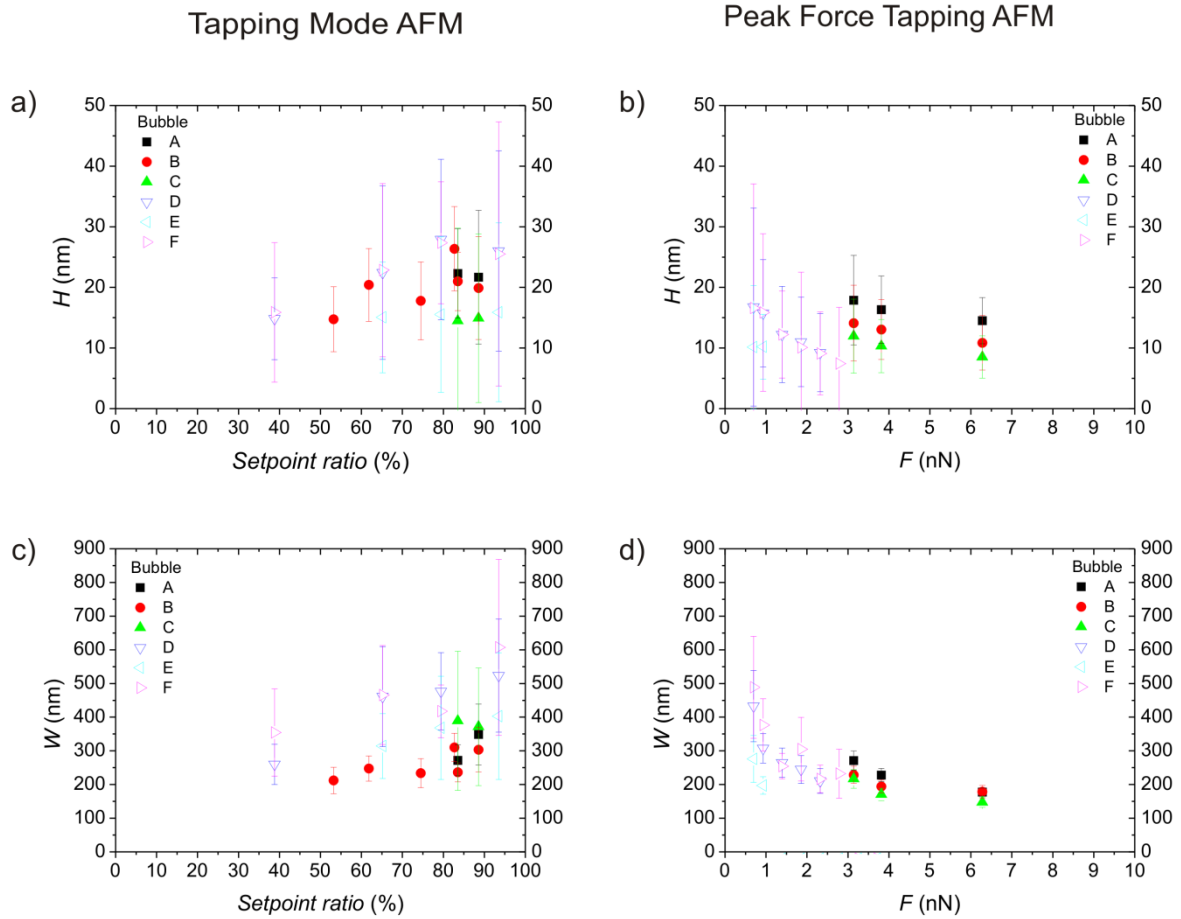


Figure S-3. Apparent nanobubble (a, b) height H , (c, d) width W scanned in TM and in PFT AFM as functions of the setpoint ratio and scanning force, respectively, measured for six bubbles marked with letters in figure 7.

7

The interaction between AFM tips and surface nanobubbles

Despite much AFM research done on surface nanobubbles, the mechanism of AFM tip-nanobubble interaction remained unclear until recently. In this chapter, we address this issue by comparing results of combined tapping mode and force volume AFM experiments with the predictions of two theoretical models of tip-bubble interaction – the capillary force model and the dynamic interaction model. We found that the bubbles interacted differently with hydrophilic and hydrophobic AFM tips and that the interaction resulted in quasi-linear deformation of the bubble surface depending on the tip properties. Based on a simple model, we calculated the nanobubble stiffness and found that it was comparable with the surface tension of water and sensitive to the presence of contamination. Our findings set strict rules concerning the parameters and cleanliness of the AFM cantilevers and tips used to image surface nanobubbles accurately with AFM.

The chapter consists of the following publication:

Characterization of the Interaction between AFM Tips and Surface Nanobubbles

Wiktoria Walczyk and Holger Schönherr

Langmuir **2014**, *30*, 7112–7126.

Reprinted with permission. Copyright (2014) American Chemical Society.

Supporting Information directly follows the article.

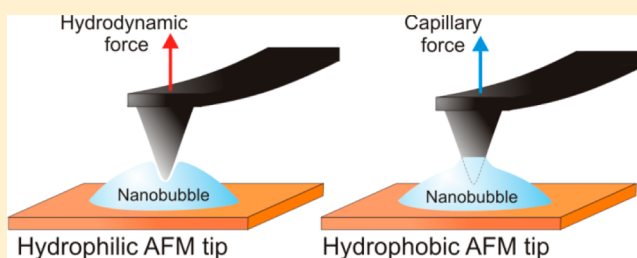
Characterization of the Interaction between AFM Tips and Surface Nanobubbles

Wiktoria Walczyk and Holger Schönherr*

Physical Chemistry I, Department of Chemistry and Biology, University of Siegen, Adolf-Reichwein-Str. 2, 57076 Siegen, Germany

S Supporting Information

ABSTRACT: While the presence of gaseous enclosures observed at various solid–water interfaces, the so-called “surface nanobubbles”, has been confirmed by many groups in recent years, their formation, properties, and stability have not been convincingly and exhaustively explained. Here we report on an atomic force microscopy (AFM) study of argon nanobubbles on highly oriented pyrolytic graphite (HOPG) in water to elucidate the properties of nanobubble surfaces and the mechanism of AFM tip–nanobubble interaction. In particular, the deformation of the nanobubble–water interface by the AFM tip and the question whether the AFM tip penetrates the nanobubble during scanning were addressed by this combined intermittent contact (tapping) mode and force volume AFM study. We found that the stiffness of nanobubbles was smaller than the cantilever spring constant and comparable with the surface tension of water. The interaction with the AFM tip resulted in severe quasi-linear deformation of the bubbles; however, in the case of tip–bubble attraction, the interface deformed toward the tip. We tested two models of tip–bubble interaction, namely, the capillary force and the dynamic interaction model, and found, depending on the tip properties, good agreement with experimental data. The results showed that the tip–bubble interaction strength and the magnitude of the bubble deformation depend strongly on tip and bubble geometry and on tip and substrate material, and are very sensitive to the presence of contaminations that alter the interfacial tension. In particular, nanobubbles interacted differently with hydrophilic and hydrophobic AFM tips, which resulted in qualitatively and quantitatively different force curves measured on the bubbles in the experiments. To minimize bubble deformation and obtain reliable AFM results, nanobubbles must be measured with a sharp hydrophilic tip and with a cantilever having a very low spring constant in a contamination-free system.



INTRODUCTION

Surface nanobubbles, which are small gas-filled structures that appear on surfaces immersed in water, offer an interesting system to investigate the interaction between solids, liquids, and gases on the nanoscale. It has been shown that nanobubbles contribute to the attraction between hydrophobic surfaces in water,^{1–3} rupture of thin liquid films,⁴ and hydrodynamic slip.⁵ Moreover, they are a useful tool for froth-flotation⁶ and cleaning surfaces fouled with proteins or nanoparticles.⁷ However, despite much research done, several nanobubble properties remain unknown or undefined, which has hampered a complete understanding: Their estimated internal pressure is anomalously high, their apparent profile is extremely flat, and the nanoscopic contact angles, measured through the condensed phase, are (much) larger than macroscopic contact angles.^{8–10} Moreover, there is no consensus within the scientific community in support of one particular stability theory. Among the most considered theories are the ones that emphasize the role of contamination,^{11–13} the underlying substrate,^{14–16} gas exchange between the bubble interior and surrounding liquid,^{17–21} or presence of surface charges.²² The lack of agreement has its source in the fact that little is known about the nanobubble–water interface

constituting the nanobubble and the unperturbed bubble dimensions.

In order to be able to answer the questions about the anomalous nanobubble contact angles and in order to develop meaningful theories concerning nanobubble stability, it is necessary to know the actual bubble shape. Until now, the information on the nanobubble shape was obtained essentially exclusively by atomic force microscopy (AFM). Numerous imaging experiments were done mainly in tapping mode (TM),^{8–10,23} contact mode (CM),^{24–27} peak force tapping (PFT),^{28–30} frequency modulation (FM),^{28,31} force spectroscopy (force-volume mode),³² noncontact mode,¹⁶ and lift mode AFM.³³ Despite the wealth of data, a substantial fraction of the results should be regarded with some reservation, because the imaging parameters have either not been controlled or were not reported. Hence, the imaging forces are not controlled or unknown, which is problematic due to the profound impact of the imaging forces on the *apparent* nanobubble dimensions (*vide infra*).^{29,34–36} Other methods

Received: April 16, 2014

Revised: May 22, 2014

Published: May 23, 2014

used to study surface nanobubbles either lack spatial resolution or cannot be operated in liquid or give information only on the bubble content, but not on the bubble shape. The list of techniques includes neutron reflectivity,³⁷ attenuated total internal reflection Fourier transform infrared (FTIR) spectroscopy,³⁸ rapid cryofixation,³⁹ quartz crystal microbalance,⁴⁰ X-ray reflectivity,^{41,42} synchrotron-based scanning transmission soft X-ray microscopy (STXM),⁴³ interference microscopy,⁴⁴ and total internal reflection fluorescence microscopy.^{45,46}

Therefore, we face the situation that only AFM related techniques allow us to determine the bubble shape. Unfortunately, as already alluded to above, it is well established that imaging of soft matter (like bubbles) with AFM may lead to several artifacts and complex sample deformation.⁴⁷ Several authors reported a strong dependence of the apparent nanobubble shape and size on the AFM scanning parameters, such as the rms amplitude of the cantilever oscillations and the amplitude set point ratio in TM AFM^{34–36,48} and the peak force in PFT AFM.^{28–30} In these AFM experiments, the apparent nanobubble height was concluded to be always lower than the actual bubble height. This is a consequence of the nonzero interaction force conditions, which results in the deformation of nanobubbles. The apparent bubble height decreases for both nonzero amplitude of the cantilever oscillations and a set point ratio lower than 100% in TM AFM, or for nonzero peak force in PFT AFM. The decrease becomes larger, the more invasive scanning conditions are used. Assuming that, during the approach, the bubble is not attracted to the tip and does not deform upward, and knowing the scanning parameters chosen to scan a particular image, we can approximate the actual nanobubble height only by extrapolation.

The sensitivity of the apparent nanobubble shape and dimensions in AFM images to scanning parameters indicates that there is a complex interaction between the AFM tip and the nanobubble during scanning. To date, this interaction has not been addressed in sufficient detail. However, to unravel the real shape and size of nanobubbles with AFM, it is crucial to understand the nature of this interaction. The AFM mode that allows one to study the interaction in most detail is FV mode AFM. Unfortunately, only few FV studies on surface nanobubbles have been carried out so far, presumably due to its slow data acquisition rate and hence inherent sensitivity to thermal and instrumental drifts.

In addition, the scarce information from force measurements on nanobubbles is inconsistent. Most authors agree that nanobubbles possess different properties and hence display different behavior than the underlying hard substrate, but the mechanism responsible for these differences is not well understood and the details of the interaction between an AFM tip and a nanobubble during the scanning remain unclear. The shapes of force–distance curves measured on nanobubbles reported by various authors vary substantially both qualitatively and quantitatively,^{12,23,25,30,32,33,49} and the observed differences cannot be clearly attributed to a change in the experimental conditions (surface, gas content, contamination). To date, the only information on bubble stiffness or deformation has been obtained in the experiments done in the peak force mode.^{29,30} Clearly, there is an urgent need to study the tip–nanobubble interaction in a systematic manner.

Here we report on an AFM FV study of argon nanobubbles of HOPG, which was focused on the elucidation of the AFM tip–nanobubble interactions for (a) hydrophilic and (b)

hydrophobic AFM tips. By analyzing the spatial variation of tip–bubble interaction forces across individual nanobubbles, we determined the unperturbed nanobubble shape and the nanobubble stiffness. Moreover, we tested two models of tip–bubble interaction and discussed possible mechanisms responsible for nanobubble deformation during the scanning in different AFM modes.

■ EXPERIMENTAL SECTION

Sample Preparation. In all experiments, freshly cleaved highly oriented pyrolytic graphite (HOPG; grade ZYH, Veeco, Santa Barbara, CA) with a water contact angle of $63 \pm 2^\circ$ was used. The static contact angle was measured with the sessile drop method with an OCA 15plus instrument (Data Physics Instruments GmbH, Filderstadt, Germany) using Milli-Q water obtained from a Millipore Direct Q 8 system (Millipore, Schwalbach, Germany) with resistivity of 18.0 M Ω /cm and surface tension of 0.072 N/m (determined by a Wilhelmy plate method). Nanobubbles were measured in argon saturated Milli-Q water. First, 20 mL of Milli-Q in a clean round-bottom flask with a Teflon inlet was degassed at a pressure of 80 mbar for 30 min at 20 °C by using a diaphragm vacuum pump (type MZ 2C, Vacuubrand, Germany) while it was sonicated continuously in a water bath sonicator (Brandelin Sonorex, Rk 100 H). Next, the flask with water was closed, removed from the ultrasonic bath, and was put under an Ar stream (no filter used) for 45 min.

Atomic Force Microscopy. The AFM measurements were carried out on a MultiMode IIIa AFM instrument (Bruker/Veeco, Santa Barbara, CA) with a vertical engage E-scanner and NanoScope version 3.10 software (Bruker/Veeco, Santa Barbara, CA). V-shaped MLTC Si₃N₄ cantilevers (Bruker AXS, Camarillo, CA) with the following spring constants were used: $k_{\text{cant}} = 0.1 \pm 0.01$ N/m and $k_{\text{cant}} = 0.7 \pm 0.07$ N/m. The cantilevers' spring constants were calibrated on an Asylum Research MFP-3D Bio instrument (Asylum Research, Santa Barbara, CA). The cantilevers were cleaned prior to the measurements for 60 s by oxygen plasma (Plasma Prep-pixelsII, SPI Supplies, West Chester, PA). To minimize the contamination of the tip, the cantilevers were inserted with minimal delay in the liquid cell and directly immersed in Ar saturated water. In all experiments, a closed liquid cell configuration was used. First, the liquid cell, the O-ring (fluorosilicone rubber) and the inlet and outlet tubes (silicone) were rinsed with Milli-Q water and with ethanol (99.9%, Merck KGaA, Darmstadt, Germany) and dried in a stream of nitrogen. Next, the liquid cell was assembled and the cantilever was inserted. Subsequently, a 1 mL sterile syringe (Braun, Injekt-F 0.01-1 mL/luer Solo) was filled with the Ar saturated water and connected to the inlet tube. No needle was used for this procedure to avoid possible contamination by the lubricant. Immediately, the water was injected in the liquid cell until the cantilever was immersed and the O-ring was filled. Then the liquid cell was placed on the sample, the O-ring was brought in contact with the sample, 0.6 mL of water was passed through the liquid cell, and after that the inlet and outlet were closed. We stress that *no* liquid exchange procedure was performed and the HOPG surface did not have contact with ethanol at any stage of the experiment. Also, the lubricant free syringe used was cleaned by Milli-Q water before use. Before the start of the AFM measurement, the system was left for 30 min to equilibrate. The nanobubbles were scanned first in TM AFM and subsequently in FV mode without changing the cantilever and the tip or replacing the liquid.

Tapping Mode AFM (TM AFM). The drive frequency used for imaging in TM AFM was 9.2 kHz for the cantilever with $k_{\text{cant}} = 0.1 \pm 0.01$ N/m, and 29.6 kHz for the cantilever with $k_{\text{cant}} = 0.7 \pm 0.07$ N/m. The free amplitude of the cantilever oscillations (in volts) was calculated from amplitude–displacement curves recorded before and after recording of the image, as an average of 50 points. Next, it was converted into free amplitude in nanometers using the appropriate value of the deflection sensitivity. The amplitude set point ratio (ratio of the set point amplitude value set during the measurements and free amplitude calculated from the corresponding amplitude–distance curve) was calculated as the mean value of two set point ratios

determined using amplitude–distance curves recorded before and after scanning a TM height image. The values of free amplitudes and set point ratios in TM measurements of nanobubbles in our experiments were 13 nm and 90% for the experiment done with the cantilever with $k_{\text{cant}} = 0.1 \pm 0.01$ N/m, and 16 nm and 90% for the experiment done with the cantilever with $k_{\text{cant}} = 0.7 \pm 0.07$ N/m. Raw TM height images were processed using a first order plane fit and a zeroth order flattening (any nanobubble was excluded). The bubble size was measured using the spherical cap fitting and no tip size correction was applied.¹⁰

Force Volume Mode AFM (FV AFM). The resolution of the FV imaging was set to 32 pixels \times 32 pixels.² The cantilever oscillation was switched off during data acquisition in FV mode. Ramp sizes and trigger thresholds were set to 223 and 30 nm in the experiment done with the cantilever with $k_{\text{cant}} = 0.1 \pm 0.01$ N/m, and to 100 and 60 nm in the experiment done with the cantilever with $k_{\text{cant}} = 0.7 \pm 0.07$ N/m. The velocity of tip approach was set to 446 nm/s and 1.02 $\mu\text{m/s}$, respectively. The force curve resolution was set to 512 points per single approach–retraction cycle. Raw deflection–distance curves were transformed into deflection–separation curves.⁵⁰ The vertical position of the tip above the substrate is represented in the plots by the tip–sample separation distance (zero separation indicates that the tip is in contact with the substrate). The deflection was recalculated into force by multiplying the measured deflection value with the corresponding cantilever stiffness. For more details on FV imaging please compare the Supporting Information.

RESULTS AND DISCUSSION

Force Volume AFM Measurements. In the experiments, argon surface nanobubbles on HOPG in water were scanned in FV AFM (details are explained in the Supporting Information) using (a) hydrophilic and (b) hydrophobic AFM tips.

First, a selected area of HOPG was scanned in TM AFM with high resolution (pixel width ~ 6 nm) to identify the positions of the nanobubbles. Subsequently, lower resolution (pixel width 60–90 nm) FV measurements were done in the area where the selected bubble was located. Figure 1 shows TM and FV images of two nanobubbles.

In the FV mode, two types of images were acquired simultaneously: (1) a FV height image and (2) a FV slice image. The FV height image shows the vertical distances over which the tip had to be moved at each point of the sample in order to reach the selected trigger threshold. In the experiment, the threshold value was set to sufficiently large values (corresponding to an upward cantilever deflection of ~ 30 – 60 nm) to ensure that the tip reaches the substrate at each point of the sample. As a result, the FV height images in Figure 1b and e do not show the nanobubbles, but the substrate under them. However, the exact location of the bubbles on the sample during the acquisition of the force data could be determined by comparing the features of the substrate visible in the FV height images with the TM height images. In addition, nanobubbles were visible in FV slice images shown in Figure 1c and f. These images show the magnitude of the force exerted on the tip (expressed as the cantilever deflection) at a particular height over the substrate, as measured from the approach force curves.

As a first step, we compare force–distance curves acquired on the substrate and on the nanobubbles. A set of typical approach and retraction force–distance curves measured on HOPG in water is shown in Figure S2 in the Supporting Information. No long-range interaction was observed in the force curves. Recently, the absence of strong long-range repulsion between a silicon-nitride AFM tip and HOPG in the areas between nanobubbles was ascribed to the interfacial gas enrichment on the sample surface due to solvent

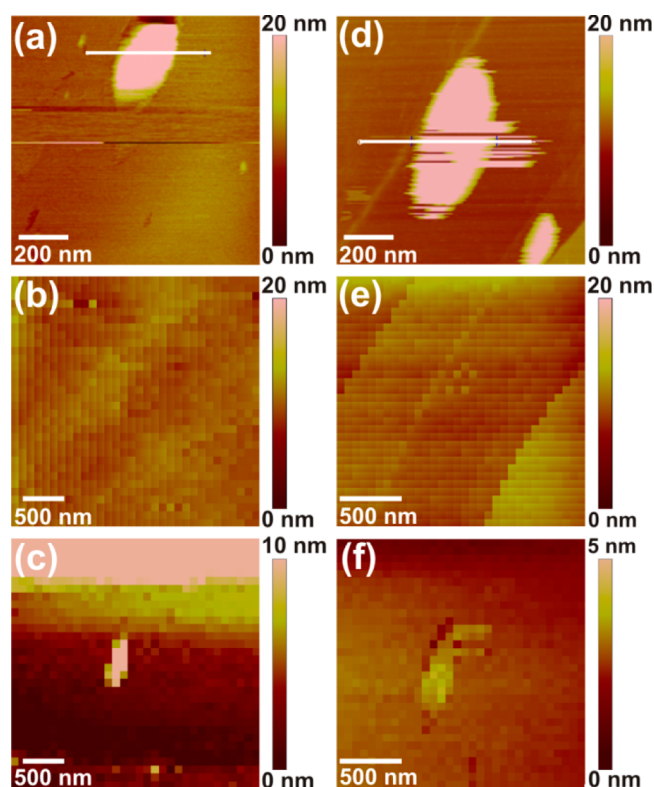


Figure 1. (a) and (d) AFM TM height images, (b) and (e) FV height images, and (c) and (f) FV slice images of two nanobubbles on HOPG. The spring constant of the cantilever was $k_{\text{cant}} = 0.1$ N/m for the data shown in panels (a)–(c), and $k_{\text{cant}} = 0.7$ N/m for the data shown in panels (d)–(f).

exchange.³² In our experiments, the long-range repulsion has not been detected because no solvent exchange was used to create nanobubbles.

Force–distance curves measured on surface nanobubbles displayed an entirely different shape than the ones measured on HOPG. Figure 2 compares two nanobubbles measured on HOPG in water (panel (a) shows the data for hydrophilic and panel (b) for hydrophobic tips). For each bubble, the height profiles and a set of force–distance curves are shown. The TM height profiles (open symbols) were measured from the TM topographic images shown in Figure 1a and d and were corrected for scanning conditions (solid line).³⁴ The bubbles were chosen such that they can be easily compared, that is, they have similar dimensions: ca. 300–350 nm in apparent width and 38 nm in apparent height. Two sets of plots accompanying the height profiles show sequences of force curves measured on the bubbles at different horizontal positions along a single scan line acquired over the bubble center. The numbers in the plots correspond to the numbers in the bubble profiles marking the locations on the sample, where a particular force curve was measured.

The force–distance curves depended on the particular tip used for a given experiment and can be divided into two groups. The bubbles shown in Figure 2 are good representatives of two observed groups. Figure 3 compares in detail the two types of force curves observed in our experiments on nanobubbles on HOPG. The raw (unprocessed) force–displacement curves are shown in the Supporting Information. In both plots in Figure 3, the onset and the end point of the tip–sample interaction (jump-in and jump-off points) were

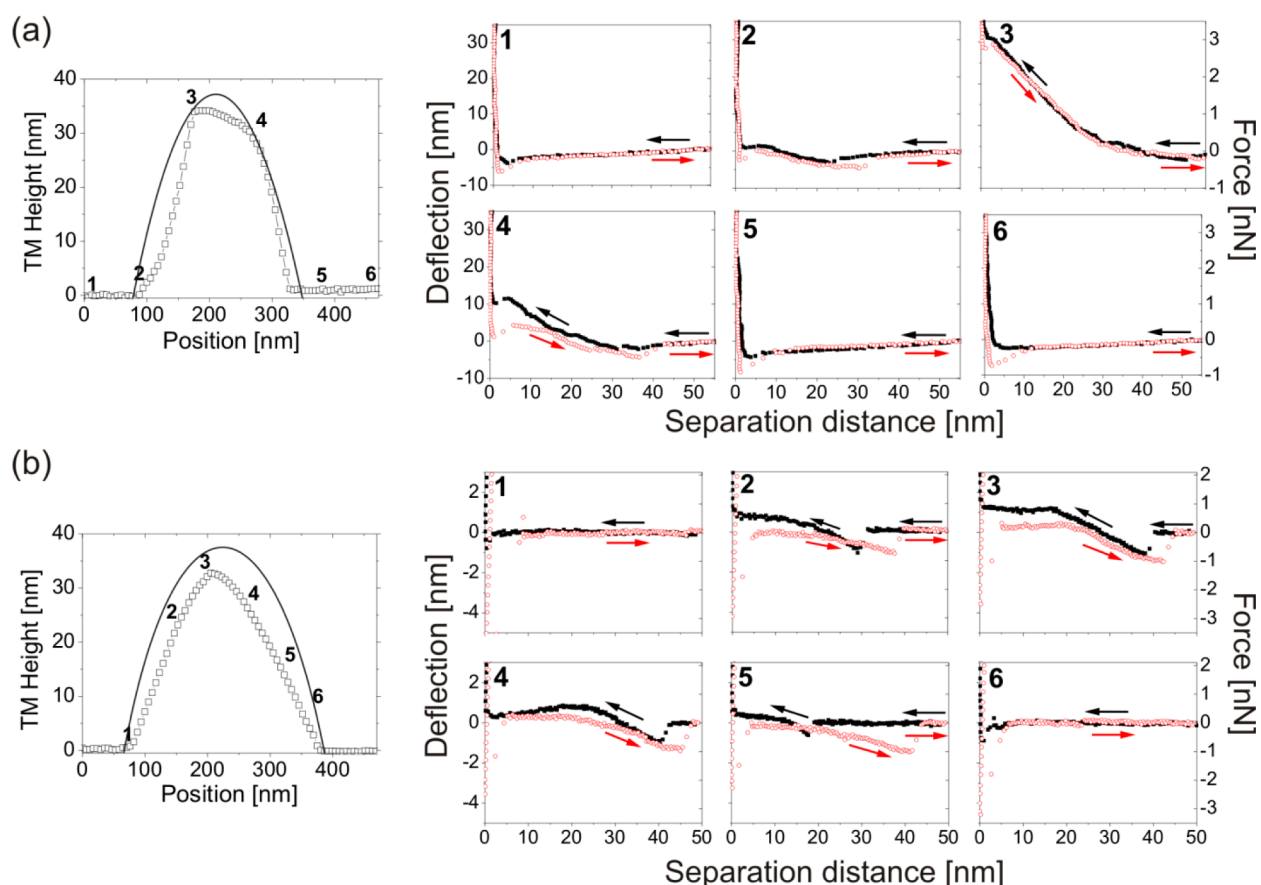


Figure 2. Apparent (open squares) and corrected (solid line) cross-sectional profiles of two nanobubble from Figure 1 shown together with the corresponding sequence of approach (black) and retraction (red) force–distance curves measured on the bubbles along single scan lines (see Figures 1a and d). The scanning was done with (a) a hydrophilic AFM tip and (b) a hydrophobic AFM tip. The numbers in the force plots correspond to the numbers in the bubble profiles indicating the horizontal positions on the sample where the force curves were acquired. The spring constant of the cantilever was $k_{\text{cant}} = 0.1 \text{ N/m}$ for (a) and $k_{\text{cant}} = 0.7 \text{ N/m}$ for (b).

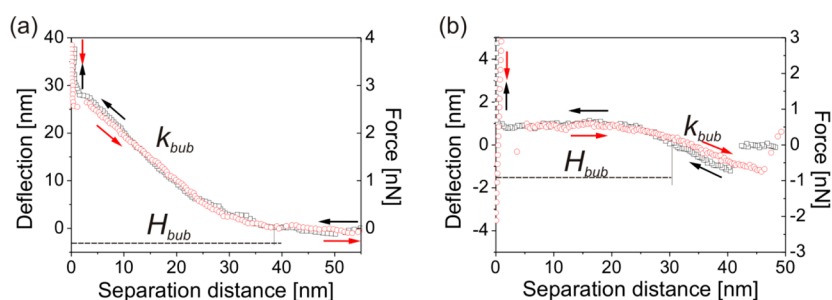


Figure 3. Comparison of two types of force–distance curves acquired on nanobubbles with (a) a hydrophilic AFM tip and (b) a hydrophobic AFM tip. The point of crossing of the zero-deflection line defines the unperturbed bubble height H_{bub} . The slope of the linear part of the curve defines the bubble stiffness k_{bub} . The spring constant of the cantilever used to acquire the data was $k_{\text{cant}} = 0.1 \text{ N/m}$ for (a) and $k_{\text{cant}} = 0.7 \text{ N/m}$ for (b).

located at separation distances of several tens of nanometers, which marked a larger range of interaction than for bare HOPG.

In the plot in Figure 3a, only repulsive forces were observed on the nanobubble. After a not very well pronounced jump-in point, the cantilever bent upward and its deflection increased linearly with decreasing tip–sample separation until the HOPG surface was reached. The shape of the retraction force curve followed the shape of the approach force curve and the jump-off point was located at roughly the same position as the jump-in point. This type of force curve was typically observed in our experiments done on surface nanobubbles⁵¹ and is similar to

the shape of the force curves acquired on macroscopic bubbles.^{52,53} Due to the absence of pronounced adhesion, we attribute this to a hydrophilic tip.

On the contrary, in the plot in Figure 3b, a significant attractive force was measured at the jump-in point. As the separation between the tip and the sample decreased, repulsive forces prevailed and the deflection of the cantilever increased linearly. For small separation distances, the gradient of the deflection decreased so that the slope transformed into a plateau. The deflection of the cantilever stayed constant over the distance of several nanometers until the HOPG surface was reached and the cantilever bent upward. Upon retraction, the

pattern was reversed. However, the jump-off point was located at the separation distance *larger* than the separation distance of the jump-in point. This caused significant hysteresis in the force curves. Because of the pronounced adhesive force, this type of curve is attributed to a hydrophobic tip. Similar features were observed in the force curves acquired on nanobubbles with not precleaned AFM tips.^{12,25,49}

A peculiar feature of the force–distance curves in Figure 3b is the plateau measured at small tip–sample separation distances both in approach and retraction force curves. The plateau indicates that no change in the interaction force occurs over a certain separation distance. The plateaus had different lengths depending on the position on the bubble being the longest in force curves acquired near the bubble center. To our knowledge, the presence of plateau in force–distance curves measured on nanobubbles has not been reported previously. In addition, we have observed similar plateaus in the amplitude–distance curves acquired on the bubble in the same experiment, subsequently after the acquisition of the force–distance curves (see the Supporting Information). Similar plateaus in the amplitude–distance curves measured on nanobubbles have been already reported.^{34,48}

From the force–distance curves, we extract information about the measured bubbles. First, we can estimate the unperturbed bubble height H_{bub} . The best available estimate of H_{bub} is the point in the force curve at which the tip is in contact with the bubble, but the net force applied on the AFM cantilever is zero. This corresponds to the position of the jump-in point in the approach force curve in Figure 3a, and to the zero-deflection crossing point in the approach force curve in Figure 3b. The exact difference between these two situations will be explained further in the Article. From the left plot, we estimate that the actual height of the bubble from Figure 1a was 38 nm, which is *in agreement* with the height of the corrected bubble profile shown in Figure 2a. In turn, the actual height of the bubble from Figure 1d estimated from the plot in Figure 3b was 30 nm, which is less than the height of the corrected bubble profile in Figure 2b.

Next, knowing H_{bub} and the exact shape of the force curve, for any force measured in the FV experiment, we can estimate the bubble deformation in the vertical direction as a deviation of the separation distance corresponding to a particular force value from the position of the H_{bub} point. This includes both upward and downward deformation.⁵⁴

The entirely different shapes of the force curves shown in Figure 3 indicate *different* conditions for tip–bubble interaction and possible bubble deformation in the experiments done on these two nanobubbles. Because the bubbles were similar in size, the observed differences may originate from properties of the bubble, the AFM tip, the liquid, and/or the substrate.

Modeling of the Tip–Nanobubble Interaction. In order to establish the conditions and the nature of the tip–bubble interaction in both our experiments, we will compare force–distance curves measured experimentally with the force–distance curves predicted by two models of tip–bubble interaction: the dynamic interaction model and the capillary force model.

Dynamic Interaction Model. First, we consider a model that assumes a dynamic interaction between soft materials. It was developed to describe deformation and forces between interacting bubbles and drops and between a drop/bubble and a spherical particle. The model agrees with a large number of experimental data acquired with various techniques,

including AFM, on droplets and bubbles of millimeter and micrometer sizes.^{55–57} We apply the model to characterize the tip–bubble interaction in the last stage of approach when a thin film of liquid is trapped between the bubble surface and the tip apex, that is, the interaction just before the contact with the substrate is established.

The model describes both the flow of the liquid in the film and bubble deformation in response to external forces. The behavior of the film, the forces, and the geometrical deformations are coupled. On one hand, hydrodynamic flow, surface forces, and variations in material properties give rise to spatial and temporal variation in forces that cause deformation of the bubble surface. On the other hand, bubble shape changes define variations in the film thickness and influence its dynamics and the interaction forces. The model neglects gravity and assumes constant surface tension and axial symmetry of the system. It describes the film down to nanometer thicknesses.

In the application of the model to our system, we will focus on interaction force. The formula that relates the interaction force F to the displacement ΔX of the tip apex follows

$$\Delta X = \frac{F}{4\pi\gamma} \left\{ \log \left(\frac{FR_{\text{bt}}}{8\pi\gamma R_c^2} \right) + 2B(\theta_{\text{nano}}) - \frac{4\pi\gamma}{k_{\text{cant}}} - 1 \right\} \quad (1)$$

where γ is the surface tension and $R_{\text{bt}} \approx ((1/R_c) + (1/R_{\text{tip}}))^{-1}$ is the reduced radius with R_c and R_{tip} denoting the radius of curvature of the bubble and of the tip, respectively. The parameter $B(\theta_{\text{nano}})$ is related to the constant volume constraint under the assumption that the bubble deforms with the constant contact angle θ_{nano} :

$$B(\theta_{\text{nano}}) = 1 + \frac{1}{2} \log \left(\frac{1 + \cos \theta_{\text{nano}}}{1 - \cos \theta_{\text{nano}}} \right) - \frac{1}{2 + \cos \theta_{\text{nano}}} \quad (2)$$

This formula is valid for high forces and for a small interaction zone and small deformation compared to the bubble size (radius of curvature). This constraint is satisfied for surface nanobubbles in our experiments. Moreover, the model assumes that the volume of the bubble is constant at all stages of interaction and the contact angle does not change. It means that the bubble contact line is not pinned to graphite surface and that it can move to adapt the bubble shape to varying force conditions. It is not clear if this scenario is true in case of surface nanobubbles and it clearly violates the hypothesis of contact line pinning as a mechanism that stabilizes the bubble. However, assuming an alternative scenario (constant radius of the bubble base) does not significantly change the results of the model for our system. Finally, the model does not include the effect of bubble compressibility (change in volume) that, as suggested by the authors, may become important for bubbles with radii below about 1 μm . This constraint is valid as long we assume that gas inside the bubble behaves as an ideal gas.

We checked how the variation of parameters of the model (R_{tip} , γ , R_c (related to θ_{nano}), and k_{cant}) influence the slope of the modeled force curve for two considered nanobubbles. In both cases, the initial points of interaction assumed for the model were located at separation distances that were equal to the unperturbed bubbles' heights of 38 and 30 nm. The unperturbed radii of curvature R_c and contact angles θ_{nano} of the bubbles were extracted from the TM AFM height images corrected for the “nonzero force” scanning conditions. We

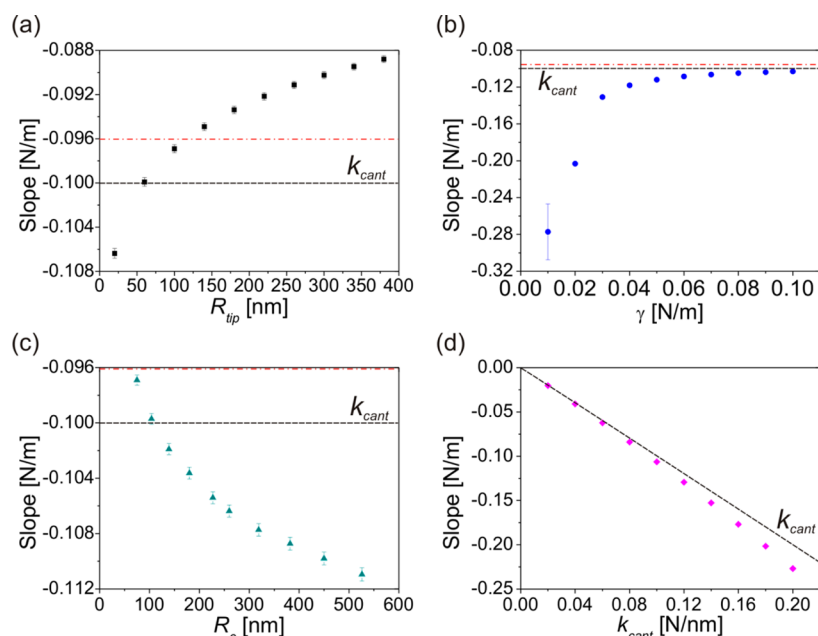


Figure 4. Slopes of the force dependence obtained from the dynamic interaction model for the nanobubble scanned with the hydrophilic tip with $k_{cant} = 0.1$ N/m as functions of different parameters of the model: (a) R_{tip} , (b) γ , (c) R_c (related to θ_{nano}), and (d) k_{cant} . The dashed line represents the level of $k_{cant} = 0.1$ N/m; the dot-dash line represents the value of the slope in the experimental force curve shown in Figure 3a.

tested a wide range of values of all considered parameters describing various experimental conditions. The slopes in the force–distance curves were calculated from the model for different values of R_{tip} in the range of 20–380 nm, γ in the range of 0.01–0.10 N/m, R_c in the range of 75–526 nm for the first analyzed bubble and in the range of 284–1724 nm for the second bubble, and k_{cant} in the range of 0.02–0.20 N/m for the first bubble and in the range of 0.3–1.2 N/m for the second bubble. Each time, we changed the value of only one parameter, while keeping the other three constant and equal to the initial values $R_{tip} = 20$ nm, $\gamma = 0.07$ N/m, and R_c and k_{cant} equal to 270 nm and 0.1 N/m for the first bubble and 540 nm and 0.7 N/m for the second bubble, respectively. All force curves are shown in Figures S5 and S7 in the Supporting Information.

For the first considered nanobubble, all force curves in the tested parameter range showed the quasi-linear behavior. The plots showing the dependences of the slopes of these force curves on four discussed parameters of the model are shown in Figure 4. The corresponding histograms of the measured slopes are shown in the Supporting Information. The dot-dash line drawn in the plots represents the level defined by the value of the slope measured in the experimental approach force curve shown in Figure 3a.

Most of the slopes of the force curves obtained from the dynamic interaction model were steeper than the slope of the force–distance curve measured experimentally on the nanobubble. This means that in most of the tested experimental conditions, changing the parameters of the model did not lead to an improvement of the fit quality. This includes also a decrease in k_{cant} . One must keep in mind that any change in k_{cant} value alters not only the outcome of the model, but also the slope of the experimental force curves (force is equal to the deflection of the cantilever (in nm) multiplied by k_{cant}). Therefore, any decrease in k_{cant} would lead to less steep slopes of both the measured and the modeled force curves, still leaving the gap between the slope values.

An increase in surface tension above the surface tension of water 0.07 N/m only slightly improves the quality of the fit. In addition, since there are no other premises that nanobubbles stiffness is significantly higher than the surface tension of water, an increase in γ in the model does not seem to be adequate.

From all four tested parameters of the dynamic interaction model, an increase in R_{tip} and a decrease in R_c of the bubble possess the greatest impact on the slope of the force curve and result in good agreement of model and data. A decrease in R_c automatically means a decrease in the nanoscopic contact angle θ_{nano} of the bubble.

On the one hand, as indicated in the plot in Figure 4c, the value of the slope in the modeled force curve would reach the value of the slope in the experimental force curve only, if R_c was decreased to below 100 nm, which corresponds to a decrease in bubble width by roughly 50% and a decrease in θ_{nano} by at least 30°. On the other hand, as shown in the plot in Figure 4a, in order to achieve the same result, R_{tip} should be increased to about 120 nm (with all other parameters unchanged). The former seems reasonable, if one takes into account that an apparent nanobubble width in an AFM image is likely to be overestimated because of the tip imaging effect (the size of the tip apex adds to the actual width of the nanobubble). An increased R_{tip} used in the model also is considered a possible scenario because the physical size of the tip apex in the AFM experiment may increase due to tip wear. However, this possibility is limited because a significant increase in R_{tip} violates the assumption of the dynamic interaction model that the tip–bubble interaction zone (directly related to the size of the tip apex) is much smaller than the size of the bubble. This restriction leaves only a small window of possible R_{tip} values that can be used in the model.

Nevertheless, one must keep in mind that an increased tip size results most likely in more pronounced tip imaging effects, an increase in the apparent nanobubble width, and a decrease in the apparent curvature of the bubble. Therefore, considering the measured apparent nanobubble width as a reference point,

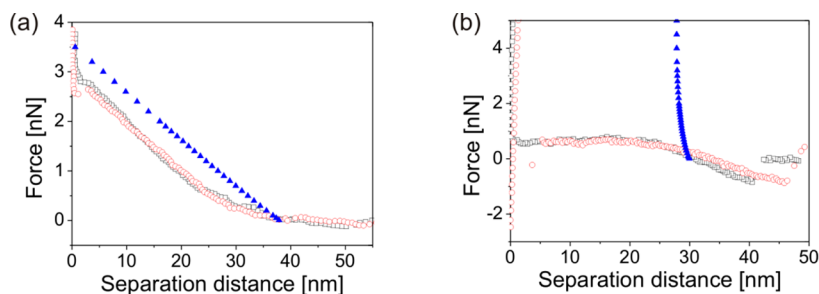


Figure 5. AFM tip–nanobubble interaction forces as functions of the separation distance to the substrate measured experimentally (open symbols) with (a) a hydrophilic AFM tip and (b) a hydrophobic tip, and calculated from the dynamic interaction model (solid symbols) for (a) tip radius $R_{\text{tip}} = 50$ nm, surface tension $\gamma = 0.07$ N/m, bubble radius of curvature $R_c = 115$ nm, contact angle $\theta_{\text{nano}} = 132^\circ$, $k_{\text{cant}} = 0.1$ N/m, and (b) $R_{\text{tip}} = 20$ nm, $\gamma = 0.07$ N/m, $R_c = 540$ nm, $\theta_{\text{nano}} = 158^\circ$, $k_{\text{cant}} = 0.7$ N/m.

if we increase the value of R_{tip} in the model, we should accordingly decrease R_c .

For example, for $R_{\text{tip}} = 50$ nm, the apparent nanobubble width should be decreased by $2R_{\text{tip}} = 100$ nm. Assuming that the nanobubble height does not change, this decreases R_c of the considered bubble to 115 nm. With $\gamma = 0.07$ N/m, and $k_{\text{cant}} = 0.1$ N/m unchanged, the force curve calculated from the dynamic interaction model has a slope equal to -0.0957 ± 0.0003 N/m that is approximately equal to the estimated value -0.0962 ± 0.0006 N/m of the slope in the experimental force curve in Figure 3a. The experimental and modeled force curves are shown together in the plot in Figure 5a. Considering all available information on the experimental system and the model, the force curve calculated from the model for the given parameters is close to the best possible fit of the experimental data acquired on the nanobubble from Figure 1a. For comparison, a force curve modeled for $R_{\text{tip}} = 120$ nm and all other parameters unchanged has a slope of -0.09582 ± 0.0003 N/m (shown in the Supporting Information).

In the plot in Figure 5a, the data set provided by the model indicates repulsive tip–bubble interaction over the entire examined separation distance range. The repulsion increased in strength for decreased separation. A 0.5 nN discrepancy between the maximum repulsive force at zero separation distance predicted by the dynamic interaction model and measured in the experiment may be caused by the fact that the model describes the interaction in the bubble center, whereas, due to the limited resolution of the FV experiment, the presented force curve was acquired *near* the bubble center. We have observed that the larger the local bubble height, the steeper the slope in the force curve and the stronger the repulsion experienced by the tip at the level of the substrate.⁵⁴ A force of 3.5 nN predicted by the model in Figure 5a was estimated to be measured for the bubble height of ~ 45 nm. This is only slightly larger than the maximum estimated bubble height. For details, see the Supporting Information. In addition, the original model was developed to describe only local and small deformations of the bubble apex. In the case of the surface nanobubble, the maximum deformation was severe and approximately equal to the bubble height. There might be additional factors, not included in the model, that influenced the interaction.

Contrary to the results obtained for the nanobubble from Figure 1a, for the bubble from Figure 1d, the discrepancy between the results of the dynamic interaction model and the experimental data was very large and the shapes of the force curves determined experimentally and predicted by the model for all tested parameters were entirely different. All force curves

calculated for varying parameters are shown in the Supporting Information. An exemplary curve is shown in Figure 5b. The presented force curve was calculated for the initial conditions $R_{\text{tip}} = 20$ nm, $\gamma = 0.07$ N/m, $R_c = 540$ nm, and $k_{\text{cant}} = 0.7$ N/m. According to the model, the repulsion between the tip and the bubble increased with decreasing tip–sample separation distance at much higher rate than in the case of the previous bubble, which was caused by the larger k_{cant} used to calculate the force. In addition, in most of the calculated force curves, the increase was not quasi-linear; therefore, the slope analysis similar to the one shown in Figure 4 could not be employed for this nanobubble.

Whereas the reasons presented above may account for the small difference between the theory and experiment observed in the force–distance curves for the nanobubble from Figure 1a, they are not able to explain the striking discrepancy observed in the force curves plotted in Figure 5b for the nanobubble from Figure 1d. In the case of the first bubble, the film of liquid between the tip apex and the bubble ruled the interaction over separation distances 0–38 nm. We conclude that this nanobubble was not directly in contact with the tip surface but wrapped around it when the tip was lowered toward the substrate. In the case of the second bubble, the dynamic interaction model gives very poor results. Therefore, we claim that in that case the interaction forces had another than hydrodynamic origin.

Capillary Force Model. As an alternative to the dynamic interaction model, we consider a capillary force model.⁵⁸ This model is commonly used to describe the interaction between AFM tips and macroscopic bubbles. The model is based on several assumptions. First, we consider a two-dimensional system shown schematically in Figure 6. A nanobubble has a shape of a spherical cap and sits on a perfectly smooth and homogeneous substrate. The height of the nanobubble H_{bub} is

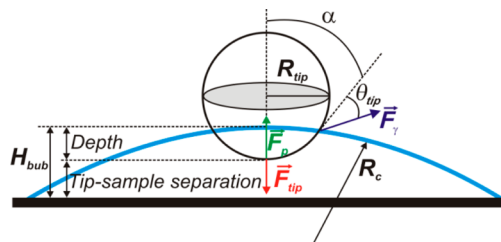


Figure 6. Schematic cross-section of the spherical AFM tip apex penetrating the surface nanobubble during the force measurement. The parameters and the interaction forces are defined in the text.

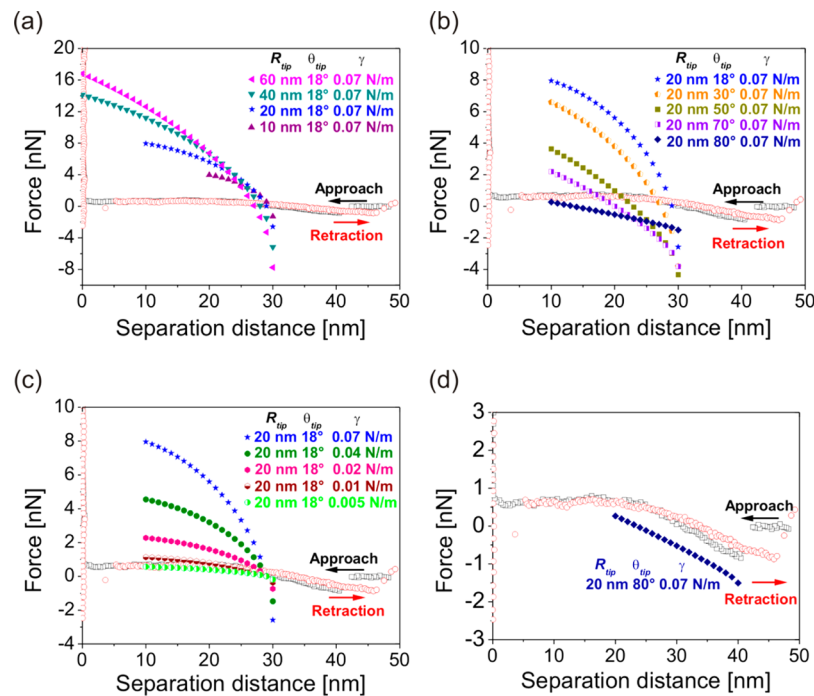


Figure 7. AFM tip–nanobubble interaction forces as functions of the separation distance to the substrate measured experimentally (open symbols) on the nanobubble from Figure 1d and calculated from the capillary force model (solid symbols). Various data sets show the influence of the values of (a) R_{tip} , (b) θ_{tip} , and (c) γ on the course of the force curves. The exact values of the parameters are indicated next to the adequate data sets. (d) Best fit of the model results to the experimental data. The spring constant of the cantilever was $k_{\text{cant}} = 0.7 \text{ N/m}$.

several times smaller than its width (base diameter) and its radius of curvature R_c . The bubble is filled with air and surrounded by the infinite bulk of water. Second, the AFM tip end interacting with the bubble is modeled as a sphere of radius R_{tip} made of smooth and relatively hydrophilic homogeneous material. We assume that the tip apex is hydrophilic so that the contact angle of water with the tip material is smaller than 90° and constant over the whole tip surface. The radius of curvature of the tip is much smaller than the radius of curvature of the bubble, and comparable to, but not smaller than, the bubble height.

The model describes the interaction between the tip end and the bubble apex at different heights; therefore, only the tip motion in the vertical direction is considered. We assume that the tip deforms the bubble surface during the interaction and that the deformation is controlled by surface tension. Next, we assume that, during the entire interaction period, we stay in a small load force regime so that the bubble responds as a Hookean spring to the applied load and its deformation is linear and much smaller than R_{tip} and R_c . The stiffness of the bubble k_{bub} is uniform over the whole surface and equal to the surface tension of water. The interaction cycle starts when the tip end contacts the bubble apex. Then, the tip is lowered until it reaches the substrate under the bubble. The depth to which the tip is lowered is equal to the downward deformation of the bubble apex and the contact line does not move upward or downward the tip. The maximum deformation is equal to H_{bub} and does not exceed R_{tip} . The scenario described does not fulfill the requirement of small perturbations and a range of interaction much smaller than R_{tip} .

Equilibrium is established between the force F_{tip} with which the tip is pressed against the bubble, the force F_γ arising from the surface tension γ acting along on the tip–bubble contact line, and the force F_p originating from the pressure difference

across the bubble wall: $\vec{F}_{\text{tip}} = \vec{F}_p + \vec{F}_\gamma$. The directions of the forces are sketched in Figure 6. The tip is lowered over the bubble so the force F_{tip} is directed downward. The resisting force F_p is directed upward and is given by the formula:

$$F_p = \Delta p (R_{\text{tip}} \cos \alpha)^2 \quad (3)$$

where Δp is the pressure difference between the inside and outside of the bubble equal to $2\gamma/R_c$, and α is the angle between the tangent to the tip surface and normal of the tip. It describes the change in the tip shape at different points of the apex (caution: the angle α is *not* the opening angle of the tip and it changes for different locations on the tip). The vertical component of the force arising from the surface tension γ and acting along the line where the bubble surface and the tip interact is equal to

$$F_\gamma = 2\pi R_{\text{tip}} \gamma \cos \alpha \cos(\alpha + \theta_{\text{tip}}) \quad (4)$$

where θ_{tip} is the contact angle of water on the tip material.

Because we assumed that $R_c \gg R_{\text{tip}}$ at the point of interaction, the bubble will appear flat to the tip and the interaction will be similar to the one between a sphere and a flat liquid surface. As a consequence, $F_p \ll F_\gamma$ so that F_p can be neglected in the force equilibrium formula. The influence of other forces, such as electrostatic, van der Waals, gravitational, hydration forces, and forces originating from the substrate, is also neglected in the model.

The final formula for the net force applied on the AFM tip in the system is

$$F_{\text{tip}} = 2\pi R_{\text{tip}} \gamma \cos \alpha \cos(\alpha + \theta_{\text{tip}}) \quad (5)$$

Similarly as for the dynamic interaction model, the results of the simulations were compared to the force–distance curves measured on two nanobubbles from Figure 1 plotted in Figure

3. As the initial values of the parameters in the model, we used the initial separation of 38 and 30 nm of the first and second bubble, respectively, $\theta_{\text{tip}} = 18^\circ$ (measured for water on Si_3N_4 wafer cleaned with plasma cleaner⁶⁰), $\gamma = 0.07$ N/m, and $R_{\text{tip}} = 20$ nm. These initial values of θ_{tip} , γ , and R_{tip} were varied to simulate different possible experimental conditions: R_{tip} in the range between 10 and 260 nm, γ in the range between 0.05 and 0.1 N/m, and θ_{tip} in the range between 18° and 90° . Each time, we changed the value of only one parameter while keeping the other two parameters constant and equal to the initial values.

The force curves calculated from the capillary force model for the bubbles from Figure 1a and d are shown in the Supporting Information. For the second bubble, a selection of data sets is shown in Figure 7. The maximum range of the interaction that could be modeled did not exceed R_{tip} , and therefore, in some of the force curves, the fitted region was smaller than the bubble height and equal to R_{tip} .

For both bubbles, the results given by the model for the initial values of the parameters (blue stars) deviated strongly from the experimental data (open symbols). Although the general repulsive character of the interaction was predicted well, in most of the force curves predicted by the capillary force model, the magnitudes of the forces were much larger than measured in the experiment for both considered bubbles. Moreover, the dependence of the force on the separation distance was nonlinear at all points of the interaction.

For all tested values of R_{tip} , the discrepancy between the theory and the model was large, and increased for increased R_{tip} . For both bubbles, a decrease in γ down to 0.01–0.005 N/m decreased the repulsive force and reduced the attractive force at the onset of the interaction. However, a good match between the modeled forces and the experimental data was reached only for extremely small values of γ , which we exclude as a physically impossible scenario in our experiments. In turn, an increase in θ_{tip} caused the flattening of the force dependence and the decrease in the attraction strength in the initial phase of the interaction. With other parameters unchanged, for $\theta_{\text{tip}} \approx 80^\circ$, the dependence was almost linear and its slope resembled the slopes in the approach force curves measured on the bubbles from Figure 1a and d. However, although for the first bubble the slope was modeled well, the attractive force at the jump-in point was overestimated. We conclude that the capillary force model did not describe the interaction between the nanobubble and the tip measured experimentally for any of experimental conditions tested. On the contrary, as shown in the plot in Figure 7b, for the second considered nanobubble, the shape of the modeled force curve resembled the experimental curve in terms both the slope and the maximum attractive force. However, the more exact fitting would require shifting the initial point of the interaction toward larger separation distances, as shown in the plot in Figure 7d. If we assume that the interaction started at the separation ~ 40 nm approximately equal to the position of the jump-in point, the magnitude of the attractive force and the slope in the force curve predicted by the model is in good agreement with the experimental data.

In sum, the assumed initial values of θ_{tip} , γ and R_{tip} gave very poor agreement between the model and the experiment. The values of the forces predicted by the model approached the values of the forces measured experimentally on the nanobubble from Figure 1d only if large θ_{tip} was used. This leaves increased hydrophobicity of the tip used in the experiment, as the only possible scenario predicted by the model in our

experiment. Therefore, according to the capillary force model, the tip used to measure the nanobubble from Figure 1d was hydrophobic and the tip–bubble interaction started above the unperturbed bubble height. If the increased attraction at the jump-in point was caused by the hydrophobicity of the tip, it is likely that the bubble surface deformed upward to meet the tip and that the interaction started at larger separation distances.⁵⁴ This validates the shift in the initial tip–sample separation distance set in the capillary force model required for the data sets to match, shown in Figure 7d.

The good agreement between the experiment and the prediction of the capillary force model observed for the bubble from Figure 1d suggests that, in this particular experiment, the deformation of the tip and the bubble during the measurement was governed by the capillary force acting along the contact line that formed around the tip, hence by the surface tension. This means that the bubble was penetrated by the (hydrophobic) tip during the AFM force measurements hence, the tip and the bubble were physically connected. Also, increased attraction and unexpectedly low repulsive forces measured with a stiff cantilever with the hydrophobic tip originated from the direct interaction between the tip apex and the bubble surface.

This scenario is entirely different from the scenario based on the dynamic interaction model sketched for the bubble scanned with the hydrophilic tip, in which the bubble was separated from the tip by a thin liquid film (vide supra). The meniscus did not form on the tip, the capillary force was absent, and the surface tension influenced the interaction and the slopes in the force curves less than in the case of the bubble scanned with the hydrophobic tip.

Knowing that the hydrophobic tip penetrated the bubble, we can explain the plateaus in the force–distance curve shown in Figure 3b. We claim that it was purely geometrical effect caused by the unique tip shape (aspect ratio) that affected the length of the contact line that formed on the tip, hence the strength of the interaction forces. We believe that the plateaus in the force–distance curves measured on the bubble originate from the parts of the AFM tip with locally (nearly) constant perimeter. The length of the contact line, and hence the magnitude of the interaction force, almost did not change with decreasing tip–sample separation distance. The plateaus were measured only in the force curves acquired near the bubble center, and only at small tip–sample separation distances, that is, at the positions where the tip was immersed deep in the bubble so that the contact line was located far from the tip apex. This suggests that the region where the tip perimeter was (nearly) constant was located far from the apex. This part of the tip did not participate in the AFM measurements done at the locations away from the bubble center.

Nanobubble Stiffness. Knowing that, in the case of the hydrophobic tip, the bubble was in direct contact with the tip, we can estimate the nanobubble stiffness and verify our earlier assumption, that its value is close to the surface tension of pure water.

Recently, a map of “Young moduli” of the sample with nanobubbles acquired in peak force AFM was published.²⁸ However, since a bubble is not solid, Young modulus may not be a proper description. Here we use a simple model valid for macroscopic bubbles⁵² that assumes that the bubble–tip system acts as two springs in the series. This method is well established for the force measurements on nanodroplets⁵⁹ and microscopic bubbles.⁵⁸ Recently, it was used to estimate the nanobubble stiffness from the force curves acquired in the PFT mode.³⁰

The model assumes that the deformation of all components of the system is linear. In our previous reports, we presented the linear dependence of the apparent bubbles' heights and widths on the peak force in peak force AFM²⁹ and on the amplitude of the cantilever oscillations and the amplitude set point ratio in TM AFM, respectively.³⁴ In addition, several authors reported linear slopes in the force–distance curves measured on nanobubbles on different substrates.^{23,33}

If the bubble–tip system acts as two springs in series, the observed slope in the force–distance curve is a function of both the deformation of the bubble and the deformation of the cantilever. According to the model, the bubble stiffness k_{bub} can be extracted from the relationship $(1/k_{\text{tot}}) = (1/k_{\text{cant}}) + (1/k_{\text{bub}})$, where k_{cant} is the spring constants of the cantilever and k_{tot} is total spring constant of the bubble–tip system equal to the modulus of the slope of the linear part of the retraction force curve (in N/m) $|\text{slope}_{\text{N/m}}|$. Importantly, the formula can be applied only if $k_{\text{cant}} > |\text{slope}_{\text{N/m}}|$.

The histograms of the slopes of the linear parts of the approach and retraction force curves acquired on the nanobubble from Figure 1d scanned with a hydrophobic tip and the calculated values of the bubble stiffness k_{bub} are shown in Figure 8.

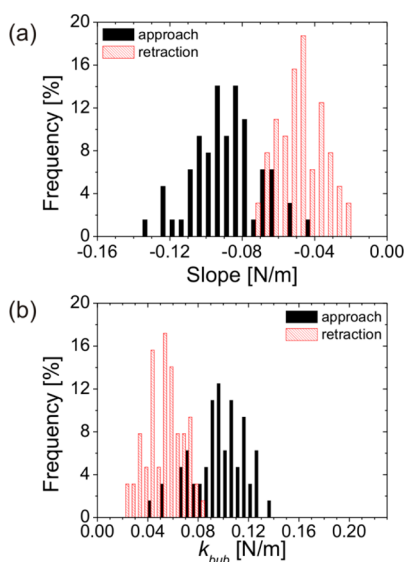


Figure 8. Histograms of the slopes of the linear parts of the force–distance curves and corresponding bubble stiffness k_{bub} for the nanobubbles from Figure 1d measured with a hydrophobic AFM tip. The spring constant of the cantilever used to acquire the data was $k_{\text{cant}} = 0.7$ N/m.

All measured slopes were negative, because we dealt either with repulsive forces (positive cantilever deflection) that increased with decreased tip–sample separation distance, or with attractive forces (negative deflection) that increased with increased separation distance. The slopes of the linear parts of the approach force curves were steeper than the corresponding slopes in the retraction curves. The condition $k_{\text{cant}} > |\text{slope}_{\text{N/m}}|$ is fulfilled for all measured slopes. The values of k_{bub} calculated from the slopes range between 0.02 and 0.14 N/m. Estimated mean values of k_{bub} were 0.10 ± 0.02 and 0.05 ± 0.01 N/m, as calculated from the approach and retraction force curves, respectively. The difference in the values is due to the hysteresis in the force curves, caused by a hysteresis of the contact angle

of the tip material and by the fact that, during the retraction, the contact between the tip and the bubble was better established, than during the retraction. We consider the value of k_{bub} calculated from the retraction force curves as more accurate estimation of the nanobubble stiffness. Commonly, the surface tension (hence stiffness) of various liquids is measured by pulling a sphere from a liquid.⁶¹

Our results mean that the nanobubble surface has a stiffness approximately equal to the surface tension of water at 20 °C (0.072 N/m). This result is similar to the result obtained from measurements done on nanobubbles in PFT mode.³⁰ This indicates that the assumption that the bubble stiffness is equal to the surface tension, common for the macroscopic bubbles, holds also for nanoscopic bubbles and that the deformation of the bubble surface is ruled by surface tension. To date, several authors suggested low surface tension as an explanation of the increased stability of nanobubbles.^{11,38} This result, together with the shape of the force–distance curves, confirmed that we dealt with nanobubbles filled with gas and not with contamination, for example, with PDMS.⁶² In addition, our finding does not support the hypothesis that nanobubbles are high-density gas state structures that contain aggregation of gas molecules in a condensed (liquidlike) form, rather than cavities only sparsely filled with gas molecules.⁶³

Interestingly, the estimated k_{bub} value is lower than the spring constant of the cantilever $k_{\text{cant}} = 0.7$ N/m used in the measurements; that is, the bubble was very soft as compared to the cantilever. A large difference between k_{bub} and k_{cant} will likely result in a large difference in the magnitude of the (vertical) deformation of the cantilever and of the bubble. A soft bubble is likely to deform more easily and to a larger extent than a stiff cantilever. As we will discuss later, this finding may have significant consequences for the height determination of surface nanobubbles attempted previously in various AFM modes.

As shown in Figure 8b, most of the values of k_{bub} measured from the retraction force–distance curves were below the value of surface tension of pure water. This result is due to the increased hydrophobicity of the tip predicted by the capillary force model and inevitably brings up an issue of the presence of contamination in the system. It has been shown that bubbles become softer and more deformable in the presence of surfactants.⁶⁴ The hypothesis that nanobubbles are covered with the contamination layer^{11,12} or the idea of pinning of the contact line to the substrate^{13,14} possibly caused by contamination serve as explanations of the unusually long-term stability and high apparent contact angle of nanobubbles. In the force curves acquired on the nanobubbles, we did not observe any features indicating deformation or breaking of a stiff, shell-like layer of contaminants surrounding the bubbles. Although several precautions had been taken to keep the system contamination-free, we are aware that the contaminants are *always* present in a nanobubble system and their presence could not be excluded in our experiment. However, its amount, nature, and origin remain unknown to us.

Finally, we emphasize that the method described above to determine k_{bub} from the slopes in the force–distance curves acquired on nanobubbles cannot be applied if the tip used in the measurement is hydrophilic. The model of two springs in the series does not describe the tip–bubble interaction conditions well for hydrophilic tips, because there is no direct contact between the tip and the bubble during the interaction. In addition, in the dynamic interaction model, the relation

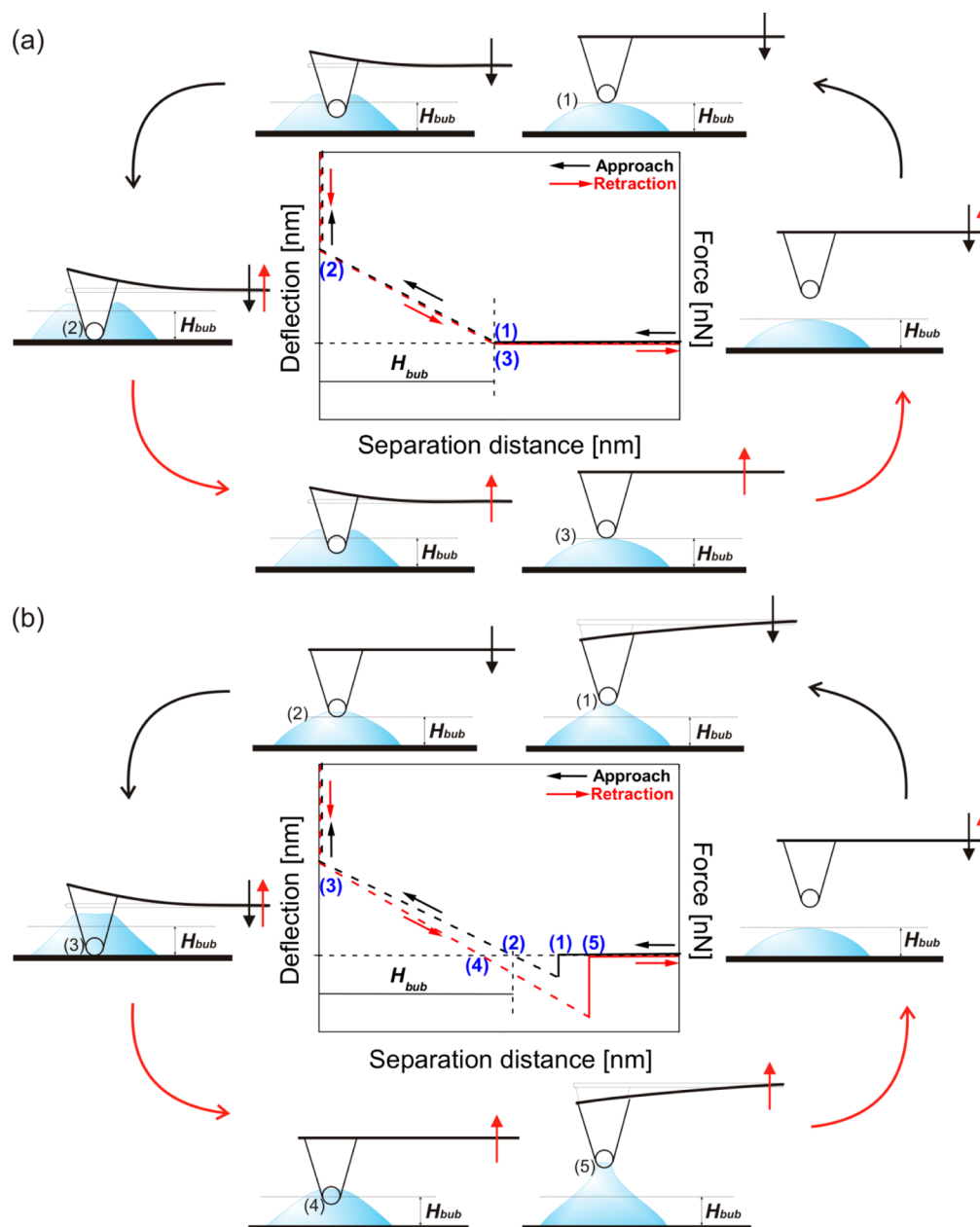


Figure 9. Typical shapes of the approach and retraction force–distance curves acquired on a nanobubble with (a) a hydrophilic AFM tip and (b) a hydrophobic AFM tip. The deflection of the cantilever gradually increases with decreasing tip–sample separation distance. The AFM cantilevers with the tips and the bubbles (drawings not to scale) are shown schematically at different stages of the interaction.

between the force and the tip–sample separation distance is not linear. Moreover, a slope of a quasi-linear dependence in the force–distance curve, similar to the one shown in Figure 5a calculated for the nanobubble scanned with a relatively soft cantilever, very often does not satisfy the condition $k_{\text{cant}} > |s\text{slope}_{N/m}|$. In the cases that the condition is fulfilled, the calculated values of k_{bub} may significantly differ from the actual nanobubble stiffness. In short, although the dynamic interaction model describes well the interaction between the hydrophilic tip and the nanobubble in the FV experiment, the scenario of the cantilever and the bubble as two springs in the series does not apply to the results provided by this model.

Bubble Deformation in AFM Experiments: Hydrophilic versus Hydrophobic Tip. From the discussion so far, it is clear that we can speak about two types of the AFM tips

that were used to measure surface nanobubbles. Now, we can reconsider the possible scenarios of the nanobubble deformation by the hydrophilic and the hydrophobic tips in the AFM experiments. The typical shapes of the approach and retraction force–distance curves acquired on the nanobubbles with the hydrophilic and with the hydrophobic tip are shown in Figure 9. They display several features that can be found in the force curves plotted in Figure 3. The schemes accompanying the plots are a visual interpretation of the data encoded in the corresponding force curves, and show the position of the tip, bending of the cantilever, and possible deformation of the bubble surface at different stages of tip–sample interaction during a single approach–retraction force curve cycle. The schemes help to understand the information encoded in the plots and the possible bubble behavior during the AFM

experiment. We stress that the drawings were not made to scale and that the actual shapes of the nanobubbles might change differently during the interaction with the real AFM tips in the experiments.

In the case of a hydrophilic tip, the repulsive forces dominate the interaction. As shown in Figure 9a, as the tip is lowered toward the bubble, the first interaction (jump-in) is measured at the separation distance approximately equal to the unperturbed bubble height H_{bub} (point 1). Importantly, at the onset of interaction, the cantilever is not bent. This is confirmed by zero attraction measured close to the jump-in point in the force–distance curve shown in Figure 3a. The jump-in is followed by the repulsion that increases (quasi-) linearly with decreased separation distance until the substrate underneath the bubble is reached (point 2). During retraction, the scenario is reversed. The repulsive force decreases as the tip is drawn further from the substrate. The interaction does not extend above the initial bubble profile, and the attractive force measured around the jump-out point is minimal (point 3). The hydrophilic tip does not directly contact the bubble at any stage of the force cycle. Instead, the tip and the bubble interact through a thin layer of liquid separating them. As the tip is lowered and subsequently retracted, increased squeezing of the liquid film generates the repulsive force between the tip and the bubble at all separation distances smaller than the unperturbed bubble height.

As shown in the schematic pictures in Figure 9a, when the hydrophilic tip is being lowered toward the substrate, the bubble “wraps” around the tip and adapts its shape to the tip profile without making a direct contact. For simplicity, we assume that only the central part of the bubble becomes deformed by the tip and that the bubble contact line remains pinned to the substrate and does not move during the force measurement. However, this might not be the case in a real FV AFM experiment.

In the case of a hydrophobic tip, the attractive and repulsive forces between the tip and the bubble compete, resulting in a more complex shape of the force curve and bubble deformation than in the case of the hydrophilic tip. As indicated in the schematic force curve sketched in Figure 9b, for the hydrophobic tip, the onset of the interaction takes place at tip–sample separation distances high *above* the unperturbed bubble surface, that is, *larger* than the unperturbed bubble height.⁵⁴ Because the hydrophobic tip attracts the bubble more than the hydrophilic tip, it is likely that the meniscus forms a neck between the tip and the bubble, which causes downward bending of the cantilever and strong attraction at the jump-in point (point 1), similar to the one in the force curve in Figure 3b. The exact magnitude of the upward deformation and the attraction strength depend on the ratio between the stiffness of the cantilever and the bubble. A cantilever that is stiffer than the bubble will deform to a lesser extent, which may lead to a substantial bubble deformation. In turn, the cantilever softer than the bubble will deform more than the bubble; that is, it will rather bend toward the bubble than let the bubble stretch upward. In the extreme case, for a very soft cantilever, the bubble will not deform upward and the position of the jump-in point in the force curve will correspond to the unperturbed bubble height. However, because relatively stiff cantilevers were used in most of the experiments done on surface nanobubbles reported so far, we suppose that in the cases when the tips used to the measurement were hydrophobic, the onset of the

interaction was located *above* the unperturbed nanobubble surface.

After the contact between the tip and the bubble has been established, the tip is lowered toward the substrate. As the hydrophobic tip approaches the substrate, the tip will be immersed deeper in the bubble. Unlike the hydrophilic tip that at the separation distance equal to H_{bub} only contacts the bubble without deforming it, the hydrophobic tip may be already immersed in the bubble so that the bubble surface may be deformed. After crossing the zero-deflection point, the upward deflection of the cantilever increases (quasi-) linearly until the tip reaches the substrate (point 3).

During the retraction, as the separation distance increases, the contact line moves down the tip. If the tip is hydrophobic, the contact line may remain attached to the tip over a long separation distance, and the bubble may stretch upward far beyond its initial size forming a neck and exerting large attractive force on the cantilever. The neck elongates and remains attached to the tip until it snaps off and the cantilever restores its initial unbent position (point 5).

The hysteresis in the force–distance curves similar to the one shown in Figure 3b is caused by the hysteresis in the contact angle of the tip material possibly caused by contaminants.

In short, force measurements done on surface nanobubbles with hydrophobic AFM tips involve direct contact between the bubble and the tip, upward bubble deformation, large adhesion, and large difference between the positions of the jump-in and jump-out points in the force–distance curve (compare with Figure 3b). All these features are absent if the measurement is done with a hydrophilic tip (compare with Figure 3a). Therefore, to minimize the nanobubble deformation during the AFM experiment, one should measure with a sharp and hydrophilic tip and with a relatively soft cantilever.

Very limited data concerning the application of the capillary force model to surface nanobubbles is available in the literature. Holmberg et al.²⁵ drew a similar conclusion based on the results of the capillary force model applied to the results of force measurements done on nanobubbles on gold. More recently, Wang et al.¹² reported a discrepancy between the (adhesion) forces calculated from the capillary force model and the force measured on a nanobubble. However, the model was applied only to a single point in the force curve, and the angle α was mistaken for the tip opening angle. The authors calculated that, to meet the measured force value, the surface tension should be as low as 0.01 N/m. This result resembles one of the scenarios predicted by the model in our experiments that was rejected as unphysical.

Our findings have an important consequence for AFM measurements of surface nanobubbles in various scanning modes. The vital information is that, in the case of hydrophilic tips, the force–distance curves acquired on nanobubbles in different FV AFM experiments will look similar, whereas in the case of hydrophobic tips the course of the force curves will be different in each experiment depending on the tip size and aspect ratio. Clearly, in the AFM experiment done on surface nanobubbles, the effects of different factors influencing the interaction will add up in a single unique force–distance curve or a bubble image. Because we do not know the exact tip size, shape, and cleanliness during the experiment, it is practically impossible to predict neither the exact character of the tip–bubble interaction during the scanning nor the bubble appearance in the AFM images. We believe that individual differences between scanning conditions and tip sizes, shapes,

and hydrophobicity explain the variety of shapes of force–distance curves and amplitude–distance curves acquired on nanobubbles in different AFM experiments. In particular, the hysteresis in the force and amplitude curves and the attractive interaction reported in the experiments on nanobubbles may be attributed to not or not adequately precleaned cantilevers and tips used.^{12,25,48} Unfortunately, the fact that the measurements were done with different cantilevers, substrates, and nucleation procedures (involving the liquid exchange) and on nanobubbles of different sizes precludes a direct comparison between the reported results.

The good agreement between the dynamic interaction model and the FV experimental data in the case of the nanobubble scanned with the hydrophilic tip discussed in this report suggests that, assuming that the tip used for the scanning is sharp and hydrophilic, nanobubble deformation in the AFM experiment has a hydrodynamic origin. We are convinced that the hydrodynamic nature of the tip–bubble interaction is responsible for the unusual spatial and temporal stability of the bubbles during scanning done in TM AFM and in peak force AFM for a wide range of scanning conditions. The presence of the thin liquid film between the bubble and the tip at all times of the interaction will prevent the tip from penetrating the bubble, attaching to it, and dragging it along the sample during the scanning. Small attractive and large repulsive forces resulting from the presence of the film will “protect” the bubble even if harsh scanning conditions will be used for imaging. This includes high scan rate and tip velocity, large amplitude of the cantilever oscillations and low amplitude set point ratio in TM, and large peak force in peak force AFM. Under all conditions, the nanobubble will adapt its shape to the tip profile and movement and will restore its original appearance as soon as the tip is withdrawn. We stress that the proposed explanation does not involve any external stabilizing mechanism and does not require the presence of any external factor, including micropancakes⁹ or pinning of the contact line and contamination layer covering the bubble.^{11–14} Moreover, we believe that the bubble instability in contact mode AFM imaging is the consequence of the large lateral forces involved. Apparently, these forces overcome the repulsion arising from the squeezing of liquid near the bubble, and the tip punctures the bubble and may drag it aside.

In the view of these results, one must consider consequences for nanobubble imaging in AFM. Hydrodynamic repulsion may be the source of height under- or overestimation. Concerning the fact that this repulsion may increase at high approach speed, it may be especially important in peak force AFM and TM AFM where approach velocity is much higher than that in FV AFM experiment. For now, however, the influence of the hydrodynamic effect on the apparent nanobubble height in the AFM images is unknown.

Finally, since the estimated nanobubble stiffness k_{bub} was of the order of 0.07 N/m, already a very small force in the range of piconewtons exerted by the tip will deform the bubble surface. In our experiment, the maximum repulsive force measured on the nanobubble was ~ 4 nN and caused severe bubble deformation (tens of nm). Because the forces involved in AFM scanning are usually in piconewton and nanonewton range, our results indicate that nanobubbles are *always* deformed during AFM imaging. In other words, nanobubbles in AFM images are *practically always* deviating from their true shape. In addition, because the size of a nanobubble and the AFM tip end are comparable, during the scanning, the tip will

deform the bubble not only locally, but rather it will distort and affect the whole bubble volume. Moreover, one may think about the tip–bubble interaction as a transfer of energy, involving work being done on interface deformation, work against the surface tension, work of tip–bubble adhesion, and work being done on the eventual rupture of the bubble surface and any layer covering it. Clearly, AFM scanning of surface nanobubbles is a complex process that requires more investigation being done.

CONCLUSIONS

Based on the results of the FV AFM measurements of surface nanobubbles on HOPG in water, we unraveled the AFM tip–nanobubble interaction and nanobubble deformation during the AFM experiment. In our experiments, the interaction resulted in mutual deformation of the bubble surface and the cantilever at all stages of the interaction. The nanobubble stiffness estimated from the slopes of the linear parts of the force–distance curves acquired on the bubbles was comparable with surface tension of water. This finding confirms the assumption that nanobubbles are very soft and presumably filled with gas. It also limits the range of the cantilevers spring constants that can yield meaningful AFM imaging results. We have shown that, in each AFM experiment, the tip and the bubble form a unique interaction system, which may lead to qualitatively and quantitatively different FV AFM results, which possess relevance also for other imaging modes. Entirely different shapes of the force curves measured on similar nanobubbles could be explained by the differences in tip sharpness, aspect ratio, and cleanliness (contact angle). By comparing the force curves measured experimentally with the variation in the interaction forces predicted by two models of the tip–bubble interaction, (1) the dynamic interaction model and (2) the capillary force model, we have revealed two mechanisms responsible for nanobubble deformation during the AFM scanning. When the measurement was done with a hydrophilic AFM tip, the tip apex interacted with the nanobubble through a thin film of liquid squeezed between the tip and the bubble surface. The bubble deformation was a dynamic effect of the drainage of the film under the influence of the external force. The bubble wrapped around the tip, adapting its shape to the tip profile and movement. The hydrodynamic origin of nanobubble deformation and the “protecting” effect of the thin liquid film offer an explanation to the unusual bubble stability observed in different AFM scanning modes and under harsh scanning conditions. In the case of the measurement done with the hydrophobic tip, the tip penetrated and directly contacted the bubble. The interaction was governed mainly by the force arising from the surface tension acting along the contact line attached to the tip. The differences between the tips in both described interaction scenarios involved qualitatively different nanobubble deformation, which was likely to affect the results of AFM imaging done with these tips. Our results indicate that the choice and control of the cantilever and the tip parameters is crucial, as it may substantially affect the nanobubble appearance in the AFM experiment, hence all the parameters derived from the measured bubble shape. To minimize the nanobubble deformation, the scanning must be done with a sharp and hydrophilic tip and with a soft cantilever. Moreover, all AFM data on nanobubbles, especially concerning the bubble shape, should be carefully acquired and critically reviewed. Finally, more investigation is needed concerning the details of the tip–

nanobubble interaction, nanobubble deformation, and the role of the parameters inherent to a particular dynamic AFM scanning modes.

■ ASSOCIATED CONTENT

📄 Supporting Information

FV AFM details, various force curves and amplitude curves acquired on the nanobubbles, and additional results of the modeling. This material is available free of charge via the Internet at <http://pubs.acs.org>.

■ AUTHOR INFORMATION

Corresponding Author

*E-mail: schoenherr@chemie.uni-siegen.de. Telephone: ++49 271 740 2806. Fax: ++49 271 740 2805.

Notes

The authors declare no competing financial interest.

■ ACKNOWLEDGMENTS

The authors would like to thank Dr. S. Druzhinin and Dr. H. Kneppel for enlightening discussions and helpful suggestions and gratefully acknowledge financial support from the Deutsche Forschungsgemeinschaft (DFG Grant No. INST 221/87-1 FUGG), the European Research Council (ERC grant to H.S., ERC Grant Agreement No. 279202), and the University of Siegen.

■ REFERENCES

- (1) Israelachvili, J. N.; Pashley, R. M. The hydrophobic interaction is long range, decaying exponentially with distance. *Nature* **1982**, *300*, 341–342.
- (2) Christenson, H. K.; Claesson, P. M. Cavitation and the interaction between macroscopic hydrophobic surfaces. *Science* **1988**, *239*, 390–392.
- (3) Parker, J. L.; Claesson, P. M.; Attard, P. Bubbles, cavities and the long-ranged attraction between hydrophobic surfaces. *J. Phys. Chem.* **1994**, *98*, 8468–8490.
- (4) Stockelhuber, K. W.; Radoev, B.; Wenger, A.; Schulze, H. J. Rupture of wetting films caused by nanobubbles. *Langmuir* **2004**, *20*, 164–168.
- (5) Maali, A.; Bhushan, B. Nanobubbles and their role in slip and drag. *J. Phys.: Condens. Matter* **2013**, *25*, 184003.
- (6) Schubert, H. Nanobubbles, hydrophobic effect, heterocoagulation and hydrodynamics in flotation. *Int. J. Miner. Process.* **2005**, *78*, 11–21.
- (7) Liu, G.; Craig, V. S. J. Improved cleaning of hydrophilic protein-coated surfaces using the combination of nanobubbles and SDS. *ACS Appl. Mater. Interfaces* **2009**, *1*, 481–487.
- (8) Craig, V. S. J. Very small bubbles at surfaces – the nanobubble puzzle. *Soft Matter* **2011**, *7*, 40–48.
- (9) Seddon, J. R. T.; Lohse, D. Nanobubbles and micropancakes: gaseous domains on immersed substrates. *J. Phys.: Condens. Matter* **2011**, *23*, 133001.
- (10) Song, B.; Walczyk, W.; Schönherr, H. Contact angles of surface nanobubbles on mixed self-assembled monolayers with systematically varied macroscopic wettability by Atomic Force Microscopy. *Langmuir* **2011**, *27*, 8223–8232.
- (11) Ducker, W. A. Contact angle and stability of interface nanobubbles. *Langmuir* **2009**, *25*, 8907–8910.
- (12) Wang, S.; Liu, M.; Dong, Y. Understanding the stability of surface nanobubbles. *J. Phys.: Condens. Matter* **2013**, *25*, 184007.
- (13) Zhang, X.; Chan, D. Y. C.; Wang, D.; Maeda, N. Stability of Interfacial Nanobubbles. *Langmuir* **2013**, *29*, 1017–1023.
- (14) Liu, Y.; Zhang, X. Nanobubble stability induced by contact line pinning. *J. Chem. Phys.* **2013**, *138*, 014706.
- (15) Brenner, M. P.; Lohse, D. Dynamic equilibrium mechanism for surface nanobubble stabilization. *Phys. Rev. Lett.* **2008**, *101*, 214505.

(16) Seddon, J. R. T.; Zandvliet, H. J. W.; Lohse, D. Knudsen gas provides nanobubble stability. *Phys. Rev. Lett.* **2011**, *107*, 116101.

(17) Petsev, N. D.; Shell, M. S.; Leal, L. G. Dynamic equilibrium explanation for nanobubbles' unusual temperature and saturation dependence. *Phys. Rev. Lett. E* **2013**, *88*, 10402.

(18) Weijs, J. H.; Lohse, D. Why surface nanobubbles live for hours. *Phys. Rev. Lett.* **2013**, *110*, 054501.

(19) Seddon, J. R. T.; Kooij, E. S.; Poelsema, B.; Zandvliet, J. W.; Lohse, D. Surface bubble nucleation stability. *Phys. Rev. Lett.* **2011**, *106*, 056101.

(20) Grosfils, P. Coarse-grained modelling of surface nanobubbles. *J. Phys.: Condens. Matter* **2013**, *25*, 184006.

(21) Berkelaar, R. P.; Zandvliet, H. J. W.; Lohse, D. Covering Surface Nanobubbles with a NaCl Nanoblanket. *Langmuir* **2013**, *29*, 11337–11343.

(22) Mazumder, M.; Bhushan, B. Propensity and geometrical distribution of surface nanobubbles: effect of electrolyte, roughness, pH, and substrate bias. *Soft Matter* **2011**, *7*, 9184–9196.

(23) Ishida, N.; Inoue, T.; Miyahara, M.; Higashitani, K. Nano bubbles on a hydrophobic surface in water observed by tapping-mode atomic force microscopy. *Langmuir* **2000**, *16*, 6377–6380.

(24) Lou, S. T.; Ouyang, Z. Q.; Zhang, Y.; Li, X. J.; Hu, J.; Li, M. Q.; Yang, F. J. Nanobubbles on solid surface imaged by atomic force microscopy. *J. Vac. Sci. Technol., B* **2000**, *18*, 2573–2575.

(25) Holmberg, M.; Kühle, A.; Garnæs, J.; Mørch, K. A.; Boisen, A. Nanobubble trouble on gold surfaces. *Langmuir* **2003**, *19*, 10510–10513.

(26) Tyrrell, J. W. G.; Attard, P. Images of nanobubbles on hydrophobic surfaces and their interactions. *Phys. Rev. Lett.* **2001**, *87*, 1761041–1761044.

(27) Agrawal, A.; Park, J.; Ryu, D. Y.; Hammond, P. T.; Russel, T. P.; McKinley, G. H. Controlling the location and spatial extent of nanobubbles using hydrophobically nanopatterned surface. *Nano Lett.* **2005**, *5*, 1751–1756.

(28) Yang, C. W.; Lu, Y. H.; Hwang, I. S. Imaging surface nanobubbles at graphite-water interfaces with different atomic force microscopy modes. *J. Phys.: Condens. Matter* **2013**, *25*, 184010.

(29) Walczyk, W.; Schön, P. M.; Schönherr, H. The effect of PeakForce tapping mode AFM imaging on the apparent shape of surface nanobubbles. *J. Phys.: Condens. Matter* **2013**, *25*, 184005.

(30) Zhao, B.; Song, Y.; Wang, S.; Dai, B.; Zhang, L.; Dong, Y.; Lü, J.; Hu, J. Mechanical mapping of nanobubbles by PeakForce atomic force microscopy. *Soft Matter* **2013**, *9*, 8837–8843.

(31) Lu, Y. H.; Yang, C. W.; Hwang, I. S. Molecular layer of gaslike domains at a hydrophobic-water interface observed by frequency-modulation atomic force microscopy. *Langmuir* **2012**, *28*, 12691–12695.

(32) Peng, H.; Hampton, P. A.; Nguyen, A. V. Nanobubbles do not sit alone at the solid–liquid interface. *Langmuir* **2013**, *29*, 6123–6130.

(33) Zhang, X. H.; Maeda, N.; Craig, V. S. J. Physical properties of nanobubbles on hydrophobic surfaces in water and aqueous solutions. *Langmuir* **2006**, *22*, 5025–5035.

(34) Walczyk, W.; Schönherr, H. Closer look at the effect of AFM imaging conditions on the apparent dimensions of surface nanobubbles. *Langmuir* **2013**, *29*, 620–632.

(35) Borkent, B. M.; de Beer, S.; Mugele, F.; Lohse, D. On the shape of surface nanobubbles. *Langmuir* **2010**, *26*, 260–268.

(36) Yang, S.; Kooij, E. S.; Poelsema, B.; Lohse, D.; Zandvliet, H. J. W. Correlation between geometry and nanobubble distribution on HOPG surface. *Europhys. Lett.* **2008**, *81*, 64006.

(37) Steitz, R.; Gutberlet, T.; Hauss, T.; Klösgen, B.; Krastev, R.; Schemmel, S.; Simonsen, A. C.; Findenegg, G. H. Nanobubbles and their precursor layer at the interface of water against a hydrophobic substrate. *Langmuir* **2003**, *19*, 2409–2418.

(38) Zhang, X. H.; Quinn, A.; Ducker, W. A. Nanobubbles at the interface between water and a hydrophobic solid. *Langmuir* **2008**, *24*, 4756–4764.

- (39) Switkes, M.; Ruberti, J. W. Rapid cryofixation/freeze fracture for the study of nanobubbles at solid–liquid interfaces. *Appl. Phys. Lett.* **2007**, *84*, 4759–4761.
- (40) Yang, J.; Duan, J.; Fornasiero, D.; Ralston, J. Kinetics of CO₂ nanobubble formation at the solid/water interface. *Phys. Chem. Chem. Phys.* **2007**, *9*, 6327–6332.
- (41) Jensen, T. R.; Jensen, M. O.; Reitzel, N.; Balashev, K.; Peters, G. H.; Kjaer, K.; Bjørnholm, T. Water in contact with extended hydrophobic surfaces: Direct evidence of weak dewetting. *Phys. Rev. Lett.* **2003**, *90*, 0861.
- (42) Mezger, M. A.; Schöder, S. A. B.; Reichert, H. A.; Schröder, H. A.; Okasinski, J. A.; Honkimäki, V. B.; Ralston, J. C.; Bilgram, J. D.; Roth, R. A. E.; Dosch, H. Water and ice in contact with octadecyltrichlorosilane functionalized surfaces: a high resolution x-ray reflectivity study. *J. Chem. Phys.* **2008**, *128*, 244705.
- (43) Zhang, L.; Zhao, B.; Xue, L.; Guo, Z.; Dong, Y.; Fang, H.; Tai, R.; Hu, J. Imaging interfacial micro- and nano-bubbles by scanning transmission soft X-ray microscopy. *J. Synchrotron Radiat.* **2013**, *20*, 413–418.
- (44) Karpitschka, S.; Dietrich, E.; Seddon, J. R. T.; Zandvliet, H. J. W.; Lohse, D.; Riegler, H. Noninvasive optical visualization of surface nanobubbles. *Phys. Rev. Lett.* **2012**, *109*, 066102.
- (45) Mirsaidov, U.; Ohl, C.-D.; Matsudaira, P. A direct observation of nanometer-size void dynamics in an ultra-thin water film. *Soft Matter* **2012**, *8*, 3108–3111.
- (46) Chan, C. U.; Ohl, C.-D. Total-internal-reflection-fluorescence microscopy for the study of nanobubble dynamics. *Phys. Rev. Lett.* **2012**, *109*, 174501.
- (47) Weisenhorn, A. L.; Khirsandi, M.; Kasas, S.; Gotzos, V.; Butt, H.-J. Deformation and height anomaly of soft surfaces studied with an AFM. *Nanotechnology* **1994**, *4*, 106–113.
- (48) Wang, Y.; Bhushan, B. Boundary slip and nanobubble study in micro/nanofluidics using atomic force microscopy. *Soft Matter* **2010**, *6*, 29–66.
- (49) Tyrrell, J. W. G.; Attard, P. Atomic force microscope images of nanobubbles on a hydrophobic surface and corresponding force-separation data. *Langmuir* **2002**, *18*, 160–167.
- (50) Ally, J.; Kappl, M.; Butt, H.-J.; Amirfazli, A. Detachment Force of Particles from Air-Liquid Interfaces of Films and Bubbles. *Langmuir* **2010**, *26*, 18135–18143.
- (51) Walczyk, W.; Hain, N.; Schönherr, H. *Soft Matter* **2014**, submitted.
- (52) Ducker, W. A.; Xu, Z.; Israelachvili, J. N. Measurements of Hydrophobic and DLVO Forces in Bubble-Surface Interactions in Aqueous Solutions. *Langmuir* **1994**, *10*, 3279–3289.
- (53) Preuss, M.; Butt, H.-J. Direct measurement of forces between particles and bubbles. *Int. J. Miner. Process.* **1999**, *56*, 99–115.
- (54) Walczyk, W.; Schönherr, H. Manuscript in preparation.
- (55) Chan, D. Y. C.; Dagastine, R. R.; White, L. R. Forces between a rigid probe particle and a liquid interface I. The repulsive case. *J. Colloid Interface Sci.* **2001**, *236*, 141–154.
- (56) Dagastine, R. R.; White, L. R. Forces between a rigid probe particle and a liquid interface II. The general case. *J. Colloid Interface Sci.* **2002**, *247*, 310–320.
- (57) Tabor, R. F.; Grieser, F.; Dagastine, R. R.; Chan, D. Y. C. Measurement and analysis of forces in bubble and droplet systems using AFM. *J. Colloid Interface Sci.* **2012**, *371*, 1–14.
- (58) Johnson, D. J.; Miles, N. J.; Hilal, N. Quantification of particle–bubble interactions using atomic force microscopy: A review. *Adv. Colloid Interface Science* **2006**, *127*, 67–81.
- (59) Connell, S. D. A.; Allen, S.; Roberts, C. J.; Davies, J.; Davies, M. C.; Tendler, S. J. B.; Williams, P. M. Investigating the interfacial properties of single-liquid nanodroplets by atomic force microscopy. *Langmuir* **2002**, *18*, 1719–1728.
- (60) Arafat, A.; Giesbers, M.; Rosso, M.; Sudhölter, E. J. R.; Schroën, K.; White, R. G.; Yang, L.; Linford, M. R.; Zuilhof, H. Covalent biofunctionalization of silicon nitride surfaces. *Langmuir* **2007**, *23*, 6233–6244.
- (61) Scheludko, A. D.; Nikolov, A. D. Measurement of surface tension by pulling a sphere from a liquid. *Colloid Polym. Sci.* **1975**, *253*, 396–403.
- (62) Hillborg, H.; Tomczak, N.; Oläh, A.; Schönherr, H.; Vancso, G. J. Nanoscale hydrophobic recovery: A chemical force microscopy study of UV/ozone-treated cross-linked poly(dimethylsiloxane). *Langmuir* **2004**, *20*, 785–794.
- (63) Wang, C.; Li, Z.; Li, J.; Peng, X.; Hu, J.; Fang, H. High density gas state at water/graphite interface studied by molecular dynamics simulation. *Chin. Phys. B* **2008**, *17*, 2646–2654.
- (64) Zhang, X.; Uddin, Md. H.; Yang, H.; Toikka, G.; Ducker, W.; Maeda, N. Effects of surfactants on the formation and the stability of interfacial nanobubbles. *Langmuir* **2012**, *28*, 10471–10477.

Supporting Information

Characterization of the interaction

between AFM tips and surface nanobubbles

*Wiktoria Walczyk and Holger Schönherr**

Physical Chemistry I, University of Siegen, Department of Chemistry and Biology, Adolf-Reichwein-Str. 2, 57076 Siegen, Germany

Corresponding Author

* schoenherr@chemie.uni-siegen.de

Force-Volume mode (FV) AFM measurement

Force Volume AFM mode is used to study mechanical properties of the sample or forces between surfaces on the nanoscale in air and in liquid environment. Unlike the Tapping Mode or the Contact Mode AFM, the FV is not strictly an “imaging” mode because the tip does not follow the surface to create a topographic image of the sample. Different purpose of the scanning imposes entirely different movement of the tip during the scanning. The schematic in Figure S1 shows the basic principles of the AFM force measurement that was carried out in the experiment.

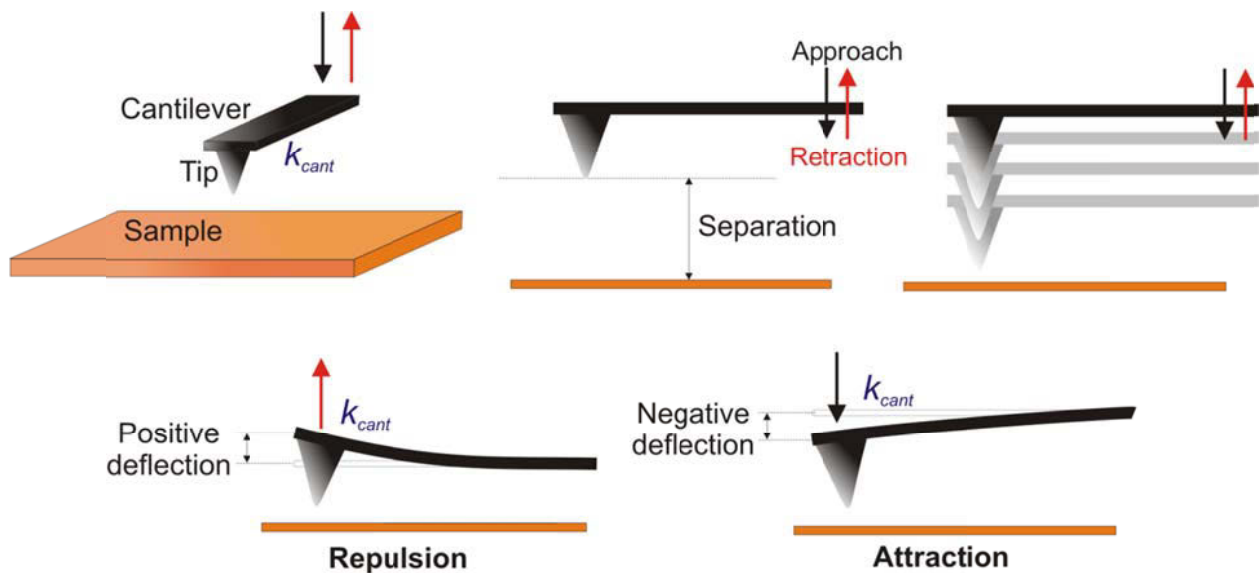


Figure S1. The principle of FV AFM measurement shown schematically. The tip is repeatedly lowered and retracted from the sample. During the movement, the deflection of the flexible cantilever end caused by the tip-sample interaction forces is measured as a function of the piezo displacement, which can be transformed to tip-sample separation distance.

Contrary to TM AFM, in the FV mode, the cantilever is usually not oscillated. At each point of the selected area of the sample, the tip mounted on the cantilever is lowered towards the substrate surface and then retracted. Because the cantilever is flexible, the forces acting on the

tip will cause a bending of the cantilever. Repulsive tip-sample interaction forces cause an upward bending (denoted as positive deflection); attractive forces will cause a downward bending (negative deflection). The magnitude of the forces acting on the tip is calculated by multiplying the deflection value by the cantilever stiffness. During a single cycle of the vertical movement of the cantilever, the deflection data of the cantilever during approach and retraction are acquired as a function of (piezo) displacement, to form a pair of force-displacement curves. The force-displacement curves may be acquired sequentially on different positions on the sample in order to create a force image of the sample.

Alternatively, the cantilever may be oscillated and a decrease in the oscillation amplitude due to interaction forces is measured as a function of the tip-sample separation. An amplitude image of the sample may be created in a similar way as a force image.

The main advantage of FV over TM AFM is the fact that the force exerted on the sample by the AFM tip is known and well controlled at each point of the area scanned. In a particular experiment, one may limit the maximum cantilever deflection that defines the maximum force exerted on the sample. This is beneficial, especially while investigating very soft and fragile samples that can be damaged easily. Alternatively, as it was done in the experiment on surface nanobubbles, one may set the maximum deflection threshold high to ensure that during the approach the tip is moved all the way down through the layer of the soft material until it meets the hard HOPG substrate.

The shapes of the force-displacement curves acquired on the sample in FV AFM contain valuable information on various mechanical properties and deformation of (soft) materials.

Force curves measured on the HOPG sample

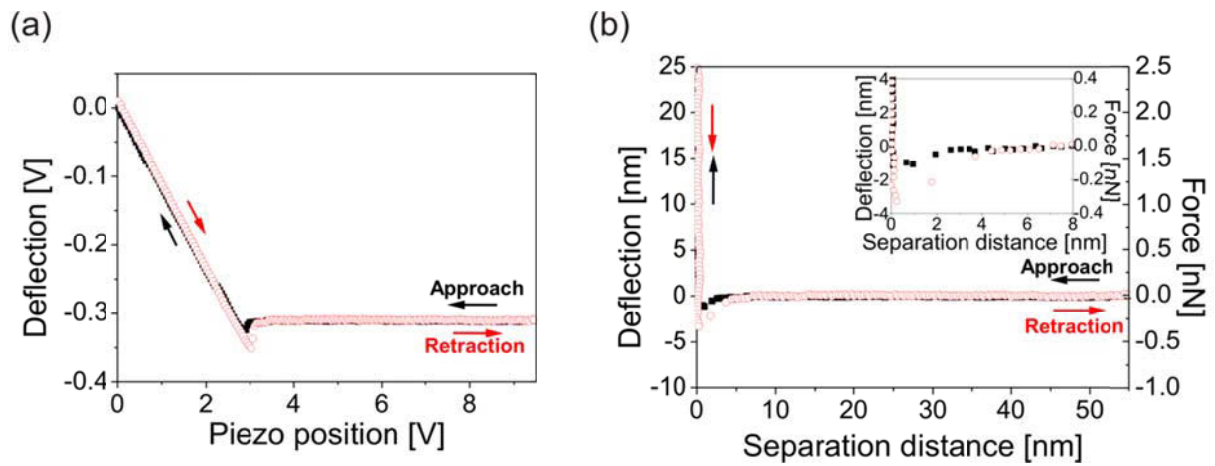


Figure S2. (a) Typical unprocessed approach and retraction force-displacement curves acquired on HOPG surface in water. These curves were converted to force-distance curves, compared in (b). In (b), the graphite surface is represented as zero separation distance. The inset shows a magnification of the data points measured at separation distances of few nanometers to the graphite. The cantilever spring constant k_{cant} was 0.1 N/m.

The initial position of the tip in the force cycle was at the point of maximum separation far from the sample surface. The separation distance gradually decreased as the tip approached the sample. The cantilever remained in its initial non-bent position, until the tip-sample separation distance of a few nanometers, where attractive short-range van der Waals forces caused a downward bending of the cantilever (snap to contact). The attraction was almost immediately followed by a strong repulsion as the tip contacted the HOPG surface. Upon retraction, the behavior of the cantilever was reversed.

Force curves measured on the nanobubbles

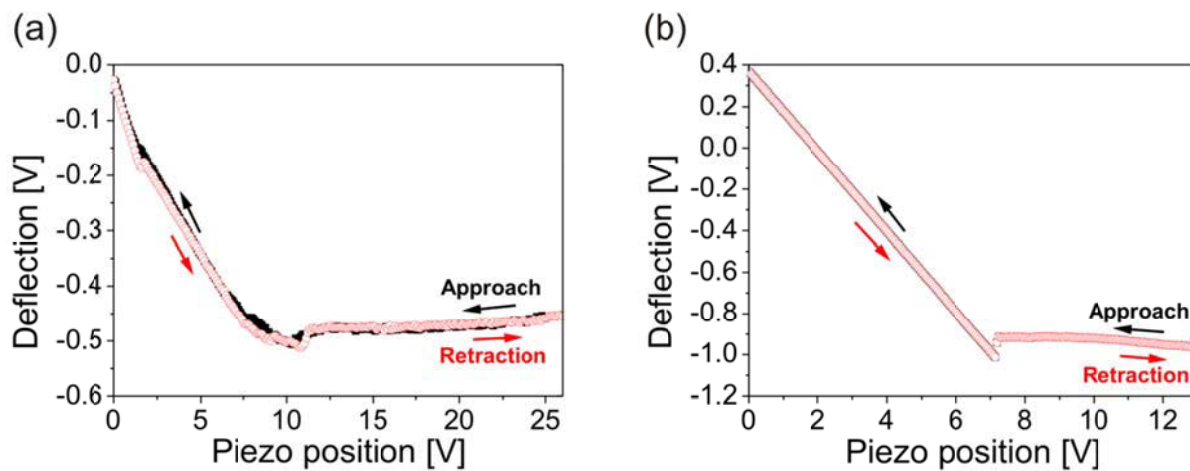


Figure S3. Unprocessed approach and retract force-displacement curves acquired on two nanobubbles. These curves correspond to the processed force curves shown in Figure 3. The spring constant of the cantilever used to acquire the data was $k_{cant} = 0.1$ N/m for (a) and $k_{cant} = 0.7$ N/m for (b).

Amplitude curves measured on a nanobubble

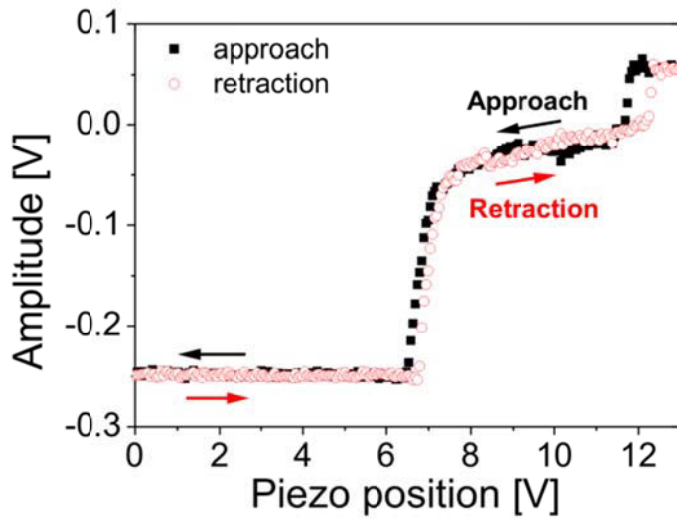


Figure S4. Unprocessed approach and retract amplitude-displacement curves acquired on a nanobubble. The plateau is similar to the plateau observed in the force-distance curves measured on the nanobubble shown in Figure 3b. The spring constant of the cantilever used to acquire the data was $k_{cant} = 0.7$ N/m.

Dynamic interaction model – modelling results

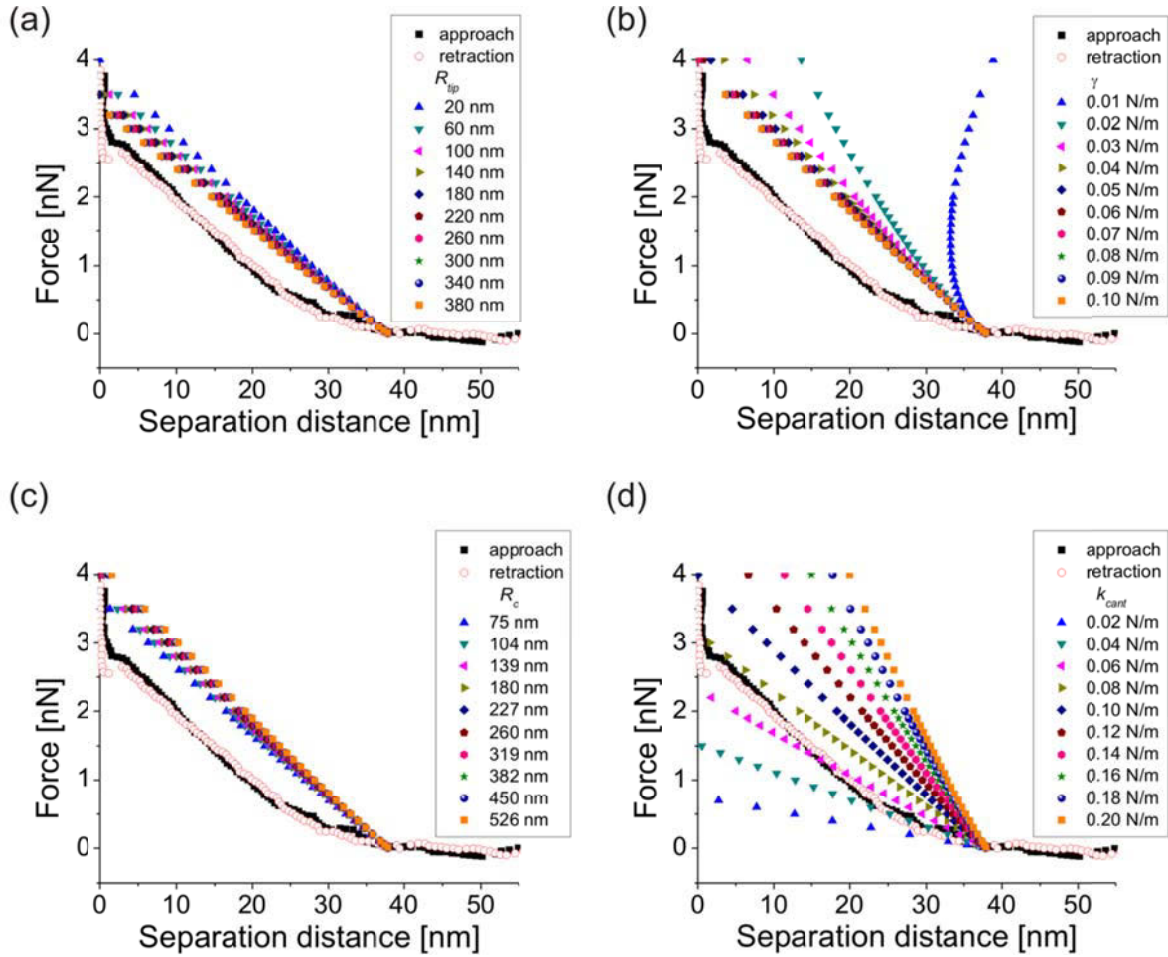


Figure S5. AFM tip-nanobubble interaction forces as a function of the separation distance to the substrate measured experimentally on the bubble with a hydrophilic tip and calculated from the dynamic interaction model for different values of the parameters: (a) radius of curvature of the tip R_{tip} , (b) surface tension γ , (c) radius of the curvature of the bubble R_c (related to the nanoscopic contact angle θ_{nano}), and (d) cantilever spring constant k_{cant} .

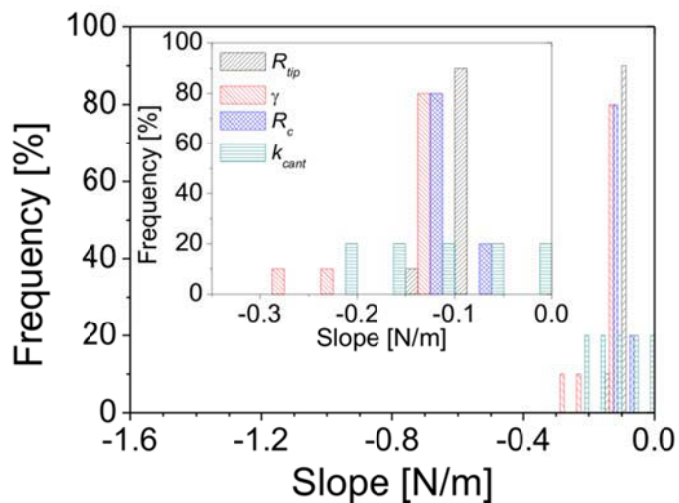


Figure S6. Histograms of slopes of the linear parts of the force-distance curves calculated for various parameters of the dynamic interaction model R_{tip} , surface tension γ , R_c (related to the nanoscopic contact angle θ_{nano}), and k_{cant} . The inset shows a magnification of the plotted data.

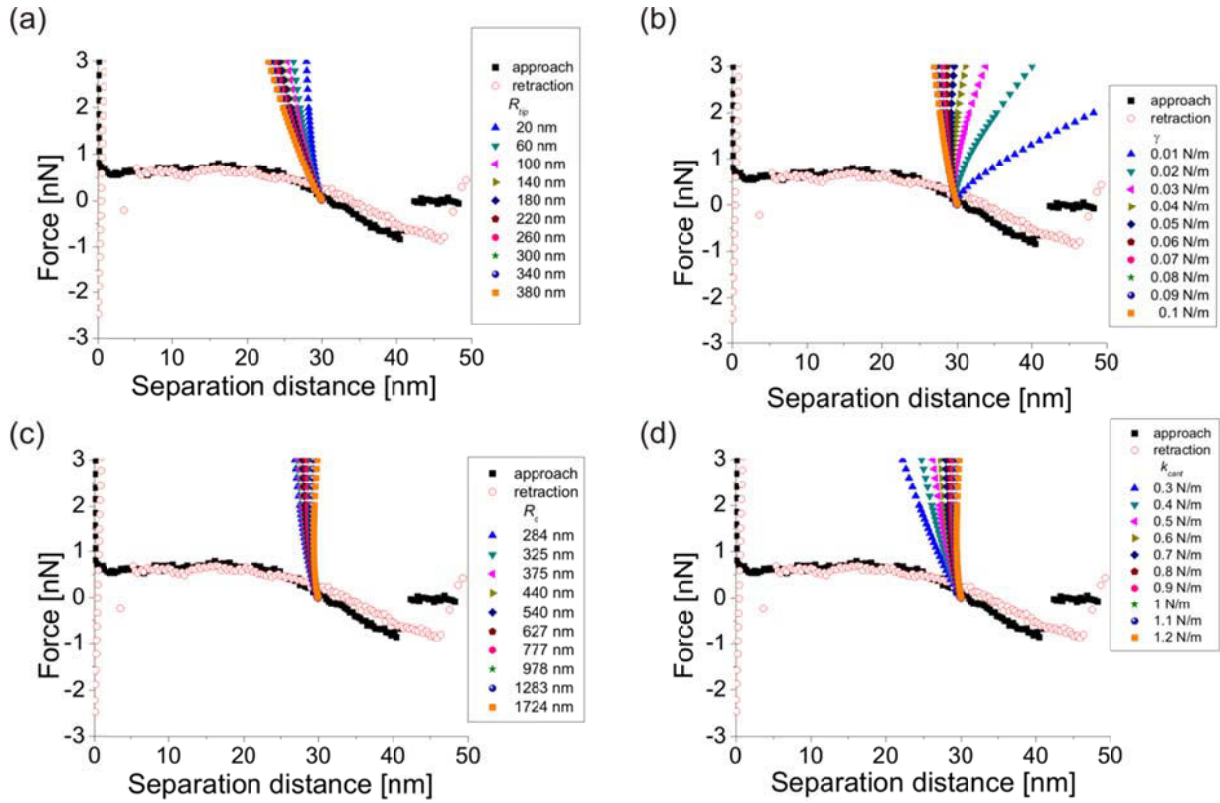


Figure S7. AFM tip-nanobubble interaction forces as a function of the separation distance to the substrate measured experimentally on the bubble with a hydrophobic tip and calculated from the dynamic interaction model for different values of the parameters: (a) radius of curvature of the tip R_{tip} , (b) surface tension γ , (c) radius of the curvature of the bubble R_c (related to the nanoscopic contact angle θ_{nano}), and (d) cantilever spring constant k_{cant} .

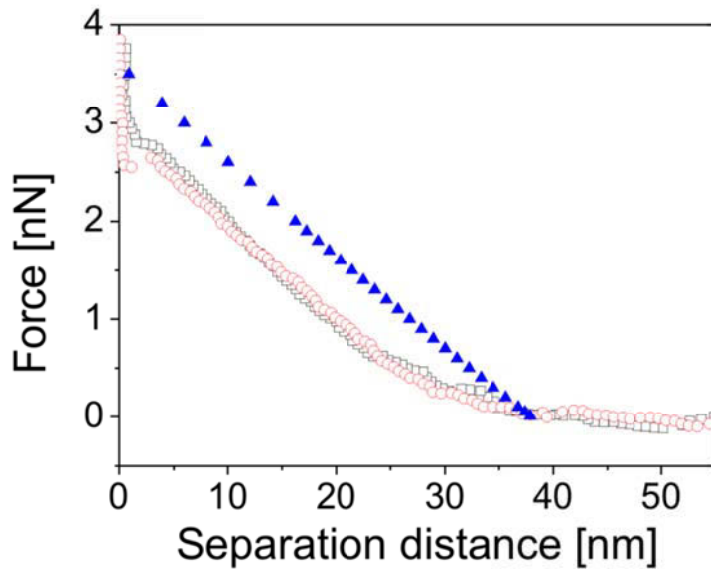


Figure S8. AFM tip-nanobubble interaction forces as a function of the separation distance to the substrate measured experimentally (open symbols) with a hydrophilic AFM tip and calculated from the dynamic interaction model (solid symbols) for tip radius $R_{tip} = 120$ nm, surface tension $\gamma = 0.07$ N/m, bubble radius of curvature $R_c = 260$ nm, contact angle $\theta_{nano} = 149^\circ$, $k_{cant} = 0.1$ N/m.

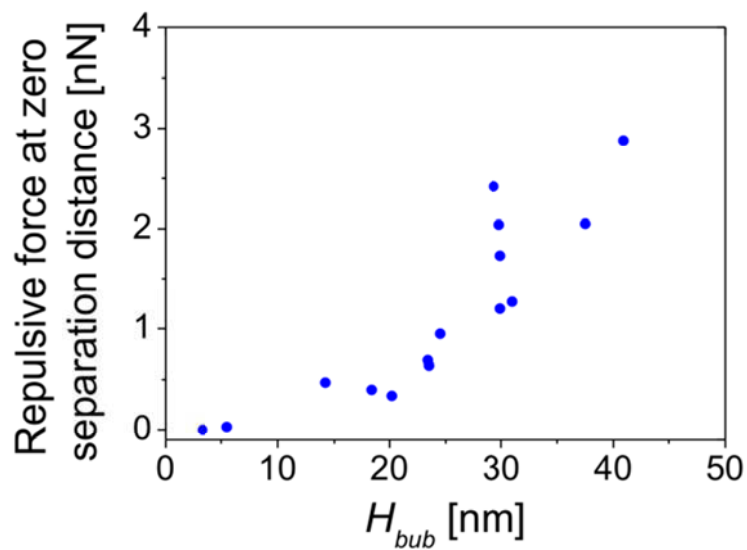


Figure S9. Repulsive force measured on the nanobubble at zero tip-sample separation distance as function of the unperturbed bubble height H_{bub} (initial tip-sample separation in the dynamic interaction model).

Capillary force model – modelling results

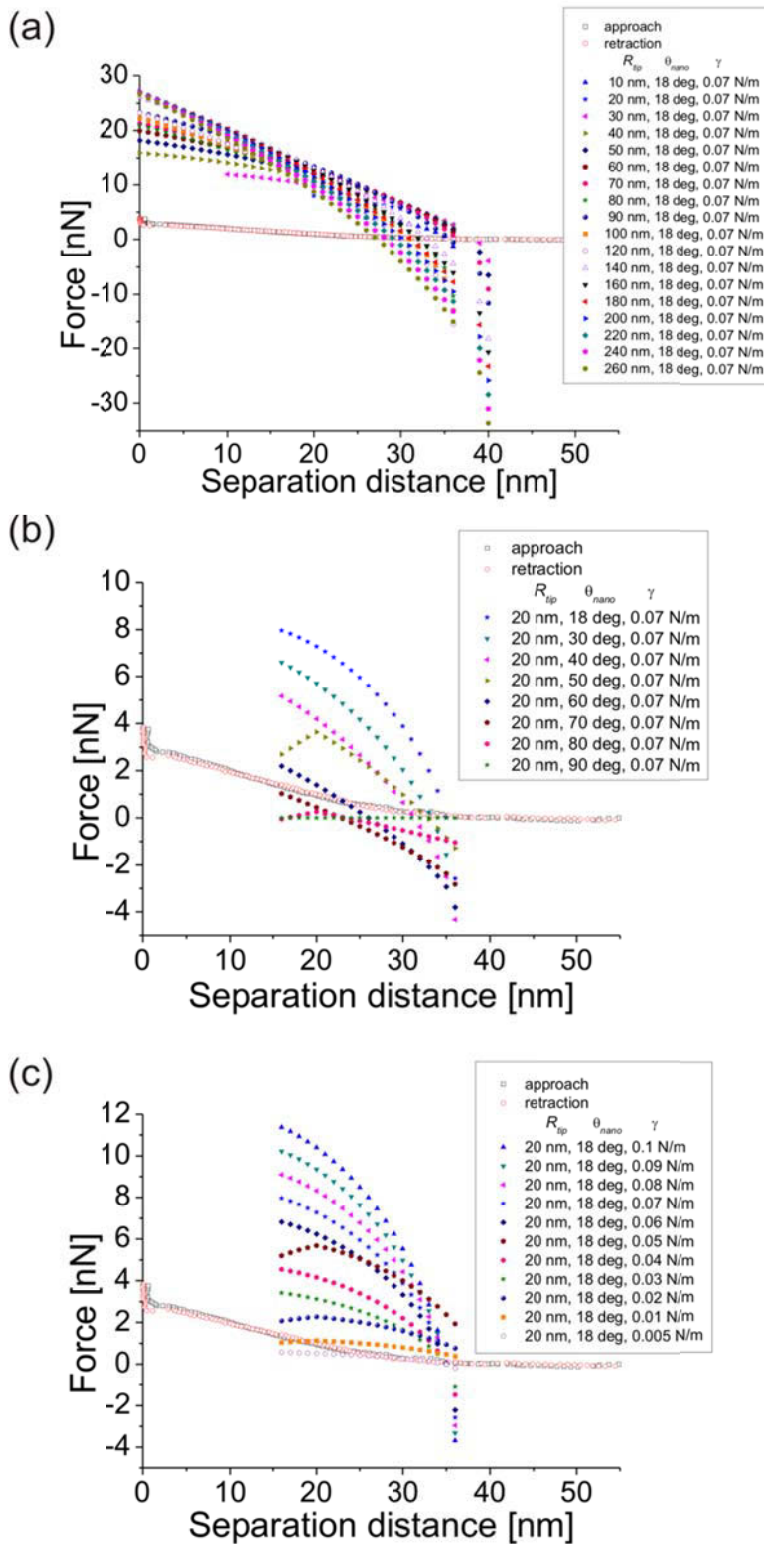


Figure S10. AFM tip-nanobubble interaction forces as a function of the separation distance to the substrate measured experimentally (open symbols) on the nanobubble in Figure 1a with the hydrophilic tip, and calculated from the capillary force model (solid symbols). Various data sets show the influence of the values of the tip radius R_{tip} , tip material contact angle θ_{tip} , and surface tension γ used in the model on the course of the force curves. The spring constant of the cantilever used to acquire the experimental data was $k_{cant} = 0.1$ N/m.

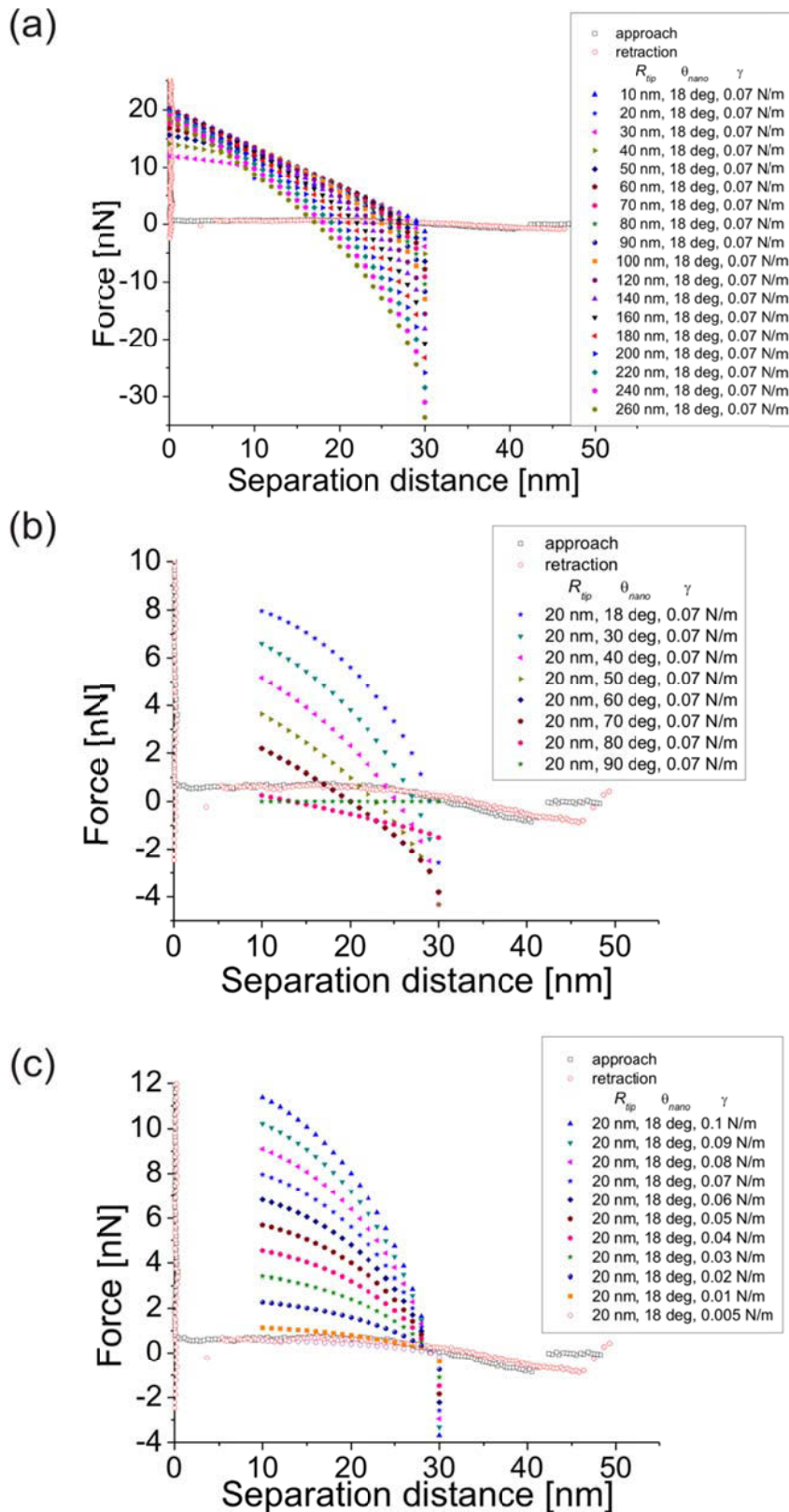


Figure S11. AFM tip-nanobubble interaction forces as a function of the separation distance to the substrate measured experimentally (open symbols) on the nanobubble in Figure 1d with the hydrophobic tip, and calculated from the capillary force model (solid symbols). Various data sets show the influence of the values of the tip radius R_{tip} , tip material contact angle θ_{tip} , and surface tension γ used in the model on the course of the force curves. The spring constant of the cantilever used to acquire the experimental data was $k_{cant} = 0.7$ N/m.

8

Hydrodynamic effect of the tip movement on surface nanobubbles

Depending on the AFM imaging mode, the tip movement during scanning is different. In particular, varying directions and speed of the tip movement may have implications for the imaging of soft samples. In this chapter, we directly compare the effect of different tip-nanobubble interactions in tapping mode, lift mode and Force Volume (FV) mode AFM. We measured and analyzed the strength and character of the interactions as functions of the vertical and horizontal position of the tip on the bubble with respect to the bubble center, and compared them with the results calculated using the dynamic tip-bubble interaction model. We found a variation in the strength of the hydrodynamic effect depending on the direction from which the tip approached the bubble during the scanning. Our findings indicate that the direction of tip movement influences the bubble deformation and should be considered, when analyzing images of nanobubbles acquired in various AFM scanning modes.

The chapter consists of the following publication:

**Hydrodynamic effects of the tip movement on surface nanobubbles:
A combined tapping mode, lift mode and force volume mode AFM study**

Wiktoria Walczyk, Nicole Hain and Holger Schönherr

Soft Matter **2014**, DOI: 10.1039/C4SM01024H

Reproduced by permission of The Royal Society of Chemistry.

Contribution in the article:

Wiktoria Walczyk: AFM data analysis , AFM tip-nanobubble interacion modelling;

Nicole Hain: AFM measurements.

The experiment was designed by **Prof. Dr. Holger Schönherr**. Based on discussions and guidance from **Prof. Dr. Holger Schönherr**, the manuscript was drafted by **Wiktoria Walczyk**, and perfected by **Prof. Dr. Holger Schönherr**.

Hydrodynamic effects of the tip movement on surface nanobubbles: a combined tapping mode, lift mode and force volume mode AFM study

Cite this: DOI: 10.1039/c4sm01024h

Wiktorja Walczyk,† Nicole Hain† and Holger Schönherr*

We report on an Atomic Force Microscopy (AFM) study of AFM tip-nanobubble interactions in experiments conducted on argon surface nanobubbles on HOPG (highly oriented pyrolytic graphite) in water in tapping mode, lift mode and Force Volume (FV) mode AFM. By subsequent data acquisition on the same nanobubbles in these three different AFM modes, we could directly compare the effect of different tip-sample interactions. The tip-bubble interaction strength was found to depend on the vertical and horizontal position of the tip on the bubble with respect to the bubble center. The interaction forces measured experimentally were in good agreement with the forces calculated using the dynamic interaction model. The strength of the hydrodynamic effect was also found to depend on the direction of the tip movement. It was more pronounced in the FV mode, in which the tip approaches the bubble from the top, than in the lift mode, in which the tip approaches the bubble from the side. This result suggests that the direction of tip movement influences the bubble deformation. The effect should be taken into account when nanobubbles are analysed by AFM in various scanning modes.

Received 10th May 2014
Accepted 18th June 2014

DOI: 10.1039/c4sm01024h

www.rsc.org/softmatter

1 Introduction

Surface nanobubbles that appear on surfaces immersed in water are responsible for the attraction between hydrophobic surfaces in water,^{1–3} rupture of thin liquid films,^{4,5} and hydrodynamic slip.⁶ They play a role in immersion lithography,⁷ froth flotation,⁸ and are a useful tool for cleaning surfaces fouled with proteins or nanoparticles.^{9,10} Furthermore surface nanobubbles have been studied by various techniques including Atomic Force Microscopy (AFM),^{11–13} neutron reflectivity,¹⁴ attenuated total internal reflection Fourier transform infrared (FTIR) spectroscopy,¹⁵ rapid cryofixation,¹⁶ quartz crystal microbalance,¹⁷ X-ray reflectivity,^{18,19} synchrotron-based scanning transmission soft X-ray microscopy (STXM),²⁰ interference microscopy,²¹ and total internal reflection fluorescence microscopy.^{22,23}

Surface nanobubbles were found to be very soft and deformable. Their stiffness is comparable with the surface tension of water.^{24,25} Based on their shape measured from AFM images, the estimated Laplace pressure exceeds the atmospheric pressure significantly, which should lead to their rapid dissolution. However, experimental observations confirmed that surface nanobubbles are stable for long periods of time.^{26,27} Importantly, the internal pressure is calculated from the

apparent nanobubble size and profile, which is extremely flat with nanoscopic contact angles higher than the macroscopic ones.^{28–30} The unusual stability and high nanoscopic contact angles observed are issues that need to be addressed by the various theories on surface nanobubbles. These theories emphasize the role of contamination,^{27,31,32} the substrate and pinning of the three phase contact line,^{33–35} gas exchange between the bubble interior and surrounding liquid,^{36–40} and the presence of surface charges.⁴¹

An accurate determination of the bubble size and shape is therefore critical. Practically all data in this respect has been derived from AFM experiments. However, it has been shown that AFM imaging may lead to several artefacts and complex sample deformation⁴² and that the shape of nanobubbles in AFM height images may not reflect the real bubble size and shape.^{24,43} It is in general difficult to extract the actual shape of nanobubbles from a single AFM image because each image combines the information about the sample, the AFM tip and a number of parameters related to the scanning procedure. So far, it has been shown that the apparent bubble height and radius of curvature of surface nanobubbles in AFM height images depend on the tip shape,³⁰ the amplitude of the cantilever oscillations and the amplitude setpoint ratio in TM (Tapping Mode) AFM^{43–46} and on the peak force in Peak Force Tapping AFM.^{25,47,48}

Moreover, the choice of the AFM tip *i.e.* size, material and cleanliness are crucial and can entirely change the result of AFM experiments on surface nanobubbles.²⁴ Only if the tip is hydrophilic, the interaction between the tip and the bubble is

Physical Chemistry I, University of Siegen, Department of Chemistry and Biology, Adolf-Reichwein-Str. 2, 57076 Siegen, Germany. E-mail: schoenherr@chemie.uni-siegen.de

† These authors contributed equally.

ruled by hydrodynamic forces. In this case a thin film of water remains between the tip and the bubble surfaces at all stages of (intermittent) contact. Pressing the tip against the bubble surface causes its deformation and a squeezing of the liquid film that gives rise to the dynamic forces acting on the tip. During the AFM measurement, the hydrophilic tip “slides” over the bubble surface and the bubble continuously adapts its shape to the shape of the tip. By contrast, a contaminated or hydrophobic tip attracts the bubble surface, penetrates the bubble during the contact and may even drag the bubble over the sample. In extreme cases, it may move nanobubbles away from the scanning area. Therefore, hydrophobic tips are not suitable to interrogate nanobubbles.

In addition, low force conditions must be employed, which demand a sharp, hydrophilic tip and a cantilever with a small spring constant as well as small amplitudes of the cantilever oscillations and high amplitude setpoint ratios in TM. During the measurement the tip always distorts the bubble surface and as a result a distorted bubble shape is detected in the height image. This effect is independent from the scanning mode. Hence in order to extract information about the actual bubble shape and size from AFM images, it is necessary (i) to know which parameters influence the bubble appearance in the experiment and (ii) to estimate their individual contributions to the particular image. Importantly, one should not directly compare images of nanobubbles acquired under entirely different (or unknown) scanning conditions.

While we can compare the data obtained using different experimental conditions in a particular scanning mode, it remains more difficult to compare results obtained in different AFM modes. Most of the experiments were carried out in TM,^{11,28,36–40,49} CM (Contact Mode),^{12,13,50,51} Peak Force Mode,^{25,47,48} FM (Frequency Modulation) mode,^{47,52} force spectroscopy (Force–Volume mode or FV mode),⁵³ non-contact mode,³⁵ and lift mode AFM.⁴⁹ All these modes have their own specific methods of data acquisition, scanning procedures and parameters involved.

In order to shed light on the response of nanobubbles to the scanning tip in different AFM modes, we conducted an experiment on surface nanobubbles in three different AFM imaging modes: TM, lift mode and FV mode AFM. In particular, we discuss the tip–bubble interactions and nanobubble deformation under different AFM imaging conditions for individual bubbles.

2 Experimental

Sample preparation

In the experiments freshly cleaved highly oriented pyrolytic graphite (HOPG) (Veeco, grade ZYH) with a water contact angle of $63 \pm 2^\circ$ was used. The static contact angle was measured with the sessile drop method with an OCA 15plus instrument (Data Physics Instruments GmbH, Filderstadt, Germany) using Milli-Q water obtained from a Millipore Direct Q8 system (Millipore, Schwalbach, Germany) with resistivity of $18.0 \text{ M}\Omega \text{ cm}^{-1}$. Nanobubbles were measured in Argon saturated Milli-Q water, which was prepared as reported earlier.²⁴

Atomic force microscopy

The AFM measurements were carried out on a MultiMode IIIA AFM instrument (Bruker/Veeco, Santa Barbara, California) with a vertical engage E-scanner and NanoScope version 3.10 software (Bruker/Veeco AXS, Santa Barbara, CA). V-shaped MLTC Si_3N_4 cantilevers (Bruker AXS, Camarillo, CA) with a spring constant of $k_{\text{cant}} = 0.05 \pm 0.005 \text{ N m}^{-1}$ was used. The spring constant was independently calibrated on an Asylum Research MFP-3D Bio (Asylum Research, Santa Barbara, California). The cantilever was cleaned prior to the measurements for 60 s by oxygen plasma (Plasma PrepITM, SPI Supplies, West Chester, USA).

In all experiments, a closed liquid cell configuration was used. First, the liquid cell, the O-ring (fluorosilicone rubber) and the silicone inlet and outlet tubes were rinsed with Milli-Q water and with ethanol (99.9%, Merck KGaA, Darmstadt, Germany) and dried in a stream of nitrogen. Next, the liquid cell was assembled and the cantilever was inserted. Subsequently, a 1 mL sterile syringe (Braun, Injekt-F 0.01-1mL/luer Solo) cleaned with Milli-Q water was filled with the Ar saturated water and connected to the inlet tube. No needle was used. Immediately afterwards the water was injected in the liquid cell until the cantilever was immersed and the O-ring was filled. Then the liquid cell was put on the sample, the O-ring was brought in contact with the sample, 0.6 mL of water was passed through the liquid cell and after that, the inlet and outlet were closed. We stress that *no* liquid exchange procedure was performed and the HOPG surface did not have contact with ethanol at any stage of the experiment. Before the start of the AFM measurement, the system was left to equilibrate for 30 min. The nanobubbles were then scanned first in TM AFM and subsequently in lift mode and in force volume mode AFM without changing the cantilever and the tip or replacing the liquid.

The TM deflection data reported in this study refer to the root mean square (rms) averaged cantilever deflection (TM deflection) that can be recorded in TM AFM as a separate channel in addition to conventional height (vertical piezo displacement to keep a constant amplitude), amplitude and phase. This deflection signal (also in deflection–displacement curves) is low-pass filtered to eliminate the high-frequency Tapping Mode oscillation. For technical details, see, *e.g.* Veeco MultiMode SPM Instruction Manual RevB Nanoscope5 pp.199–200.

Lift mode

Deflection images were acquired in the interleave scan in the linear lift mode. Each line was first scanned in the forward direction (trace) in TM with the following settings: drive frequency 29.6 kHz, free amplitude 46 nm and setpoint ratio 94%. After completing the line, the tip was lifted 200 nm in order to pull the tip off the surface. Next, the cantilever oscillation was switched off, the tip was lowered to the requested lift height and the line was rescanned at fixed lift height above the start point of the line in the backward direction (retrace) in the lift mode, *i.e.* the lift mode scan did not follow the contour of the line recorded in TM during the trace scan. All AFM

deflection images shown here are retrace images. Raw height and deflection images were processed using a 1st order plane fit and a 0th order flattening (with nanobubbles excluded). The data analysis was performed with Nanoscope software version 3.10. The bubble size in TM height images was measured using the spherical cap fitting without applying a correction for the tip size.³⁰

Force volume mode (FV AFM)

In this mode, the tip was lowered and retracted at each point of the selected area of the sample and the interaction forces during approach and retraction were measured. The resolution of the grid of positions imaged was limited to 32×32 pixels.² The cantilever oscillation was switched off. The tip approach velocity was set to $1.02 \mu\text{m s}^{-1}$ and the force curve resolution to 512 points per single force curve cycle. The raw deflection–distance curves were transformed into deflection–separation curves.⁵⁴ The vertical position of the tip above the substrate is represented in the plots by the tip–sample separation distance. The deflection was recalculated into force by multiplying the measured deflection value with the cantilever stiffness.

3 Results

In the experiments, argon surface nanobubbles were investigated in TM, lift mode and FV AFM. Fig. 1 shows the principles of data acquisition and details of the tip operation in scanning in the three considered imaging modes. In TM AFM, the cantilever is oscillated near resonance and the oscillating tip moves slowly horizontally along the scan line following the sample surface. In the lift mode, the tip moves horizontally at the fixed separation distance (lift height) to the planar substrate, while the deflection of the cantilever is recorded. In the FV mode, the tip is moved for each pixel vertically in and out of contact with the surface.

First, a $5 \times 5 \mu\text{m}^2$ area of HOPG containing nanobubbles was scanned in TM AFM. The acquired height and deflection images are shown in Fig. 2a. Apart from the atomic steps and surface nanobubbles, the graphite surface was flat and homogeneous without visible microp pancakes²⁸ or contamination. The five largest bubbles, marked in the image with numbers, had apparent heights between 10 and 15 nm, and apparent widths between 300 and 700 nm. In the TM deflection image acquired simultaneously with the height image, the color scale encodes

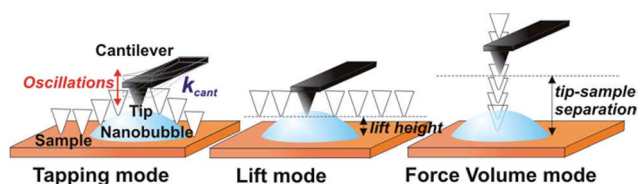


Fig. 1 Schemes of the movement of the AFM tip during scanning in the different AFM modes. In tapping mode and in lift mode the tip is moved horizontally along the scan line, whereas in the force volume mode the tip is moved pixel by pixel vertically at a fixed position on the sample.

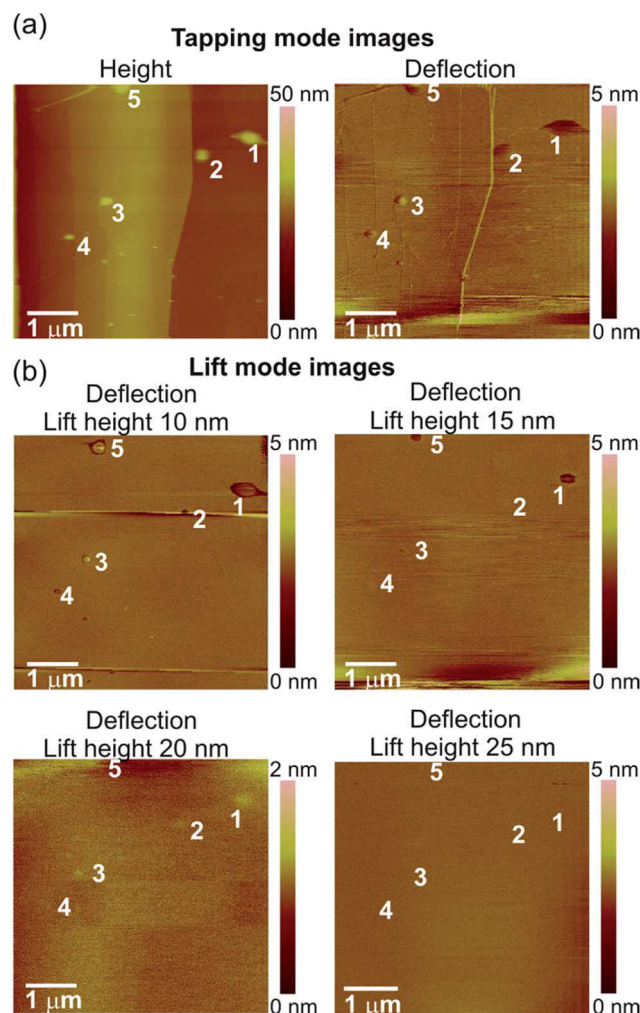


Fig. 2 (a) AFM TM height and deflection and (b) lift mode images (deflection of the cantilever at different lift heights between 10 and 25 nm) of surface nanobubbles on HOPG in water. The five largest nanobubbles are marked with numbers. The cross-sections of the bubble no. 1 are shown in Fig. 5.

the cantilever bending. The locations of the nanobubbles could be recognized as circular spots. Dark color marked the positions on the sample, where the cantilever bent more downwards, and bright color marked the positions, where the cantilever bent more upwards, as compared to its bending on the graphite surface. The bubbles in the TM deflection image and the corresponding bubbles in the TM height image had similar widths.

Next, the same area of the sample was rescanned in the lift mode. Each line of the image was scanned in TM mode on the way forward (from left to right), while on the way back (from right to left) the scanning was done with the cantilever lifted over the substrate at a certain lift height. It means that during the scanning of a single image, the tip was moved up and down repeatedly because of the continuous switching between TM and lift mode. During the lift mode data acquisition the deflection of the cantilever was measured as the tip was being moved horizontally over the sample. The lift height was increased for each image from 10 to 120 nm in 5–10 nm steps.

Four deflection images measured over the sample at lift heights of 10 nm, 15 nm, 20 nm and 25 nm are shown in Fig. 2b.

The lift mode deflection images were featureless over most of the scanned area of the sample. This means that there was no interaction between the tip and the graphite when the separation distance was larger than 10 nm. Surface nanobubbles were visible in the lift mode images as dark circular spots located at the positions that correspond to the positions of the bubbles identified in the TM height images. In the lift mode deflection image acquired at a lift height of 10 nm, the width of each bubble was slightly smaller than the apparent width of the footprint of the corresponding bubbles in the TM height image in Fig. 2a. Interestingly, although all five bubbles were visible in the lift mode deflection image, some appeared with dark contrast, while other appeared bright. As the lift height increased to 15 nm, the bubbles in the deflection image appeared dark and considerably smaller (bubbles 1, 3 and 5) or they disappeared from the image (bubbles 2 and 4). At a lift height of 20 nm, the bubbles were visible as slightly bright spots almost undistinguishable from the substrate (mind the different vertical color scales in Fig. 2b). Finally, at lift heights of 25 nm and larger the deflection images were featureless.

To explain the different deflection signals in the lift mode images, we have analysed force data acquired on the same bubbles in FV mode AFM. In addition, these force measurement also afforded information on the cantilever deflection on the bubble, but acquired in a different way than in the lift mode. In the FV experiment, the tip was lowered and retracted at several positions on the bubble, and the forces acting on the tip (deflection of the cantilever) at different tip-sample separation distances were measured. In the measurement, FV height image and FV slice image of the HOPG sample with the nanobubbles were acquired simultaneously. Both images are displayed in Fig. 3. The FV height image shows how much the AFM tip was moved in the vertical direction at each point of the sample in order to reach the requested maximum deflection threshold (always exceeding a nanobubble height). The FV slice image shows the magnitude of the cantilever deflection at a particular height over the substrate (here, comparable with the bubble height). The nanobubbles were visible only in the FV slice image. By comparing the sample features in the FV height image with the TM height image shown in Fig. 2a, the bubbles

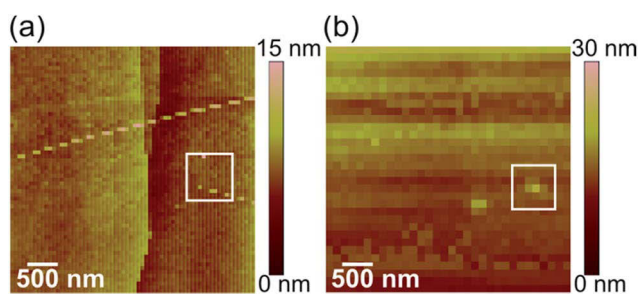


Fig. 3 (a) FV AFM height image and (b) FV AFM force slice image of HOPG with nanobubbles. Nanobubble no. 1 from Fig. 2 is marked with a box.

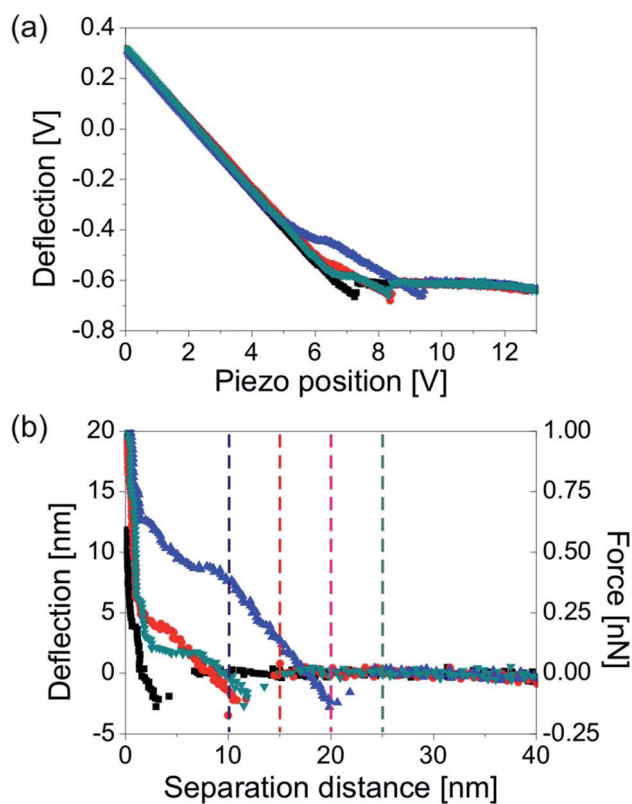


Fig. 4 (a) Unprocessed force–displacement and (b) force–distance curves acquired on nanobubble no. 1 from Fig. 2. The deflection measured at positions 10 nm, 15 nm, 20 nm and 25 nm (marked with four vertical lines) are plotted in Fig. 5b. The data were acquired with a cantilever with a spring constant $k_{\text{cant}} = 0.05 \text{ N m}^{-1}$.

in the FV slice image could be identified. Bubble no. 1 is marked with a box. Exemplary force curves measured on this bubble are shown in Fig. 4. For clarity, only approach force curves are shown in the plots.

Since we know how the deflection of the cantilever changed with the tip-sample separation distance, we could extract the information on the deflection at a particular separation distance to the substrate. In Fig. 5, we directly compare the results of the lift mode and force measurements done on nanobubble no. 1 from Fig. 2. The graphs show the deflection signals measured at different tip-sample separation distances imposed on the bubble height profile. Three cross-sections of the bubble no. 1 are plotted. The first cross-section (open squares) shows the apparent shape of the bubble measured directly from the TM height image. The second cross-section (black solid squares) is the bubble profile corrected for non-ideal scanning conditions *i.e.* non-zero amplitude of the cantilever oscillations and amplitude setpoint ratio lower than 100%.⁴³ The corrected bubble height was estimated to be 17 nm. The third cross-section (solid squares – shown only in the plots in Fig. 5b) is the bubble profile reconstructed from the force–distance curves (the procedure is described further in this article). Because of the low spatial resolution of the FV measurement, the reconstructed profile only roughly resembles

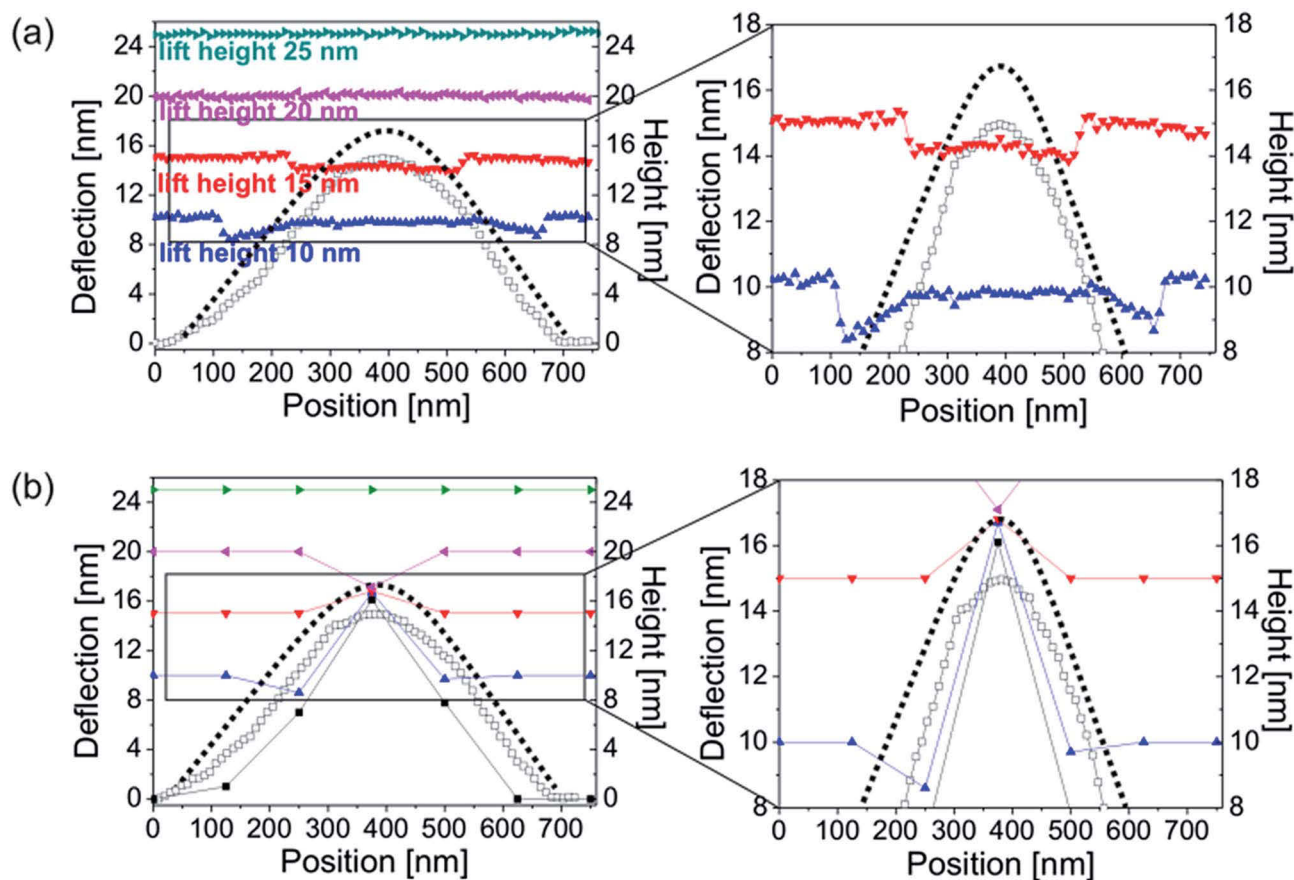


Fig. 5 Deflection of the AFM cantilever over bubble no. 1 from Fig. 2 (a) measured directly in lift mode scans at lift heights of 10 nm, 15 nm, 20 nm and 25 nm, and (b) measured from the approach force–distance curves acquired on the bubble in the FV mode at tip–sample separation distances of 10 nm, 15 nm, 20 nm and 25 nm. The apparent (black open squares) and corrected (black solid squares) bubble profiles measured from the TM AFM height image are compared to the profile estimated from the force–distance curves (black squares in panel b). The plots on the right hand side showing the bubble top are a magnification of the adequate part of the plots on the left hand side. The data were acquired with a cantilever with a spring constant $k_{\text{cant}} = 0.05 \text{ N m}^{-1}$.

the spherical cap. Nevertheless, its height was similar to the height of the corrected TM profile.

The measured and calculated bubble profiles were used as a reference in order to show the deflection of the cantilever measured at different tip–sample separation distances. The deflections plotted in Fig. 5a were extracted from the lift mode images shown in Fig. 2b. The deflections plotted in Fig. 5b were measured from the force–distance curves acquired over the nanobubble at the separation distances of 10 nm, 15 nm, 20 nm and 25 nm, as marked with four vertical lines in the force plot in Fig. 4b. All plotted deflections were measured along a single scan line approximately over the bubble center.

For simplicity, in each case we assumed that the cantilever was in an unbent position and its deflection was zero, when it was far away from the bubble. However, in order to give a better overview of the experiment and the results, all cantilever deflections in Fig. 5 are plotted at the levels approximately equal to the actual separation to the substrate, where the tip end was located during the experiment. For example, zero cantilever deflection away from the bubble is plotted as equal to 10 nm, if

it was measured at the lift height/tip–sample separation of 10 nm, and as equal to 15 nm if it was measured at the lift height/tip–sample separation of 15 nm, and so on. Consequently, all data points located below the initial deflection level indicate a downward bending of the cantilever at these positions, whereas data points located above this level indicate an upward bending. The values of TM deflection measured directly on the sample were not included in the plots.

In TM AFM in liquid, the cantilever always bends as soon as the tip interacts with the surface. However, because at the same time the cantilever is oscillated, the tip–bubble interaction conditions are different than in the other two imaging modes. For this reason, we cannot quantitatively compare the TM deflection signal with the results obtained in the other modes.

In the plots in Fig. 5, all deflections measured over the bubble at tip–sample separation distances smaller than or equal to the corrected local bubble height were non-zero. Regardless the direction of the tip movement – horizontal in the lift mode and vertical in the FV measurement, the cantilever started to bend when the tip approached the bubble, and remained bent

until the tip left the bubble. Interestingly, the spatial extent of non-zero deflection was slightly larger in the lift mode than in the FV mode.

Now, we will look in detail at the deflection of the cantilever at different tip-sample separation distances. In the lift mode, at lift heights of 10 nm and 15 nm the deflection measured on the bubble was smaller than the one measured on the substrate (*i.e.* the cantilever bent downwards). However, the deflection value varied at different positions over the bubble. This is clearly visible in the right plot in Fig. 5a that shows in detail the data points acquired at lift heights of 10 nm and 15 nm. It is clear that at a lift height of 10 nm, the downward deflection of the cantilever was the largest (~ 2 nm) near the rim just outside the bubble. When the tip interacted with the bubble, the deflection decreased in magnitude to ~ 0.5 nm and stayed approximately constant at all positions while traversing the bubble, until the tip reached the bubble rim and the deflection increased again to ~ 2 nm. A similar behavior of the cantilever could be observed at a lift height of 15 nm, however, the tip-bubble interaction was weaker so that the cantilever bent downward only by ~ 1 nm and this bending was nearly constant on all positions over the bubble – the data points formed an almost straight line in the plots in Fig. 5a. The deflection data for the lift heights of 20 nm and 25 nm were featureless.

If we look at the plots in Fig. 5b that show the cantilever deflection values over the same bubble measured from the force–distance curves, we observe a similar cantilever response to the bubble as measured in the lift mode. At a tip-sample separation distance of 10 nm, the deflection near the bubble rim was slightly decreased (bending down by ~ 1 nm) as compared to the deflection measured away from the bubble. In turn, near the bubble center, the measured deflection value was increased and the cantilever bent upwards by ~ 6 nm. A similar but weaker (~ 2 nm) upward bending of the cantilever near the bubble center was observed at a tip-sample separation distance of 15 nm. Unfortunately, we cannot discuss the changes in the cantilever deflection at different horizontal positions over the bubble because of the small spatial resolution of the FV measurement. At a tip-sample separation distance of 20 nm, a weak (~ 3 nm) downward bending of the cantilever on the bubble was observed in the FV mode, whereas no change in the deflection signal was measured over the bubble in the lift mode. Finally, the deflection data extracted from the force–distance curves was featureless at a separation of 25 nm to the substrate.

4 Discussion

The cantilever deflection signal measured on the nanobubbles varied depending on the tip-sample separation distance and the horizontal position of the tip over the bubbles, as shown in Fig. 2 and in Fig. 5.

In the experiment, the nanobubbles were visible in the lift mode deflection image, when the lift height was smaller than the unperturbed bubble heights. The statement is supported by the results shown in Fig. 2. Only the largest bubbles no. 1 and no. 5 shrank, but did not disappear in the lift mode deflection image acquired at a lift height of 15 nm. The corrected heights

of these bubbles measured from the TM image were equal to 17 nm and 18 nm, respectively. Therefore they were both larger than the lift height level. The heights of the remaining bubbles no. 2, 3 and 4 were smaller and equal to ~ 12 nm. In addition, as shown in the plots in Fig. 5a, no tip-sample interaction was detected at separation distances larger than the bubble height.

If we assume that the nanobubble resembles a spherical cap, the shrinking of the circular spots representing the bubbles in the lift mode deflection images acquired at increased tip-sample separation distances might be a pure geometrical effect and approximately corresponds to a decrease in circumferences of the bubbles at increased heights above the HOPG. In other words, in the lift mode images done at different lift heights, we can see different horizontal “slices” of the bubbles. The data shown in the plots in Fig. 5 confirm this hypothesis. At small tip-sample separation distances the total horizontal distance, over which the tip interacted with the bubble, was larger than at increased separation distances, which is the consequence of different bubble widths at different distances to the substrate. These results explain not only why the bubbles shrank in the deflection images acquired at increased lift heights, but also why small bubbles disappeared from deflection images sooner than large bubbles.

If we decrease the lift height, the lateral size of the bubble in the deflection image will approach the bubble width measured from the TM height image. For zero lift height, the bubble width measured in the deflection image and in the TM height image should be equal. If we compare the TM height image shown in Fig. 2 with the TM deflection image (acquired directly on the sample), and with the lift mode deflection image (acquired at a lift height of 10 nm), we see that the bubbles have similar footprint widths in the TM height and deflection image, while they appear slightly smaller in the lift mode image (at 10 nm lift height). For example, for the bubble no. 1, the widths are 656 nm (TM height), 675 nm (TM deflection) and 607 nm (lift height 10 nm, lift mode deflection). The TM bubble width and the horizontal extent of the deflection signal measured at 10 nm lift height can also be seen in the plot in Fig. 5a. The observation that a single nanobubble displayed similar widths in various imaging channels or modes, was reported for Peak Force AFM experiments.^{25,47,48}

Previously, the qualitative agreement between the results obtained in the FV mode and in lift mode AFM indicates that the variations in the deflection signal with the tip-sample separation distance were well reflected in the shapes of the force–distance curves. As shown in the exemplary force curves in Fig. 4b, the deflection of the cantilever on the bubble changed in the magnitude or/and the direction depending on the distance of the tip to the sample. We believe that this effect explains the switching between positive (upward bending) and negative (downward bending) deflection values observed in the deflection images in Fig. 2b acquired at different lift heights. In addition, because each change in the deflection sign from positive to negative values or *vice versa* required crossing the zero deflection point at a certain tip-sample separation distance, our results explain why sometimes nanobubbles did not appear in the deflection image acquired at small lift

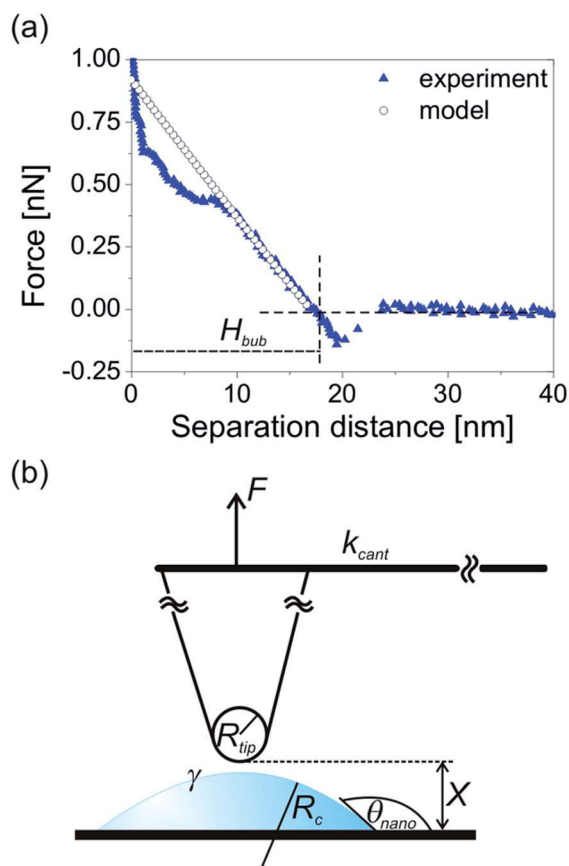


Fig. 6 (a) Approach force–distance curve acquired on the bubble no. 1 from Fig. 2 and forces calculated from the dynamic interaction model. The data were acquired and calculated with the cantilever with spring constant $k_{\text{cant}} = 0.05 \text{ N m}^{-1}$. (b) A schematic diagram of AFM tip interacting with surface nanobubble. The parameters used in the dynamic interaction model are defined.

heights/tip-sample separations, and reappeared in the deflection image done for larger lift heights/separations. Finally, because force–distance curves acquired on bubbles of different vertical sizes have different shapes, our results also explain, why different bubbles appear as bright or dark in a single lift mode deflection image measured at a fixed tip–sample separation distance.

As already mentioned, the deflection data extracted from the force curves resembles the lift mode deflection data qualitatively. However, larger cantilever bending was detected in the force measurement, which suggests stronger tip–bubble interaction. The maximum deflection measured on the bubble in the force mode was as large as 6 nm (which corresponds to a repulsive force of 0.3 nN), whereas the maximum deflection measured in the lift mode did not exceed 2 nm (which corresponds to an attractive force of 0.1 nN). Taking into account that the same cantilever and tip was used in the whole course of the experiments, this result is puzzling. The cantilever seemed to be less sensitive in the lift mode than in the force measurement. The lack of precise control of the tip–sample separation distance due to the open feedback loop system used in the lift mode cannot account for the observed discrepancy.

In order to explain the difference in the interaction strength, we need to focus on the tip–bubble interaction. Force–distance curves acquired on the bubble are a valuable source of information. First, from the course of the force curve we could measure the unperturbed nanobubble height H_{bub} .²⁴ As shown in the example in Fig. 6a, for each force–distance curve acquired on the bubble, the local unperturbed bubble height H_{bub} is equal to the separation distance of the zero-deflection crossing point that follows the jump-in event. The height extracted from the force curves measured near the bubble center will be larger than the height extracted from the force curves measured near the bubble edge. This method was used to reconstruct the bubble profile plotted in Fig. 5b (black squares).

Next, we apply the dynamic interaction model to the force curve measured approximately at the bubble center.^{55–57} The model characterizes the interaction between a hydrophilic AFM tip and a nanobubble at the last stage of tip approach when a thin film of liquid is trapped between the bubble surface and the tip apex, as sketched in Fig. 6b.²⁴

The relation between the displacement ΔX of the tip apex and the interaction force F experienced by the tip is given by

$$\Delta X = \frac{F}{4\pi\gamma} \left\{ \log \left(\frac{FR_{\text{bt}}}{8\pi\gamma R_c^2} \right) + 2B(\theta_{\text{nano}}) - \frac{4\pi\gamma}{k_{\text{cant}}} - 1 \right\} \quad (1)$$

where k_{cant} is the stiffness of the cantilever, γ is the surface tension and the reduced radius R_{bt} is given by

$$R_{\text{bt}} \approx \left(\frac{1}{R_c} + \frac{1}{R_{\text{tip}}} \right)^{-1} \quad (2)$$

where R_c is the curvature of the bubble and R_{tip} is the radius of the tip apex. $B(\theta_{\text{nano}})$ is a parameter related to the constant volume constraint under the assumption that the bubble deforms with the constant contact angle θ_{nano} . It is described by eqn (3):

$$B(\theta_{\text{nano}}) = 1 + \frac{1}{2} \log \left(\frac{1 + \cos \theta_{\text{nano}}}{1 - \cos \theta_{\text{nano}}} \right) - \frac{1}{2 + \cos \theta_{\text{nano}}} \quad (3)$$

This formula is valid for high forces and for a small interaction zone and small deformations compared to the bubble size (radius of curvature). This constraint is satisfied for surface nanobubbles in our experiments. Moreover, the model assumes that the volume of the bubble is constant at all stages of interaction and the contact angle does not change. The initial separation used as an input parameter in the model was chosen as 17 nm and is equal to the unperturbed bubble height H_{bub} extracted from the force curve. The values of other parameters used in the model were as follows: tip radius $R_{\text{tip}} = 20 \text{ nm}$, surface tension $\gamma = 0.07 \text{ N m}^{-1}$, cantilever stiffness $k_{\text{cant}} = 0.05 \text{ N m}^{-1}$. The forces calculated from the model formed a force curve shown in Fig. 6a.

The good agreement between the force curves from the model and from the experiment indicates that (1) the AFM tip used for the scanning was sharp and hydrophilic, (2) the interaction forces between the tip and the nanobubble in the AFM experiment had a hydrodynamic origin. This result means that a thin liquid film was present between the tip apex and the

bubble during the measurement. The increased repulsion measured on the bubble in the experiment originated from the squeezing of the film and the displacement of water from the shrinking space between the bubble surface and the approaching AFM tip.

The discrepancy in interaction strengths measured for the same bubble in lift mode and in FV AFM is the manifestation of a different nature of tip-bubble interaction in both AFM modes that is caused by different directions of tip movement. As shown in Fig. 1, during scanning in lift mode, the tip is moved horizontally so that it approaches the bubble only from the side. On the contrary, during the force measurement, the tip is displaced only in the vertical direction so that it approaches the bubble from the top. Because the geometry of the interaction, and the speed and direction of the tip movement differed in the lift mode and in the force measurement, the hydrodynamic effect and the cantilever response were different. Apparently, the bubble top resisted the squeezing of the liquid film by the tip more than the bubble side and the cantilever bent more upwards during the force measurement than during the scanning done in the lift mode.

An upward bending of the cantilever was measured only on the bubble near the bubble center. Near the edges of the bubble, the cantilever bent downwards both in the lift mode and in the FV mode. The local variations in the deflection signal with the spatial position of the tip over the bubble observed in the plots in Fig. 5 suggest different tip-bubble interactions near the bubble periphery as compared to the bubble center. Spatial variations of various parameters extracted from the force-distance curves or amplitude-distance curves were also reported in the experiments done in Peak Force AFM,^{25,47,48} in FV AFM,⁵⁸ and in amplitude spectroscopy (Amplitude Volume) AFM.⁴⁶

As shown in the plots in Fig. 5, the total spatial extent of non-zero cantilever deflection signal in the horizontal direction was larger in the lift mode than in the FV mode at a fixed tip-sample separation distance. In the lift mode, when the tip was approaching the bubble from the side, it started to bend downwards at the distance about 100 nm from the position of the estimated unperturbed bubble surface, *so before* the bubble. After passing through the bubble, the cantilever returned to the unbent position about 100 nm *after* the position of the unperturbed bubble surface. No analogous behavior was observed in the FV experiment. However, in the vertical direction, the spatial extent of non-zero deflection signal measured in FV was larger than in the lift mode. As shown in the plots in Fig. 5, in the FV mode, downward bending of the cantilever was measured over the bubble top for a tip-sample separation of 20 nm, whereas no interaction was measured in the lift mode for the lift height of 20 nm.

The difference in the spatial extent of the tip-bubble interaction measured in lift mode and in FV mode can again be explained by different tip movement in these two modes. In FV, the tip approached the bubble vertically from the top and hence the interaction region was extended in the vertical direction. The initial attraction that caused bending of the cantilever at the separations larger than the local bubble height H_{bub} is well

visible in the force curve plotted in Fig. 6a. This effect could be caused by a jump of the bubble interface towards the tip. By contrast, in lift mode, the interaction region was extended in the horizontal direction because the tip was approaching the bubble from the side and the bubble interface moved sideways towards the tip. In both cases, the tip shape might also play a role and the interaction of the bubble surface with the tip apex was different from its interaction with the tip side.

We expect that the tip-bubble interaction and nanobubble deformation in TM AFM will be the resultant of the effects arising from the horizontal movement of the tip over the bubble and the simultaneous vertical movement due to cantilever oscillations.

The information on the deflection of the cantilever on surface nanobubbles available in the literature is consistent with our results. Janda *et al.* studied nanobubbles in aqueous solution on graphite in modified AFM dynamic force mode.²⁶ Deflection measurements were done simultaneously with topographic imaging and the deflection was measured at zero tip-sample separation. The deflection signal was nearly zero on the substrate and negative on all nanobubbles. The bubbles' footprints in the deflection image had approximately the same widths as the widths of the corresponding bubbles in the topographic image. Zhang *et al.*⁴⁹ conducted a series of measurements in lift mode AFM on nanobubbles on octadecyltrichlorosilane (OTS) modified silicon substrates in ~ 0.5 CMC Tween 20 solution, and obtained results comparable to ours. In the experiment, the bubble height and width estimated from TM height image were 44 nm and 375 nm, respectively. The deflection on the bubble was measured at lift heights varied between 10 and 160 nm. In all lift mode images, the deflection on the bubble was different from the deflection measured on the substrate. It changed from the positive values all over the bubble for low lift heights to negative values for increased lift heights (the switch from positive to negative took place between 20 and 40 nm lift height). At 10 nm lift height, the area of the bubble visible in the image was slightly smaller than the area of the bubble base in the TM height image. Then, the apparent bubble area decreased for the lift heights increased from 10 nm to 40 nm. With a further lift height increase up to 160 nm, the footprint area stayed approximately constant and the deflection became weaker until 160 nm, when the bubble disappeared completely from the image. No information about the strength of the interaction and a magnitude of deflection was provided. In the view of our findings, the results of Zhang *et al.* showing non-zero deflection signal detected far above the estimated bubble height indicate the presence of a strong attractive interaction between the tip and the bubble. Our suggestion is in line with the authors' conclusion drawn in their report that the surfactant solution made nanobubbles more pliable. Therefore, it was possible that the bubble in the lift mode experiment was stretched upwards toward the tip far above its regular height.

In our experiment, no forces were detected at tip-sample separation distances exceeding the bubble height by 80 nm. We conclude that *no* flow was present anywhere above or around the bubble up to at least 120 nm. Our finding is in line with the

results reported by other authors, and obtained using various techniques.^{23,59}

The generalization of our findings to other systems including soft organic or polymeric clusters or (ultra)small droplets *etc.* appears to us very relevant. Unfortunately, the physics is for the following reasons system-dependent and it seems that a generalization may only work for standardized systems:

(a) tapping mode AFM is dominated by energy dissipation, which is system-dependent, primarily depending on relaxation channels and characteristic times, among others;

(b) intermolecular forces that govern attraction and repulsion depend on the medium as well as on the particular molecules and their arrangement;

(c) the tip shape in 3D determines the range of interaction forces and the local contact geometry; this varies with each tip and should be explicitly considered;

(d) AFM tip functionality (*e.g.* by functionalization with monolayers) may possess an effect on (a) and (b) and hence need to be considered separately.

Although a complete description of these factors for random systems may be not feasible, it should be in reach for well-defined systems.

5 Conclusions

Based on the results of our combined AFM TM, lift mode and FV measurements of argon nanobubbles on HOPG in water, we have shown that the interaction between the AFM tip and the surface nanobubble was weak and limited to the volume occupied by the bubble and to its closest vicinity. No interaction with the liquid above or around the bubble surface was detected. The strength and the character (repulsive or attractive) of the interaction depended on the vertical and horizontal position of the tip over the bubble. Attractive forces dominated the region near the bubble rim, whereas repulsive (or less attractive) forces dominated the region near the bubble center. The appearance of the bubble in the lift mode deflection images varied depending on the shape of the individual force–distance curves, and on the bubble size.

Good agreement between the results of the experiment and of the dynamic interaction model indicated that the AFM tip was hydrophilic and interacted with nanobubbles through a thin film of liquid. The hydrodynamic effect arising from squeezing the thin film during the measurements played a role in the interaction and influenced the cantilever response during the scanning. Its strength and spatial extent were closely related to the character and direction of the tip movement during the scanning. In lift mode, the tip approached the nanobubble only from the side and the hydrodynamic repulsion was less pronounced so that only a weak interaction between the tip and the bubble was measured. In the FV mode, the tip approached the bubble only from the top, and the hydrodynamic effect and measured repulsion were stronger.

Finally, we have shown that the nanobubble appearance in the AFM images not only depends on the tip shape and cleanliness, and the scanning parameters chosen, but also is sensitive

to the measuring conditions related to the scanning mode utilized in the AFM experiment. Because the hydrodynamic effect is related to the bubble deformation, its possible consequences for the measurements of nanobubble dimension must be taken into account, especially when measuring nanobubbles in the AFM scanning modes that involve complex tip movement.

Acknowledgements

The authors would like to thank Dr S. Druzhinin and Dr H. Knepe for enlightening discussions and helpful suggestions and gratefully acknowledge financial support from the Deutsche Forschungsgemeinschaft (DFG grant no. INST 221/87-1 FUGG), the European Research Council (ERC grant to HS, ERC grant agreement no. 279202) and the University of Siegen.

Notes and references

- 1 J. N. Israelachvili and R. M. Pashley, *Nature*, 1982, **300**, 341.
- 2 H. K. Christenson and P. M. Claesson, *Science*, 1988, **239**, 390.
- 3 J. L. Parker, P. M. Claesson and P. Attard, *J. Phys. Chem.*, 1994, **98**, 8468.
- 4 K. W. Stockelhuber, B. Radoev, A. Wenger and H. J. Schulze, *Langmuir*, 2004, **20**, 164.
- 5 Z. Wu, X. Zhang, X. Zhang, J. Sun, Y. Dong and J. Hu, *Chin. Sci. Bull.*, 2007, **52**, 1913.
- 6 A. Maali and B. Bhushan, *J. Phys.: Condens. Matter*, 2013, **25**, 184003.
- 7 Y. Wei, S. Brandl, F. Goodwin and D. Back, *Future Fab. Intl.*, 2007, **22**, 65.
- 8 H. Schubert, *Int. J. Miner. Process.*, 2005, **78**, 11.
- 9 G. Liu and V. S. J. Craig, *ACS Appl. Mater. Interfaces*, 2009, **1**, 481.
- 10 S. Yang and A. Dusterwinkel, *Langmuir*, 2011, **27**, 11430.
- 11 N. Ishida, T. Inoue, M. Miyahara and K. Higashitani, *Langmuir*, 2000, **16**, 6377.
- 12 S. T. Lou, Z. Q. Ouyang, Y. Zhang, X. J. Li, J. Hu, M. Q. Li and F. J. Yang, *J. Vac. Sci. Technol., B: Microelectron. Nanometer Struct.*, 2000, **18**, 2573.
- 13 J. W. G. Tyrrell and P. Attard, *Phys. Rev. Lett.*, 2001, **87**, 1761041.
- 14 R. Steitz, T. Gutberlet, T. Hauss, B. Klösgen, R. Krastev, S. Schemmel, A. C. Simonsen and G. H. Findenegg, *Langmuir*, 2003, **19**, 2409.
- 15 X. H. Zhang, A. Quinn and W. A. Ducker, *Langmuir*, 2008, **24**, 4756.
- 16 M. Switkes and J. W. Ruberti, *Appl. Phys. Lett.*, 2007, **84**, 4759.
- 17 J. Yang, J. Duan, D. Fornasiero and J. Ralston, *Phys. Chem. Chem. Phys.*, 2007, **9**, 6327.
- 18 T. R. Jensen, M. O. Jensen, N. Reitzel, K. Balashev, G. H. Peters, K. Kjaer and T. Bjørnholm, *Phys. Rev. Lett.*, 2003, **90**, 086101.
- 19 M. A. Mezger, S. A. B. Schöder, H. A. Reichert, H. A. Schröder, J. A. Okasinski, V. B. Honkimäki, J. C. Ralston, J. D. Bilgram, R. A. E. Roth and H. Dosch, *J. Chem. Phys.*, 2008, **128**, 244705.

- 20 L. Zhang, B. Zhao, L. Xue, Z. Guo, Y. Dong, H. Fang, R. Tai and J. Hu, *J. Synchrotron Radiat.*, 2013, **20**, 413.
- 21 S. Karpitschka, E. Dietrich, J. R. T. Seddon, H. J. W. Zandvliet, D. Lohse and H. Riegler, *Phys. Rev. Lett.*, 2012, **109**, 066102.
- 22 U. Mirsaidov, C.-D. Ohl and P. Matsudaira, *Soft Matter*, 2012, **8**, 3108.
- 23 C. U. Chan and C.-D. Ohl, *Phys. Rev. Lett.*, 2012, **109**, 174501.
- 24 W. Walczyk and H. Schönherr, *Langmuir*, 2014, 7112–7126.
- 25 B. Zhao, Y. Song, S. Wang, B. Dai, L. Zhang, Y. Dong, J. Lü and J. Hu, *Soft Matter*, 2013, **9**, 8837.
- 26 P. Janda, O. Frank, Z. Bastl, M. Klementová, H. Tarábková and L. Kavan, *Nanotechnology*, 2010, **21**, 95707.
- 27 X. Zhang, D. Y. C. Chan, D. Wang and N. Maeda, *Langmuir*, 2013, **29**, 1017.
- 28 J. R. T. Seddon and D. Lohse, *J. Phys.: Condens. Matter*, 2011, **23**, 133001.
- 29 V. S. J. Craig, *Soft Matter*, 2011, **7**, 40.
- 30 B. Song, W. Walczyk and H. Schönherr, *Langmuir*, 2011, **27**, 8223.
- 31 W. A. Ducker, *Langmuir*, 2009, **25**, 8907.
- 32 S. Wang, M. Liu and Y. Dong, *J. Phys.: Condens. Matter*, 2013, **25**, 184007.
- 33 Y. Liu and X. Zhang, *J. Chem. Phys.*, 2013, **138**, 014706.
- 34 M. P. Brenner and D. Lohse, *Phys. Rev. Lett.*, 2008, **101**, 214505.
- 35 J. R. T. Seddon, H. J. W. Zandvliet and D. Lohse, *Phys. Rev. Lett.*, 2011, **107**, 116101.
- 36 N. D. Petsev, M. S. Shell and L. G. Leal, *Phys. Rev. Lett. E*, 2013, **88**, 10402.
- 37 J. H. Weijs and D. Lohse, *Phys. Rev. Lett.*, 2013, **110**, 054501.
- 38 J. R. T. Seddon, E. S. Kooij, B. Poelsema, J. W. Zandvliet and D. Lohse, *Phys. Rev. Lett.*, 2011, **106**, 056101.
- 39 P. Grosfils, *J. Phys.: Condens. Matter*, 2013, **25**, 184006.
- 40 R. P. Berkelaar, H. J. W. Zandvliet and D. Lohse, *Langmuir*, 2013, **29**, 11337.
- 41 M. Mazdumer and B. Bhushan, *Soft Matter*, 2011, **7**, 9184.
- 42 A. L. Weisenhorn, M. Khirsandi, S. Kasas, V. Gotzos and H.-J. Butt, *Nanotechnology*, 1993, **4**, 106.
- 43 W. Walczyk and H. Schönherr, *Langmuir*, 2013, **29**, 620.
- 44 B. M. Borkent, S. de Beer, F. Mugele and D. Lohse, *Langmuir*, 2010, **26**, 260.
- 45 S. Yang, E. S. Kooij, B. Poelsema, D. Lohse and H. J. W. Zandvliet, *EPL*, 2008, **81**, 64006.
- 46 B. Bhushan, Y. Wang and A. Maali, *J. Phys.: Condens. Matter*, 2008, **20**, 485004.
- 47 C. W. Yang, Y. H. Lu and I. S. Hwang, *J. Phys.: Condens. Matter*, 2013, **25**, 184010.
- 48 W. Walczyk, P. M. Schön and H. Schönherr, *J. Phys.: Condens. Matter*, 2013, **25**, 184005.
- 49 X. H. Zhang, N. Maeda and V. S. J. Craig, *Langmuir*, 2006, **22**, 5025.
- 50 M. Holmberg, A. Kühle, J. Garnæs, K. A. Mørch and A. Boisen, *Langmuir*, 2003, **19**, 10510.
- 51 A. Agrawal, J. Park, D. Y. Ryu, P. T. Hammond, T. P. Russel and G. H. McKinley, *Nano Lett.*, 2005, **5**, 1751.
- 52 Y. H. Lu, C. W. Yang and I. S. Hwang, *Langmuir*, 2012, **28**, 12691.
- 53 H. Peng, P. A. Hampton and A. V. Nguyen, *Langmuir*, 2013, **29**, 6123.
- 54 J. Ally, M. Kappl, H.-J. Butt and A. Amirfazli, *Langmuir*, 2010, **26**, 18135.
- 55 D. Y. C. Chan, R. R. Dagastine and L. R. White, *J. Colloid Interface Sci.*, 2001, **236**, 141.
- 56 R. R. Dagastine and L. R. White, *J. Colloid Interface Sci.*, 2002, **247**, 310.
- 57 R. F. Tabor, F. Grieser, R. R. Dagastine and D. Y. C. Chan, *J. Colloid Interface Sci.*, 2012, **371**, 1.
- 58 W. Walczyk and H. Schönherr, manuscript submitted.
- 59 E. Dietrich, H. J. W. Zandvliet, D. Lohse and J. R. T. Seddon, *J. Phys.: Condens. Matter*, 2013, **25**, 184009.

9

On the shape and deformation of surface nanobubbles in AFM

In this chapter, we address the issue of deformation of the nanobubble/water interface by the AFM tip during imaging. Because the interaction between the bubble and the tip is different in case of hydrophilic and hydrophobic tips, we compare the nanobubble deformation in different experimental conditions. By analyzing the tip-bubble interaction strength and the magnitude of the bubble deformation as functions of vertical and horizontal position of the tip on the bubble, we sketch two possible scenarios of nanobubble deformation depending on whether the AFM tip penetrates the nanobubble during scanning or merely “slides” over its surface. In addition, we look at the consequences of the imaging for the apparent bubble shape and contact angle in AFM images. Based on the experimental results, we estimate the extent of the discrepancy between the apparent and the actual nanobubble dimensions and speculate about possible mechanisms responsible for this effect.

The chapter consists of the following manuscript submitted for publication:

**On the Dimensions and the Profile of Surface Nanobubbles:
Tip-Nanobubble Interactions and Nanobubble Deformation in Atomic
Force Microscopy**

Wiktoria Walczyk and Holger Schönherr

2014 (manuscript submitted for publication).

Supporting Information directly follows the article.

On the dimensions and the profile of surface nanobubbles: Tip-nanobubble interactions and nanobubble deformation in Atomic Force Microscopy

*Wiktoria Walczyk and Holger Schönherr**

Physical Chemistry I, University of Siegen, Faculty of Natural Sciences and Engineering,
Department of Chemistry and Biology, Adolf-Reichwein-Str. 2, 57076 Siegen, Germany

KEYWORDS Surface nanobubbles, atomic force microscopy, tip surface interactions,
gas-water interface deformation

ABSTRACT: The interactions between argon surface nanobubbles and AFM tips on HOPG (highly oriented pyrolytic graphite) in water and the concomitant nanobubble deformation were analyzed as a function of position on the nanobubbles in a combined Tapping Mode and Force-Volume mode AFM study with hydrophilic and hydrophobic AFM tips. Based on the detailed analysis of force-distance curves acquired on the bubbles, we found that for hydrophobic tips the bubble interface may jump toward the tip and that the tip-bubble interaction strength and the magnitude of the bubble deformation were functions of vertical *and* horizontal position of the tip on the bubble and depended on the bubble size, and tip size and functionality. The spatial variation is attributed to long-range attractive forces originating from the substrate under the bubbles, which

dominate the interaction at the bubble rim. The non-uniform bubble deformation leads to a non-uniform underestimation of the bubble height, width and contact angle in conventional AFM height data. In particular, scanning with a hydrophobic tip resulted in severe bubble deformation and distorted information in the AFM height image. For a typical nanobubble, the upward deformation may extend up to tens of nanometers above the unperturbed bubble height and the lateral deformation may constitute 20 % of the bubble width. Therefore, only scanning with a hydrophilic tip and no direct contact between the tip and the bubble may reduce nanobubble deformation and provide reliable AFM images that can be used to estimate adequately the unperturbed nanobubble dimensions. The deformation and underestimation of the bubble size and shape lead to the conclusion that the profile of surface nanobubbles is much closer than previously thought to a nearly flat bubble profile and hence that the Laplace pressure is much closer to the atmospheric pressure. Together with line pinning this may explain the long nanobubble lifetimes observed previously.

INTRODUCTION

The invention of the Atomic Force Microscopy (AFM) several decades ago, afforded the possibility to study the behavior and deformation of soft samples of microscopic and nanoscopic dimensions.¹ It is, however, also well established that soft samples may be deformed or even damaged during AFM scanning.² In many systems, this effect is undesired, not only because of the possible damage of fragile samples, but mainly due to the possibly erroneous information about the sample provided in these AFM images. In particular, AFM height images of soft samples may not reflect the real dimensions and shapes of the samples as a consequence of the deformation caused by the forces exerted by the tip. This effect was observed for a variety of materials from rubbers and polymers to biological materials, liquid films, bubbles and droplets.³⁻⁷ The list includes also surface nanobubbles – gaseous domains with the dimensions of several tens to hundreds of nanometer that form on substrates immersed in water.^{8,9}

The small dimensions and the low stiffness^{10,11,12} of nanobubbles as compared to the size of an AFM tip and the stiffness of a cantilever, respectively, render nanobubbles extremely prone to deformation during AFM scanning. The same holds true for silicone polymer nanodroplets, which were very recently proposed to be a possible explanation of various experimental observations in the literature.¹³ The possibility of nanobubble deformation leading to distorted AFM images has been repeatedly brought up since the first AFM images of nanobubbles were published.^{14,15} Also, in order to explain the absence of nanobubbles in the images, some authors concluded that the nanobubbles that originally had been present on the sample, were deformed by the AFM tip and / or scraped away from the scanned area.¹⁶⁻¹⁸ The deformation of nanobubbles seems to be a

common phenomenon present to different extent in experiments performed in various AFM modes: TM (Tapping Mode),^{14,15,17-22} CM (Contact Mode),^{15,16,23,24} Peak Force mode,^{10-12,25,26} FM (Frequency Modulation) mode,^{25,27} FV (Force-Volume) mode,^{11,12,28} and lift mode AFM.^{20,29}

So far, it has been shown that the *apparent* nanobubble dimensions in AFM images depend on the scanning parameters: The apparent bubble height and width decrease with increased amplitude of the cantilever oscillations and with decreased amplitude setpoint ratio in TM AFM^{19,21,22,30} and with increased peak force in Peak Force tapping AFM^{10,25,26}. Moreover, it has been established that nanobubbles interact differently with hydrophobic tips than with hydrophilic tips,¹² and that they respond differently to a vertical or horizontal approach of the same AFM tip during scanning.²⁹

Although we already know which parameters influence the extent of nanobubble deformation in the AFM experiments, several questions remain unanswered. It is not clear (i) how a nanobubble deforms and (ii) how its shape changes *during* scanning. In addition, we do not know (iii) how much the bubble deformation contributes to the apparent nanobubble shape in the AFM height image, and hence, what the unperturbed bubble dimensions are.

The information about the nanobubble deformation and about the unperturbed bubble profile is crucial because it affects the values of parameters derived from the bubble dimensions and influences any theory that relies on these parameters. So far, the estimated internal pressure of a typical nanobubble is anomalously high, the lifetime is several orders of magnitude longer than predicted, and the apparent profile is extremely flat with nanoscopic contact angles higher than macroscopic ones.^{8,9,17} All these

conclusions are based on the apparent shapes of nanobubbles estimated from AFM images and as shown more recently some of these data may suffer from experimental errors or uncertainties. Therefore also the theories put forward to explain the unusual nanobubbles properties³⁰⁻⁴² need to be tested critically against possible AFM artefacts.

The importance and urgency of a systematic study on the nanobubble deformation during the AFM scanning is strengthened by the fact that the AFM is so far the only technique that provides information about the bubble dimensions and shape concurrently.

Alternative techniques used to study nanobubbles – attenuated total internal reflection Fourier transform infrared spectroscopy,⁴³ rapid cryofixation,⁴⁴ quartz crystal microbalance,⁴⁵ X-ray reflectivity,^{46,47} synchrotron-based scanning transmission soft X-ray microscopy,⁴⁸ interference microscopy,⁴⁹ total internal reflection fluorescence microscopy,^{50,51} and much more recently fluorescence lifetime imaging microscopy (FLIM)^{52,53} – either do not provide any or no absolute information on the nanobubble dimensions (width or height) or the resolution is too low to compete with AFM data.

In addition, knowledge of the shape and properties of bubbles is important in the view of currently anticipated and future applications of surface nanobubbles. It has been shown that nanobubbles are useful for cleaning surfaces^{54,55} and contribute to the attraction between hydrophobic surfaces in water,⁵⁶⁻⁵⁸ rupture of thin liquid films,⁵⁹ and drag reduction.⁶⁰ Considering the growing number of research on the possible presence of nanobubbles in the variety of non-biological and biological systems,⁶¹ the list of applications of nanobubbles is certainly not complete.

Here we investigated AFM tip-nanobubble interactions in detail and in particular tip-induced nanobubble deformation based on the results of TM and FV AFM measurements

of individual argon surface nanobubbles on HOPG. Expanding on a previous report,¹² the variation of tip-bubble interaction forces for different positions on individual bubbles with respect to their centers and related parameters is analyzed here for various experimental conditions for the first time and the consequences of this phenomenon, also in relation to previously published data, are critically discussed.

EXPERIMENTAL

Sample preparation: In all experiments, freshly cleaved highly oriented pyrolytic graphite (HOPG) (VEECO, grade ZYH) with a water contact angle of $63 \pm 2^\circ$ was analyzed. The static contact angle was measured with the sessile drop method with an OCA 15plus instrument (Data Physics Instruments GmbH, Filderstadt, Germany) using Milli-Q water obtained from a Millipore Direct Q 8 system (Millipore, Schwalbach, Germany) with resistivity of 18.0 M Ω /cm and surface tension of 0.072 N/m. Argon nanobubbles were measured in Ar saturated Milli-Q water as reported previously (see also Supporting Information).¹²

Atomic Force Microscopy: The AFM measurements were carried out on a MultiMode IIIa AFM instrument (Bruker/Veeco/Digital Instruments, Santa Barbara, California) with a vertical engage E-scanner and NanoScope version 3.10 software (Bruker AXS, Santa Barbara, CA). V-shaped MLTC Si₃N₄ cantilevers (Bruker AXS, Camarillo, CA) were used with the spring constants $k_{cant} = 0.1 \pm 0.01$ N/m (hydrophilic) and $k_{cant} = 0.7 \pm 0.07$ N/m (hydrophobic). The cantilevers' spring constants were independently calibrated on an Asylum Research MFP-3D Bio (Asylum Research, Santa Barbara, California). The cantilevers were cleaned prior to the measurements for 60 s by oxygen plasma (Plasma Prep-II, SPI Supplies, West Chester, USA). In order to minimize the contamination of the

tip the cantilevers were inserted with minimal delay in the liquid cell and directly immersed in water. In all experiments, a closed liquid cell configuration was used as described previously (see also Supporting Information).¹²

Tapping mode (TM AFM): The drive frequency used for imaging was 9.2 kHz (cantilever with $k_{cant} = 0.1 \pm 0.01$ N/m) and 29.6 kHz (cantilever with $k_{cant} = 0.7 \pm 0.07$ N/m), respectively. The values of free amplitudes and setpoint ratios in TM measurements of nanobubbles in our experiments were 13 nm and 90 % for the hydrophilic tip and 16 nm and 90 % for the hydrophobic tip (for details see reference 12). Raw TM height images were processed using a 1st order plane fit and a 0th order flattening (with nanobubbles excluded). The bubble size was measured using the spherical cap fitting; no tip size correction was applied.¹⁷

Force Volume mode (FV AFM): The FV data was captured with a force curve resolution of 512 points per force curve cycle and a lateral resolution of 32×32 pixels² with no cantilever oscillation. The ramp sizes and trigger thresholds were set to 223 nm and 30 nm in the experiment done with the hydrophilic tip, and to 100 nm and 60 nm in the experiment done with the hydrophobic tip. The velocities of tip approach were set to 446 nm/s and 1.02 $\mu\text{m/s}$, respectively. Raw deflection-distance curves were transformed into deflection-separation curve⁶² so that the vertical position of the tip end above the substrate was represented in the plots by the tip-sample separation distance. The deflection was recalculated into force by multiplying the measured deflection value by corresponding cantilever stiffness.

RESULTS

Argon surface nanobubbles on HOPG in water were scanned both with hydrophilic and hydrophobic AFM tips. In each experiment, the positions of nanobubbles were initially identified in high resolution (pixel size ~6 nm) TM AFM images. Next, a FV image with lower resolution (pixel size 60-90 nm) was acquired on a particular nanobubble. The bubbles analyzed in both experiments had similar dimensions estimated based on their apparent size in TM height images. Typical nanobubbles height profiles are shown in Figure 1. Figure 1a shows a bubble that was scanned with a hydrophilic tip, Figure 1b – a bubble that was imaged with a hydrophobic tip. The apparent TM height profiles (black open squares) were obtained from the TM topographic images shown in the insets of the plots. The solid line represents the bubble profile estimated for zero force scanning conditions, i.e. zero amplitude of the cantilever oscillations and 100% setpoint ratio.²¹ For each bubble, a set of exemplary FV force-distance curves is plotted, showing a sequence of force curves measured on the bubbles at different horizontal positions along a single scan line acquired over the bubble center. The numbers in the plots mark the locations on the sample, where a particular force curve was obtained and correspond to the numbers in the plots of bubble profiles.

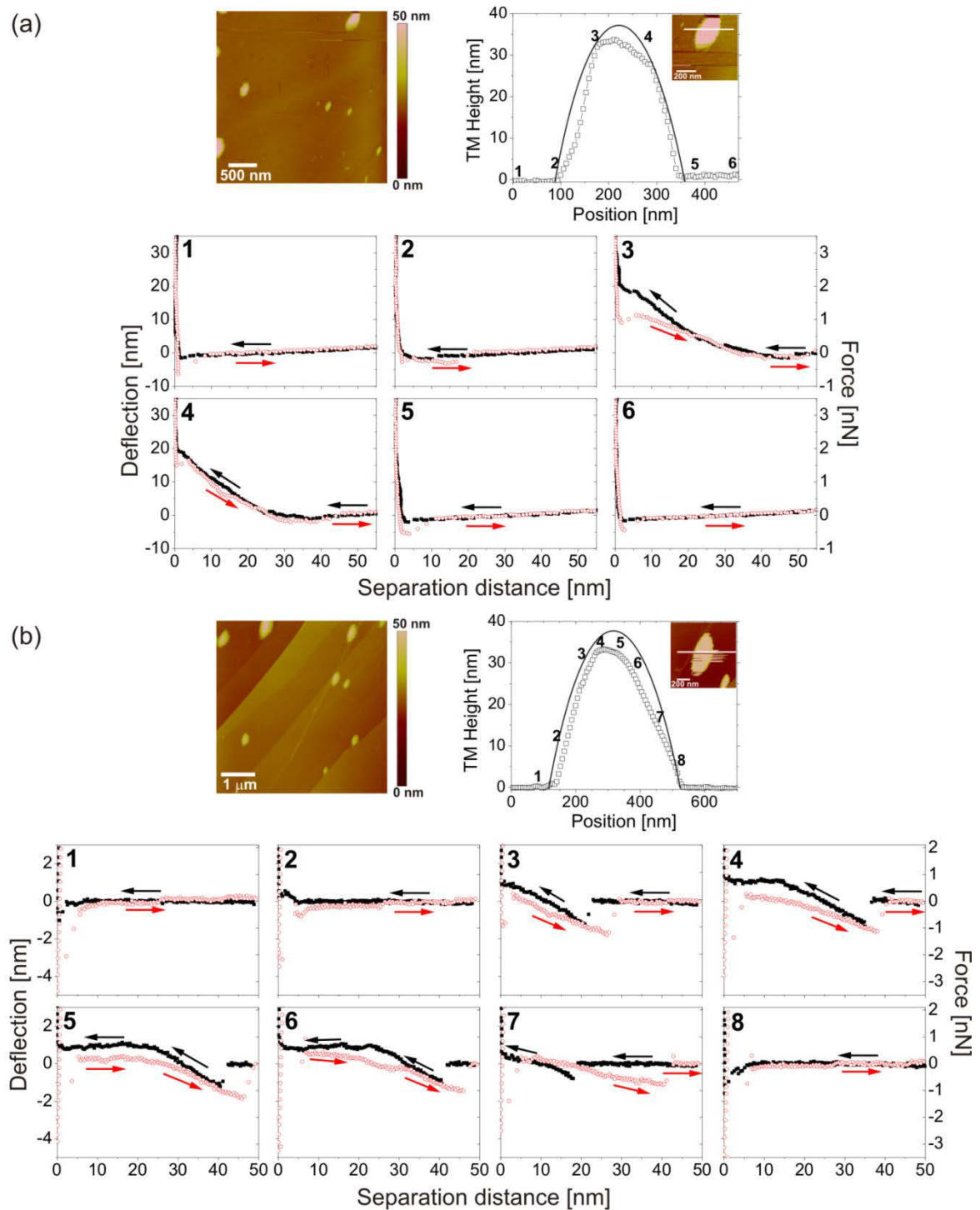


Figure 1. AFM TM height images and cross-sectional plots of the apparent (black squares) and estimated (solid lines) profiles of the nanobubble scanned with (a) a hydrophilic tip ($k_{cant} = 0.1$ N/m), (b) a hydrophobic tip ($k_{cant} = 0.7$ N/m). The sequences of approach (black) and retraction (red) force-distance curves were measured on the bubbles along single scan lines located approximately at the bubble centers. The numbers in the plots correspond to the numbers in the profiles and mark the horizontal positions on the sample, where the force curves were acquired.

The force curves shown in Figure 1 represent two types of force-distance curves acquired on the nanobubbles. They possess, as discussed previously,¹² entirely different shapes that depend on whether the scanning was done with a hydrophilic or with a hydrophobic AFM tip. The characteristic features of the force curves acquired on the bubble with a hydrophilic tip (Figure 1a) are the presence of a linear slope, a very small hysteresis, no or little attraction, similar positions of the corresponding jump-in and jump-out points. On the contrary, the force-distance curves acquired on the bubble in Figure 1b with a hydrophobic tip display large adhesion, large attraction, jump-out points at larger separation distances than the corresponding jump-in points, a non-linear dependence of force on separation distance, and a large hysteresis.

We analyze the force curves acquired on both nanobubbles in order to investigate the interaction between the AFM tips and the bubbles during imaging. Several parameters that can be extracted from a typical force curve acquired on the nanobubbles are defined in Figure 2. The schemes surrounding the plots show in a simplified way the position of the tip, the bending of the cantilever and the possible deformation of the bubble-water interface at different stages of a single approach-retraction force curve cycle. Importantly, in the experiment, the actual shape of the bubble might change differently during the interaction with a real AFM tip.

The best available estimate of the unperturbed bubble height H_{bub} is the position of the point no. 2 in the force curves in Figure 2, i.e. the tip-sample separation distance at which the tip interacts with the bubble, but the net force applied on the AFM cantilever is zero (see schemes). Next, as defined in the plot in Figure 2b, the difference between the jump-in and jump-out positions (points 1 and 6) in the approach and the retraction force curves

is the adhesion distance D_{adh} . This parameter is related to the adhesive force between the tip and the bubble. The distance measured on the approach curve from the jump-in point to the point, at which the linear part of the force curve crosses the zero deflection line (the distance between points 2 and 1) is the deformation distance on approach D_{rec} (this definition assumes a jump of the bubble interface toward the tip).¹² From a similar measurement done on the retraction curve, the deformation distance on retraction D_{adv} may be obtained. As shown in the schematic drawing in the bottom of Figure 2a, the maximum upward deformation of the bubble surface upon retraction is the sum of D_{rec} and D_{adh} measured from the corresponding force curve. For a given nanobubble (with constant properties) the parameters D_{adv} and D_{rec} characterize the AFM tip. D_{adv} is related to the advancing and D_{rec} to the receding contact angle of the liquid on the tip material. In addition, we can estimate from the force curve the cantilever deflection at the point of the maximum downward bending (point 5 in the plot in Figure 2b) the rupture or maximum adhesive force F_{adh} . While D_{adh} describes the range of separation distances over which the adhesion force plays a role, F_{adh} describes the strength of the adhesion.

A comparison of the plots in Figures 2a and 2b reveals that in the case of measurement done with an ideally sharp and hydrophilic tip, the hysteresis in the force-distance curves acquired on a nanobubble is zero. Consequently, all presented parameters with exception of H_{bub} are equal to zero. In other words, D_{adh} , F_{adh} , D_{adv} and D_{rec} are non-zero only, if there is a hysteresis in the force curves. This is obviously the case, if the bubble is scanned with a hydrophobic tip, as shown in the plot in Figure 2b.

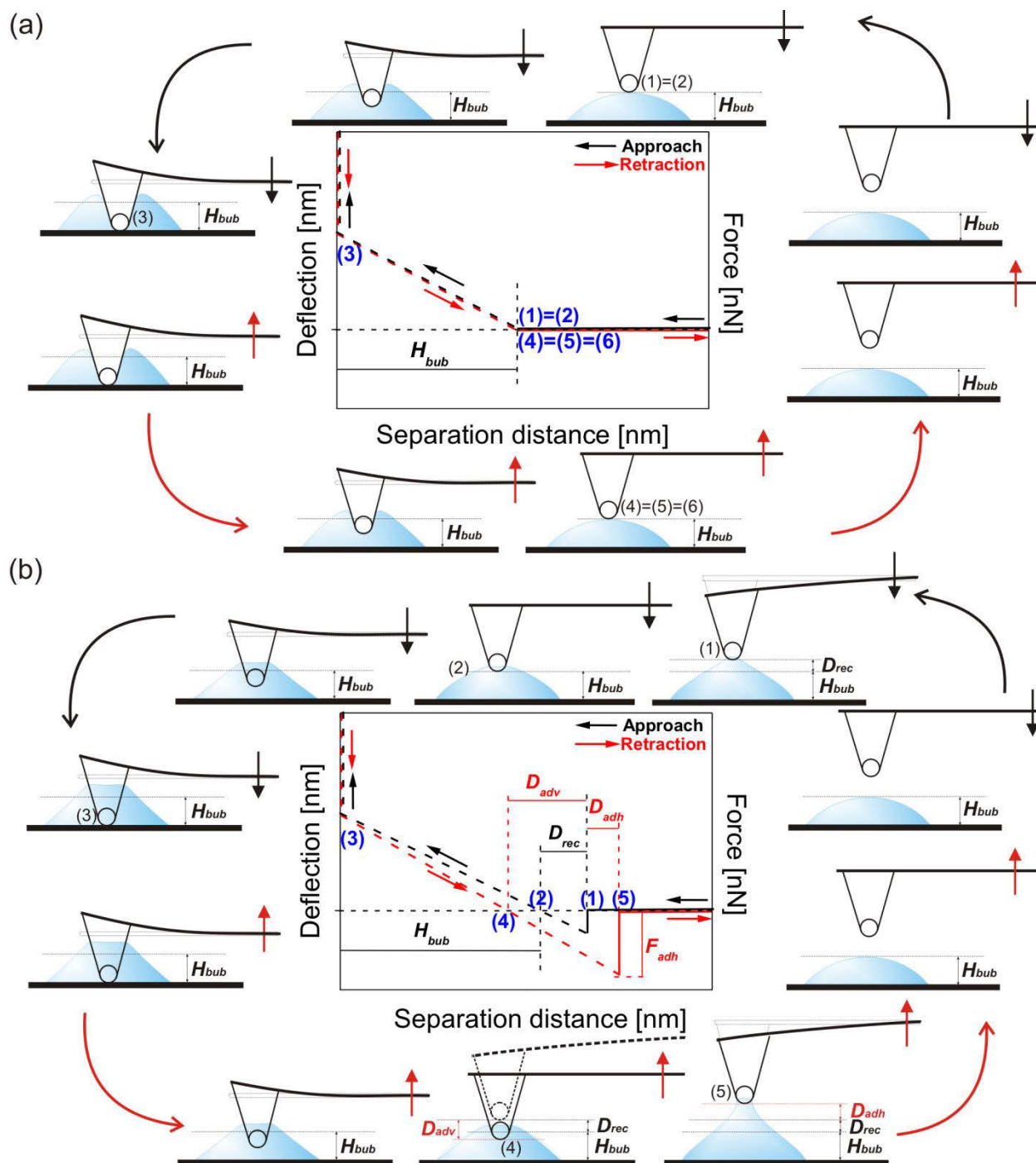


Figure 2. Typical approach and retraction force-distance curves acquired on a nanobubble (a) with a hydrophilic AFM tip, (b) with a hydrophobic AFM tip. The position and the bending of the cantilever and the possible bubble deformation are shown schematically at different stages of the interaction (drawing not to scale). The parameters are described in the text.

First, we determine the unperturbed bubble profile. The local bubble height H_{bub} measured from the individual force-distance curves shown in Figure 1a and 1b can be plotted against the horizontal position of the tip over the bubble. The height profiles of both measured bubbles reconstructed in this way are plotted in Figure 3 together with the height profiles estimated from TM AFM images. Both bubbles were chosen such that they had similar estimated dimensions, with 300-400 nm in width and around 38 nm in height. Despite the low resolution of the FV images, the shapes of both reconstructed profiles resemble well a spherical cap shape. For the nanobubble scanned with a hydrophilic tip, the height and the width of the reconstructed profile are similar to the height and width estimated for zero force scanning condition, as shown in the plot in Figure 3a. For the bubble scanned with a hydrophobic tip, the situation is different. In the corresponding plot in Figure 3b, the height of the reconstructed profile is significantly smaller than the height estimated from the TM AFM data.

Next, we discuss the values of the four parameters D_{adh} , F_{adh} , D_{adv} and D_{rec} defined in Figure 2 that were determined from the force curves acquired on two nanobubbles. Figures 4 and 5 show the data for D_{adh} and F_{adh} , and for D_{adv} and D_{rec} , respectively. The values of the parameters measured from the force curves measured on all positions over the bubble are plotted for each bubble as functions of the unperturbed local bubble height H_{bub} . Large H_{bub} correspond to the positions near the bubble center and small H_{bub} correspond to the positions near the bubble rim. This is shown schematically in the pictures placed next to the data points in the plots. Shifting from small to large H_{bub} values corresponds to moving the tip from the bubble periphery toward the bubble center along the radius of the bubble base. The data from the force curves shown in Figure 1 measured along a single scan line, plotted for each bubble as functions of the horizontal

position of the tip across the bubble are shown in the Supporting Information (Figures S-1 and S-2).

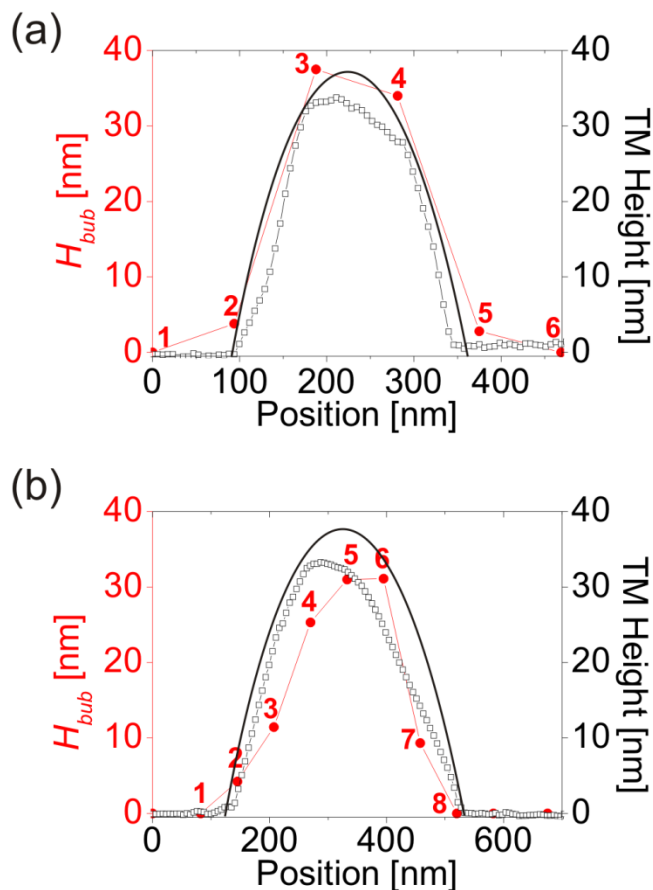


Figure 3. Cross-sectional profiles of (a) the nanobubble scanned with a hydrophilic tip, (b) the nanobubble scanned with a hydrophobic tip. In both plots three profiles are shown: the apparent profile measured from the TM height image (open symbols), the profile estimated for zero interaction conditions (solid line), and the profile reconstructed from the force-distance curves (solid symbols in red).

In the plots shown in Figure 4, adhesion distances D_{adh} and maximum adhesion forces F_{adh} measured on the bubble scanned with the hydrophobic tip were larger and showed a stronger dependence on H_{bub} than D_{adh} and F_{adh} measured on the bubble with the hydrophilic tip. The maximum D_{adh} measured on the bubble with the hydrophobic tip was nearly 40 nm, which was twice the maximum value of D_{adh} measured on the bubble scanned with the hydrophilic tip. Hence even at the bubble rim, the nanobubble stays

attached to the tip to 40 nm separation distance before it detaches. From the plot in Figure 4b, it is clear that for the bubble scanned with the hydrophobic tip, D_{adh} depended on the position of the tip over the bubble and was larger near the bubble periphery and smaller near the bubble center. For the bubble scanned with the hydrophilic tip, D_{adh} was found to be independent from H_{bub} .

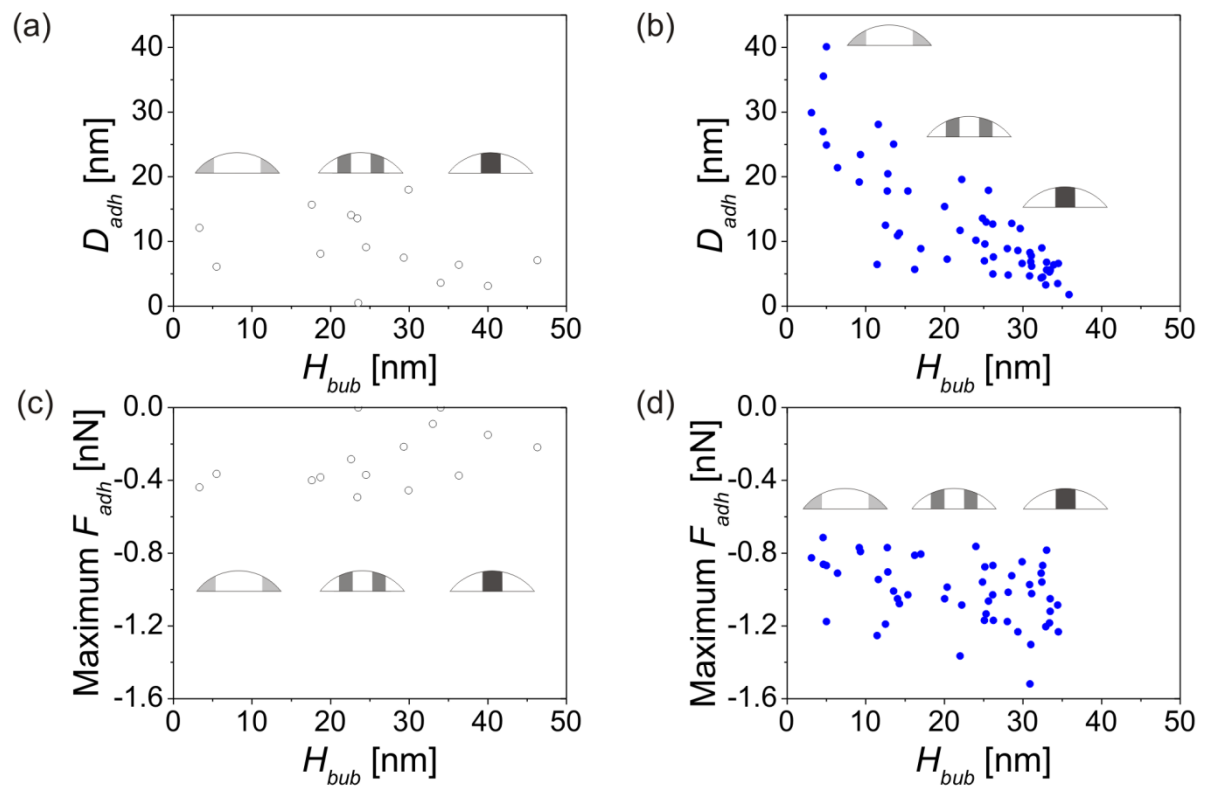


Figure 4. (a) D_{adh} measured for the nanobubble scanned with a hydrophilic tip, (b) D_{adh} measured for the nanobubble scanned with a hydrophobic tip, (c) F_{adh} measured for the nanobubble scanned with a hydrophilic tip, (d) F_{adh} measured for the nanobubble scanned with a hydrophobic tip. The values measured from all force curves acquired on the particular bubble are plotted as a function of the unperturbed local bubble height H_{bub} .

As shown in the plot in Figure 4d, F_{adh} measured on the bubble with the hydrophobic tip spanned the range between -0.7 and -1.6 nN with most of the values being smaller than -1.2 nN. The measured force was large all over the bubble and increased in magnitude when the tip was shifted toward the bubble center. For the bubble scanned with the

hydrophilic tip, F_{adh} was small and did not exceed -0.6 nN. In contrast to the bubble scanned with the hydrophobic tip, F_{adh} decreased as the tip was moved toward large H_{bub} values near the bubble center.

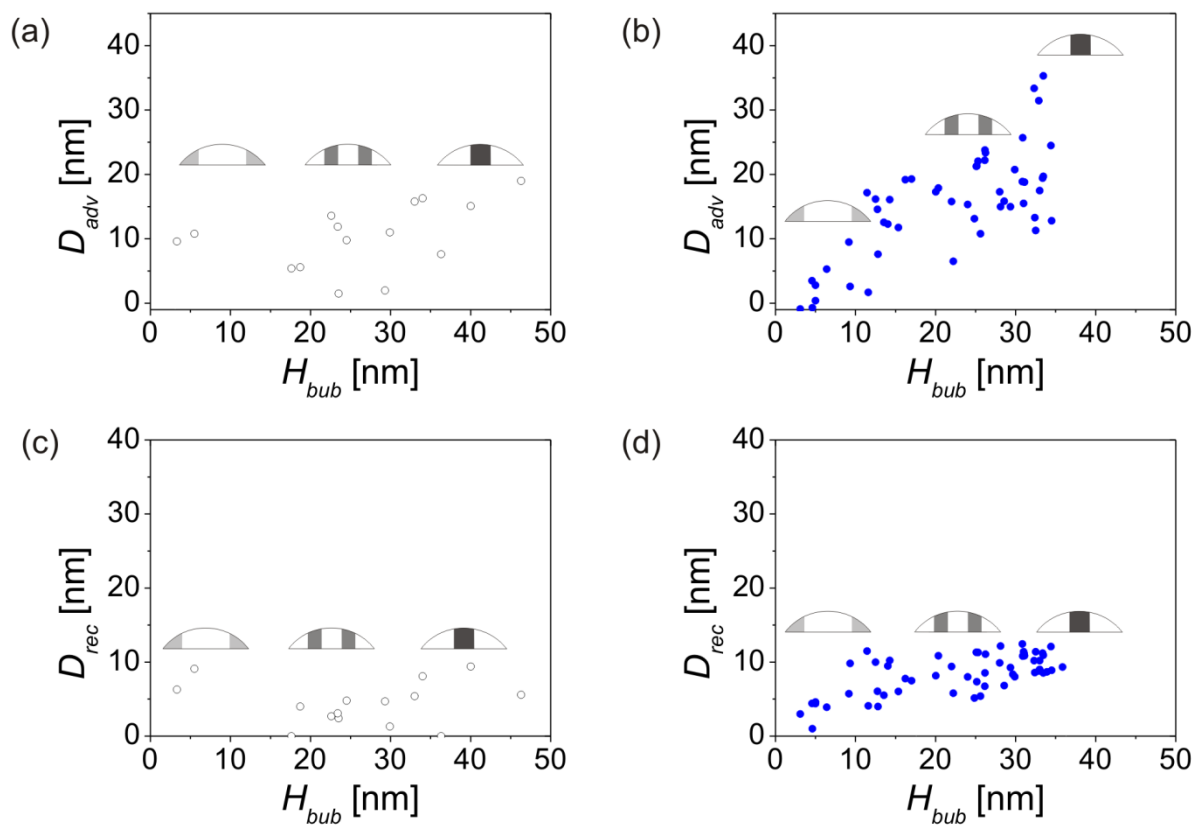


Figure 5. (a) D_{adv} measured for the nanobubble scanned with a hydrophilic tip, (b) D_{rec} measured for the nanobubble scanned with a hydrophobic tip, (c) D_{rec} measured for the nanobubble scanned with a hydrophilic tip, (d) D_{adv} measured for the nanobubble scanned with a hydrophobic tip. The values measured from all force curves acquired on the particular bubble are plotted as a function of the unperturbed local bubble height H_{bub} .

In the plot in Figure 5b, D_{adv} measured on the bubble with the hydrophobic tip showed a dependence on local bubble height H_{bub} and decreased as the tip was moved away from the bubble center. The maximum D_{adv} value of nearly 40 nm was measured in the force curve acquired near the bubble center; the minimum value of D_{adv} close to 0 nm was measured near the bubble periphery. Such D_{adv} variations were not observed for the

bubble scanned with the hydrophilic tip, as shown in the plot in Figure 5a. At all positions on the bubble, D_{adv} was nearly constant and did not exceed 20 nm.

Finally, the deformation distance on approach D_{rec} was smaller than D_{adv} for both bubbles and only slightly exceeded 10 nm. For the bubble scanned with the hydrophilic tip, D_{rec} was approximately constant, irrespective of the horizontal position of the tip over the bubble. For the bubble scanned with the hydrophobic tip, D_{rec} increased slightly for increased H_{bub} .

As a next step in our analysis of force curves, we determine the total distance over which the tip interacted with the bubbles in both experiments. We use the fact that the positions of the jump-in point in the approach force curve and the jump-out point in the retraction force curve indicate the onset and the end of the tip-bubble interaction, respectively (Figure 6). For each bubble, a cross-sectional plot shows an exemplary cross-section of the bubble and the variation of the parameters measured along a single scan line. The general plot shows the data as a function of the unperturbed local bubble height H_{bub} . Solid line represents the position of the bubble surface above the substrate.

For both bubbles, the separation distances of the jump-in points to the bubble surface were comparable and smaller than 10 nm. They were smaller than the separation distances of the jump-out points and independent from H_{bub} . In the case of the separation distances of jump-out points, there was a clear difference between the data points acquired on the bubbles with hydrophilic and with hydrophobic tips. As shown in the plots in Figure 6a, when the bubble was scanned with a hydrophilic tip, the difference between the positions of the jump-in points and the jump-out points was small (<15 nm) and independent from the local bubble height. On the contrary, as shown in Figure 6b, for

the bubble scanned with a hydrophobic tip, the difference between the positions of the jump-in points and the jump-out points was on average larger and it increased with decreasing bubble height, from ~ 10 nm near the bubble center up to ~ 40 nm near the bubble edge.

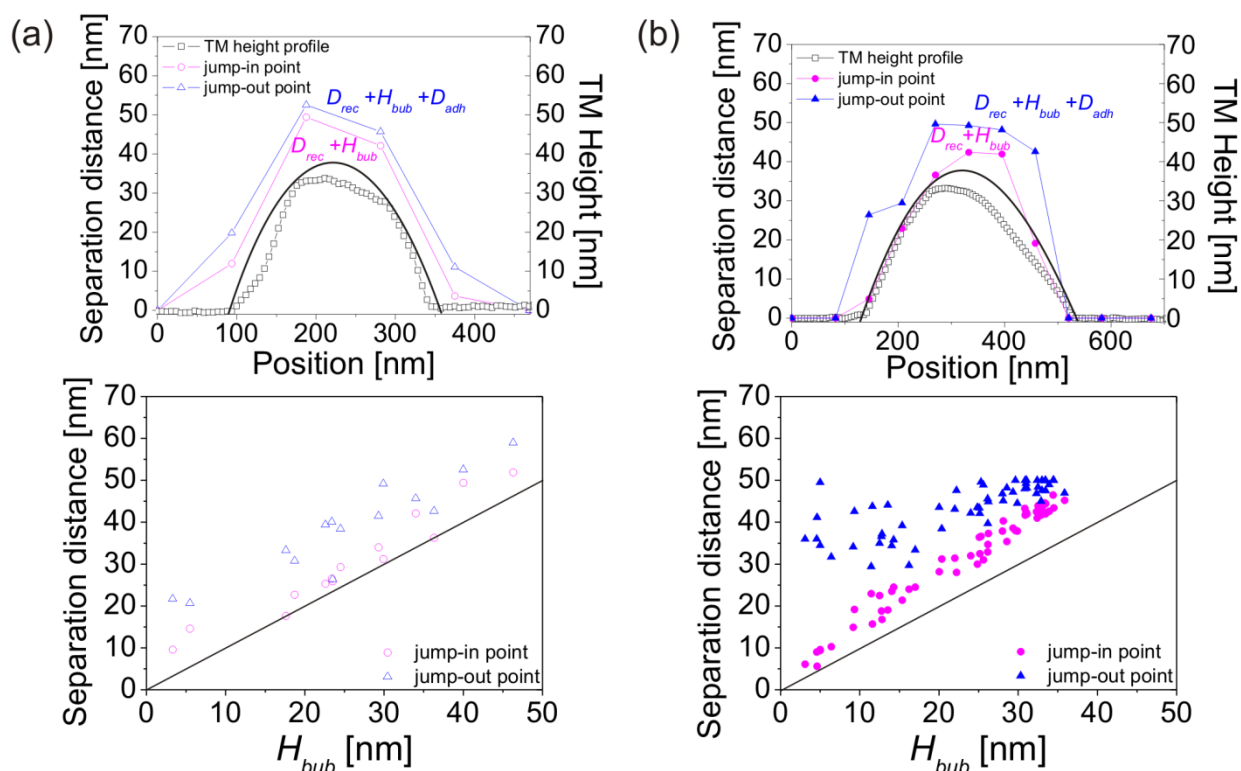


Figure 6. The position of the jump-in and jump-out points in the force-distance curves marking the onset and the end of the tip-nanobubble interaction (contact), respectively, measured for the bubble scanned with (a) a hydrophilic tip, (b) a hydrophobic tip. In the upper graphs, the values are plotted as a function of the horizontal position of the tip along the scan line. In the lower graphs, the values are plotted as a function of the unperturbed local bubble height H_{bub} .

Finally, we look at the slopes of the (quasi-)linear parts of approach and retraction force curves acquired on the nanobubbles with hydrophilic and hydrophobic tips. The values of the slopes are plotted in Figure 7 as a function of H_{bub} measured at the location on the sample, where the particular force curve was acquired.

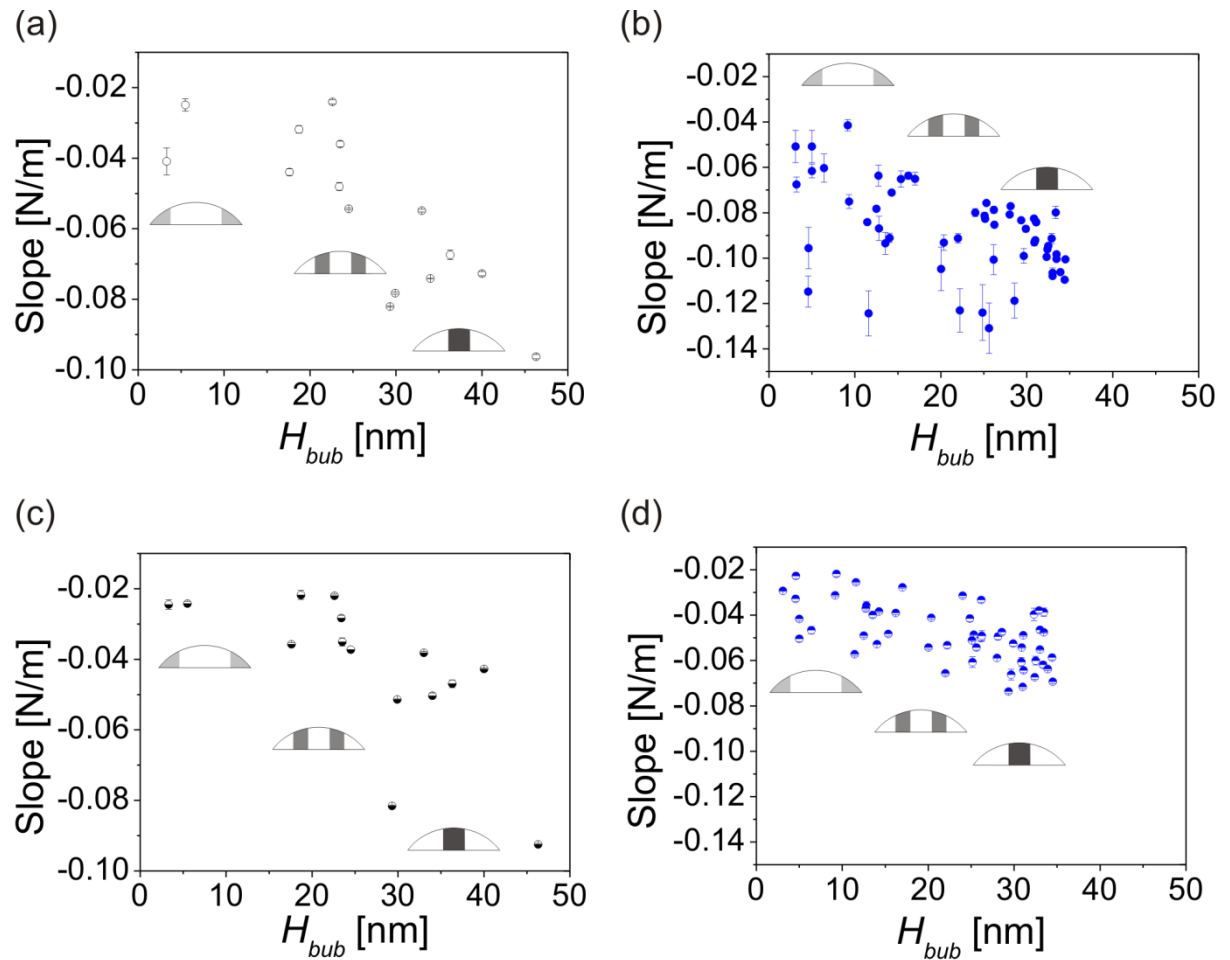


Figure 7. Slopes of the (quasi-)linear parts of the force curves acquired on nanobubbles plotted as a function of the unperturbed local bubble height H_{bub} . (a) Approach curves measured with a hydrophilic tip, (b) approach curves measured with a hydrophobic tip, (c) retraction curves measured with a hydrophilic tip, (d) retraction curves measured with a hydrophobic tip.

All measured slope values are negative. During the approach, the repulsive forces (positive deflection) increased with decreasing tip-sample separation. During the retraction, we dealt with attractive forces (negative deflection) that increased, i.e. became more negative, as the separation distance increased. In the plots, we observe a dependence of the slope values on the bubble height i.e. on the position on the bubble, where the curve was acquired. For both bubbles, the slopes became steeper and more negative as H_{bub} increased. We have observed that in the case of the force curves measured with the

hydrophobic tip, the slopes in the retraction curves showed less irregularity than the slopes in the approach curves and the data points in Figure 7d were less scattered than in Figure 7b. This was caused most likely by the fact that during the retraction, the contact of the bubble with the tip surface was already well established, which was not always the case on approach.

DISCUSSION

Based on the experimental data acquired in TM and FV AFM on individual nanobubbles with tips with different hydrophobicity, we determined several parameters that characterize the bubbles and their interactions with the tips during the scanning. These data provide insight into how the AFM scanning influenced the apparent bubble shape in the AFM “height” images obtained and what can be learned about the unperturbed nanobubble size and shape.

In Figure 3a, the reconstructed profile of the nanobubble scanned with a hydrophilic tip had similar dimensions as the profile estimated from the TM height image for zero force scanning conditions. This result confirms our earlier findings¹² and shows that the apparent bubble dimensions measured from the TM height image and the knowledge of the values of the amplitude of the cantilever oscillations and the setpoint ratio used to scan the image are sufficient to determine the actual bubble shape, if the tip is ideally hydrophilic and sharp. This is in many experiments *not* the case. As shown in Figure 3b, in the case of the bubble scanned with a hydrophobic tip, the height of the reconstructed profile was significantly smaller than the height of the estimated profile. This means either that the position of zero deflection crossing point in the force curve did not reflect the unperturbed bubble height or that the estimation based on the TM height image was

erroneous and did not apply in the case of nanobubbles scanned with a hydrophobic tip. It can be concluded that in the case of the scanning of nanobubbles with a hydrophobic or mildly hydrophobic tip, the real bubble profile and dimensions cannot be determined with certainty.

The entirely different shapes of the force curves in Figure 1, acquired on nanobubbles with hydrophilic and hydrophobic tips, are reflected in different values and different spatial dependences of D_{adh} , F_{adh} , D_{adv} and D_{rec} . From the plots in Figure 4 and Figure 5, it is clear that these four parameters were non-zero even for a “hydrophilic” tip, which is contrary to what had been suggested in Figure 2a. Obviously, the tip used in the experiment was not ideal, which resulted in the not uncommon hysteresis observed in the force curves. We stress that the hysteresis was much smaller than the hysteresis in the curves shown in Figure 1b or reported previously.^{10,11,14,20,23,28,32} Nevertheless, the values of D_{adh} , F_{adh} , D_{adv} and D_{rec} measured from curves acquired with the hydrophilic tip were smaller and showed no or only a weak dependence on the bubble height H_{bub} , whereas for the hydrophobic tip, the values were larger and varied with H_{bub} . So far, the spatial dependences of the parameters has been reported,^{10,25,26,30} but no consistent explanation has been offered.

These results are not surprising. From earlier analysis of the data from the same set of experiments, we know that the nature of the tip-bubble interaction was entirely different in the case of the scanning done with hydrophilic and hydrophobic tips.¹² Increased adhesion was caused by the capillary force acting along the contact line that formed on the tip, when it contacted the bubble during the measurement. In the case of the

hydrophilic tip, no direct contact between the tip and the bubble resulted in weaker attractive forces measured.

In order to determine the actual nanobubble shape, we need to know more about the bubble deformation. We can analyze the information from the force curves in order to determine the interaction at different points on the bubble. Next, having information about the spatial variation in the interaction, we can estimate the changes in the bubble shape during the scanning.

Although different forces were involved in the interaction in the experiments done with hydrophilic and hydrophobic tips, as shown in Figure 6, for *both* bubbles the interaction between the tip and the bubble started and ended at separation distances *well above* the unperturbed bubble surface. This result means that the bubble surface might deform upwards.^{12,29} The distances D_{rec} and $D_{rec} + D_{adh}$ define the possible maximum upward deformation of the bubble on approach and on retraction, respectively. As shown in Figure 6, for a particular force curve, the sum of H_{bub} and D_{rec} or $D_{rec} + D_{adh}$ is equal to the separation distances of jump-in and jump-out points, respectively. We can estimate that the upward bubble deformation on approach was between few up to 10 nm and comparable for both tips, and on retraction was up to 15 nm for the hydrophilic tip and up to 45 nm for the hydrophobic tip, depending on H_{bub} . If we compare these values with the estimated (maximum) bubble heights of ~ 40 nm, the deformation of 10 nm corresponds to an increase of the bubble height by 25 % or more and to an apparent increase in the curvature and in the Laplace pressure by approximately 20 % or more, assuming that the bubble contact line was pinned.^{32,33} In fact, the true values of deformation might be even

larger because we do not know the actual vertical positions of the contact line on the hydrophobic tip with certainty.

Based on the data shown in Figure 6b, the upward bubble deformation was smaller on approach than on retraction. According to the plots shown in Figures 5b and 5d, for the bubble scanned with the hydrophobic tip, D_{adv} was on average larger than D_{rec} , hence the receding contact angle of the tip material was smaller than the advancing contact angle. Therefore, it is likely that the bubble surface stayed attached longer to the tip and the bubble deformed more upwards during the retraction than during the approach. A similar trend has been observed in the experiments done on bubbles of microscopic size probed with spherical particles.⁶² Based on the plots in Figures 5b and 5d, we can estimate the variation in the contact angles of the tip material, depending on how deep the tip was immersed into the bubble. For the tip sizes between 20 and 60 nm, the advancing and the receding contact angles at the tip apex were both estimated to 18-30°. Away from the apex, the advancing contact angle increased to 60-140° whereas the receding contact angle increased to 40-70°. The smaller the (assumed) tip size, the larger the estimated values of the contact angles. The *difference* between D_{adv} and D_{rec} that corresponds to the difference between the advancing and the receding contact angles increased with increased H_{bub} (see Supporting Information, Figure S-3). This suggests that the tip material was more hydrophobic away from the apex. This might be caused by contaminations on the tip or local changes in the shape or curvature of the tip.

In the case of the hydrophilic tip, the described scenario of nanobubble deformation does *not* apply because there was no direct contact between the tip and the bubble during the force cycle. From Figure 6a, we know that the tip-bubble interaction extended above the

estimated unperturbed bubble profile during both approach and retraction, but interaction forces acted through the film of liquid remaining between the bubble and the tip apex, and did not necessarily caused bubble stretching in the upward direction. Because the bubble did not contact the tip directly, we cannot use D_{adv} and D_{rec} to learn more about the contact angle of the tip material. However, a low contact angle ($\sim 18^\circ$) of the tip material was confirmed in our previous report.¹²

In our experiment reported here, we observed spatial variations in D_{adh} measured from the force curves acquired on the bubble with the hydrophobic tip similar to the variations measured by Wang et al.³⁰ from amplitude-distance curves. As shown in Figure 4b, D_{adh} was larger for small H_{bub} near the bubble periphery that indicates that at these positions the bubble remained attached to the tip over a relatively larger distance, as compared to its unperturbed local height. This was caused most likely by the fact that the bubble simultaneously stretched upwards and deformed sideways during the retraction, so that it could remain attached to the tip. At each point, the vertical distance over which the bubble could be stretched (the jump-out point position) was limited only by the bubble volume, and therefore it was almost independent from the horizontal position of the tip over the bubble, as confirmed by the plot in Figure 6b. In consequence, D_{adh} measured for small H_{bub} was increased compared to D_{adh} measured for large H_{bub} . The absence of a dependence of D_{adh} on H_{bub} in Figure 4a for a hydrophilic tip further confirms the scenario presented above. The absent direct contact between the tip and the bubble prevented the stretching of the bubble interface sideways, and therefore D_{adh} did not increase for small H_{bub} . Consequently, in Figure 6a, the data points marking the jump-out positions follow the data points for the jump-in points.

As shown in Figure 4d, for the bubble scanned with the hydrophobic tip, the increase in D_{adh} near the bubble periphery was *not* followed by an increase in F_{adh} . This opposes the statement of Wang et al.³⁰ that the tip-bubble surface area (and hence the length of the contact line and the magnitude of the force) increased, when the tip was shifted off the bubble center. As a comparison, in the Peak Force Tapping AFM done with a low peak force, unchanged or slightly increased adhesion was measured near the bubble edges as compared to the center.^{10,25,26} In our experiment, only the bubble scanned with a hydrophilic tip showed a similar dependence. This suggests that the tips used in the mentioned Peak Force experiments were hydrophilic.

Next, we discuss the tip-bubble interaction and bubble deformation at separation distances smaller than the unperturbed bubble height. Independent from the type of tip used in the experiment, a positive cantilever deflection was measured for both bubbles at separation distances smaller than H_{bub} . We know from the force curves acquired on the nanobubbles that the tip apex reached the graphite substrate at each point of the scanned area. We assume that at this point of the measurement, the maximum downward deformation of the bubble was equal to the *local* unperturbed height H_{bub} (compare with Figure 2); hence it was largest at the bubble center and smallest near the bubble periphery. At any intermediate vertical position of the tip end between H_{bub} and the substrate, the bubble deformation was approximately equal to the difference between H_{bub} and the current tip-sample separation distance. Near the bubble periphery, only the very end of the tip interacted/was in contact with the bubble, whereas near the bubble center, the tip was “immersed” several tens of nanometers deep into the bubble. We emphasize that the exact value of the bubble deformation depended also on the vertical position of the contact line on the tip in the case of the hydrophobic tip. In turn, the deformation of

the bubble scanned with a hydrophilic tip might be influenced by the temporarily changing thickness of the water film between the tip and the bubble that might add to the measured nanobubble height. We assume that the thickness of this film in our experiment did not exceed several nanometers.

We have also shown above that the deformation of the nanobubbles depended both on the vertical and on the horizontal position of the tip on the bubble, independent from the hydrophobicity of the tip. The variations in the slope values shown in Figure 7, measured from the force curves acquired at different spatial positions on the bubbles, are manifestations of this effect. The slopes in the force curves measured at the locations near the bubble center were relatively steeper for both bubbles than the slopes in the curves measured near the bubble periphery. This result means that during the measurement, the deflection of the cantilever and the deformation of the bubble increased with decreased tip-sample separation distance relatively faster at points on the sample located close to the bubble center than at the points located near the bubble periphery. Our finding may have significant consequences for AFM measurements of surface nanobubbles. Because the deformation of the bubble surface is related to the force exerted on the sample, the extent of the bubble deformation will vary depending on the scanning conditions and the position of the tip.

The most straightforward example for the effect the varying slopes may have on the height measurement is Peak Force AFM. We have shown that the downward deformation of a nanobubble increased for increased peak force and varied depending on the spatial position of the tip on the bubble²⁶ (see also Supporting Information, Figures S-4 and S-5). This presumably reflected the variations in the slope of the individual force-distance

curves. A relatively less steep slope and forces that increase slowly with decreasing separation required that the tip had covered a larger vertical distance, before it reached the peak force level, than in the case of a steep slope and fast increasing force. We conclude that the relatively large local deformation measured near the bubble periphery corresponded to relatively less steep slopes in the curves acquired at these points.

Therefore, the nanobubble measured in the Peak Force AFM displayed similar local variation in the slopes of the force curves as the bubbles measured in our experiments. On the contrary, in another Peak Force experiment, the deformation measured on the bubble seemed uniform over whole bubble surface,²⁵ which was presumably caused by a very low peak force value set in this measurement and different cantilever and tip used.

On the one hand, a relatively large bubble deformation along the periphery will result in a relatively large height underestimation at these points. On the other hand, a relatively small bubble deformation near the center will correspond to a relatively small height underestimation due to this effect. This non-uniform height underestimation will result in the change in the apparent bubble shape – the bubble will appear higher and less wide in the AFM height image than it really is. In addition, most likely, the thin air layer that constitutes the bubble near its periphery will not offer much resistance to the tip action, and will be deformed/penetrated instantly even for small scanning force and, therefore, it will not appear in the height image and the apparent nanobubble width will be underestimated. We roughly estimate that due to this effect, the width of a nanobubble may be underestimated by at least ~20% and the radius of curvature may be underestimated by at least ~25%, assuming nearly zero force scanning conditions. This was the case in the Peak Force experiment, in which the bubbles in the height image displayed apparent widths smaller than the sizes of their corresponding footprints visible

in the dissipation and adhesion images.²⁶ Finally, this erroneous apparent bubble shape in the height image will result in a decreased apparent contact angle (water side) i.e. it will lead to an *underestimation* of the contact angle. Since the contact angles measured for nanobubbles are already much higher than the macroscopic contact angles, further flattening of the bubble applied as a correction for the AFM measurement would mean that, we end up with an almost completely flat structure with a contact angle toward 180° that has a large radius of curvature and hence a small Laplace pressure. As a rough estimate, if the apparent radius of curvature of a nanobubble is underestimated by 25%, the necessary correction for the Laplace pressure would require the apparent value to be lowered 25 %. For a typical nanobubble with an apparent height and width of 30 nm and 350 nm, respectively, that has an apparent contact angle of 160° , the corrected Laplace pressure would drop from 0.27 MPa to a pressure of approximately 0.20 MPa.

Importantly, the larger is the force used as a threshold in the measurements, the more severely underestimated will be the nanobubbles' heights and widths. It means that for increased scanning forces, the bubbles in the AFM height images will deviate more and more from their unperturbed shapes and their apparent contact angles will decrease. Such a decrease in the apparent nanobubble height, width and contact angle have been observed in PFT AFM for high scanning forces.²⁶

Interestingly, in TM AFM a decrease in the apparent height and width and an *increase* in the apparent contact angle were observed for decreased amplitude setpoint ratio (for increased scanning force threshold).²¹ This was most likely caused by the different imaging mechanism employed which is based on the damping of high frequency oscillations and hence local energy dissipation.

We hypothesize that spatial variations of the slope of the force-distance curves acquired on the nanobubbles are a manifestation of spatially varying strength of the long-range attractive forces originating from the substrate under the bubbles. Long-range van der Waals forces possibly influenced the tip-bubble interaction over tens of nanometers.⁶³ A simple estimate suggests that the force is significant, but cannot account alone for the observed effects. Certainly, any attractive force originating from the substrate influences the cantilever bending more near the bubble periphery than near the bubble center. Near the bubble edge, the majority of the tip apex interacted with the graphite and only small part of the tip interacted with the bubble (and with the graphite through a thin air layer). The more the tip was shifted toward the bubble center, the weaker was the influence of the substrate and the stronger was the influence of the deformed bubble surface. The change in force was gradual and was reflected in the gradual change in the slope values measured in the experiments shown in Figure 7. The fact, that a change in the slopes was observed for both hydrophilic and hydrophobic tips further validates the hypothesis of the influence of long-range van der Waals forces. As a comparison, short-range van der Waals forces influenced the tip-bubble interaction up to the separation distances of few nanometers, and their influence on the tip-bubble interaction was equal, disregarding the position of the tip on the sample. The attraction strength varied from fractions of nN to few nN, depending presumably on the size of the tip. Stronger short-range interaction measured in the force-distance curves acquired on the bubble with the hydrophobic tip might be the result of the increased tip size.

It is possible that a strong tip-sample interaction close to the substrate will cancel or (over)compensate any interaction with the thin air layer covering the sample. Therefore, it is also possible that there is a minimum air thickness, which will be “visible” for the tip in

each AFM experiment. Any air layer of thickness equal to or smaller than this minimum value will not appear in the AFM height image (i.e. it will appear as substrate). We estimate that this critical thickness of such an air layer in TM AFM experiment does not exceed a few nanometers. However, the exact value will depend on the scanning parameters, the tip geometry and cleanliness, and other parameters. If this effect is strong, the edge of nanobubble will not appear in the AFM height image and the apparent bubble width will be underestimated. The necessary correction of the bubble shape will reduce the curvature of the bubble leading to nearly completely flat bubble profile.

These results bring up an issue of the dependence of bubble parameters on the bubble size. In the Peak Force experiment,²⁶ the apparent bubble height decreased linearly with increased peak force. The ratio of the decrease was larger for larger bubbles i.e. their apparent heights decreased faster in the height image with increased peak force than for smaller bubbles. This means that larger bubbles were deformed to a larger extent by the tip than small bubbles for comparable forces. Similar observations were done in TM AFM.²¹ The apparent bubble height decreased with increased amplitude of the cantilever oscillations and with decreased setpoint ratio. In both cases, the rate of decrease depended on the bubble size (height) and was faster for larger bubbles.

In Figure 7, we saw that in our experiment the slopes in the force curves varied with local H_{bub} for a single bubble and were steeper for increased H_{bub} . This resulted in a height reduction that was smaller at the points with larger H_{bub} . Therefore, on the one hand, in Peak Force and TM experiments, we observed that smaller nanobubbles were deformed relatively less during the scanning and their actual height was less underestimated than the height of larger nanobubbles. On the other hand, in the FV and Peak Force

experiments, we observed that a single bubble was deformed downwards relatively less at the points, where its height was larger and that its actual height at these points was less underestimated. We combine these two results and conclude that the degree of deformation of the bubble size (a) depends on the bubble size and (b) is a function of the spatial position on the bubble. The apparent bubble profile in an AFM height image will be the resultant of these two effects. A small nanobubble will be deformed downwards relatively less than a large one, but for both bubbles, the deformation in the center will be the smallest, and the deformation along the bubble periphery will be the largest.

The nanobubble size dependence and non-uniform distribution of deformation was most likely the reason for the variation in the apparent contact angle for small and large bubbles observed in the Peak Force and TM AFM experiments. In both cases, the contact angle was a function of the bubble size – larger bubbles had smaller apparent contact angle than smaller bubbles.

CONCLUSIONS

We presented the results of the measurements of argon surface nanobubbles on HOPG in water done in FV AFM mode with hydrophilic and hydrophobic tips. If the tip used for the scanning was ideally hydrophilic, the actual bubble shape could be estimated from the apparent bubble dimensions measured from the TM height image based on the values of the amplitude of the cantilever oscillations and the setpoint ratio used to scan the image.

The procedure does not apply if the scanning was done with a (mildly) hydrophobic tip.

In the case of the hydrophobic tip, the bubble surface was in direct contact with the tip during the whole interaction period, which resulted in severe bubble surface deformation.

Especially, the bubble was stretched upwards and sideways when the tip was located off the bubble center. For the hydrophilic tip, the presence of the thin liquid film between the tip and the bubble minimized bubble deformation and prevented stretching of the bubble surface sideways. Independently from the hydrophobicity of the tip used, the deformation of the bubbles in the vertical direction depended both on the vertical and on the horizontal position of the tip on the bubble. It increased with decreased tip-sample separation distance relatively faster at the points on the sample located close to the bubble periphery than at the points located near the bubble center. This effect was most likely caused by spatially varying strength of the long-range attractive van der Waals forces from the substrate under the bubbles.

Spatially non-uniform and bubble size dependent deformation leads to a non-uniform and bubble size dependent underestimation of the bubble height and width in the AFM height images for non-zero force scanning conditions. This in turn will lead to an apparent contact angle underestimation, i.e. the curvature of the bubble will appear larger in the AFM topographic image than it really is. The results of Peak Force tapping experiments^{25,26} confirmed that this effect was stronger, the larger the peak force was in the measurements. We may conclude that surface nanobubbles are almost completely flat, pancake-like structure with large radius of curvature, instead of having a spherical cap shape, and possess an inner pressure close to the atmospheric pressure. In the view of these results, all AFM data concerning the bubble shape and related parameters as well as stability theories built on AFM evidence should be critically reviewed.

ASSOCIATED CONTENT

Experimental details, cross-sectional plots, details of the nanobubble deformation. This material is available free of charge via the Internet at <http://pubs.acs.org>.

AUTHOR INFORMATION

Corresponding Author

*E-mail: schoenherr@chemie.uni-siegen.de

Notes

The authors declare no competing financial interest.

ACKNOWLEDGMENT

The authors would like to thank Dr. S. Druzhinin and Dr. H. Knepe for enlightening discussions and helpful suggestions and gratefully acknowledge financial support from the Deutsche Forschungsgemeinschaft (DFG grant no. INST 221/87-1 FUGG), the European Research Council (ERC grant to HS, ERC grant agreement No. 279202) and the University of Siegen.

REFERENCES

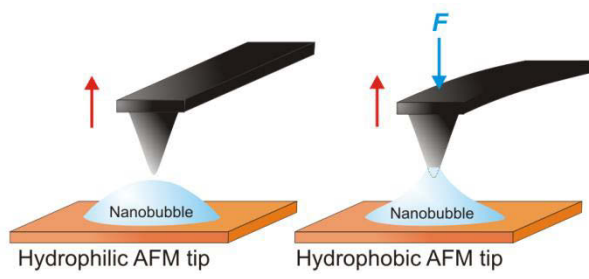
- (1) Binnig, G.; Quate, C. F.; Gerber, Ch. Atomic Force Microscope. *Phys. Rev. Lett.* **1986**, *56*, 930–933.
- (2) Weisenhorn, A. L.; Khirsandi, M.; Kasas, S.; Gotzos, V.; Butt, H.-J. Deformation and height anomaly of soft surfaces studied with an AFM. *Nanotechnology* **1993**, *4*, 106–113.
- (3) Chen, X.; Davies, M. C.; Roberts, C. J.; Tendler, S. J. B.; Williams, P. M.; Davies, J.; Dawkes, A. C.; Edwards, J. C. Interpretation of tapping mode atomic force microscopy data using amplitude-phase-distance measurements. *Ultramicroscopy* **1998**, *75*, 171–181.
- (4) Schönherr, H.; Frank, C. W. Ultrathin films of poly(ethylene oxides) on oxidized silicon. 2. In situ study of crystallization and melting by hot stage AFM. *Macromolecules* **2003**, *36*, 1199–1208.

- (5) Vancso, G. J.; Schönherr, H. *Scanning Force Microscopy of Polymers*; Springer: Berlin, **2010**.
- (6) Morris, V. J.; Kirby, A. R.; Gunning, A. P. *Atomic Force Microscopy for Biologists*; Imperial College Press: London, **2010**.
- (7) Connell, S. D. A.; Allen, S.; Roberts, C. J.; Davies, J.; Davies, M. C.; Tendler, S. J. B.; Williams, P. M. Investigating the Interfacial properties of single-liquid nanodroplets by atomic force microscopy. *Langmuir* **2002**, *18*, 1719–1728.
- (8) Craig, V. S. J. Very small bubbles at surfaces – the nanobubble puzzle. *Soft Matter* **2011**, *7*, 40–48.
- (9) Seddon, J. R. T.; Lohse, D. Nanobubbles and micropancakes: gaseous domains on immersed substrates. *J. Phys. Condens. Matter* **2011**, *23*, 133001.
- (10) Zhao, B.; Song, Y.; Wang, S.; Dai, B.; Zhang, L.; Dong, Y.; Lü, J.; Hu, J. Mechanical mapping of nanobubbles by PeakForce atomic force microscopy. *Soft Matter* **2013**, *9*, 8837–8843.
- (11) Song, Y.; Zhao, B.; Zhang, L.; Lü, J.; Wang, S.; Dong, Y.; Hu, J. The Origin of the „Snap-In” in the Force Curve between AFM Probe and the Water/Gas Interface of Nanobubbles. *ChemPhysChem* **2014**, *15*, 492–499.
- (12) Walczyk, W.; Schönherr, H. Characterization of the interaction between AFM tips and surface nanobubbles. *Langmuir* **2014**, *30*, 7112–7126.
- (13) Berkelaar, R. P.; Dietrich, E.; Kip, G.; Kooij, S.; Zandvliet, H.; Lohse, D. Exposing nanobubble-like objects to a degassed environment. *Soft Matter* **2014**, *10*, 4947–4955.
- (14) Ishida, N.; Inoue, T.; Miyahara, M.; Higashitani, K. Nano bubbles on a hydrophobic surface in water observed by tapping-mode atomic force microscopy. *Langmuir* **2000**, *16*, 6377–6380.
- (15) Lou, S. T.; Ouyang, Z. Q.; Zhang, Y.; Li, X. J.; Hu, J.; Li, M. Q.; Yang, F. J. Nanobubbles on solid surface imaged by atomic force microscopy. *J. Vac. Sci. Technol. B* **2000**, *18*, 2573–2575.
- (16) Agrawal, A.; Park, J.; Ryu, D. Y.; Hammond, P. T.; Russel, T. P.; McKinley, G. H. Controlling the Location and Spatial Extent of Nanobubbles Using Hydrophobically Nanopatterned Surface. *Nano Letters* **2005**, *5*, 1751–1756.
- (17) Song, B.; Walczyk, W.; Schönherr, H. Contact angles of surface nanobubbles on mixed self-assembled monolayers with systematically varied macroscopic wettability by Atomic Force Microscopy. *Langmuir* **2011**, *27*, 8223–8232.
- (18) Bhushan, B.; Wang, Y.; Maali, A. Coalescence and movement of nanobubbles studied with tapping mode AFM and tip-bubble interaction analysis. *J. Phys.: Condens. Matter* **2008**, *20*, 485004.

- (19) Borkent, B. M.; de Beer, S.; Mugele, F.; Lohse, D. On the shape of surface nanobubbles. *Langmuir* **2010**, *26*, 260–268.
- (20) Zhang, X. H.; Maeda, N.; Craig, V. S. J. Physical properties of nanobubbles on hydrophobic surfaces in water and aqueous solutions. *Langmuir* **2006**, *22*, 5025–5035.
- (21) Walczyk, W.; Schönherr, H. Closer Look at the Effect of AFM Imaging Conditions on the Apparent Dimensions of Surface Nanobubbles. *Langmuir* **2013**, *29*, 620–632.
- (22) Yang, S.; Kooij, E. S.; Poelsema, B.; Lohse, D.; Zandvliet, H. J. W. Correlation between geometry and nanobubble distribution on HOPG surface. *Europhys. Lett.* **2008**, *81*, 64006.
- (23) Holmberg, M.; Kühle, A.; Garnæs, J.; Mørch, K. A.; Boisen, A. Nanobubble Trouble on Gold Surfaces. *Langmuir* **2003**, *19*, 10510–10513.
- (24) Tyrrell, J. W. G.; Attard, P. Images of Nanobubbles on Hydrophobic Surfaces and Their Interactions. *Phys. Rev. Lett.* **2001**, *87*, 1761041–1761044.
- (25) Yang, C. W.; Lu, Y. H.; Hwang, I. S. Imaging surface nanobubbles at graphite-water interfaces with different atomic force microscopy modes. *J. Phys.: Condens. Matter* **2013**, *25*, 184010.
- (26) Walczyk, W.; Schön, P. M.; Schönherr, H. The effect of PeakForce tapping mode AFM imaging on the apparent shape of surface nanobubbles. *J. Phys.: Condens. Matter* **2013**, *25*, 184005.
- (27) Lu, Y. H.; Yang, C. W.; Hwang, I. S. Molecular layer of gaslike domains at a hydrophobic-water interface observed by frequency-modulation atomic force microscopy. *Langmuir* **2012**, *28*, 12691–12695.
- (28) Peng, H.; Hampton, P. A.; Nguyen, A. V. Nanobubbles Do Not Sit Alone at the Solid–Liquid Interface. *Langmuir* **2013**, *29*, 6123–6130.
- (29) Walczyk, W.; Hain, N.; Schönherr, H., Hydrodynamic effects of the tip movement on surface nanobubbles: A combined tapping mode, lift mode and force volume mode AFM study. *Soft Matter* **2014**, in press. DOI: 10.1039/C4SM01024H.
- (30) Wang, Y.; Bhushan, B. Boundary slip and nanobubble study in micro/nanofluidics using atomic force microscopy. *Soft Matter* **2010**, *6*, 29–66.
- (31) Ducker, W. A. Contact angle and stability of interface nanobubbles. *Langmuir* **2009**, *25*, 8907–8910.
- (32) Wang, S.; Liu, M.; Dong, Y. Understanding the stability of surface nanobubbles. *J. Phys.: Condens. Matter* **2013**, *25*, 184007.
- (33) Zhang, X.; Chan, D. Y. C.; Wang, D.; Maeda, N. Stability of Interfacial Nanobubbles. *Langmuir* **2013**, *29*, 1017–1023.

- (34) Liu, Y.; Zhang, X. Nanobubble stability induced by contact line pinning. *J. Chem. Phys.* **2013**, *138*, 014706.
- (35) Brenner, M. P.; Lohse, D. Dynamic Equilibrium Mechanism for Surface Nanobubble Stabilization. *Phys. Rev. Lett.* **2008**, *101*, 214505.
- (36) Petsev, N. D.; Shell, M. S.; Leal, L. G. Dynamic equilibrium explanation for nanobubbles' unusual temperature and saturation dependence. *Phys. Rev. Lett. E* **2013**, *88*, 10402.
- (37) Weijis, J. H.; Lohse, D. Why Surface Nanobubbles Live for Hours. *Phys. Rev. Lett.* **2013**, *110*, 054501.
- (38) Grosfils, P. Coarse-grained modelling of surface nanobubbles. *J. Phys.: Condens. Matter* **2013**, *25*, 184006.
- (39) Berkelaar, R. P.; Zandvliet, H. J. W.; Lohse, D. Covering Surface Nanobubbles with a NaCl Nanoblanket. *Langmuir* **2013**, *29*, 11337–11343.
- (40) Seddon, J. R. T.; Kooij, E. S.; Poelsema, B.; Zandvliet, J. W.; Lohse, D. Surface Bubble Nucleation Stability. *Phys. Rev. Lett.* **2011**, *106*, 056101.
- (41) Dietrich, E.; Zandvliet, H. J. W.; Lohse, D.; Seddon, J. R. T. Particle tracking around surface nanobubbles. *J. Phys.: Condens. Matter* **2013**, *25*, 184009.
- (42) Lhuissier, H.; Lohse, D.; Zhang, X. Spatial organization of surface nanobubbles and its implications in their formation process. *Soft Matter* **2014**, *10*, 942–946.
- (43) Zhang, X. H.; Quinn, A.; Ducker, W. A. Nanobubbles at the interface between water and a hydrophobic solid. *Langmuir* **2008**, *24*, 4756–4764.
- (44) Switkes, M.; Ruberti, J. W. Rapid cryofixation/freeze fracture for the study of nanobubbles at solid-liquid interfaces. *Appl. Phys. Lett.* **2007**, *84*, 4759–4761.
- (45) Zhang, X. Quartz crystal microbalance study of the interfacial nanobubbles. *Phys. Chem. Chem. Phys.* **2008**, *10*, 6842–6848.
- (46) Jensen, T. R.; Jensen, M. O.; Reitzel, N.; Balashev, K.; Peters, G. H.; Kjaer, K.; Bjørnholm, T. Water in contact with extended hydrophobic surfaces: Direct evidence of weak dewetting. *Phys. Rev. Lett.* **2003**, *90*, 0861.
- (47) Mezger, M. A.; Schöder, S. A. B.; Reichert, H. A.; Schröder, H. A.; Okasinski, J. A.; Honkimäki, V. B.; Ralston, J. C.; Bilgram, J. D.; Roth, R. A. E.; Dosch, H. Water and ice in contact with octadecyl-trichlorosilane functionalized surfaces: a high resolution x-ray reflectivity study. *J. Chem. Phys.* **2008**, *128*, 244705.
- (48) Zhang, L.; Zhao, B.; Xue, L.; Guo, Z.; Dong, Y.; Fang, H.; Tai, R.; Hu, J. Imaging interfacial micro- and nano-bubbles by scanning transmission soft X-ray microscopy. *J. Synchrotron Rad.* **2013**, *20*, 413–418.

- (49) Karpitschka, S.; Dietrich, E.; Seddon, J. R. T.; Zandvliet, H. J. W.; Lohse, D.; Riegler, H. Nonintrusive Optical Visualization of Surface Nanobubbles. *Phys. Rev. Lett.* **2012**, *109*, 066102.
- (50) Mirsaidov, U.; Ohl, C. -D.; Matsudaira, P. A direct observation of nanometer-size void dynamics in an ultra-thin water film. *Soft Matter* **2012**, *8*, 3108–3111.
- (51) Chan, C. U.; Ohl, C. -D. Total-Internal-Reflection-Fluorescence Microscopy for the Study of Nanobubble Dynamics. *Phys. Rev. Lett.* **2012**, *109*, 174501.
- (52) Hain, N.; Handschuh-Wang, S.; Druzhinin, S. I.; Schönherr, H. Probing Surface Nanobubbles with Fluorescence Lifetime Imaging Microscopy. *manuscript in preparation*.
- (53) Hain, N.; Wesner, D.; Zheng, S.; Handschuh-Wang, S.; Schönherr, H. Druzhinin, S. I.; Schönherr, H. Nanobubbles and Nanodroplets Studied by Combined AFM and Fluorescence Lifetime Imaging Microscopy. *manuscript in preparation*.
- (54) Liu, G.; Craig, V. S. J. Improved cleaning of hydrophilic protein-coated surfaces using the combination of nanobubbles and SDS. *ACS Appl. Mater. Interfaces* **2009**, *1*, 481–487.
- (55) Yang, S.; Dusterwinkel, A. Removal of nanoparticles from plain and patterned surfaces using nanobubbles. *Langmuir* **2011**, *27*, 11430–35.
- (56) Israelachvili, J. N.; Pashley, R. M. The hydrophobic interaction is long range, decaying exponentially with distance. *Nature* **1982**, *300*, 341–342.
- (57) Christenson, H. K.; Claesson, P. M. Cavitation and the interaction between macroscopic hydrophobic surfaces. *Science* **1988**, *239*, 390–392.
- (58) Parker, J. L.; Claesson, P. M.; Attard, P. Bubbles, cavities and the long-ranged attraction between hydrophobic surfaces. *J. Phys. Chem.* **1994**, *98*, 8468–8490.
- (59) Stockelhuber, K. W.; Radoev, B.; Wenger, A.; Schulze, H. J. Rupture of wetting films caused by nanobubbles. *Langmuir* **2004**, *20*, 164–168.
- (60) Maali, A.; Bhushan, B. Nanobubbles and their role in slip and drag. *J. Phys.: Condens. Matter* **2013**, *25*, 184003.
- (61) Ball, P. Nanobubbles are not a Superficial Matter. *ChemPhysChem* **2012**, *13*, 2173–2177.
- (62) Ally, J.; Kappl, M.; Butt, H. -J.; Amirfazli, A. Detachment Force of Particles from Air-Liquid Interfaces of Films and Bubbles. *Langmuir* **2010**, *26*, 18135–18143.
- (63) Loskill, P.; Hähl, H.; Faidt, T.; Grandthyll, S.; Müller, F.; Jacobs, K. Is adhesion superficial? Silicon wafers as a model system to study van der Waals interactions. *Adv. Colloid Interface Sci.* **2012**, *179-182*, 107–113.



On the dimensions and the profile of surface nanobubbles: Tip-nanobubble interactions and nanobubble deformation in Atomic Force Microscopy

*Wiktoria Walczyk and Holger Schönherr**

Physical Chemistry I, University of Siegen, Faculty of Natural Sciences and Engineering,
Department of Chemistry and Biology, Adolf-Reichwein-Str. 2, 57076 Siegen, Germany

Corresponding Author

* schoenherr@chemie.uni-siegen.de

Supporting Information

EXPERIMENTAL

Sample preparation: In all experiments freshly cleaved highly oriented pyrolytic graphite (HOPG) (grade ZYH, VeecoO, Santa Barbara, CA) with a water contact angle of $63 \pm 2^\circ$ was used. The static contact angle was measured with the sessile drop method with an OCA 15plus instrument (Data Physics Instruments GmbH, Filderstadt, Germany) using Milli-Q water obtained from a Millipore Direct Q 8 system (Millipore, Schwalbach, Germany) with resistivity of 18.0 M Ω /cm and surface tension of 0.072 N/m (determined by a Wilhelmi plate method). Nanobubbles were measured in Argon saturated Milli-Q water. First, 20 mL of Milli-Q in a clean round-bottom flask with a Teflon inlet were degassed at a pressure of 80 mbar for 30 min at 20°C by using a diaphragm vacuum pump (Type MZ 2C, Vacuubrand, Germany), while it was sonicated continuously in a water bath sonicator (Brandelin Sonorex, Rk 100 H). Next, the flask with water was closed, removed from the ultrasonic bath, and was put under an Ar stream (no filter used) for 45 min.

Atomic Force Microscopy: The AFM measurements were carried out on a MultiMode IIIa AFM instrument (Bruker/Veeco/Digital Instruments, Santa Barbara, CA) with a vertical engage E-scanner and NanoScope version 3.10 software (Bruker / Veeco, Santa Barbara, CA). V-shaped MLTC Si₃N₄ cantilevers (Bruker AXS, Camarillo, CA) with the following spring constants were used: $k_{cant} = 0.1 \pm 0.01$ N/m and $k_{cant} = 0.7 \pm 0.07$ N/m. The cantilevers' spring constants were calibrated on an Asylum Research MFP-3D Bio (Asylum Research, Santa Barbara, California). The cantilevers were cleaned prior to the measurements for 60 s by oxygen plasma (Plasma Prep-II, SPI Supplies, West Chester,

USA). In order to minimize the contamination of the tip, the cantilevers were inserted with minimal delay in the liquid cell and directly immersed in water.

In all experiments, a closed liquid cell configuration was used. First, the liquid cell, the O-ring (fluorosilicone rubber) and the inlet and outlet tubes (silicone) were rinsed with Milli-Q water and with ethanol (99.9 %, Merck KGaA, Darmstadt, Germany) and dried in a stream of nitrogen. Next, the liquid cell was assembled and the cantilever was inserted. Subsequently, a 1 mL sterile syringe (Braun, Injekt-F 0.01-1ml/luer Solo) was filled with the Ar saturated water and connected to the inlet tube. No needle was used for this procedure in order to avoid the possible contamination by the lubricant. Immediately, the water was injected in the liquid cell until the cantilever was immersed and the O-ring was filled. Then the liquid cell was placed on the sample, the O-ring was brought in contact with the sample, 0.6 mL of water was passed through the liquid cell and after that the inlet and outlet were closed. We stress that *no* liquid exchange procedure was performed and the HOPG surface did not have contact with ethanol at any stage of the experiment. Also, the lubricant free syringe used was cleaned by Milli-Q water before use. Before the start of the AFM measurement, the system was left for 30 min to equilibrate. The nanobubbles were scanned first in TM AFM and subsequently in FV mode without changing the cantilever and the tip or replacing the liquid.

Tapping mode (TM AFM): The drive frequency used for imaging in TM AFM was 9.2 kHz for the cantilever with $k_{cant} = 0.1 \pm 0.01$ N/m, and 29.6 kHz for the cantilever with $k_{cant} = 0.7 \pm 0.07$ N/m. The free amplitude of the cantilever oscillations (in Volts) was calculated from amplitude-displacement curves recorded before and after recording of the image, as an average of 50 points. Next, it was converted into free amplitude in

nanometers using the appropriate value of the deflection sensitivity. The amplitude setpoint ratio (ratio of the setpoint amplitude value set during the measurements and free amplitude calculated from the corresponding amplitude-distance curve) was calculated as the mean value of two setpoint ratios determined using amplitude-distance curves recorded before and after scanning a TM height image. The values of free amplitudes and setpoint ratios in TM measurements of nanobubbles in our experiments were 13 nm and 90 % for the experiment done with the cantilever with $k_{cant} = 0.1 \pm 0.01$ N/m, and 16 nm and 90 % for the experiment done with the cantilever with $k_{cant} = 0.7 \pm 0.07$ N/m. Raw TM height images were processed using a 1st order plane fit and a 0th order flattening (any nanobubble was excluded). No tip size correction was applied. The bubble size was measured using the spherical cap fitting.

Force Volume mode (FV AFM): In this mode the tip was lowered and retracted at each point of the selected area of the sample and the interaction forces during approach and retraction were measured. The resolution of the imaging was limited to 32×32 pixels². The cantilever oscillation was switched off during data acquisition in FV mode. Ramp sizes and trigger thresholds were set to 223 nm and 30 nm in the experiment done with the cantilever with $k_{cant} = 0.1 \pm 0.01$ N/m, and to 100 nm and 60 nm in the experiment done with the cantilever with $k_{cant} = 0.7 \pm 0.07$ N/m. The velocity of tip approach was set to 446 nm/s and 1.02 $\mu\text{m/s}$, respectively. The force curve resolution was set to 512 points per single approach-retraction cycle. Raw deflection-distance curves were transformed into deflection-separation curves. The vertical position of the tip above the *substrate* is represented in the plots by the tip-sample separation distance (zero separation indicates that the tip is in contact with the substrate). The deflection was recalculated into force by multiplying the measured deflection value with the corresponding cantilever stiffness.

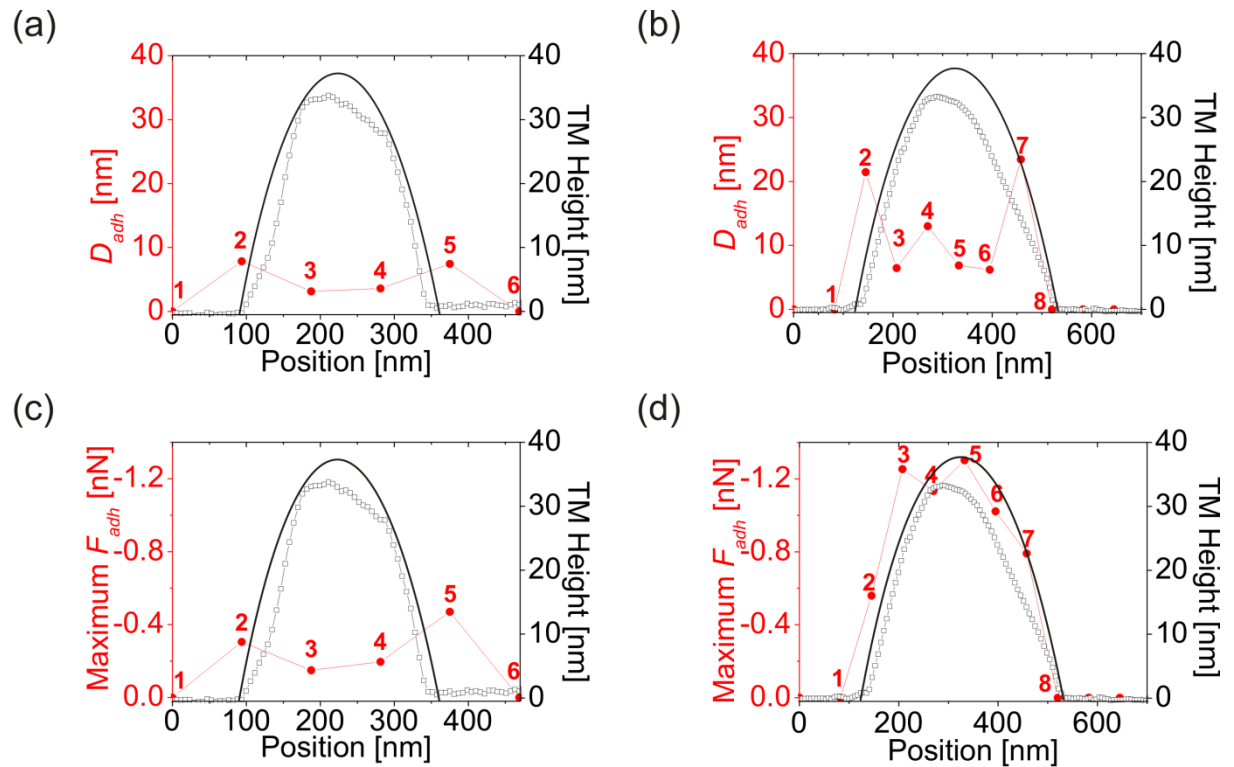


Figure S-1. (a) D_{adh} measured for the nanobubble scanned with a hydrophilic tip, (b) D_{adh} measured for the nanobubble scanned with a hydrophobic tip, (c) F_{adh} measured for the nanobubble scanned with a hydrophilic tip, (d) F_{adh} measured for the nanobubble scanned with a hydrophobic tip. In each cross-sectional plot, the values are plotted as a function of the horizontal position of the AFM tip along the scan line. The data measured from the force curves (solid red circles) are compared with the apparent (open black squares) and estimated (solid line) bubble profiles from TM AFM height images.

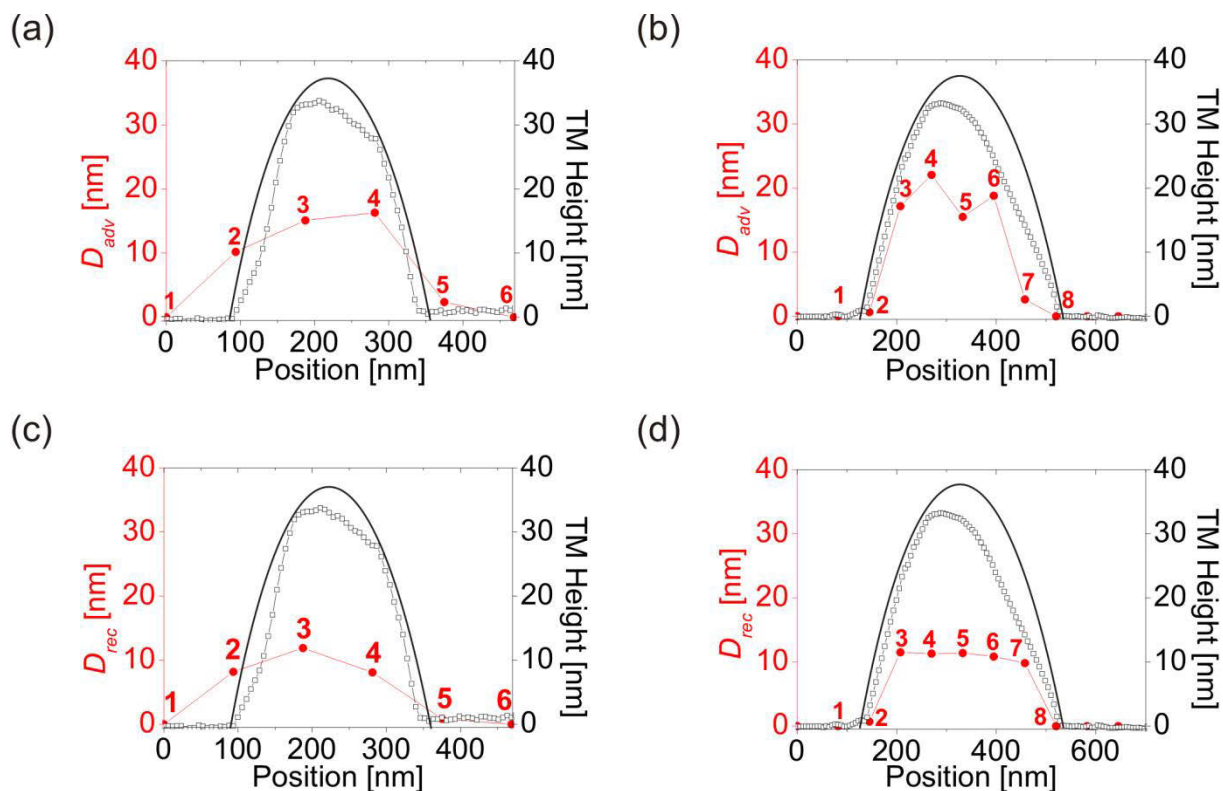


Figure S-2. (a) D_{adv} measured for the nanobubble scanned with a hydrophilic tip, (b) D_{rec} measured for the nanobubble scanned with a hydrophobic tip, (c) D_{adv} measured for the nanobubble scanned with a hydrophilic tip, (d) D_{rec} measured for the nanobubble scanned with a hydrophobic tip. In each cross-sectional plot the values are plotted as a function of the horizontal position of the AFM tip along the scan line. The data measured from the force curves (solid red circles) are compared with the apparent (open black squares) and estimated (solid line) bubble profiles from TM AFM height images.

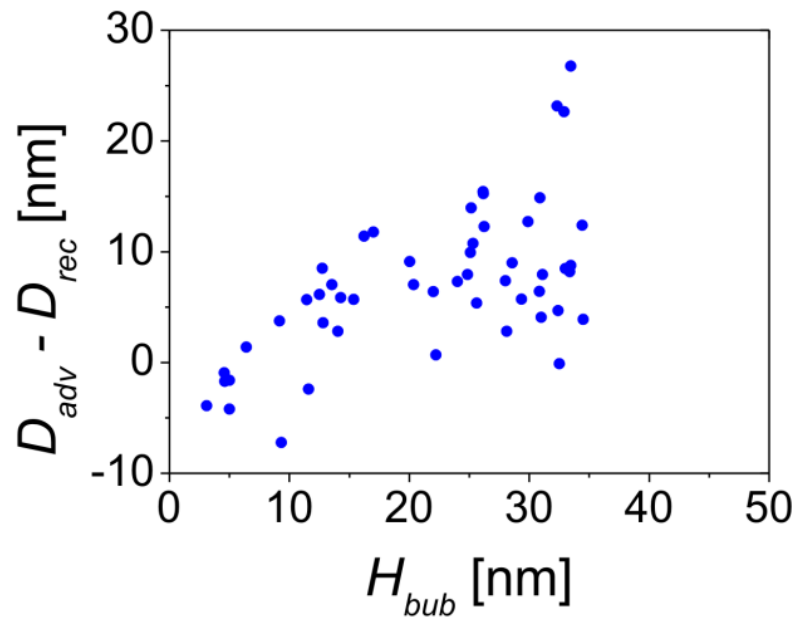


Figure S-3. Difference between the distances D_{adv} and D_{rec} as a function of the unperturbed local bubble height H_{bub} , measured from the force-distance curves acquired on the nanobubble with a hydrophobic tip.

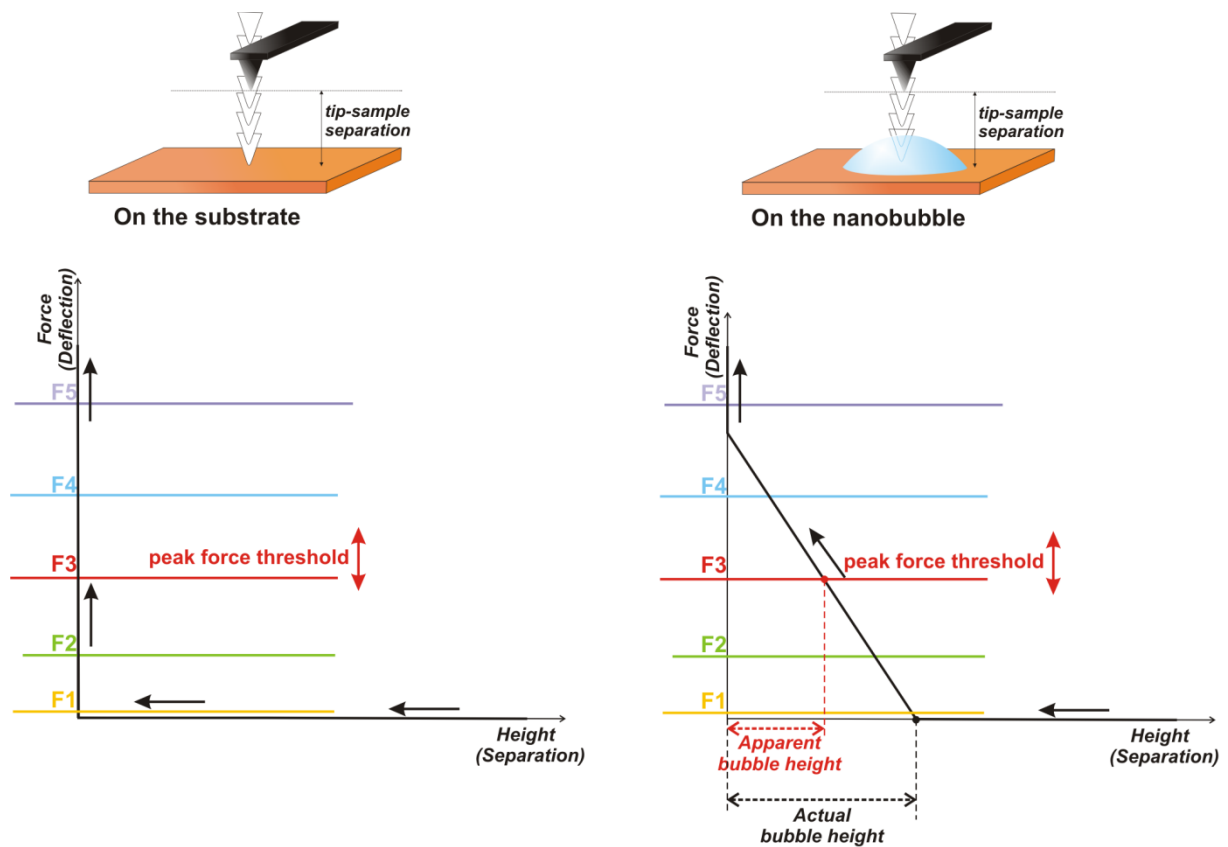


Figure S-4. Schematically shapes of AFM force-distance curves acquired on a hard substrate and on a soft nanobubble. The horizontal lines define the exemplary thresholds set by the peak force. The separation distance of the zero-deflection crossing point in the left force curve denotes the actual bubble height. The separation distance of the crossing point of the slope in the force curve with the line representing the force level indicates the apparent bubble height, as would be measured in an AFM height image scanned with this particular peak force.

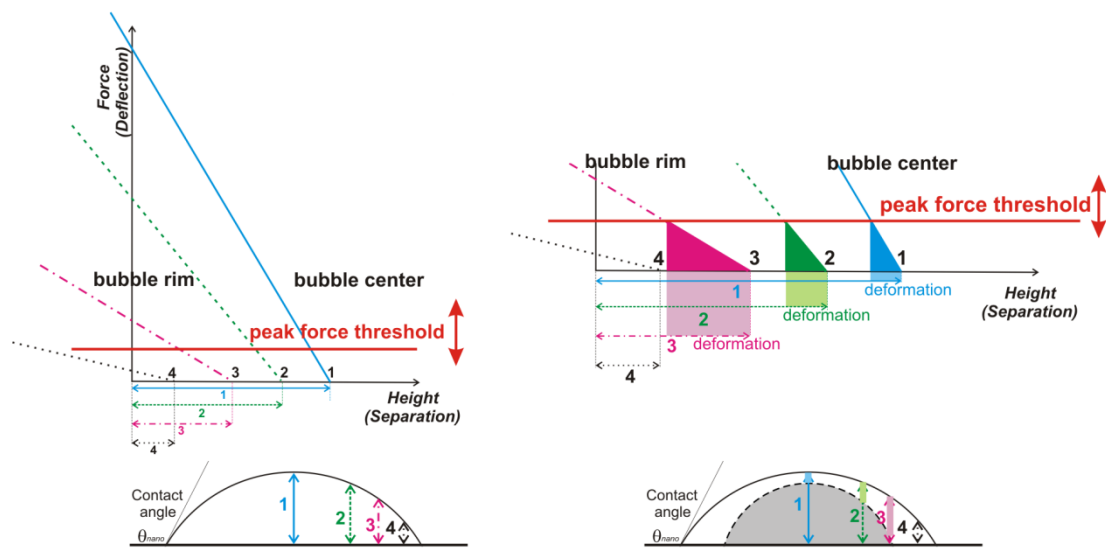


Figure S-5. The effect of varying steepness of the slopes of the force-distance curves on the measurement of the apparent nanobubble height. For a fixed peak force threshold, the apparent bubble height will be underestimated more and the bubble will be deformed to a larger extent near the bubble rim (less steep slopes) than near the bubble center (steeper slopes). A non-uniform underestimation of the actual bubble height will lead to a more protruding bubble shape with an underestimated width of the base and a smaller apparent contact angle (water side).

Conclusions and outlook

During the last two decades, Atomic Force Microscopy (AFM) has played an increasingly important role in research on surface nanobubbles. However, a systematic investigation on the impact of the AFM imaging parameters and forces on the results it provides was lacking. In this thesis, this issue has been addressed by performing detailed studies on the effect of AFM imaging conditions on the apparent dimensions of nanobubbles displayed in the AFM images obtained. In particular, an explanation has been sought for the unusually high apparent contact angles of nanobubbles (measured through water) observed experimentally. The aim of the research was to determine the actual nanobubble dimensions.

Main results

The results presented in the previous chapters prove that:

- (1) surface nanobubbles are soft, easily deformable structures with a stiffness comparable with the surface tension of pure water;
- (2) there exist at least two distinct mechanisms ruled by different forces that are responsible for the interaction between AFM tips and surface nanobubbles;
- (3) during imaging, the tip deforms the nanobubbles so that they do not display their actual dimensions in the AFM height images;
- (4) the substrate under nanobubbles affects the tip-nanobubble interaction forces and influences the bubble deformation;
- (5) these factors are not the sole reasons for the high apparent contact angles of nanobubbles observed in the AFM images;
- (6) the choice of AFM imaging modes and associated parameters may substantially affect the appearance of nanobubbles in the AFM images, hence influences all the parameters derived from the measured nanobubble profiles.

The results explain previous contradicting and confusing observations such as:

- (1) the unusual nanobubble stability under severe imaging conditions;
- (2) the large variation in the shapes of reported force-displacement curves acquired on nanobubbles;
- (3) the low reproducibility of the dimensions of nanobubbles in the images acquired under seemingly similar imaging conditions;
- (4) the differences in the reported dependences of apparent bubble dimensions on the amplitude setpoint ratio in Tapping Mode (TM) AFM;^{1,2}
- (5) the alleged dependence of nanobubble parameters on the bubble size;^{2,3} and
- (6) the effect of scan speed on the bubble appearance in the AFM images.⁴

AFM tip-nanobubble interactions

By comparing experimental data with the results provided by two models of the AFM tip-nanobubble interaction i.e. the capillary force and the dynamic interaction model, respectively, it has been found that the strength and character of the interaction depends strongly on the tip material, size and cleanness. In Chapter 7, it has been shown that when the measurement was done with a relatively hydrophilic AFM tip, the interaction forces originated from the hydrodynamic effect, which arises from squeezing a thin film of liquid between the tip apex and the bubble surface. These results were confirmed in Chapter 8 showing that the strength of the hydrodynamic effect depended also on the direction and speed of the tip movement with respect to the bubble. In case of the hydrophobic tip, the interaction during the measurement was governed mainly by the force arising from surface tension acting along the three-phase contact line attached to the tip.

In Chapter 5 and in Chapter 6, it has been shown that nanobubbles appeared smaller, both in the height and in the width, in the AFM height images measured for increased maximum imaging force (peak force) in Peak Force Tapping mode, or for increased free amplitude of the cantilever oscillation and decreased amplitude setpoint ratio in TM AFM. In fact, there will be no 'ideal' or 'optimal' imaging conditions because nanobubbles will always be deformed during the AFM measurement, even when the imaging forces are reduced to the piconewton range. This is not surprising since, as shown in Chapter 7, nanobubbles are very soft – softer than a typical AFM cantilever. Therefore they will deform easily by any external force applied. The larger

the force, the larger the bubble deformation and the lower the apparent bubble height in the AFM height images.

However, as described in Chapters 7 to 9, the qualitative and quantitative differences between the tips involved qualitatively different deformation of the nanobubble shape during the imaging. In fact, the interaction between the tip and the nanobubble resulted in mutual deformation of the bubble surface and the cantilever that differed depending on which forces governed the interaction. It has been shown that in case of tip-bubble attraction the bubble interface deformed towards the tip, the effect being stronger when a stiff cantilever was used. In addition, the bubble was stretched upwards and sideways when the tip apex was located off the bubble center. For a typical nanobubble, the upward deformation may extend up to tens of nanometers above the unperturbed bubble height, especially if the measurement is done with a hydrophobic tip that penetrates the bubble surface and directly contacts the bubble during imaging. For a relatively hydrophilic tip, the bubble deformation is a dynamic effect of the drainage of the liquid film between the tip and the bubble under the influence of external force. The presence of the film prevents stretching of the bubble surface upwards and sideways. In addition, when the hydrophilic tip is pressed against the bubble interface, the hydrodynamic effect “protects” the bubble from being penetrated. Instead, the bubble wraps around the tip adapting its shape to the tip profile and movement without establishing contact (wetting) with the tip material. A similar scenario does not hold for a relatively hydrophobic tip, for which the hydrodynamic effect is absent.

The “protecting” effect of the thin liquid film offers an explanation for the unusual bubble stability observed in different AFM scanning modes and under harsh scanning conditions. At the same time, the presence of the film governs the nanobubble deformation, and its possible consequences for the measurements of nanobubble dimensions must be taken into account while imaging nanobubbles in various AFM modes. A detailed study of this issue makes an interesting topic for future research. In particular, more investigation would help to improve the dynamic interaction model⁵ by adapting it to nanoscopic bubbles and droplets. This could include a series of experiments performed under conditions of controllably varied surface tension obtained by purposely introducing contamination in the system. Subsequently, the model might be used to study spatial and temporal evolution of the bubble shape during the interaction with AFM tip. Finally, the analysis of the tip-nanobubble interaction and nanobubble deformation in the AFM imaging modes that involve

complex tip movement such as TM AFM would be a valuable source of information about the relation between the actual and the apparent nanobubble shapes.

During the work, it has become clear that the cleanliness of AFM tip is crucial to the stability of the imaging process and the quality of the images. When the tip is hydrophobic, e.g. due to contamination, an accidental contact between the tip and the bubble might occur during the imaging when the tip and the bubble surface are separated by only a few nanometers. If this is the case, the bubble wets the tip material and therefore attaches to the tip apex and forms a meniscus around it. For a low-viscosity liquid such as water, this happens very quickly⁶ – on a time scale of about 10 ns, which is much shorter than the typical period of the cantilever oscillation in liquid ($\sim 10 \mu\text{s}$) in TM AFM. If this happens, the cantilever oscillation is heavily damped and the contact causes deformation of the bubble surface and possibly (increased) tip contamination. All these effects are detrimental to the accuracy in measuring nanobubble dimensions.

Rules of AFM imaging of surface nanobubbles

Based on the work presented in this thesis, a set of rules of AFM imaging of surface nanobubbles (and possibly other very soft microscopic structures) has been determined. In order to minimize bubble deformation and obtain reliable AFM results one must:

- (1) avoid that solid surface is exposed to a contaminated liquid/gas interface during filling of the AFM liquid cell, and minimize the contact of water with possibly contaminated surfaces;
- (2) choose a cantilever with a very low spring constant (preferably less than 0.07 N/m) and a sharp hydrophilic tip; pre-clean the cantilever and the tip;
- (3) preferably use an AFM imaging mode that allows direct control of the magnitude of the imaging force;
- (4) minimize the imaging force in order to minimize the bubble deformation and the tip wear; while measuring in TM AFM, minimize the amplitude of cantilever oscillation and maximize the setpoint ratio;
- (5) control and note the values of imaging parameters before, during and after scanning an image; if possible, record several images of the same nanobubbles to allow the data comparison;

- (6) carefully process and analyze the data considering available information about the system and the imaging conditions;
- (7) avoid the comparison of apparent data acquired under different (or unknown) experimental conditions.

Actual nanobubble dimensions

The question that has propelled the work presented in this thesis states: Is it possible to estimate the actual nanobubble dimensions and to reconstruct the nanobubble shape using information about the effect of the AFM technique on the apparent nanobubble dimensions in the images? In order to answer this question, one must first look back at the results of the TM and Peak Force Tapping AFM experiments described in Chapter 5 and in Chapter 6. Based on the detailed analysis of experimental data, a method has been proposed to estimate the actual unperturbed nanobubble dimensions based on their apparent dimensions and the values of corresponding imaging parameters. The method involved extrapolation of the apparent nanobubble dimensions to the ideal non-invasive scanning conditions – 100% amplitude setpoint ratio and zero free amplitude of the cantilever oscillation in case of TM AFM, and zero peak force in case of Peak Force Tapping AFM. Importantly, as shown in Chapter 9, because this method is based on the implicit assumption that the attraction between the AFM tip and the bubble interface is absent, it may be applied only if the measurement was done with a relatively hydrophilic tip. As described in Chapter 7 and in Chapter 9, this can be deduced from the shape of force-distance curves measured on the bubble (quasi-linear slope, low attraction, low hysteresis, etc.).

Relying purely on “quantitative” data (bubble height), the extrapolation method does not allow a distinction between hydrophobic and hydrophilic AFM tips. Consequently, since the character of the tip-nanobubble interaction and the nanobubble deformation in a particular experiment are unknown, it is not clear how the dimensions estimated based on the acquired data are related to the actual nanobubble dimensions. In the experiments described in Chapter 7 and in Chapter 9, it has been shown that in case of (mildly) hydrophobic tip, this uncertainty may lead to a significant under- or overestimation of the actual nanobubble size (height). On the contrary, the method yielded reasonable results when the imaging was done with relatively hydrophilic tips. It has been proven that in the absence of the attraction between the nanobubble surface and the tip apex, the estimated

values of the nanobubble height were in good agreement with the actual unperturbed heights measured from force-distance curves acquired on the bubbles.

This is a remarkable result since in TM AFM, the imaging relies on damping of the cantilever oscillation and not directly on monitoring changes in the imaging force. In addition, in TM, the estimation is a two-step procedure involving first the extrapolation of the bubble height to 100% setpoint ratio conditions for a given non-zero amplitude of the cantilever oscillation, and subsequently, the extrapolation of the estimated value to zero amplitude conditions. Since one cannot obtain empirical data measured for non-zero amplitudes at 100% setpoint ratio, in the second step of the estimation procedure, one must rely on the height-amplitude dependence measured at 90-95% setpoint ratio assuming that it does not significantly differ from the expected dependence for 100% setpoint ratio. Moreover, as discussed in detail in Chapter 5, in addition to the fact that the quantitative dependence of nanobubble dimensions on the setpoint ratio is different for different amplitude values and, consequently, that the complementary dependence of the nanobubble size on the amplitude varies depending on the setpoint ratio, both dependences are also functions of the (actual) nanobubble size. To simplify, larger nanobubbles respond differently than smaller nanobubbles to the imaging done under similar conditions, and their deformation, hence change in the apparent dimensions will be quantitatively different. This effect should also be taken into account when estimating the actual nanobubble height.

Compared to TM AFM, Peak Force Tapping AFM allows a more straightforward and more accurate estimation of the actual nanobubble dimensions. As described in Chapter 6, it can be done either by direct extrapolation of the apparent data to zero force conditions (taking into account the influence of bubble size on the size-force dependence) or by combining the information from height, deformation and adhesion images. This feature, as well as better control of the forces put on the sample, makes Peak Force Tapping mode more suitable to image surface nanobubbles than TM AFM. Another benefit of Peak Force Tapping mode is that it allows simultaneous acquisition of images showing sample topography, deformation and other force-related parameters (however, it is not entirely clear how the data is processed), and provides one with raw force data measured for each point of the scanned area of the sample. Such an abundance of information facilitates subsequent data analysis.

Faced with the fact that, to date, most of the research on surface nanobubbles has been performed in the TM AFM, and knowing the character of the (hydrophilic)

tip-nanobubble interaction, it would be beneficial to investigate how the nanobubble deformation is influenced by the oscillating movement of the AFM tip and by damping of the oscillation amplitude. In particular, in order to more accurately estimate the actual nanobubble shape, it might be interesting to learn about the details of nanobubble deformation for various imaging conditions such as e.g. large and small amplitudes of the cantilever oscillation or varied oscillation frequency.

Another issue that requires more investigation is the (quasi)-linear character of various dependences observed experimentally. The extrapolation methods proposed in Chapter 5 and in Chapter 6 were based on the linear dependence of the bubble height (and possibly other parameters) on the oscillation amplitude, the setpoint ratio, and the peak force. In addition, in Chapter 7 and in Chapter 8, several of the force-distance curves measured experimentally on the nanobubbles and calculated from the tip-bubble interaction models (mainly from the dynamic interaction model) displayed linear slopes. However, in the formulas describing the tip-bubble interaction, the dependence between the force applied on the tip and the distance (cantilever deflection) was non-linear. Why then are linear dependences so prevailing in the experimental data? Future research that would establish the exact character of the dependences measured experimentally might provide answer to this question.

Going back to the question about the actual nanobubble dimensions, several ways have been shown to obtain relatively accurate estimation of the unperturbed nanobubble height. Now one needs to focus on other parameters such as bubble width, curvature and contact angle.

Nanosopic contact angle

In this thesis, the issue of the nanobubble contact angle has repeatedly been addressed. In the experiments, bubbles on two sorts of substrates were investigated – binary self-assembled monolayers (SAMs) of octadecanethiol (ODT) and 16-mercapto hexadecanoic acid (MHDA) on ultraflat template-stripped gold (Chapter 4), and highly oriented pyrolytic graphite (HOPG) (Chapters 5 to 9). On the macroscopic length scale, the materials displayed a range of contact angles with water. The SAMs substrates had the contact angles between $107^\circ \pm 1^\circ$ and $15^\circ \pm 3^\circ$, depending on the ODT/MHDA ratio; the HOPG had the contact angle of $63^\circ \pm 2^\circ$. Yet, on the nanoscopic scale, bubbles displayed high apparent contact angles ($>130^\circ$) on almost all the samples, with exclusion of only the most hydrophilic ones described in Chapter 4. These nanoscopic contact angles were always larger than the

corresponding macroscopic contact angles. These results are surprising because flat surfaces that have macroscopic contact angle with water at room temperature greater than 150° have not been reported. However, as already mentioned in the previous chapters, these results are in agreement with the substantial experimental evidence reported so far.^{1,2,7,8} At this point, it is interesting to note that, on the one hand, in Chapter 4 it has been observed that the nanoscopic contact angle varied with the varied wettability of the samples; on the other hand, in the experiments described in Chapters 5 to 9, measured contact angles were between $\sim 130^\circ$ and $\sim 175^\circ$ for the nanobubbles on the HOPG sample. Interestingly, contrary to nanobubbles, nanodroplets investigated with the AFM did not display such a striking contact angle anomaly while being exposed to similar experimental conditions, level of contamination, possibility of imaging artefacts etc.^{9,10}

It is likely that very close to the substrate, the shape of the three-phase contact line deviates from that of a spherical cap due to action of surface forces.¹¹ Unfortunately, this effect cannot be observed by means of the AFM due to limited resolution of the technique, finite size of an AFM tip, deformation of the surface, roughness of the substrate and the tip. In the experiments, it has been determined that the apparent nanobubble contact angle and the contact angle discrepancy are not induced solely neither by the AFM imaging, nor by the tip convolution, nor by the bubble height underestimation caused by the invasive imaging conditions. Instead, the apparent contact angle is strongly influenced by a complex interplay between the parameters describing the imaging, the bubble, the tip and the cantilever, and the substrate. These issues have been extensively investigated in Chapter 7, Chapter 8 and Chapter 9 and it has been established that the tip-bubble interaction strength depended on the vertical and horizontal position of the tip on the bubble with respect to the bubble center. Attractive forces dominated the region near the bubble rim, whereas repulsive (or less attractive) forces dominated the region near the bubble center. This spatial variation of the interaction strength was most likely due to long-range attractive forces originating from the substrate under the bubble, which dominated the interaction at the bubble rim.

Spatial dependences

It has been shown that non-uniform tip-bubble interaction led to the non-uniform size-dependent nanobubble deformation and caused the non-uniform bubble size-dependent underestimation of the bubble height, width and, consequently,

the underestimation of the nanoscopic contact angle. This means that the curvature of nanobubbles will appear larger in the AFM topographic images than it really is. The detailed analysis of this effect led to the conclusion that, assuming that the spherical-cap shape model is valid, surface nanobubbles have nearly flat pancake-like profiles with large radii of curvature and Laplace pressure close to the atmospheric pressure. As a continuation of the presented work, more research on the topic of the tip-nanobubble interaction is needed in order to obtain more accurate estimation of the actual nanobubble dimensions and their internal pressures. In particular, the knowledge of the details of the interplay between forces originating from the bubble interface and from the substrate near the bubble rim would help to improve the quality of the estimation of the actual nanobubble width.

The findings concerning the non-uniform nanobubble deformation may explain the dependence of parameters on the bubble size observed in the experiments. In chapter 5, it has been shown that the severity of the underestimate of the actual bubble dimensions increased with increasing bubble height and radius of curvature. Similarly, as described in Chapter 6, the size underestimation for a non-zero peak force was more pronounced for larger bubbles. This variation was attributed to the difference in Laplace pressure – bubbles with larger radii of curvature, which possessed smaller Laplace pressures, showed more pronounced force-induced apparent size reduction. However, as described in detail in Chapter 9, the mechanism responsible for the dependence of parameters on the apparent bubble size involves more factors than merely Laplace pressure. It has been shown that the non-uniform nanobubble deformation – larger near the rim than near the bubble center – depended on the local bubble height at a particular point. According to the same reasoning applied to bubbles of different sizes, smaller bubbles will deform relatively more than larger bubbles. However, if, at the same time, smaller bubbles are indeed stiffer than larger bubbles, as suggested above, they will deform relatively less. Obviously, the issue of size-dependent nanobubble stiffness is still unclear and requires more investigation. Future research on nanobubble deformation would require a comprehensive and careful consideration of possible sources of under- and overestimation of bubble dimensions. This might imply the necessity of revision of existing AFM data on surface nanobubbles and reconsideration of several issues such as, for instance, the role of line tension. The aim would be to identify the most important factors and to describe quantitatively their combined impact on the apparent bubble shape in order to develop a universal method to determine the actual nanobubble dimensions. This research might help to resolve several other

issues such as the alleged dependence of bubble curvature on the nanoscopic contact angle^{2,3} and the variation in the apparent contact angle of nanobubbles measured on HOPG.

Pinning

Assuming that surface nanobubbles are gaseous domains, the predicted very flat shape of bubbles explains their prolonged stability¹² and the uniformity of their contact angles. However, it is yet unclear which mechanism is responsible for the extraordinary flatness of nanobubbles. Seemingly, different mechanism plays a dominant role on nanoscale than on macroscale. Among the possible scenarios is the pinning of three-phase contact line to the substrate,¹³ which has recently gained increasing attention as a possible nanobubble stabilization mechanism. In Chapter 6, it has been shown that in Peak Force Tapping AFM, the adhesion, deformation and dissipation channels displayed the unaltered footprint area of the bubble also for large peak forces i.e. in those cases, when the apparent bubble width was significantly reduced in the height image. The pinning of the contact line is one of possible explanations of these results. Similarly, the observed variation in the apparent (and estimated actual) contact angles of nanobubbles on HOPG between approximately 130° and 175° could be related to pinning. However, so far, it is difficult to make any definitive statement. In future research, it would be beneficial to determine how the nanobubble stability due to pinning depends on physical and chemical roughness of the sample and whether it can explain nanobubble stability to increased temperature.¹⁴ In addition, the hypothesis of pinning brings up two other yet unresolved issues: the presence and the role of contamination¹⁵ and micropancakes.¹⁶ Both topics have been widely discussed, also throughout this thesis, but the consensus has not been reached so far. Another pinning-related question that arises, concerns the difference in nanobubble appearance on hydrophobic vs hydrophilic surfaces. Clearly, more investigation is needed to address the presented issues. In addition, in the view of recent reports on the possibility that many reported surface nanobubbles may consist of contamination,¹⁷ there is a great urgency to chemically characterize nanobubbles, micropancakes and nanobubble-micropancake composites.

Final remarks

The work presented in this thesis shows that a choice of the measurement technique is one of the most important factors in the research on surface nanobubbles. In the view of the complexity of AFM and its considerable influence on nanobubble appearances in the images, there is great need of finding an independent detection and measuring method. In addition, the recently revived discussion on the origin of nanobubbles and their nature (composition)¹⁷ creates a necessity to critically review the existing procedures to generate nanobubbles in order to determine and possibly minimize the problem of contamination in the system.

Since it has not yet been unequivocally resolved whether surface nanobubbles are gaseous or liquid domains, it is important to note that although the experiments described in this thesis were done under the assumption that surface nanobubbles are gaseous domains, the results presented in the previous chapters, as well as these conclusions, remain valid also in the case when “nanobubbles” are liquid contaminant droplets. Clearly, AFM cannot help to unequivocally solve this issue of nanobubble composition.

From the material presented in this thesis, it has become clear that, independently from the chemical nature of surface nanobubbles, critical verification of the AFM data and the theories built based on the information derived from AFM images is a necessary step toward meaningful description of nanobubbles. In sum, future research on the topic of the AFM measurements of nanobubbles should involve systematic investigations concerning the quantitative details of the nanobubble deformation, the tip-nanobubble interaction, and the role of the parameters inherent to a particular AFM scanning mode. It might be also beneficial to consider how the presented findings on the AFM on surface nanobubbles can be adapted to the AFM studies performed on other soft matter systems on nanoscale e.g. nanodroplets.

Independently on the AFM studies, practical applications of surface nanobubbles and their possible presence in various systems make also interesting topics for future research. To give only few examples: the possible biological impact of nanobubbles, their role in various (natural) phenomena, creation of patterned surfaces, and applications in microfluidics are the issues that are particularly interesting not only from the fundamental but also from the practical point of view.

However, before moving to nanobubbles in complex systems, the remaining uncertainties need to be addressed in a consistent and systematic way. This includes verification of mixed and controversial results on a number of topics concerning e.g. the nucleation method, the presence of water depletion layer near hydrophobic surfaces, the dependence of contact angle on the nanobubble curvature, and stability theories.

References

- 1 Zhang, X. H.; Maeda, N.; Craig, V. S. J. Physical Properties of Nanobubbles on Hydrophobic Surfaces in Water and Aqueous Solutions. *Langmuir* **2006**, *22*, 5025–5035.
- 2 Borkent, B. M.; de Beer, S.; Mugele, F.; Lohse, D. On the shape of surface nanobubbles. *Langmuir* **2010**, *26*, 260–268.
- 3 v. Limbeek, M. A. J.; Seddon, J. R. T. Surface Nanobubbles as a Function of Gas Type. *Langmuir* **2011**, *27*, 8694–8699.
- 4 Bhushan, B.; Wang, Y.; Maali, A. Coalescence and movement of nanobubbles studied with tapping mode AFM and tip-bubble interaction analysis. *J. Phys.: Condens. Matter* **2008**, *20*, 485004.
- 5 Chan, D. Y. C.; Dagastine, R. R.; White, L. R. Forces between a Rigid Probe Particle and a Liquid Interface. I. The Repulsive Case. *J. Colloid Interface Sci.* **2001**, *236*, 141–154.
- 6 Checco, A. Droplet Morphology at Nanometer Scale (in *Nanoscale Liquid Interfaces - Wetting, Patterning and Force Microscopy at the Molecular Scale* ed. by Ondarçuhu, T.; Aimé, J.-P.) *Pan Stanford Publishing* **2013**.
- 7 Zhang, X. H.; Li, G.; Maeda, N.; Hu, J. Removal of Induced Nanobubbles from Water/Graphite Interfaces by Partial Degassing. *Langmuir* **2006**, *22*, 9238–9243.
- 8 Zhang, X.; Uddin, M. H.; Yang, H.; Toikka, G.; Ducker, W.; Maeda, N. Effects of Surfactants on the Formation and the Stability of Interfacial Nanobubbles. *Langmuir* **2012**, *28*, 10471–10477.
- 9 Checco, A.; Guenoun, P.; Daillant, J. Nonlinear Dependence of the Contact Angle of Nanodroplets on Contact Line Curvature. *Phys. Rev. Lett.* **2003**, *91*, 186101.
- 10 Zhang, X. H.; Ducker, W.; Formation of interfacial nanodroplets through changes in solvent quality. *Langmuir* **2007**, *23*, 12478–12480.
- 11 Getta, T.; Dietrich, S. Line tension between fluid phases and a substrate. *Phys. Rev. E* **1998**, *57*, 655–671.
- 12 Zhang, X. H.; Quinn, A.; Ducker, W. A. Nanobubbles at the interface between water and a hydrophobic solid. *Langmuir* **2008**, *24*, 4756–4764.
- 13 Zhang, X.; Chan, D. Y.; Wang, D.; Maeda, N. Stability of Interfacial Nanobubbles. *Langmuir* **2013**, *29*, 1017–23.
- 14 Zhang, X.; Lhuissier, H. E.; Sun, C.; Lohse, D. Surface Nanobubbles Nucleate Microdroplets. *Phys. Rev. Lett.* **2014**, *112*, 144503.
- 15 Ducker, W. A. Contact angle and stability of interfacial nanobubbles. *Langmuir* **2009**, *25*, 8907–8910.
- 16 Zhang, X. H.; Zhang, X.; Sun, J.; Zhang, Z.; Li, G.; Fang, H.; Xiao, X.; Zeng, X.; Hu, J. Detection of Novel Gaseous States at a HOPG-Water Interface. *Langmuir* **2007**, *23*, 1778–1783.
- 17 Berkelaar, R. P.; Dietrich, E.; Kip, G.; Kooij, S.; Zandvliet, H.; Lohse, D. Exposing nanobubble-like objects to a degassed environment. *Soft Matter* **2014**, *10*, 4947–4955.

Summary

Nanoscale gas bubbles on surfaces immersed in water, investigated in this thesis, termed “surface nanobubbles”, with diameters hundred times smaller than the diameter of a human hair and ten times smaller than the diameter of a red blood cell belong to the realm of nanoscale. Since surface nanobubbles involve three phases, i.e. gas, liquid and solid, they present an excellent system to study wetting of surfaces on the nanoscale, which becomes increasingly important in nanotechnology, biology and other fields.

The work presented in this thesis aimed toward a better understanding of the role of Atomic Force Microscopy (AFM), which is the technique that is commonly used to investigate surface nanobubbles, in the outcome of the analysis of the shape and dimensions of nanobubbles. In particular, it is highly necessary to recognize the discrepancy between the apparent nanobubble shape visible in AFM images and the actual unperturbed shape of nanobubbles. This issue is particularly important because the knowledge about actual nanobubble curvature and contact angle is crucial for solving the puzzle of the long-term stability of nanobubbles, which would undoubtedly accelerate current research in the field.

After a brief introduction in Chapter 1 into the occurrence and the role of bubbles in systems on different length scales, Chapter 2 presents basic information on the wetting and the AFM technique, and summarizes experimental and theoretical work done on surface nanobubbles in the last two decades. Several issues such as the morphology, nucleation, stability and practical applications of nanobubbles are addressed in detail. The general presentation of the topic in Chapter 2 sets the foundations for the experimental work described in the thesis.

Chapter 3 provides the motivation behind the research and presents the main scientific challenges addressed in the thesis. It also describes the research hypotheses and lists the objectives of the experiments presented in the subsequent chapters.

The high apparent contact angle, seemingly independent from the hydrophobicity of the substrate, is one of the features of surface nanobubbles that are in contradiction with theoretical predictions. With the AFM being practically the only source of information on nanobubble dimensions, the question arose whether the unusually flat profile of nanobubbles had its source in the AFM imaging or was caused by an independent mechanism. In order to address this issue, we conducted a series of AFM experiments described in Chapter 4 to investigate the contact angles of nanobubbles on surfaces with controllably varied wettability. The first part of the chapter describes in detail the method of sample preparation; the second part focuses on the AFM results. We have established that the apparent nanoscopic contact angle of nanobubbles decreases with decreased hydrophobicity of the substrates; however, its value always exceeds the corresponding macroscopic value, hence the flat shape of nanobubbles is not induced merely by the AFM scanning. In the experiments, very low contact angles of nanobubbles on hydrophilic substrates were measured for the first time.

The mechanism of AFM imaging requires that a non-zero force is exerted on the sample. This makes the AFM an invasive technique, especially for investigating soft samples like surface nanobubbles. Even though it has been suspected in nanobubble research that nanobubbles may become deformed during the imaging process, the magnitude of the effect was unknown and its eventual impact on the acquired experimental data was usually neglected.

We systematically investigated the issue of nanobubble deformation in two AFM imaging modes most commonly used to study surface nanobubbles – tapping mode (TM) AFM and Peak Force Tapping AFM. In the experiment performed in TM, which is described in Chapter 5, we varied two parameters that define the magnitude of the force applied on a sample during the imaging – the amplitude of the cantilever oscillations and the amplitude setpoint ratio – in order to establish a quantitative relation between the values of the parameters and the change in the apparent nanobubble dimensions in the AFM height images. The results allowed us to develop a method to estimate the actual dimensions of nanobubble in a particular TM experiment based on their apparent shapes and sizes, and the values of the scanning parameters used to acquire the image.

The results of the complementary experiment performed in Peak Force Tapping AFM are presented in Chapter 6. In this experiment, we systematically investigated how the apparent nanobubble size changed for varying peak scanning force exerted on

the sample during the imaging. A detailed comparison of the results obtained in TM and in Peak Force mode led to the conclusions that nanobubble deformation is a common phenomenon in the AFM, and that nanobubbles are always deformed while imaged with the AFM, i.e. that they do not display their actual dimensions in the AFM height images. In addition, we have shown that the extent and the character of nanobubble deformation vary depending on the utilized imaging mode.

Knowing the effects of the AFM scanning on the apparent nanobubble dimensions in the AFM height images, we focused on the nanobubble shape and, in particular, on the nanobubble shape deformation. Because the nanobubble deformation is caused directly by the interaction forces between the nanobubble surface and the apex of a sharp tip used as a probe in the AFM imaging, in our next experiments, we aimed to characterize the tip-nanobubble interaction and to describe its role in determining the apparent nanobubble shape and dimensions in the AFM images. So far, this topic has not been thoroughly studied and the nature of the tip-nanobubble interaction forces was unknown.

First, in the experiment described in Chapter 7, we have determined the stiffness of the nanobubble interface and we have found that it is comparable with the surface tension of water, which is consistent with the assumption that surface nanobubbles are gaseous domains. These findings supported our earlier hypothesis that nanobubbles are very soft, compared to the stiffness of an AFM cantilever, hence they will easily become deformed during the imaging. In addition, we have discovered that, depending on the cleanliness and the size of an AFM tip, the interaction between the tip and the nanobubble is governed by different forces that create entirely different experimental conditions and lead to different nanobubble deformation. In particular, a hydrophobic AFM tip likely penetrates the bubble during imaging and both the interaction strength and the bubble deformation are governed mainly by the capillary force acting through a three-phase contact line that forms on the tip. On the contrary, a hydrophilic tip interacts with the bubble through a thin liquid film that separates the tip apex from the bubble surface at all times during the imaging. In this scenario, the bubble deformation is determined by the hydrodynamic effect arising from squeezing the film as the tip approaches the bubble.

Further details about the hydrodynamic effect and the interaction between hydrophilic tips and nanobubbles during the AFM imaging are provided in Chapter 8 that describes a combined experiment performed on nanobubbles in lift mode and in Force Volume AFM. In this experiment, we investigated the effect of varying direction and speed of the tip movement during the imaging on the nanobubble deformation. We have found that the magnitude and the character of the deformation varied depending on whether the tip approached the bubble from the top or from the side. These findings may have significant consequences for the nanobubble deformation in the AFM imaging modes that involve different tip movement protocol during the measurement.

Finally, in Chapter 9, we analyze in detail the nanobubble deformation as a function of the position of the tip on the bubble under different experimental conditions. We show that the magnitude of deformation and the strength of the tip-bubble interaction display complex dependences on the size of the bubble and the tip, and on the relative position of the tip on the bubble with respect to its center and its distance to the surface. After discussing the possible reasons of the spatial dependence of the nanobubble deformation, we consider the consequences of this effect for the shape of nanobubbles in the AFM images. Based on our findings, we deduce the unperturbed nanobubble shape that differs from its apparent shape and from the shape of macroscopic bubbles. Namely, we postulate that the AFM imaging leads to an underestimation of the apparent nanobubble contact angle, which implies that nanobubbles are very flat structures with a Laplace pressure that only slightly exceeds the atmospheric pressure.

Zusammenfassung

Bringt man Oberflächen in Kontakt mit Wasser, bilden sich nanoskopische Gasblasen, sogenannte Oberflächennanoblasen („Surface Nanobubbles“), die in dieser Arbeit untersucht wurden. Mit einem Durchmesser hundertmal kleiner als der des menschlichen Haares und zehnmals kleiner als der roter Blutkörperchen gehören sie zum Nanokosmos. Da an Oberflächennanoblasen Grenzflächen der drei Phasen Gas, Flüssigkeit und Feststoff auftreten, bilden sie ein ideales System zum Studium der Benetzbarkeit von Oberflächen auf der Nanoebene – einer Thematik von zunehmender Bedeutung für die Nanotechnologie, Biologie und anderer Bereiche.

Das Ziel der in dieser Dissertation durchgeführten Arbeiten ist ein besseres Verständnis der Rasterkraftmikroskopie (AFM) und der Auswirkung verschiedener Messparameter auf die apparenten Dimensionen der Nanoblasen. Dies ist von besonderer Bedeutung, da die mittels AFM gewonnenen Daten die Basis für die Berechnung der Krümmungsradien und Kontaktwinkel der Nanoblasen bilden. Aus diesen Parametern ergeben sich bislang nicht zufriedenstellend beantwortete Fragen nach der unerwartet langen Lebensdauer der Nanoblasen, so dass eine grundlegende Überprüfung der experimentellen Befunde einer weiteren theoretischen Betrachtung vorausgehen muss.

Nach einer kurzen Einführung zum Auftreten und der Bedeutung von Blasen in Systemen unterschiedlicher Längenskalen in Kapitel 1, stellt Kapitel 2 grundlegende Informationen zu der Benetzung von Oberflächen sowie der AFM-Technik dar und fasst den Stand der Forschung zu Surface Nanobubbles der letzten zwei Dekaden zusammen. Dabei werden Themen wie die Morphologie, Keimbildung und Stabilität sowie praktische Anwendungen von Nanoblasen detailliert behandelt. Diese allgemeinen Betrachtungen legen die Basis für die experimentellen Arbeiten, die in dieser Dissertation behandelt werden.

Kapitel 3 thematisiert die Fragestellungen, die diese Forschungsarbeit begründen und die wissenschaftlichen Herausforderungen, die hier behandelt werden. Dabei werden die Forschungshypothesen diskutiert und die daraus abgeleiteten Zielsetzungen der Experimente dargelegt, welche in den folgenden Kapiteln beschrieben werden.

Der hohe Kontaktwinkel, der anscheinend unabhängig von der Hydrophobie des Substrats ist, ist eine der Eigenschaften von Nanoblasen, die im Widerspruch zu theoretischen Vorhersagen steht. Da AFM praktisch die einzige Technik ist, die Informationen zu den Dimensionen von Nanoblasen liefern kann, stellte sich die Frage, ob das ungewöhnlich flache Profil der Nanoblasen auf die AFM-Messungen selbst zurückzuführen ist, oder durch einen weiteren unabhängigen Mechanismus hervorgerufen wird. Um dieses Problem zu bearbeiten, haben wir eine Reihe von AFM Experimenten durchgeführt und die Kontaktwinkel der Nanoblasen auf Oberflächen von systematisch variiert Benetzbarkeit bestimmt (Kapitel 4). Der erste Teil des Kapitels beschreibt detailliert die Probenpräparation; der zweite Teil befasst sich mit den AFM Ergebnissen. Wir haben festgestellt, dass der apparente nanoskopische Kontaktwinkel der Nanoblasen mit abnehmender Hydrophobie des Substrates sinkt. Allerdings übersteigt er immer den entsprechenden makroskopischen Wert, so dass das flache Profil der Nanoblasen nicht allein durch den AFM Scan hervorgerufen wird. In diesen Experimenten wurden erstmals sehr niedrige Kontaktwinkel von Nanoblasen auf hydrophilen Oberflächen gemessen.

Das Prinzip der AFM-Abbildung erfordert, dass eine gewisse Kraft auf die Probe ausgeübt wird. Dadurch wird AFM zu einer invasiven Technik, insbesondere bei der Untersuchung weicher Proben wie Nanoblasen. Auch wenn seit Beginn der Forschung an Nanoblasen vermutet wurde, dass die Blasen durch den Abbildungsprozess deformiert werden können, war das Ausmaß unbekannt und die möglichen Auswirkungen auf die experimentellen Resultate wurden weitgehend vernachlässigt.

Wir haben das Problem der Deformation von Nanoblasen systematisch für zwei Abbildungs-Modi untersucht, die häufig in Studien von Nanoblasen eingesetzt werden – Tapping Mode (TM) AFM und Peak Force Tapping AFM. In den Experimenten im TM, die in Kapitel 5 beschrieben sind, haben wir zwei Parameter variiert, die die Größe der auf die Probe übertragenen Kraft definieren – die Amplitude der Schwingung des Cantilevers und das Verhältnis von Setpoint und Amplitude. So konnten Zusammenhänge zwischen den Werten dieser zentralen Scan-Parameter und den apparenten Dimensionen der Nanoblasen quantifiziert werden.

Diese Ergebnisse erlaubten es uns, eine Methode zu entwickeln, durch die aus den apparenten Dimensionen einer Nanoblase und den jeweiligen Scanparametern die tatsächliche Gestalt einer Nanoblase abgeschätzt werden kann.

Die Ergebnisse der entsprechenden Peak Force Tapping AFM Experimente sind in Kapitel 6 dargestellt. In diesen Experimenten haben wir systematisch die apparente Größe der Nanoblasen in Abhängigkeit von der maximal ausgeübten Kraft untersucht. Ein detaillierter Vergleich der Resultate aus Tapping Mode und Peak Force AFM hat zu dem Ergebnis geführt, dass die Deformation der Nanoblasen ein generelles Phänomen bei AFM Abbildungen ist, d.h. die tatsächliche Gestalt der Nanoblasen wird durch die gemessene Topographie nicht korrekt wiedergegeben. Weiterhin haben wir gezeigt, dass das Ausmaß und der Charakter der Deformation der Nanoblasen von dem jeweiligen Abbildungsmodus abhängen.

Nachdem die Auswirkungen eines AFM-Scans auf die apparenten Dimensionen der Nanoblasen in topographischen AFM Abbildungen herausgearbeitet waren, haben wir die Aufmerksamkeit auf die Gestalt der Nanoblasen uns insbesondere auf die Deformation der Gestalt gelegt. Da die Deformation der Nanoblasen direkt durch die Wechselwirkungskräfte zwischen der Blase und dem Apex der AFM Spitze hervorgerufen wird, zielten unsere nächsten Experimente darauf ab, die Interaktion der AFM-Spitze und der Nanoblase zu charakterisieren und ihren Einfluss auf die Form und Dimension der Nanoblase im AFM-Bild zu beschreiben. Bislang wurde dieser Aspekt nicht tiefergehend analysiert und die Natur der Wechselwirkungskräfte zwischen Spitze und Nanoblase war unbekannt.

Zuerst haben wir in den Experimenten beschrieben in Kapitel 7 die Steifigkeit der Oberfläche der Nanoblasen bestimmt. Diese liegt im Bereich der Oberflächenspannung von Wasser, was mit der Annahme konsistent ist, dass es sich bei den Nanoblasen um gasgefüllte Domänen handelt. Das Ergebnis unterstützte unsere Hypothese, dass Nanoblasen verglichen mit der Steifigkeit von AFM-Cantilevern sehr weiche Strukturen sind und sich während der Abbildung leicht deformieren lassen. Weiterhin haben wir herausgefunden, dass abhängig von der Sauberkeit und Größe der AFM-Spitze die Interaktion zwischen einer Nanoblase und der AFM-Spitze von verschiedenen Kräften bestimmt wird, die gänzlich verschiedene experimentelle Bedingungen schaffen und zu unterschiedlichen Deformationen der Nanoblasen führen. So penetriert eine hydrophobe Spitze die Blase während der Abbildung und sowohl die Stärke der Wechselwirkung als auch die Deformation der Blase werden bestimmt von Kapillarkräften, die in dem Drei-Phasengebiet

an der Spitze wirken. Im Gegensatz dazu interagiert eine hydrophile Spitze mit der Nanoblaste über einen dünnen Flüssigkeitsfilm, der zu jeder Zeit eine Grenzfläche zwischen der Spitze und der Blase bildet. In diesem Fall wird die Deformation der Blase von hydrodynamischen Effekten bestimmt, die bei dem Herauspressen des Flüssigkeitsfilms zwischen der Blase und der sich nähernden Spitze auftreten.

Weitere Details des hydrodynamischen Effekts und der Wechselwirkung hydrophiler Spitzen und Nanoblasten während der Abbildung mit AFM finden sich in Kapitel 8, das ein kombiniertes Experiment im Lift Mode und im Force Volume Mode beschreibt. In diesem Experiment haben wir den Effekt einer unterschiedlichen Richtung und Geschwindigkeit der Spitzenbewegung auf die Deformation der Blasen untersucht. Wir fanden einen Unterschied im Ausmaß und der Art der Deformation abhängig davon, ob sich die Spitze der Blase von oben oder von der Seite nähert. Diese Ergebnisse können signifikante Auswirkungen auf die Deformation von Nanoblasten haben, wenn Abbildungsmodi eingesetzt werden, die unterschiedliche Protokolle der Spitzenbewegung während der Messung nutzen.

In Kapitel 9 haben wir abschließend eine detaillierte Analyse der Deformation der Nanoblasten in Abhängigkeit von der Position der Spitze auf der Blase unter verschiedenen experimentellen Bedingungen vorgenommen. Hier zeigen wir, dass die Größe der Deformation und die Stärke der Wechselwirkung zwischen der Spitze und einer Blase eine komplexe Abhängigkeit von der Größe der Spitze und der Blase sowie der relativen Position der Spitze bezüglich des Mittelpunkts der Blase und dem Abstand zur Blase aufweist. Nach der Diskussion möglicher Gründe der ortabhängigen Deformation der Nanoblasten betrachten wir die Konsequenzen für die Form von Nanoblasten in AFM-Abbildungen. Basierend auf unseren Ergebnissen leiten wir die Form einer unbeeinflussten Nanoblaste ab, die sich sowohl von ihrer apparenten Form als auch von der Form makroskopischer Blasen unterscheidet. Somit kommen wir zu dem Schluss, dass der apparente Kontaktwinkel basierend auf AFM-Abbildungen unterschätzt wird, was bedeutet, dass Nanoblasten sehr flache Strukturen sind und der Laplace-Druck den Atmosphärendruck leicht übersteigt.

Acknowledgements

Actually, I wanted to work with microbubbles. But apparently, life had different plans for me. When I first heard about surface nanobubbles, I still was a student in the Physics of Fluids group at the University of Twente in the Netherlands, looking for a topic of my Master project. (Un)fortunately, at this time, there was not any project available involving microbubbles. I could choose between flow in a channel, numerical simulations, or nanobubbles. “Fine” I thought “let it be nanobubbles, ‘nanobelletjes’, at least they are bubbles. Only pity, that I will not even see what I work with.” At this moment, I did not know that these tiny bubbles would become such a big part of my life for the next several years. Without much pondering, I hopped on this (bubble) train* and it took me on a journey toward unknown through ever-changing scientific landscape.

In retrospect, it was a fascinating experience to see how this (at the time) very new topic of surface nanobubbles was developed, how new ideas were born and grew or died, how initially each new observation led to more questions than answers, how the current knowledge about nanobubbles has been built piece by piece by researchers all over the world. I am thankful that I could not only observe the whole process but also participate in it and even contribute my piece. This experience has taught me to be curious, to be humble, to be critical, and to be confident in defending my position. The perspective that I have gained and the skills I have learnt during the time of my PhD will stay with me for the rest of my life.

In the PhD phase of my scientific journey I was accompanied by several people who helped me, directly or indirectly, to develop the project and to shape it into its final form.

* The “bubble train” really exists, although one cannot travel with it.

First of all, I would like to thank my supervisor Holger Schönherr for his long term guidance and support, for inviting me from a “nice and flat Nederland” to a “nice and hilly Siegerland” and trusting me with a nanobubble project. I am extremely grateful for long hours of discussions that have been a constant intellectual (and linguistic) challenge. Dank je wel, Holger, I enjoyed them a lot. I thank him for sharing his knowledge, paying attention to details and constantly encouraging me to improve and not to agree for less than “the best”. I particularly appreciate his undying conviction that “there is a method in this (nanobubble data) madness” and his inspiring enthusiasm for science.

Next, I want to express my gratitude towards all co-workers and colleagues from the Physical Chemistry I, who helped me at various stages of my project. I am thankful to Davide Tranchida and to Bo Song for introducing me to the AFM equipment, teaching me the operation of Bioscope and watching my first steps in a chemical lab. I would like to thank Rose-Marie Beyer-Neidhardt for helping with all formalities and infallibly guiding me through the meanders of German bureaucracy. My special thanks go to Gregor Schulte for fixing the AFMs and my computer, answering hundreds of my questions, and allowing me to decorate the orange funnel from the SEM lab with the Dutch national colors. I thank Mohammad Raoufi for SEM measurements of the AFM tips and for his friendship and all the help, especially during my first year in Germany. محمدر، خیل ی متشکرم. I am grateful to Daniel Wesner for his help with the Nanoscope, all the discussions and for improving the German translation of the Summary of my thesis. I thank Nicole Hain for sharing the AFM-on-nanobubbles experience. I also want to thank Sergey Druzhinin for helpful ideas, inspiring discussions, and challenging questions.

I am thankful to all my PC I colleagues for introducing me to various chemical topics, for their help in the chemical lab, especially for answering my questions believing that it is possible to teach a physicist some chemistry. I am especially thankful to Lars Birlenbach for giving me a chemistry book. I thank them for all the questions, ideas and remarks that helped me to improve my research and the way to present it. Especially, I would like to thank my office-mates Ekram Wassel, Simon Haas, Stephan Handschuh, Mir Morteza Sadat Ebrahimi, Manuel Roesener, Faria Afzal, Elena Sperotto and the others for their company, all their help, and for teaching me German (and Persian).

I am thankful for the fruitful collaboration with the Materials Science and Technology of Polymers group at the University of Twente (UT) in Enschede, The Netherlands. In particular, I am grateful to Julius Vancso for giving me an opportunity to work with Peak Force Tapping AFM, to Peter Schön for his hospitality and assistance with the measurements, and to Clemens Padberg for his help with all technical issues.

I would like to acknowledge Detlef Lohse and James Seddon from the Physics of Fluids group, UT, The Netherlands for helpful discussions on nanobubbles.

I thank the University of Siegen for granting a financial support.

Finally, I want to thank my parents and my friends for constant love and support, for understanding (or even sharing) my enthusiasm for bubbles of various kinds, and for constantly reminding me that there is a life beyond PhD. Without you all, I would not have reached the end point of this project. I would not even have dared to start. Dziękuję! Thank you! Dankje! ! ڄرسى Grazie!

Wiktorja

